Tesfaye Haimanot Tarekegn

Downstream suspended sediment dynamics of reservoir sediment flushing

November 2015

Doctoral thesis in Science for MAnagement of Rivers and their Tidal System,

Cycle: II

Primary Institution:

Department of Civil, Environmental and Mechanical Engineering, University of Trento

Secondary Institution:

Department of Physical Geography, Queen Mary University of London

Supervisors:

Prof. Maurizio Righetti, University of Trento

Dr. Marco Toffolon, University of Trento

Prof. Geraldene Wharton, Queen Mary University of London

Thesis Examination Committee:

Prof. Philippe Belleudy, LTHE-Université Grenoble Alpes, France

Dr. Kees Sloff, Delft University of Technology, The Netherlands

Prof. Luigi Fraccarollo, University of Trento, Italy

The SMART Joint Doctorate Programme

Research for this thesis was conducted with the support of the Erasmus Mundus Programme[1], within the framework of the Erasmus Mundus Joint Doctorate (EMJD) SMART (Science for MAnagement of Rivers and their Tidal systems). EMJDs aim to foster cooperation between higher education institutions and academic staff in Europe and third countries with a view to creating centres of excellence and providing a highly skilled 21st century workforce enabled to lead social, cultural and economic developments. All EMJDs involve mandatory mobility between the universities in the consortia and lead to the award of recognised joint, double or multiple degrees. The SMART programme represents collaboration among the University of Trento, Queen Mary University of London, and Freie Universität Berlin. Each doctoral candidate within the SMART programme has conformed to the following during their 3 years of study:

i.   Supervision by a minimum of two supervisors in two institutions (their primary and secondary institutions).

ii.   Study for a minimum period of 6 months at their secondary institution.

iii. Successful completion of a minimum of 30 ECTS of taught courses.

iv.   Collaboration with an associate partner to develop a particular component/ application of their research that is of mutual interest.

v.   Submission of a thesis within 3 years of commencing the programme.

"የጥበብ መጀመሪያ እግዚአብሔርን መፍራት ነው፡፡"

መዝሙረ ዳዊት ፻፲፩፥፲

This work is dedicated to

Lensa Esaw

and

Nathan Tesfaye

ACKNOWLEDGMENTS

ABSTRACT

Reservoir sediment flushing is increasingly considered beneficial to reduce sedimentation of reservoirs and maintain sediment supply downstream of impounded rivers. Nevertheless, flushing of the accumulated sediments downstream of the dam also bears numerous negative impacts. In this study, first the most important downstream impacts of fine sediment releases of flushing were identified based on previously published research of twenty case studies in eleven countries. The results showed that the long-term as well as short term biological and physical impacts decreased with distance from the dam. The temporal scale of impacts on macro-invertebrates could span from few weeks or a month to several months while the effect on fish could last for a number of years. The impacts on downstream vegetation dynamics is driven by many years of flushing activities. The study also enabled proposing generic management strategies aimed to reduce the impacts.

Second, fine sediment transport in coarse immobile bed, which is a common phenomenon downstream of dams during flushing releases, dam removal and also in many mountain and canyon rivers, was investigated. Particularly, the dynamics of the downstream erosion and transport of fine sediments released during sediment flushing was investigated based on a series of flume experiments that were carried out in immobile gravel bed and using a one-dimensional (1-D) suspended sediment transport model developed in the present study. In the framework of the flume experiment, firstly gravel bed roughness, porosity and roughness density were exclusively extracted from gravel surface elevation data in which developing a spatial filter to overcome elevation errors was carried out. Secondly a new technique to acquire fine sediment erosion in immobile coarse bed in running water condition was developed. The method proved to be the back bone of all fine sediment erosion experiments conducted in the present study and could be used for similar studies. This study presents a first work of direct measurement of erosion rate and characterizing its spatial heterogeneity in gravel bed. The experimental data of erosion rate of fine sediments showed that it varied spatially with high erosion rate on the stoss side of gravels and less on the lee side conforming to sweeps and ejections characteristics in coherent flow structure of gravel bed flows. Erosion rate was significantly affected by increase in roughness of immobile gravel bed with high erosion rate noticed when sand level was reduced although the effect on stream-wise velocity was not significant. The vertical profile of erosion rate was found to decrease linearly and showed an exponential decay in time in the gravel matrix.

Third, a new non-equilibrium erosion rate relation is proposed. Drag force profile in the interfacial sublayer of clean gravel bed was found to be scaled well with roughness density and allowed predicting the effective shear stress distribution available for fine sediment entrainment with an empirical equation.

The new relation is a modified version of the pick-up rate function of van Rijn (1984b) in which the predicted shear stress in the roughness layer was implemented. The most important finding was that if the shear stress distribution in the interfacial sublayer is predicted, a relation for sand bed condition can be applied to predict fine sediment erosion rate in immobile gravel bed. This approach is conceptually superior to previous approaches where erosion rate in sand bed condition was scaled empirically for various fine sediment bed level within the interfacial sublayer.

Finally, the effect of the interaction between hydrodynamic and sediment wave dynamics of sediment flushing on spatial pattern of sediment deposition was investigated. The 1-D model was developed to include major processes observed in sediment flushing: sediment wave celerity correction, variable bed roughness, bed exchange in immobile bed, hindered settling velocity and rough bed porosity. The proposed erosion rate relation showed encouraging results when implemented in the 1-D model. The wave celerity factor did not show significant effect on the spatial lag in immobile bed condition although was significant in sand bed condition. Variable bed roughness modified both the flow field and sediment deposition in which larger length of sediment deposit was noted. The immobile bed porosity allowed modelling clogged depth of fine sediments. The model was also found to be very valuable to investigate flushing scenarios that reduce significant deposition through the analysis of the dependence of deposition on peak-to-base flow and intermittence of releases. The highest peak-to-base flows produced the longest and thickest region of deposition while those with the lowest ratio produced the shortest and thinnest. A single flushing release followed by clear water release reduced area or length of sediment deposition more than intermittent flushing followed by inter- and post-flushing clear water releases. In the latter case, the peak of concentration reduced but remained higher for longer duration than the former, which suggests that a large quantity of clear water release has to be available.

Overall, the present research represents a step forward in understanding relevant processes involved in the downstream transport of fine sediments released during sediment flushing and the associated impacts that can help the development of better management strategies and predictive tools.

CONTENTS

LIST OF FIGURES

LIST OF TABLES

1. INTRODUCTION

Dams were built and used to regulate rivers over 5000 years including the period of ancient Egyptian civilization (Petts and Gurnell, 2005). Currently there are about 50,000 large dams worldwide (ICOLD, 2013). These dams are operated to continuously trap sediment, without specific provisions for sustained long-term use (Morris and Fan, 2010), causing severe reservoir sedimentation problems. Today the total annual worldwide rate of loss of reservoir storage capacity due to reservoir sedimentation is about 0.5 to 1.9 % (Liu et al., 2004a). Reservoir sedimentation has even become a major setback for economic and sustainable development in many developing countries due to siltation of hydropower and irrigation dams (Basson, 2010). The altered flow regimes downstream of dams and the interruption of transfer of sediments from headwater source areas (Kondolf, 1997; Petts and Gurnell, 2005) have also brought significant changes to the flow and sediment regimes of many large rivers. Such changes have significant effects on downstream river substrate and ecological state thus resulting in disturbance of habitats for various aquatic organisms (Brooker, 1981).

To reduce reservoir sedimentation, various active and passive techniques have been developed including sediment flushing, sluicing, dredging and soil conservation and watershed management (e.g. Di Silvio, 2004). Among these, sediment flushing, defined as the scouring of previously deposited sediments by hydraulic method and release through bottom outlets of the reservoir, is the most effective, economic and fastest method to reduce reservoir sedimentation (Liu et al., 2002b). Sediment flushing can be beneficial not only by reducing sedimentation of reservoirs but also by increasing sediment supply downstream (e.g. Sumi and Kantoush, 2010). However, the high flows induced by the sudden release of water and high concentration of fine sediments often causes significant effects on downstream river reaches (e.g. Ma et al., 2012). Its downstream biological, physical and chemical impacts are further complicated by the scale and extent of the impacts that vary depending on downstream river morphology, ecological diversity, channel characteristics, hydrologic regime, the type of flushing operations and other factors. A detailed analysis of downstream impacts of sediment flushing obtained from many contrasting case studies may improve our understanding and help to develop a common management strategy. Nevertheless, despite many scientific studies reported different case studies, there is a lack of a comprehensive inter-disciplinary review of the impacts of fine sediment releases by flushing operations in various environmental and geomorphic settings. It can be argued that such analysis will be very useful to develop and propose best management strategies and identify suitable modelling exercises to assess downstream impacts.

Flushing operations introduce large quantity of fine sediments (non-cohesive suspended sediments in the size range from 0.062 mm to 2 mm) that are transported downstream. The channel bed downstream of a dam is usually deprived of sediment supply and suffers from continuous erosion of the channel bed and this leaves only coarser and immobile beds, which is often called a degraded and armoured bed (Kondolf, 1997). Thus, the fine sediments released during flushing operations are transported in the immobile coarse bed (e.g. Wren et al., 2011). Similar phenomenon is also common in natural rivers such as mountain, alpine and canyon rivers whose bed consist of coarse bed and distinguishable isolated roughness elements, such boulders or clasts (e.g., Wohl, 2000; Papanicolaou et al., 2004) that are transported in rare events and most of the sediments passing trough are fine sediments (Grams and Wilcock, 2014). Moreover, in many rivers the sediment load comprises largely fine sediments and a decrease in fine sediment supply relative to transport capacity could lead to parts of underlying bed substrate become exposed and transport occurs over a bed that consists partially of fine sediment and partially of large immobile particles (e.g. Kleinhans et al., 2002). This transport phenomenon is complicated by non-equilibrium transport and unsteady flows generated during flushing operations and the transport, entrainment and deposition of the released fine sediments in the immobile coarse bed becomes difficult to predict (Wren et al., 2011). Despite the relevance of this transport phenomenon in natural rivers and events such as sediment flushing very little research has been conducted to understand and model the processes of fine sediment transport in immobile coarse bed. Particularly, a proper description of erosion (entrainment) rates of fine sediments in immobile coarse beds are essential to develop predictive models for planning sediment flushing operations, post flushing cleaning of the clogged beds and including planning dam removal (e.g. Cui et al., 2008).

Modelling the downstream transport of released fine sediments is very useful to understand main processes observed during flushing transport, identify release scenarios, and assess potential downstream environmental impacts. Most of previous modelling exercises of sediment flushing were aimed to understand deposition and erosion processes within the reservoir so as to improve flushing efficiency (e.g. Lai and Shen, 1996; Olsen, 1999; Chang et al., 1996; Lui et al., 2004b; Yang and Simões, 1998). Nevertheless, development of numerical models to study downstream transport processes and the downstream morphological effects of the released sediments has been limited until recently (e.g. Liu et al., 2004a; Rathbun and Wohl, 2001; Gallerano and Cannata, 2011; Tarekegn et al., 2014). The characteristics of the downstream transport of released fine sediments can be considered different from fluvial transport that occurs during flood events (e.g. Brandt and Swenning, 1999; Tarekegn et al., 2014). The transport during flushing operations is often characterized by time lag between released sediment and hydrodynamic waves, high sediment concentration and an immobile coarse channel bed, processes that

are not included in many existing sediment transport models. Field observations of released liquid and solid discharges of sediment flushing indicate that a significant time lag occurs between the liquid and solid discharge as the waves propagate downstream (Brandt and Swenning, 1999; Brandt, 2005). These lags could lead to spatial lags in the waves and could affect the spatial pattern of sediment deposition (e.g. Tarekegn et al., 2014). Nevertheless, the mechanism how the temporal and spatial pattern of the deposition is controlled by the interaction between the two waves is not yet clear. Thus developing a simplified modelling tool that enable one to understand the effects of such interactions on the depositional pattern is useful, specifically to model the process at large spatial scale since the wave interactions are observed at larger spatial scales. In connection to this a proper description of the sediment wave celerity could prove crucial but in many numerical models this is neglected. Similarly since the sediment concentration is very high, sediment deposition could be significantly affected by hindered settling (van Maren et al., 2009) and model formulations that take into account this phenomenon are required which are often lacking. On the other hand, modelling practices currently in use for predicting the transport and entrainment of fine sediments are developed for channel bed conditions that have the same grain size as in suspension. It is useful develop modelling approaches that predict the transport of the released fine sediment in immobile coarse bed which is a common phenomenon downstream of dams during flushing operations. In connection to this the prediction of sediment deposition within the roughness elements of the immobile bed is useful to quantify bed clogging and the variability in bed roughness that could affect the hydrodynamic wave.

The PhD thesis is organized into five main parts. Chapter 2 describes a first work on comprehensive and inter-disciplinary review of major downstream impacts of sediment flushing practices. The review focused on physical, biological and chemical impacts of sediment releases obtained from 20 different case studies in 11 countries reported by around 36 scientific studies. The review identified important management strategies to reduce downstream negative impacts of sediment flushing.

Chapter 3, 4 and 5 are based on laboratory experiments involving non-equilibrium uniform fine sediment (d_{50} = 425μm and 500μm) transport in immobile gravel bed (d_{50} = 24.89mm). Chapter 3 describes immobile gravel bed roughness characterization based on random field approach and identifies the challenges of data acquisition by Position Sensitive Detector (PSD) laser sensors. In this Chapter gravel surface elevation data errors are identified and a normalized median filter was proposed to eliminate the errors. The effect of the errors on bed roughness characterization such as vertical length scale, horizontal length scale and second order structure function was significant. Thus a proper quality check is recommended. The gravel surface elevation data was finally used to estimate the vertical and horizontal length scales, bed porosity and roughness density that were used in Chapter 4 and 5. An important

observation from the bed roughness characterization was the roughness density can be scaled as a function of bed porosity and mean diameter of immobile gravel bed, thus a universal relation was developed. The developed relationship was used in drag force estimation in Chapter 5 and can also be useful to predict drag force in immobile coarse bed in general.

In Chapter 4 and 5 experiments aimed to study non-equilibrium fine sediment erosion, by suspended transport, in immobile gravel bed are presented in detail. Chapter 4 describes development of a very simple and economic laboratory scale imaging technique to estimate fine sediment erosion rate in immobile gravel bed in running water condition. The method is found to be very useful to acquire very rapid changes in fine sediment bed level in the interfacial sublayer of immobile gravel bed at a spatial resolution as small as the mean diameter of the fine sediments. The method helps to estimate erosion (sediment pickup) rate in non-equilibrium transport condition and enable acquiring erosion datasets to characterize spatial and temporal characteristics of erosion in rough bed such as immobile gravel bed. In Chapter 5 a set of ten experimental runs that were conducted to characterise spatial pattern of fine sediment erosion and derive a relation to predict non-equilibrium fine sediment erosion rate in immobile gravel bed are presented. The experimental datasets were used to investigate the relationship between spatial pattern of erosion and turbulent flow structure in immobile gravel bed, effect of immobile bed roughness on fine sediment erosion and selected flow variables and finally develop a non-equilibrium fine sediment erosion rate relation. Experimental datasets of flow in gravel bed were also used to characterise shear stress in the interfacial sublayer of gravel bed and its implications on fine sediment erosion. The main output of this chapter is a new erosion rate relation.

Chapter 6 describes development of a one-dimensional (1-D) suspended sediment transport model that is aimed to study characteristics of sediment and hydrodynamic waves of sediment flushing. The model is able to predict sediment concentration, thickness of sediment deposit in sand bed and in immobile gravel bed and identify optimal flushing scenarios. Flushing data of Cachí Reservoir is used in many of the model analysis. The erosion rate formula developed in Chapter 5 was also implemented in the numerical model and tested for its usability by comparing it with other two existing entrainment relations for immobile bed conditions. For this purpose, experimental datasets of deposition of fine sediment transport in immobile coarse bed were obtained from literature. Some of the important processes implemented in the numerical model include wave celerity factor, hindered settling velocity, immobile bed porosity, and variable bed roughness. The numerical model enabled to analyse the effect of wave celerity, immobile bed porosity and variable bed roughness on sediment deposition and test selected flushing scenarios that reduce significant sediment deposition downstream.

2. DOWNSTREAM IMPACTS OF FINE SEDIMENT RELEASES AND IMPLICATIONS FOR MANAGEMENT: AN INTERDISCIPLINARY REVIEW

Summary

Fine sediment releases downstream of dams during sediment flushing operations are becoming one of the most important environmental concerns of impoundments or dams. The recent booms in hydropower dams and increasing interests for river restoration have renewed the concerns about the impacts on rivers. However, there is a lack of a comprehensive inter-disciplinary review of the impacts of sediment releases by flushing operations in various environmental and geomorphic settings. Moreover, the environmental implications of the releases on river ecosystems remain complex and vary from one case study to another and could also depend on the mode of flushing operations and many other factors. In this chapter a systematic review and synthesis of selected downstream impacts of sediment flushing gathered from key literatures are presented. The review focused on biological, physical and chemical impacts of fine sediment releases on river channels downstream of dams. Finally, management strategies are recommended based on empirical evidences collected from twenty case studies obtained from published research. Impacts which need further studies are also recommended.

2.1. INTRODUCTION

Early researches (e.g. Petts, 1984) thoroughly described major morphological and ecological impacts of impounded rivers. These studies identified the challenges of sediment depletion and hydrological and hydraulic alterations downstream of dams and their implications on various river ecological units and channel morphology. But in most recent works there is an increasing concern over the increased sediment supply, arising from sediment releases by sediment flushing from reservoirs for the purpose of sedimentation management (e.g. Brandt and Swenning, 1999; Zuellig et al., 2002; Lui et al., 2004a; Asaeda and Rashid, 2012) and to maintain sediment supply or reduce sediment discontinuity downstream of dams (e.g. Sumi and Kantoush, 2010), on the physical, chemical and biological state of rivers downstream of dams. The recent global boom in hydropower dams (Zarfl et al., 2014) has renewed the concerns about the impacts on many rivers. Increasing interests for river restoration has also led to a number of dams to be removed (Grant and Lewis, 2015) which could lead to large quantity of fine sediments released downstream. Studies show that sediment releases significantly affect the downstream geomorphic and ecological state of a river (e.g. Rathburn and Wohl, 2001; Stanley and Doyle, 2002; Wohl and Cinderelli, 2000; Rathburn and Wohl, 2003; Brandt and Swenning, 1999). The impacts are

mainly related to elevated sediment flux and large liquid discharge with the associated alteration on channel bed morphology and deterioration of water chemistry in the receiving stream (Ma et al., 2012; Brandt and Swenning, 1999; Garric et al., 1990). Though many studies exist in the scientific literature reporting the downstream impacts of sediment releases, there is a lack of a comprehensive inter-disciplinary review of the impacts of sediment releases by flushing operations in various environmental and geomorphic settings. Espa et al. (2014) highlighted only few studies reporting the impact of sediment flushing operations on aquatic habitats and biota. In this study a systematic interdisciplinary review of the different downstream environmental (physical, biological and chemical) impacts of sediment releases (Section 2.3), are presented based on up-to-date literature resources. Finally best management strategies are proposed based on the empirical evidence obtained from the literature (Section 2.4).

2.2. SEDIMENT FLUSHING FROM RESERVOIRS

2.2.1.   Sediment flushing characteristics

Sediment flushing, defined as the scouring of previously deposited sediments by hydraulic method and release through bottom outlets of the reservoir, is the most effective, economic and fastest method to reduce severe reservoir sedimentation (Liu et al., 2004a). The released solid discharge (sediments) during flushing generally comprises of gravel, sand, silt, clay and sometimes mud itself (e.g. Mastrorillo and Dauba, 1999; Collier, 2002; Brandt and Swenning, 1999; Wohl and Cenderelli, 2000; Sumi and Kantoush, 2010; Takazi et al., 2002). The quantity of sediments released in the initial phase of release is very large reaching the peak after short period of time (Brandt and Swenning, 1999). Typically solid discharge – liquid discharge temporal pattern observed at downstream stations, during flushing operations, indicate that at the initial phase of sediment releases the peak of liquid discharge is released before the sediment peak (Brandt and Swenning, 1999) (Figure 2-1). This result in time lag between liquid and solid discharge and the lag increases further downstream and observed to govern the deposition of the released sediments (e.g. Tarekegn et al., 2014; Brandt and Swenning, 1999). The temporal lag is due to the difference in travel time of liquid and solid discharge and since most of sediments are released at the end of main flushing period and at the beginning of free flow phase. At initial phase of the release there is abundant stream power to erode and entrain river bed sediments downstream of the dam (e.g. Brandt and Swenning, 1999). The duration of the peak sediment load plays important role in the downstream impacts of flushing especially related to sediment deposition and physical harm to aquatic biota.

2.2.2.   Characteristics of sediments deposited in reservoirs

Sediments enter reservoirs as bed load, suspended load and also dissolved load and nearly all (>90%) will accumulate in the reservoir (e.g. Vericat and Batalla, 2005). The quantity of sediments carried in suspension exceeds those enter as bed load (coarser) by a factor of 5 to 10 (Scheuerlein, 1991) and so is the composition of the deposited sediments. The coarser sediments are deposited at the entrance of the reservoir while fine sediments typically deposit uniformly in the basin (e.g. Brandt, 2005) but mainly close to the dam (Bednarek, 2001; Huan and Lizano, 2014). The concentration profile in the water column is nearly uniform except in very upstream areas (e.g. Huan and Lizano, 2014).

Reservoirs act as sinks for many inorganic and organic substances (Hannan, 1979) and may contain relatively high levels of nutrients (nitrogen and phosphorus) and organic matter, contaminants (metals and organic substances) and elements such as silica, iron and sulphur, organochlorine compounds (e.g. pesticides) and toxins such as hydrogen sulphide (Wildi et al., 2004; Teodoru and Wehrli, 2005; Graf, 1990). The fine deposits have higher metal concentrations due to large volume ratio (Foster and Chalesworth, 1996). Deposits which are finer and near the dam within the reservoir basin are rich in nutrient and organic content (Asaeda and Rashid, 2012). The nutrient contents in the reservoir decrease away from the dam implying spatial heterogeneity of nutrient sources in the reservoir (Asaeda and Rashid, 2012). Figure 2-1 shows all the major components of sediment and water characteristics stored in the reservoir.
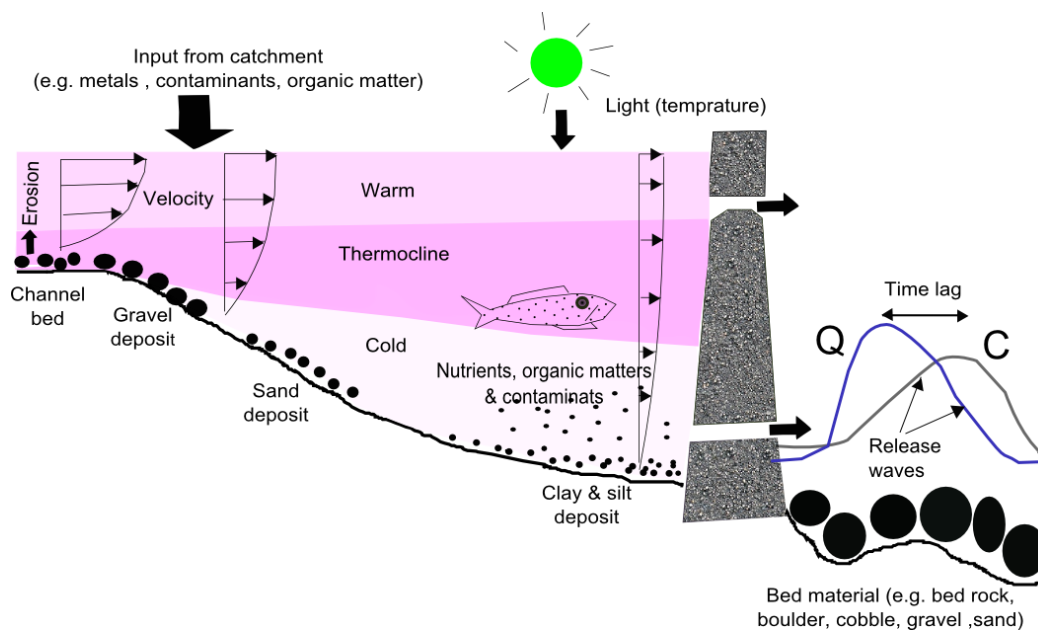
Figure 2-1.Conceptual diagram of characteristics of reservoir storage, sedimentation and sediment releases

Furthermore, during flooding the organic matters are transported and deposit near the dam (de Junet et al., 2005). The grain size distribution, porosity, shapes, contamination level, organic content of deposited sediments generally depends on the upstream watershed lithology, land-use activities, soil erosion control activities, hydrological setting and topography and the bed material of impounded river and its flow regime. In many reservoirs, the deposited sediments can range from silt and clay to boulders with more proportion of gravel in mountain reservoirs (Stillwater Science, 2002) and clay minerals also (Takazi et al., 2002).

2.3.DOWNSTREAM IMPACTS OF SEDIMENT FLUSHING

Reservoir sediment flushing has been used for reservoir sedimentation management over many decades with early studies on its environmental impacts reported in 1924 (e.g. Kanthack, 1924). Sediment flushing impacts on downstream river can be classified as physical, chemical and biological impacts. The physical impacts are direct changes of flow discharge (Q), sediment load (Qs) and concentration (C), temperature (T) and river morphology. The chemical impacts are alterations of downstream river water and sediment quality especially the concentration of dissolved oxygen (DO), sediment-bound contaminants and excess nutrient supply. The biological impacts are related to impacts on aquatic fauna (e.g. fish, invertebrates, vegetation). These impacts can be conceptualized as first, second and third order impacts based on Petts' (1984) impact classification (Figure 2-2). The first order impacts occur immediately during flushing operation such as changes in DO, T, Q, C and Qs. The first order impacts lead to alterations in channel morphology, channel substrate compositions, fine sediment infiltration, and smothering of benthos and fish. Intermediate impacts on biota also exists which is related to immediate effect of high erosive power of hydrodynamic wave generated by the release. The third order impacts are as the result of second order impacts such as lack of food availability for fish or change in flooding pattern and enhanced deposition of sediments. Details of the physical, biological and chemical impacts are discussed in Sections 2.3.1-2.3.3.
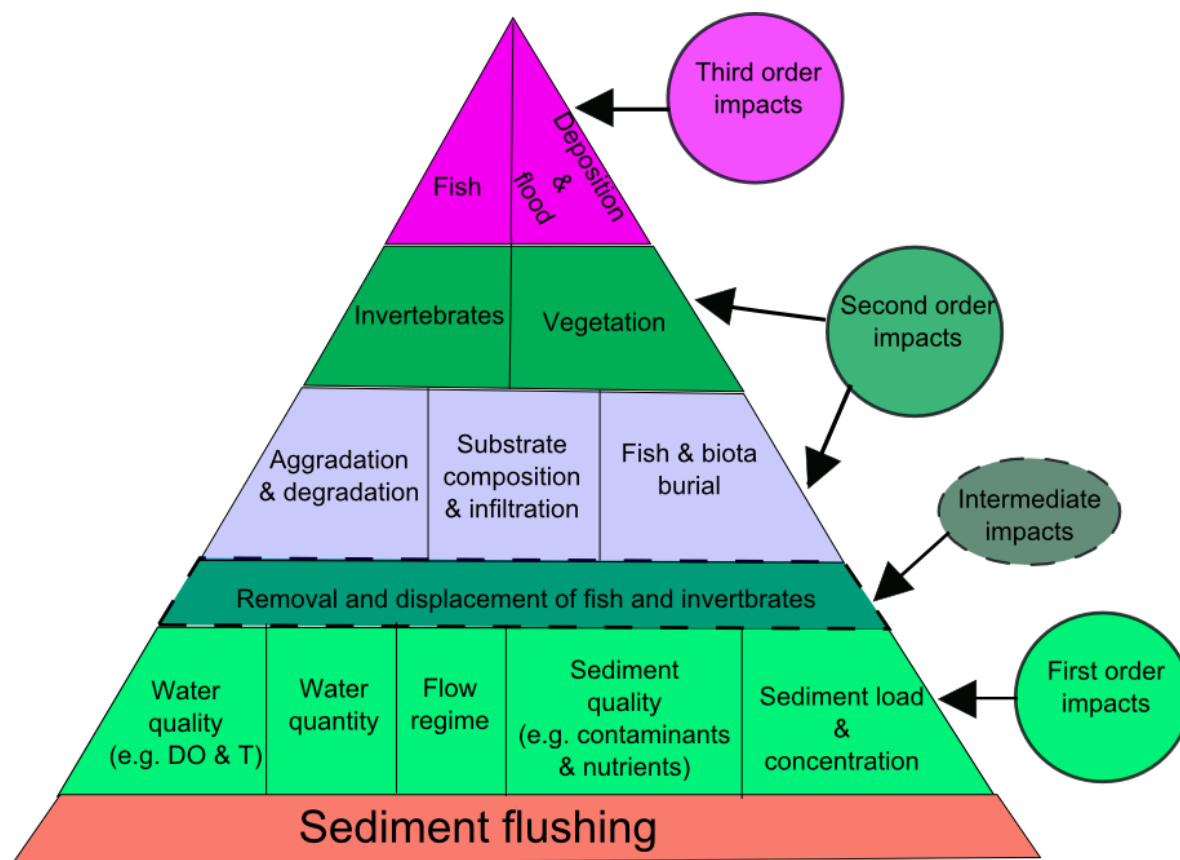
Figure 2-2. Conceptual diagram of downstream impacts of sediment flushing (after Petts, 1984)

2.3.1. Physical impacts

Table 2-1 shows the various physical impacts of sediment flushing. The discharge released during flushing operation can exceed few years return period flood (e.g. Camenen et al., 2013) and bank full discharge and water level of the natural flooding. It could reach up to 4-10 times more than the pre-flushing discharge in river downstream of the dam (e.g. Brandt and Swenning, 1999; Collier, 2002). When flushed sediments are fine flow resistance in downstream channel will reduce and thus the water level will get lower (Sloff, 1991).

The quantity of released sediments could range from several hundred cubic meters to thousands (e.g. Camenen et al., 2013; Brandt and Swenning, 1999; Wohl and Cenderelli, 2000; Sumi and Kantoush, 2010; Collier, 2002). The peak concentration of the release can reach up to 249 g/l with a sediment load of 100 tons/s (e.g. Brandt and Swenning, 1999) and up to 1200 folds higher than the concentration under normal flow condition (e.g. Bergstedt and Bergersen, 1997). The sediment concentration however depends on regulatory measures of flushing operations (e.g. Espa et al., 2013; Crosa et al., 2010),

efficiency of the flushing operation (e.g. Scheuerlein, 1995), and period of flushing operations (e.g. Buermann et al., 1995). Generally the highest concentration is observed near the dam and decreases rapidly in downstream directions. The concentration at the peak of the release is significant in relation to adverse downstream impacts (Espa et al., 2014; Espa et al., 2013; Crosa et al., 2010). The changes in the discharge regime, sediment regime and concentration affects sediment transport dynamics (Cui et al., 2008), turbulent flow structure and settling velocity (van Maren et al., 2009) and the sediment hysteresis (time lag) (Brandt, 1999) in rivers.

Sediment flushing causes both channel degradation and aggradations (Brandt and Swenning, 1999). Figure 2-3 shows deposition observed following sediment flushing. Degradation occurs in upstream areas below the dam during initial phase of release due to high erosive power of the hydrodynamic wave. Aggradations occur both in channel bed and banks with more proportion in channel and decreases proportionally with distance from the dam (Brandt and Swenning, 1999; Wohl and Cenderelli, 2000). The deposits can reach over many hundred thousands of tones (Brandt and Swenning, 1999; Asaeda and Rashid, 2012). The deposition can block channels and could cause downstream flooding during flushing (e.g. Brandt and Swenning, 1999; Sloff, 1991). The deposited materials near the dam are coarse with the grain sizes decreasing proportionally with distance from the dam. Coarse deposits remain for extended period after flushing while fine deposits are eroded by subsequent flooding (e.g. Wohl and Cenderelli, 2000; Doeg and Koehn, 1994). But fine sediment releases in steep rivers have shown no significant deposition (e.g. Gray and Ward, 1982, Espa et al., 2013). These show that the grain size of the released sediments and the timing of subsequent flooding control the long-term morphologic impacts of sediment flushing and also downstream habitat stability. The fine sediments preferentially deposit in pools (Wohl and Cenderelli, 2000; Zuellig et al., 2002; Cui et al., 2008) and riffles and bars are also affected by deposition (Camenen et al., 2013; Wohl and Cenderelli, 2000; Asaeda and Rashid, 2012). Regular sediment flushing over many years (3 decades) causes long-term channel aggradations with more deposition in downstream reaches (e.g. Sumi and Kantoush, 2010). The long-term grain sizes of the deposits decreases proportionally with distance from the dam (e.g. Sumi and Kantoush, 2010) showing the short-term and long term impacts of flushing shows similar behaviour. This shows that flushing operations modify the long-term bed-material composition.

Figure 2-3. Channel and bank surficial deposits before (left) and after (right) sediment flushing of Cachí reservoir in Reventazón River at 2 km downstream of the dam (Brandt, 2005)

The deposition of the fine sediments in the interstitial spaces of coarse bed could lead to bed clogging by infiltration of fine sediments (Schalchli, 1995). Figure 2-4 shows typical example of fine sediment deposition following sediment flushing resulting in destruction of habitats by internal and external colmation of gravel substrate. Fine sediment infiltration modifies habitats of macroinvertebrates, salmonids, and other aquatic organisms by reducing exchange of water (e.g. Heppell et al., 2009), dissolved oxygen and particulate matters in the coarse substrate and hyporheic zone. Fine sediment releases during sediment flushing can lead to infiltration (Camenen et al., 2013) but some case studies reported no infiltration (e.g. Evans and Wicox, 2014). Subsequent high flows following sediment releases could re-work the bed and reduce residence time of the fine sediments limiting infiltration. Coarse sediment releases however could enhance bed heterogeneity and thus increase available areas for refuges and increase in hyporehic exchange (Stewart, 2006). Fine sediment release experiments in immobile gravel bed channel shows that sand sized sediments will infiltrate only few diameters of the immobile gravel bed, regardless of sediment release rate (Wooster et al., 2008). The rapid release of the fine sediments is less likely to increases sediment infiltration as compared to the same amount of releases over a longer time period (Wooster et al., 2008). Generally, the quantity of fine sediment infiltrated is influenced by various hydrodynamic and sediment parameters such as bed shear stress (Evans and Wilcox, 2013), suspended sediment concentration (Khullar et al., 2013), fine sediment cohesion (Packman et al., 2000), the arrangement of bed surface grains (Cooper and Tait , 2009), the occurrence of bed forms (Packman and MacKay, 2003), the existence of a vertical hydraulic gradient within the rough bed (Schälchli ,1992) and even the presence of a biofilm (Arnon et al., 2010). Figure 2-5 shows the dynamic mechanism of infiltration of fine sediments in coarse bed.

Figure 2-4. Clean gravel substrate (left) and gravel clogged through internal and external colmation (Bechteler, 2006)
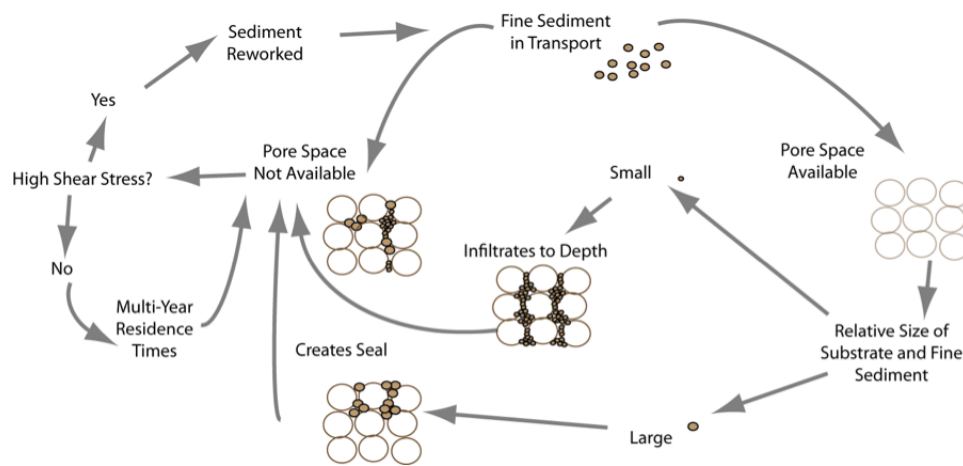
Figure 2-5. Mechanism of fine sediment infiltration in coarse gravel bed (Evans and Wilcox, 2014)

The changes in temperature of rivers downstream of dams by reservoir releases have been identified to have very significant impacts on instream-biota (Petts, 1984). There are very few studies that highlighted the effect of sediment flushing on thermal regimes in rivers downstream of dam. Alteration in temperature regimes during sediment flushing have shown increases (Gutzmer et al., 1996), decreases (e.g. Lui et al., 2004a) and in some cases remains unchanged (e.g. Buermann et al., 1995). The temperature of the release observed to modulate DO concentrations and increased downstream from the dam (e.g. Lui et al., 2004a). Overall, temperature during flushing operations could increase or decrease depending on time of the year of the release, depth of reservoir outlets and whether the reservoir is in temperate or tropical climatic regions.

Table 2-1. Physical impacts of sediment flushing

Dam and River	Variables	Physical impacts	Remarks	Source
Cache Reservoir, Reventazone River (Costa Rica)	Q,C, Qs, deposition	High Q & C, bank and channel aggradation	The timing of Q (>4 folds) & C (>249g/l), are affected. A deposition of 295,000 tons on 30 km stretch	Brandt and Swenning (1999)
Alto Mora Dam (Italy)	Water level	High increase	Time to peak was short and peak remained constant for the period of release	Brachi & Gallati (1992)
Phalaborwa Barrage (South Africa)	Q, C,T	Increase in Q & C, no obvious change in T	Q increase by nearly 5-year return flood and C up to 95g/l	Buermann et al. (1995)
Rangipo Dam, Tongariro River (New Zealand)	Substrate & deposition	Channel aggradation	Increased level of surface sand gravel deposit (sand eroded and dispersed by natural flooding)	Collier (2002)
Spencer Hydropower Dam, Niobrara River (US)	T & C	Small increase in T and high C	An increase in daily water T by $3 - 4$ ^{o}C and fourfold increase in C along 63.3km	Gutzmer et al.(1996); Hesse & Newcomb (1982)
Dashidaira Dam, Kurobe River (Japan)	T	Decreased	very low T (9.0 - 17.5^{o}C)	Lui et al.(2004a)
Ova Spin Reservoir (Switzerland)	T	Increased	High T during emptying than free flow through the reservoir	Halgh (1996)
Martin-la-Porte reservoir, Arc River, France	Q, infiltration, deposition, Qs	Q and C increased, sediment load increased	Q exceeded few years return flood, few cms of infiltration in gravel bars, Qs up to 150000m3, C up to 50g/l, deposition over 1/3 of gravel bar	Camenen et al. (2013)
Halligan Reservoir, North Fork Cache la Poudre River (US)	Qs ,deposition		Qs of 5352 tons and deposition in pools (up to 4.3 m deep) with little in riffles	Wohl and Cenderelli (2000)
Dashidaira Dam, Kurobe River (Japan)	C,Qs, deposition, substrate	High C, Aggradation	C of max 90g/l ,Qs of 910,000-1010,000 m^3 and large channel aggradation (mostly downstream)	Sumi & Kantoush (2010) & Kantoush et al., 2011
Weir, Armstrong Creek (Australia)	C and Qs, deposition	Increased	Qs up to 100 m3 and C up to 4.61g/L, sand deposition near the weir and silt and fines upto 2km - 4.5km downstream	Doeg & Kohen (1994)
River Mur (Austria)	Qs, C & deposition	High Qs &C	Qs up to 80,000 m^3 and C up to a maximum of 11 mg/L, fine sediment deposit in bank zones	Bechteler (2006)
Valgrosina reservoir (Italy)	C,Qs & deposition	High C & Qs, no obvious deposition	C up to maximum of 70-80 g/l and the latter up to 249 g/l & Qs of 100 tons/s	Espa et al. (2013) Crosa et al.(2010)
Verbois dam, Rhone River (Switzerland)	C	C increased	C >45g/l (increased by 50 folds)	Peter et al.(2014)
Low head dam, Wind River (US)	C	Very high C	C up to 18g/L, 1200 folds higher (peak C for 5hrs below the dam and for 18hrs at 29km downstream)	Bergstedt &Bergersen (1997)

Dashidaira Dam, Kurobe River (Japan)	Deposition ,Qs, C	Channel aggradations, high Qs, high C	28Mkg sediment deposit in 17km, C thousands more than normal C, sand deposition over gravel bars	Asaeda & Rashid (2012)
Guernsey Reservoir, North Platte River (US)	Deposition	No deposition & change in bed composition	no obvious deposition, even in pools or no change in river bed material was observed	Gray& Ward (1982)
Halligan Reservoir, North Fork Cache la Poudre River (US)	Deposition	Increased deposition	The deposition over more than 9.6 km of the river from the reservoir (thin deposit over riffle and larger deposit in pools)	Zuellig et al.(2002)

C - Sediment concentration, Q - Flow discharge, T - Temperature and Q_s - Sediment load

2.3.2.   Chemical impacts

Sediment flushing operations have been shown to result in downstream changes in both the water and sediment quality (Table 2-2). Flushing introduces not only high concentration of sediments (high turbidity) but also flow with low dissolved oxygen (DO) (e.g. Hesse and Newcomb, 1982), elevated level of heavy metals (e.g. Peter et al., 2014), high concentration of ammonia (e.g. Roux, 1984), increased level of organic matter and nutrients (e.g. Takazi et al., 2007; Asaeda and Rashid, 2012), and also soluble reactive materials such as phosphorous (e.g. Gray and Ward, 1982). The release of these chemical attributes beyond the required level will results in significant alterations in ecology of the river.

The concentration of DO in water column and channel beds is very important for survival of fish species and it should not drop below 5mg/L. During sediment flushing the DO concentration could increase (e.g. Gray and Ward, 1982; Peter et al., 2014), decrease (e.g. Buermann et al., 1995; Brandt, 1999; Hesse and Newcomb, 1982; Takazi et al., 2007) or remains unchanged (Crosa et al., 2010) in downstream river. The reductions are due to the release of oxygen-depleted hypolimnic water, high oxygen demanding organic sediments (e.g. Takazi et al., 2007) and increased turbidity which shades primary producers reducing oxygen production (Brandt, 1999; Morris and Fan, 2010). The concentration of DO increases proportional to the distance from the dam due to oxygen rich water influx from tributaries and low oxygen demand by organic sediments as most deposit in upstream reaches (Buermann et al., 1995; Scheuelein et al., 1995). The concentration of DO is also regulated inversely by the temperature of the released flow (Lui et al., 2004a).

Sediment bound contaminants are released during flushing posing significant downstream environmental threats (Sloff, 1991). Flushing introduces large proportion of heavy metals (Wu and Hong, 1989; Peter et al., 2014), organic matter and ammonia (Asaeda and Rashid, 2012; Roux, 1984), chemical compounds (e.g. NO_3^-, SO_4^{+2}) (Peter et al., 2014), and excess concentration of nutrients (e.g. N and P) (Asaeda and Rashid, 2012; Asaeda, 2014), increases metal content in benthic invertebrates (Peter et al., 2014), affects trace metal partitioning, speciation and bio-availability (Peter et al., 2014). The downstream nutrient level in deposited sediments can increase up to 90 % and remain high for over a year (Asaeda and Rashid, 2012; Takazi et al., 2007). This shows that the nutrient balance in downstream will be altered and this will lead to new nutrient equilibrium and colonization of plant species. The concentration of nutrients in the flow could remain high for several weeks if they are bound to suspended sediments (Gray and Ward, 1982). An emission of CH_4 from reservoir releases is larger than reservoir surface emission (Kemenes et al., 2007) despite no study reported the effect of flushing on downstream CH_4 emission.

Table 2-2.Chemical impacts of sediment flushing

Dam and River	Variable	Chemical impacts	Remarks	Sources
Spencer Dam, Niobrara River (US)	DO	Decreased	DO dropped to 3.5 mg/L during flushing	Hesse & Newcomb (1982)
Dashidaira Dam , Kurobe River (Japan)	C,N , S ,EC and DO	Increased (C,N,C& EC) & decreased (DO)	High organic content led to depletion of DO	Takazi et al. (2007)
				Peter et al. (2014)
Verbois dam, Rhone River (Switzerland)	DO	Both increase & decrease (DO)		
	Heavy metals (Ca^{+2},K^+ and Na^+) & NO_3^-	Increase in heavy metals	NO_3^- increased by fourfolds	
	Al, Co, Mn and Ni (dissolved)	Increased		
	Co, Cr, Ni, Fe and Pb	Increased	After sediment flushing	
	Mg^{+2}, Cl^{-1} and SO_4^{2-}	Decreased		
Dashidaira Dam , Kurobe River (Japan)	Total nitrogen (TN) & phosphorus (TP)	Increased	TN & TP increased from 0.2mg to 26 mg (TN/L) and 0.002mg to 13 mg(TP/L) respectively (>100 folds)	Asaeda and Rashid (2012)
Guernsey Reservoir, North Platte River (US)	DO and dissolved phosphorus	Increased	high level of DO and increase in P for hours to weeks	Gray and Ward (1982)
Verbois and Geinissiat Reservoirs, Rhone River (Switzerland and France)	Organic matter (OM) & ammonia (NH_4)	Increased	OM increased by 52% in suspended sediments and high levels of NH_4 (12mg/L)	Roux (1984)
Cache Reservoir, Reventazone River (Costa Rica)	DO	Decreased	DO decreased during flushing events	Brandt (1999)
Phalaborwa Barrage ,Olifants River (SA)	DO	Decreased	A drop in DO to 0.1 mg/L for several hours	Buermann et al. (1995)
Dashidaira Dam , Kurobe River (Japan)	DO	Decreased	DO was observed to be related to T	Lui et al. (2004a)
Val Grosina reservoir, Adda River (Italy)	DO	No obvious decrease	Low OM & low temperature effect	Crosa et al.(2010)
Gezhouba Resrevoir, Yangtze River (China)	P_b	Increased (in concentration)		Wu and Hong (1989)

DO-Dissolved Oxygen, C-Carbon, N-nitrogen and S-Sulphur

2.3.3.   **Biological impacts**

Of all downstream impacts of sediment flushing, biological impacts have been the most studied (Table 2-3). Adverse biological impacts of sediment releases are due to the direct effects of increased flow and suspended sediments, nutrients and contaminants during flushing and due to downstream morphological alterations of river habitats following sedimentation of the released sediments (Crosa et al., 2010). The most common downstream biological impacts of sediment flushing are the negative effects on fish, and organisms living at the surface of river bottom (e.g. benthic invertebrates, underwater vegetation) and in the interstitial system of bottom sediments (e.g. juvenile stages of surface water organisms, groundwater organisms, and interstitial population proper).
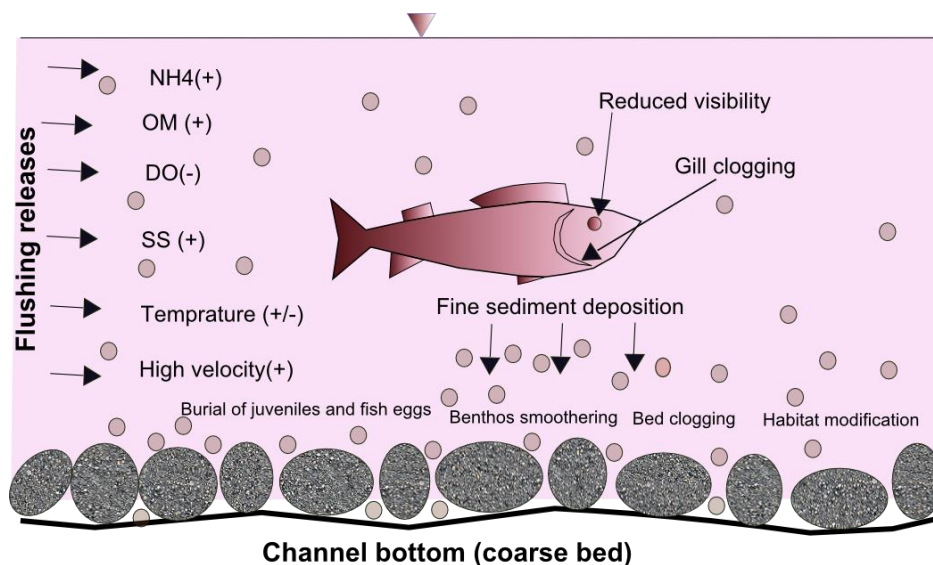
Figure 2-6. Main drivers of adverse impacts of sediment flushing on fish (increase (+) & decrease (-))

The negative impacts of sediment flushing on fish are driven by the physical, chemical and biological alterations in the river during and after the flushing. Sediment flushing affects fish by reducing biomass and density (Crosa et al., 2010), abundances (Mastorillo and Dauuba, 1999), changing age structure (Crosa et al., 2010) and reducing species diversity (Roux, 1984) during and after flushing. Figure 2-6 shows stresses imposed by sediment flushing that negatively impact fish species. Major alterations that occur and negatively affect fishes include low level of dissolved oxygen (Buermann et al., 1995), increased turbidity or concentration (Buermann et al., 1995; Doeg and Koehn, 1994), pollution by contaminants (e.g. NH_4) (Roux, 1984), lack of food availability (Collier, 2002), burial and modifications of habitats (Mastorillo and Dauba, 1999), deformation and dehydration of gills (Kinoshita et al.,2002) and drift by high velocity flow (Figure 2-6). The reduction in DO, high sediment concentrations   and agitation and flushing out of fish along with sediments are main causes of fish kills (Buermann et al.,

1995; Roux, 1984; Moore et al., 1991; Buchholz and Knofczynski, 1988).The released sediment concentration during flushing exceeds the standard concentration for fish health, 25mg/L (Bilotta, 2012). High fish kills are among juveniles and varied among fish species (Crosa et al., 2010; Mastorillo and Dauba, 1999). Changes in thermal regime during flushing are not reported to affect fish. The adverse impacts generally decrease proportional to the distance from the dam (Bechteler, 2006; Doeg and Koehn, 1994) and vary among different fish species and age groups (Crosa et al., 2010; Mastorillo and Dauba, 1999; Espa et al., 2013). Recovery of fish population to pre-release condition following sediment flushing could take large number of years (Doeg and Koehn, 1994; Crosa et al., 2010).

Macro-invertebrates form central function in stream ecosystem and integrate every tropic level. The adverse impacts of flushing on macro-invertebrates are associated with reductions in number of taxa (abundance) (Gray and Ward, 1982; Espa et al., 2013; Crosa et al. 2010; Doeg and Kohen, 1994; Hesse and Newcomb, 1982; Peter et al.,2014), species diversity (Bechteler, 2006; Peter et al., 2014), density and richness (Zuellig et al., 2002; Collier, 2002; Peter et al.,2014), changes in benthic community function and structure (Zuellig et al., 2002) and elevated level of metals (Peter et al., 2014).
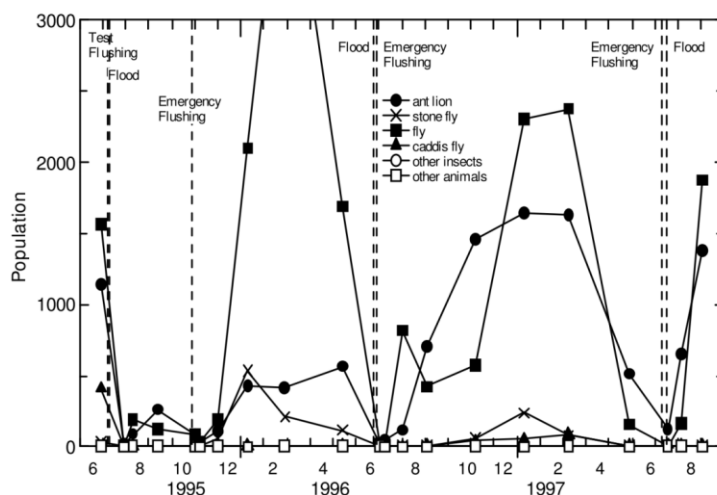
Figure 2-7.The impact of sediment flushing on transitions of number of population of benthic organisms (IEA, 2006)

Figure 2-7 shows the long term dynamics of number of benthic organisms in response to sediment flushing (IEA, 2006). The number of benthic organisms decreases immediately after sediment flushing (IEA, 2006) and remain low over few months (Peter et al., 2014). Generally, the impacts decrease proportional to the distance from the dam (Bechteler, 2006) and vary among ranges of taxa (Doeg and Koehn, 1994). The recovery of macro-invertebrates to pre-release condition could take few weeks or a month (Gray and Ward, 1982; IEA, 2006) to up to several months (Zuellig, 2002).
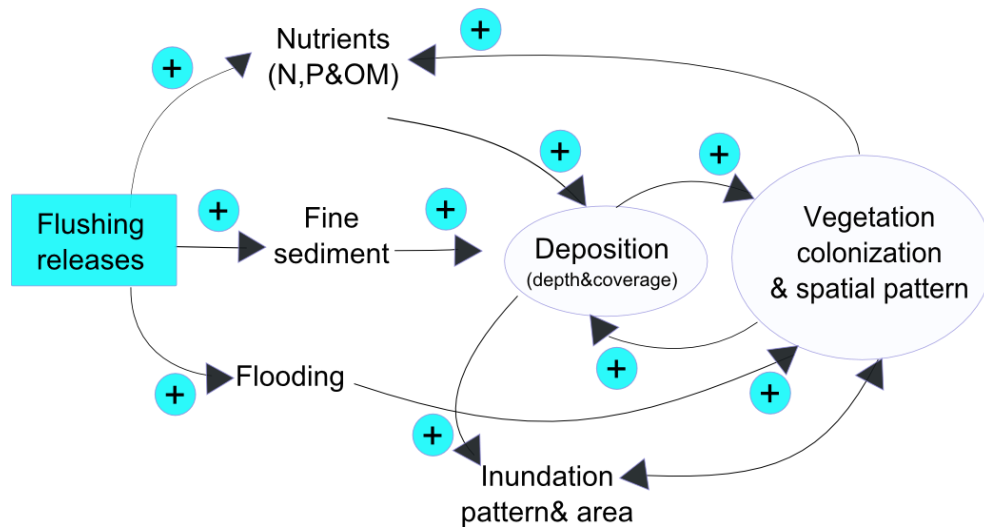
Figure 2-8. The downstream dynamics of vegetation growth and colonization due to long-term sediment flushing activities (increase (+))

Regular sediment flushing conducted over several years enhances vegetation growth in downstream morphological units such as gravel bars by supplying nutrients and building moist and thick layer of fine sediment deposits (Asaeda and Rashid, 2012; Asaeda et al., 2014). It also activates colonization of certain vegetation species leading to some species out colonize the other (Sakamoto et al., 2010). The succession of vegetation enhances trapping of released sediments allowing more deposition and a change in flooding pattern and footprints of vegetation growth (Asaeda et al., 2014). Nevertheless, no significant impact on crop growth is observed (Hori et al., 2006). Figure 2-8 shows the complex feedback mechanisms and dynamics of vegetation growth and colonization in downstream channel and gravel bars due to long-term flushing operations. Flushing also reduces in benthic algae abundances by smothering and drift (Gray and Ward, 1982b).

In summary, many studies reported first order impacts (e.g. Brandt and Swenning, 1999; Peter et al., 2014), with some on second order impacts (Brandt and Swenning, 1999; Collier, 2002; Wohl and Cenderelli, 2000; Tarekegn et al., 2014) and very many on third order impacts (e.g. Crosa et al., 2010; Espa et al., 2013; Asaeda and Rashid, 2012; Asaeda et al., 2014; Zuellig et al., 2002) of flushing. Of all impacts, biological impacts are the most studied impacts with most emphasis on fish and macro-invertebrates. The impacts on vegetation dynamics is less documented (e.g. Asaeda and Rahid, 2012; Asaeda et al., 2014). In Section 2.4 some of the key recommendations aimed to mitigate the impacts are discussed.

Table 2-3.Biological impacts of sediment flushing

Dam and River	Variable	Biological impacts	Remarks	Sources
Val Grosina Reservoir, Adda River (Italy)	Fish biomass and density	Decreased	73% and 66% decrease in fish density and biomass	Crosa et al. (2010)
	Fish age structure	High kills	Long term-impairment of the age structure	
Labarre & Ferriers Dams, River Ariege (France)	Fish abundance, habitat availability & use, species	Decreased abundance	Flushing changed habitat from boulders & pebbles to gravel, sand and mud	Mastorillo &Dauuba (1999)
		No mortality		
Val Grosina Reservoir, Adda River (Italy)	Abundance of zoobenthic assemblages	Impairment of benthic community	Recovered after 3 months	Espa et al. (2013); Crosa et al. (2010)
Spencer Dam, Niobrara River (US)	Fish kills	High kills	22,500 fish kills during flushing	Hesse & Newcomb (1982)
Halligan Reservoir ,North Fork Cache la Poudre River (US)	Fish kills	High deaths	4000 rainbow and brown trout deaths	Wohl & Cenderelli (2000);Wohl (1998)
Weir (flushing) in Armstrong Creek (Australia)	Fish population	High reduction	Up to 93.2 % decrease at 150m below the weir	Doeg & Kohen (1994)
	Number of benthic invertebrates	Decreased	63.90% and 39.70% reductions in the abundance & number of taxa. Reductions varied from 25% to 100% among various macroinvertebrate taxa	
Phalaborwa Barrage ,Olifants River (South Africa)	Fish kills	High no of deaths	Due to high C (1500 mg/L) and decreases in DO (0.1mg/L)	Buermann et al. (1995);Moore et al.(1991)
Verbois & Geinissiat Reservoirs, Rhone River (Switzerland and France)	-Fish kills, death of larvae and juveniles -Species diversity, composition & biomass	-Death of fish, larvae and juveniles -Reductions in species composition & biomass	Anoxic flows resulted in death of all fish species Due to deposition of sediments in channel habitats	Roux (1984)
Dashidaira Dam , Kurobe River (Japan)	Rainbow trout	Gill deformation & dehydration		Takazi et al. (2002)

Sabo Dam, Hiru-Dani River (Japan)	Fish	Block gill lamellas	Due to adherence of smectite particles	Kinoshita et al. (2002)
St. Georgen &Murau Dams, Mur River (Austria)	Fish population count	Decreased	No fish at 1km downstream of the dam. A loss of 75% (4.5km) & 75% (9km)	Bechteler (2006)
Verbois dam, Rhone River (Switzerland)	Presence and number of species	Absence of fauna & decrease in species		
	Invertebrate richness	Drastic decrease	Four folds decrease macroinvertebrate taxon richness	Peter et al.(2014)
	Levels of metals (Al, Mn, Fe, Co, Ni)	Increased in invertbrates		
Rangipo Dam, Tongariro River (New Zealand)	Invertebrate density	Significant decline	Due to erosion of invertebrates associated with periphyton	Collier (2002)
Guernsey Reservoir, North Platte River (US)	Number of macroinvertebrates	Both significant decreases & increases	90 % decrease in chironomids (family of flies) Increase in number of some invertebrates (e.g. mayflies and oligochaetes)	Gray & Ward (1982)
Spencer Dam, Niobrara River (US)	Number of macroinvertebrates	Decreased		Hesse & Newcomb (1982)
Halligan Reservoir, North Fork Cache la Poudre River (US)	Benthic macroinvertebrate density & taxa richness	Decreased	Significant decreases near the dam	Zuellig et al.(2002)
Dashidaira Dam , Kurobe River (Japan)	Number of benthic organisms	Significant reductions	Decreases in number of benthic organisms (e.g. ant lion, stone fly, fly, caddis fly and other insects)	IEA (2006)
Dashidaira Dam , Kurobe River (Japan)	Channel vegetation cover	Increased	Colonization of herbaceous plants by nutrient supply and deposition	Asaeda & Rashid (2012), Asaeda et al. (2014), Sakamoto et al. (2010)
Dashidaira Dam , Kurobe River (Japan)	Vegetation succession and colonization	Increased	Enhanced sediment deposition and changed flood pattern	
	Crop (rice) production	No effect	No any effect on the growth, yield of rice & soil quality	Hori et al. (2006)
Guernsey Reservoir, North Platte River (US)	Benthic algae abundances	Significant decline	90 % reduction in benthic algae abundances with no recover for nearly a year	Gray and Ward (1982b)

2.4. MANAGEMENT IMPLICATIONS AND RECOMMENDATIONS

Sediment flushing is likely to remain as a widespread practice but scientific studies of the impacts of sediment releases can be used to inform management and develop recommendations for mitigating against the downstream impacts. The following management recommendations are drawn from empirical evidences obtained from the literature review.

Firstly, flushing should be conducted regularly and more frequently, at least once per year, since it reduces the magnitude of the release and avoids high peak C (Crosa et al., 2010; Zuellig et al., 2002). A gradual release also reduces bed degradation, rate of increase in C, release rate of contaminated sediments and nutrients and deposition on bed substrate (Gray and Ward, 1982b) nevertheless high rate of releases of short duration have minimal ecological impacts (Major et al., 2008; Downs et al., 2009). Inter-flushing clear water releases also reduce concentration peaks (Espa et al., 2013;Crosa et al., 2010).

Secondly, flushing operations should be conducted in selected seasons of the year: considering post-flushing water availability and spawning and recruitment seasons of fauna. Avoiding flushing during spawning, emergence and recruitment seasons of fauna and dispersal and germination season of unwanted plant species reduces the impacts significantly (Gray and Ward, 1982b; Asaeda et al., 2014; Hesse and Newcomb, 1982). Flushing before flooding or snow melt season is highly recommended and reduces impacts (Collier, 2002; Wohl and Cenderelli, 2000).

Thirdly, environmental impact assessment is important before planning sediment flushing operations. The assessment should focus on the characteristics of reservoir sediment deposits (physicochemical), quantity of solid and liquid releases, and downstream river channel gradient and cross-sections (Wohl and Rathburn, 2003; Downs et al., 2009; Lui et al., 2004a), the peak and duration of sediment concentration (Crosa et al., 2010; Scheurelein, 1995;Gallerano and Cannata, 2011), and scope for operational modification of flushing (Gutzmer et al., 1996; Fruchard and Camenen, 2012) and considerations for alternative methods such as hydro-suction (Hotchkiss and Huang, 1995), sediment bypassing (Sumi and Kantoush, 2010), environmental friendly flushing (Fruchard and Camenen, 2012). The downstream ecological units, potential impacts of the release, their recovery and responses, and period of recruitment and spawning, and suitability of tributaries for escape (Buermann et al., 1995) should also be studied.

Finally, the magnitude of adverse impacts of sediment flushing and the time required for recovery are generally site specific. However, a general management recommendation for sediment flushing alternatives can be drawn. It is also important to highlight that numerical models would be very crucial for the environmental impact assessment, to identify proper peak concentration and test flushing scenarios.

2.5. CONCLUSIONS

Fine sediment releases by flushing operations triggers a cascade of processes that cause complex responses with numerous downstream impacts and this study reports important negative implications of the practice and proposes management strategies. First, based on previously published research, a conceptual framework (Figure 2-2) of the first, second and third order impact of fine sediment releases is developed. The most important first order impacts are extremely high sediment concentration and load, high level of sediment bound contaminants and flooding. The high sediment concentration and load causes aggradation in channel and banks of downstream river although channel degradation could occur during initial stage of the release. The negative biological impacts of fine sediment releases are mainly due to the direct effects of increased flow and suspended sediments, nutrients and contaminants during flushing and downstream morphological alterations of river habitats following sedimentation of the released sediments. Of all impacts, biological impacts are the most studied impacts with most emphasis on fish and macro-invertebrates. The impacts on vegetation dynamics is less documented although it is observed that vegetation growth is initiated by nutrient rich fine sediment releases that eventually alter downstream channel morphology and flooding regime. The impacts of contaminants released during sediment flushing are not documented in most of the case studies which highlights particular attention. The spatial and temporal scales of adverse downstream impacts varied from case to case. It is found out that the downstream impacts of sediment flushing are proportional to the distance from the dam. The sediment concentration, grain size distribution of the deposits, channel and bank aggradation, effects on fish and macro-invertebrates, effect on dissolved oxygen concentration decreases with distance away from the dam. The grain size of the released sediments and the timing of subsequent flooding control both the temporal scale and long-term morphologic impacts of sediment flushing. The temporal scale of impacts on macro-invertebrates could span from few weeks or a month to several months while the effect on fish could last for a number of years. The impacts on channel vegetation are reported to be driven by many years of flushing activities unlike other impacts mentioned in this study. This study proposed general recommendations for best management practices based on experiences obtained from review of numerous reports of flushing activities conducted under different hydrologic, geomorphologic, ecological and operational conditions.

3.   IMMOBILE GRAVEL BED ROUGHNESS CHARACTERISATION

Summary

Gravel bed characteristics and roughness are widely quantified based on particle size distributions and random field of surface elevations. The gravel surface elevation data acquired in this work is by Position Sensing Detector (PSD) triangulation sensor which is commonly used for surface profiling and distance measurements at high resolutions. Nevertheless the data contained significant elevation errors characterized by unusual peaks. The peaks are observed to be directional and dominant on curved surface of the gravel particles whose curvature lies opposite to the direction of the receiver of the laser sensor. Thus, this study investigated the sources of the errors, quantified the errors and developed methods to remove them. The effect of the elevation errors on bed roughness characterisation is evaluated based on statistical roughness characteristics: second order-structure functions, horizontal and vertical roughness length scales and statistical distributions. The error filtered data is finally used to quantify geometrical and roughness characteristics of the bed. Gravel bed porosity is estimated based on surface elevation data and independently with water displacement method. A theoretical relation for estimating roughness density is also developed based on gravel surface elevation data and for rough beds of selected roughness elements. It is found out that roughness density of gravel bed can be described based on solely on bed porosity and horizontal length scale.

3.1. INTRODUCTION

Channel bed roughness description is crucial since it controls various processes of flow hydrodynamics and channel morphology. The energy carried by flows is also modified by the resistance imposed by bed roughness which comprises of particle and form roughness (Griffiths, 1989). The resistance (a measure of energy loss by flow) depends on the channel bed material particle size, shape, orientation and spatial arrangements. Generally bed roughness controls the mean flow velocity, turbulence characteristics, and sediment transport processes. In gravel bed channels flows where there is no bed form flow resistance is due to particle roughness which is as a result of viscous drag on the bed surface and form drag due to small scale roughness elements, such as the gravel particles.

In many practical applications and some hydraulic research activities (e.g. turbulence) the effects of bed particle roughness in near bed flow field is represented by a simple roughness length scales, such as equivalent sand roughness height, which are described by a single grain-size index, for instance,

representative grain size of the bed material (d_{50} or d_{84}) (e.g. Nikuradse, 1933; Keulegan, 1938). However many studies criticized such approach, first because field measurements of roughness length scales varied 2 to 4 folds larger than representative grain sizes (e.g. Bathurst,1985), second, the approach does not take in to account the spatial heterogeneity of the bed surface and its impact on flow resistance (Cooper et al., 2008). Moreover, the complex arrangements of bed particles that affect bed roughness significantly such as orientations, packing, and protrusions are poorly represented by representative grain size. Cooper et al. (2008) highlighted that such representations are especially very poor in gravel bed conditions where the bed surfaces are very irregular and can have different magnitude of effects on flow resistance between low and high flow conditions. Nikora et al. (1998) highlighted that bed roughness will only be well predicted considering grain-size distribution, particle orientation, bed arrangement as well as concentration and geometry of features of bed surface. Currently there are comprehensive approaches to represent bed roughness based on statistical properties of bed surface data (e.g. Nikora et al., 1998).

With the advancement of data acquisition technologies it is possible to measure gravel (river) bed surface elevations which enable one to capture bed spatial heterogeneity and bed surface geometry. The gravel bed surface can be considered as a random field of surface elevations Z(x, y, t), where Z is surface height at coordinates x and y at time t. Statistical analyses of bed surface elevation data proved to predict gravel grain orientations that are driven by water flow and also vertical and horizontal roughness scales (e.g. Nikora et al., 1998; Aberle and Nikora, 2006). Nikora et al. (1998) found out that hydraulic roughness can be well represented by scale dependent parameters that comprise vertical roughness scale and horizontal roughness scales which are both derived statistically from random field of surface elevations. Statistical tools such as probability distribution functions and two-dimensional (2-D) second order structure functions are widely used to quantify surface structure and roughness parameters (e.g. Nikora et al., 1998; Aberle and Nikora, 2006).

The measurement of gravel surface as random field of surface elevations has become very common with availability of high resolution imaging and laser scanning techniques. However the accuracy of the measurement of the surface elevation and errors associated with the measurement techniques could affect estimation of bed roughness. Hodge et al. (2009) quantified errors in surface elevation data of gravel bed acquired by Terrestrial Laser Scanning (TLS) due to surface geometry, reflectivity and inherent instrument precision. The effect of such measurement errors on grain-scale roughness characterization requires careful assessment. PSD laser scanners are widely used in laboratory scale to acquire gravel surface elevation data (e.g. Mohajeri et al., 2014).   In this study gravel surface elevation errors associated with PSD laser scanning technique are explored. The main aims are to investigate the sources of the errors, quantify the errors and develop methods to remove the errors. For this purpose high resolution

(1.0 mm) measurements of surface elevation of a gravel bed and a bed composed of spherical balls with different colours and surface texture (diameter = 25 mm) were conducted in laboratory flume. The effect of the errors on statistical parameters that describe grain-scale roughness and the spatial structure of the rough bed are investigated. The acquisition, post-processing, statistical analysis of gravel bed surface elevation data are presented and results are discussed.

3.2. GRAVEL BED TOPOGRAPHY MEASUREMENT TECHNIQUES

The most widely used non-contact or remotely sensed acquisition of micro-topography of gravel surfaces in both two- (2-D) and three- (3-D) dimensions are bed profilers, laser scanners and stereo-photogrammetric techniques (Nikora et al., 1998; Smart et al., 2004). A new approach based on 3-D printing of gravel bed topography has emerged in recent year (Bertin et al., 2014). Acoustic bed profiler are widely and successfully deployed to acquire underwater bed topography (e.g. Coleman, 1997) despite their coarse spatial resolution which is limited by high sampling time requirements for fine scale data acquisition. Time of flight terrestrial laser scanners (TLS) and ground based light detection and ranging technologies have significantly improved spatial resolution as well as vertical accuracy (up to 0.5 μm - 0.1 mm) of measurements of gravel bed surface topography both at laboratory scale (e.g. Aberle and Nikora, 2006; Cooper and Tait, 2009) and field scale (e.g. Hodge et al., 2009). Laser scanning is the most precise wide range topography measurement technique and is widely used in gravel bed surface topography acquisition at laboratory scale (e.g. Aberle, 2007; Smart et al., 2004). The laser sensors are designed to reconstruct topography data based on the principle of triangulation. The sensors can be classified, based on the mechanism they detect light, as position sensing detectors (PSD) and charge coupled devices (CCD). The data acquired by TLS contain systematic errors and need careful post processing but laser scanners have no significant post processing requirements. Stereo-photogrammetric techniques make use of two overlapping images to reconstruct high resolution 3-D topography with in the common field of view of the images. The method is used in laboratory scale to acquire bed surface elevation with high horizontal (up to 1.5 mm) and vertical (1 - 2 mm) resolution (Butler et al, 2001; Brasington and Smart, 2003; Chandler et al., 2001; Bertin and Friedrich, 2014). This method is relatively easy to set up in the lab and in the field despite it requires careful calibration procedures (Bertin and Friedrich, 2014). Despite the development of many alternative measurement techniques, small measurement errors could significantly affect the quality of the surface elevation data and its derivatives (Lane et al.,2005) and the effect is more pronounced in low relief surfaces (Hodge et el.,2009).

3.3.PSD TRIANGULATION SENSOR AND OPERATION PRINCIPLES

3.3.1.   PSD triangulation sensor

Position sensing detector (PSD) is a single element detector that converts incident light into continuous position data and single axis types are those often used in triangulation sensors. The detector chip has two output electric signals at its two ends that respond to the position of the imaged light spot in the detector. The amount of current from each output is proportional to the position of the imaged spot on the detector and the spot position is calculated from the relative values of the outputs as the ratio of the difference to the sum of the output currents. It is essentially an analogue device and is very advantageous in high speed data sampling (up to 200 kHz or faster). It also offers other advantages as it has a good dynamic light reception capability and very high natural resolution. However, it has some limitations that are mainly related to its lack of ability to display the profile of the detector pattern and it determines the centre of gravity of all lights that fall on the detector area to measure distance. When more than one light spot or other light falls on the detector it will report the position of the centre of all light which could possibly result in erroneous signal. The texture of the surface being measured can cause considerable variations in measurements of position as surface texture may distort the light spot. This will shift the centre of gravity of the light spot and thus measure erroneous position data. The laser scanner used in the laboratory measurement of gravel bed surface elevation uses PSD sensor.

3.3.2.   Operating principles

PSD triangulation scanning is an active scanning system that uses laser light to probe the environment. This technique is called triangulation because the laser beam, the camera and the laser emitter form a triangle. The laser light source is used to project laser beam on the target being measured and a portion of the beam is reflected through focusing optics and received by the detector to reconstruct distance. The distance measurement by laser triangulation sensors are achieved by projecting a laser beam light onto the target and calculating the distance from a reference point by determining where the reflected light falls on a detector (Figure 3-1). As the point of laser beam falling on the object moves closer to or farther from the reference point, the spot position on the detector changes. Figure 3-1 shows that the axes of the emitted and the received beams enclose an angle θ that changes if the target (surface A or B) is shifted closer (θ increases, θ_A) or farther (θ decreases, θ_B) with respect to the vertical of the emitted laser sensor. The angle θ is determined by the position of the refracted beams (A1 and B1) on PSD. The distance of the target from the laser sensor is then easily obtained through geometrical relations involving the angle θ and the distance of the points.
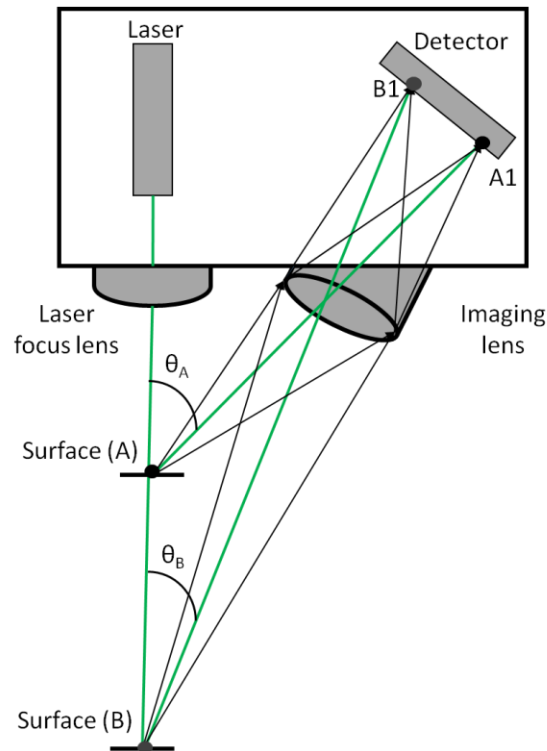
Figure 3-1. Illustration of the principle of the triangulation laser sensor used to measure the elevation of two different points

3.4. SOURCES OF ERRORS IN THE DATA

Measurements of displacement by PSD laser triangulation sensor can be acquired in nearly any material including plastics, ceramics, rubber and paper (MEL Mikroelektronik GmbH, 2002). However, some measurement errors are inevitable depending on target reflectivity and target geometry although instrument design is important.

3.4.1.   Target reflectivity

Laser triangulation operates by imaging the reflected spot of the light from the target on to the PSD thus whether the target is diffusive or specular will affect the quality of the measurements. The sensor performs well when the surface is characterised by diffuse reflectance as light is more likely to be reflected from the surface to the detector. The change in reflectivity of the target, which depends on colour and surface finish of the target, will change the level or intensity of light reaching the detector thus affecting the distance measurement. The distance is computed based on the centre of gravity of the entire reflected spot on the detector so it is very sensitive to spurious reflections from changing surface conditions that could reduce measurement accuracy. On the other hand a target with differential (partly low and partly high) reflectivity within the laser spot can falsely bias the centroid of the image of the spot

creating an error in measurements. However, small spot size detectors can reduce the effect of differential reflectivity. Thus measurements conducted in a consistent matte finish (using diffuse sensor head) or specular or highly polished targets (using specular laser head) are highly preferred for better performance. Differential reflectivity can be caused by sharp edges between different colours on the target and surface textures. ML/5-200 can perform well with a minimum diffuse reflection of 10% (MEL Mikroelektronik GmbH, 2002).

3.4.2.   Target geometry

PSD sensor measurement performance is high when target is positioned normal to the laser head as it prevents tilt errors. However, the effect of tilt on the measurement could also depend on the surface reflective properties of the target. For instance, ideally diffuse target will allow proper measurements on surfaces tilted 30° or more from the normal. Laser triangulation sensors are also capable of measuring surface topography of curved surfaces especially when the laser beam is positioned facing directly toward the centre of the target curvature. Such sensor orientation eliminates any "tilt" seen by the laser. In addition, the orientation of the head should be such that the curved surface does not skew the laser triangulation angle. Figure 3-2 shows a proper sensor orientation (laser head moving towards right) that avoids deflection of laser be by target shape and obstruction by target features.
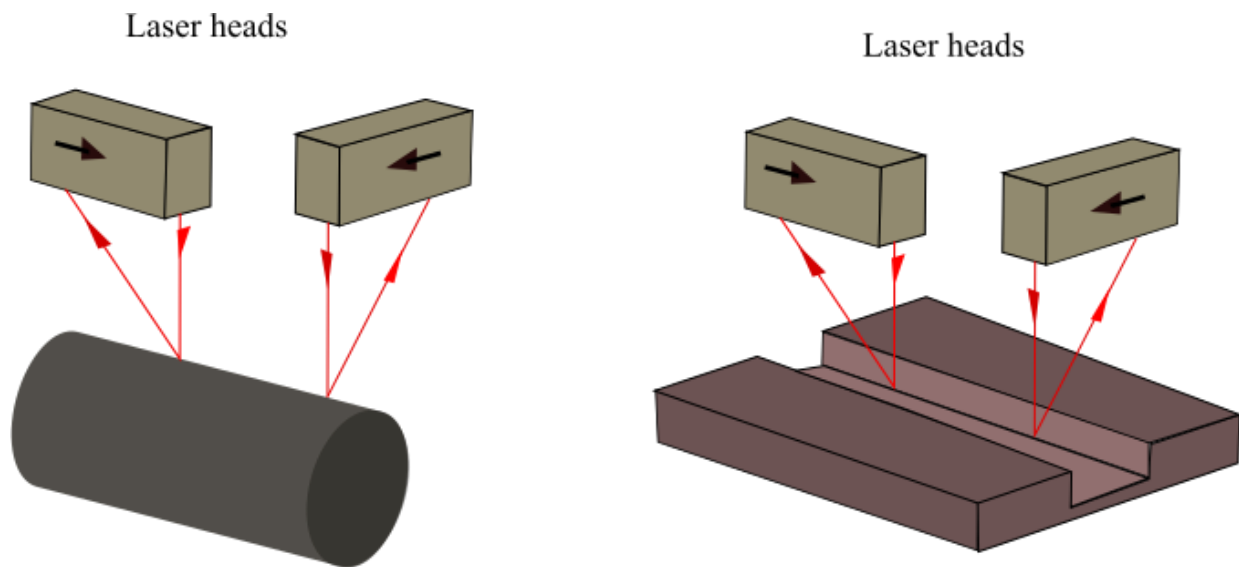
Figure 3-2. The laser beam deflected by target shape (left) and obstructed by target features (right)

Gravel beds are characterised by various surface geometry and particle arrangements and orientations. Therefore, each particle has random tilt and surface curvature in different directions while the laser scanner sensor can only be oriented in one direction (stream-wise). Thus, measurements of bed surface elevation of gravel particles can be affected by target shape, tilt, obstruction and combinations of all. Figure 3-3 shows illustration of the laser acquisition orientation and a hypothetical gravel particle. Figure 3-3 (left) shows that the reflected laser beam projected at P1 or further below could be potentially obstructed and deflected and could significantly affect the accuracy of elevation measurement. This shows that elevation errors could be expected in the curvature side of gravel particles that face opposite to reflected laser beam. There could also be differential reflectance especially at the edge of gravel particle due to reflectance of laser beam from the gravel edge and its bottom although the spot diameter is 2 mm. The laser light projected at P2 and P4 could be affected by target tilt effect but this could be minimal as a tilt as large as 30° is expected to have good performance; no tilt effect at P3. The black arrows show the movement direction of laser head during data acquisition.
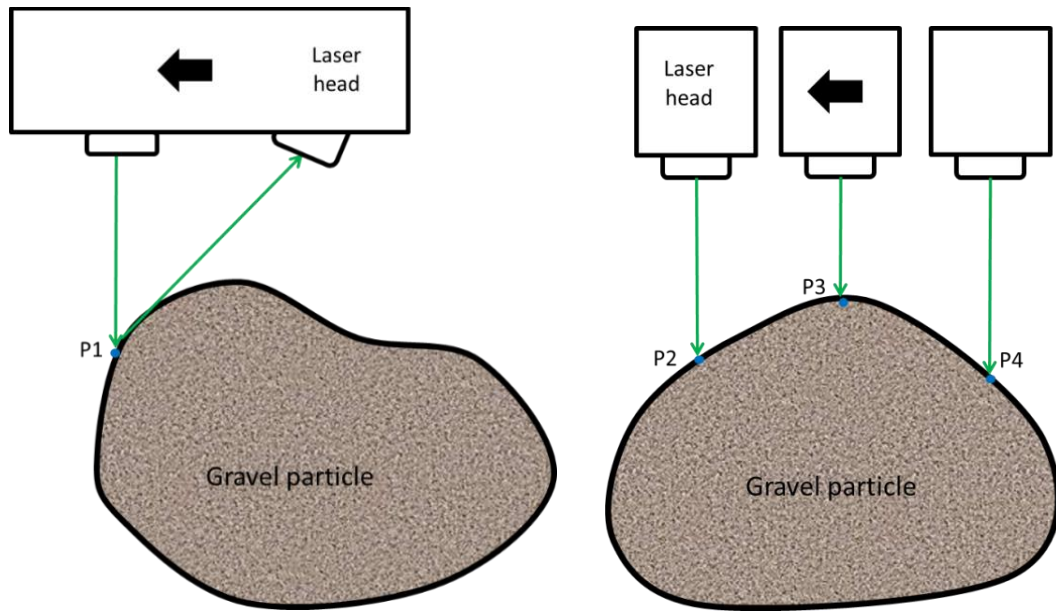
Figure 3-3.Gravel particle orientation and the acquisition orientation of the laser head (laser scans stream-wise (left) and span-wise (right) directions)

3.5. MATERIALS AND METHODS

3.5.1.   Laboratory set up for data acquisition

The surface elevation data of both sphere beds and gravel bed , that were placed in laboratory flume, were measured by M5L/200 laser scanner (MEL Mikroelektronik GmbH, 2002) with a stream-wise sampling

interval of $\Delta x = 1.0$ mm, a lateral spacing of $\Delta y = 0.3$ mm, and with a vertical resolution of 0.1 mm. The different sampling intervals in x and y directions are due to minimum step width of the stepper-motor of the span-wise system of the laser scanner. The laser scanner was mounted by two light emitting (optical distance sensor) sensors and a receiving (PSD) sensor positioned at an angle of 25°. This type of sensor is advantageous since it emits smaller light spot to register fine differences in object's structure and better accuracy with striped objects (light/dark transition within the spot). Table 3-1 shows the specifications of the laser scanner. The vertical range of data acquisition of the device is 200 mm (-100 to +100 mm) where only objects located in the distance range from 240 to 440 mm from the light spot (diameter = 2 mm) of the laser are acquired at a sampling rate of 40 kHz. The type of output data output was in volts thus converted to mm after a proper calibration curve was developed. The range of measurements in volts is ±10 V. The acquired surface elevation data of both the sphere beds and gravel bed were re-sampled to have equal intervals δx and $\delta y = 1$ mm before subsequent analysis using MATLAB$^{\circledR}$.

Table 3-1. Technical specification of M5L-200 laser scanner

Specifications	*Values*
Range (mm)	±100
Reference distance (mm)	340
Linearity error (μm)	600
Resolution (noise) (μm)	60
Spot diameter (mm)	2
Distance laser-receiver (mm)	150.5
Laser wavelength (nm)	675

3.5.2.   Sphere bed materials and acquired data

Before the measurements were conducted the flume was subjected to low light intensity level from the surrounding. First, for the sphere beds, four wooden plates of 85 mm by 137 mm were prepared where in each plate 15 spheres of diameter 25mm placed as shown in Figure 3-4. The first set of spheres were painted black polished (hereafter BP), the second black-opaque (hereafter BO), the third white-opaque (hereafter WO) and the last red-polished (hereafter RP). This colour arrangement allowed investigating the effect of target colour (reflectivity) on measurement accuracy of PSD laser scanner. Figure 3-5 shows the acquired surface elevation data of the sphere beds shown in Figure 3-4.
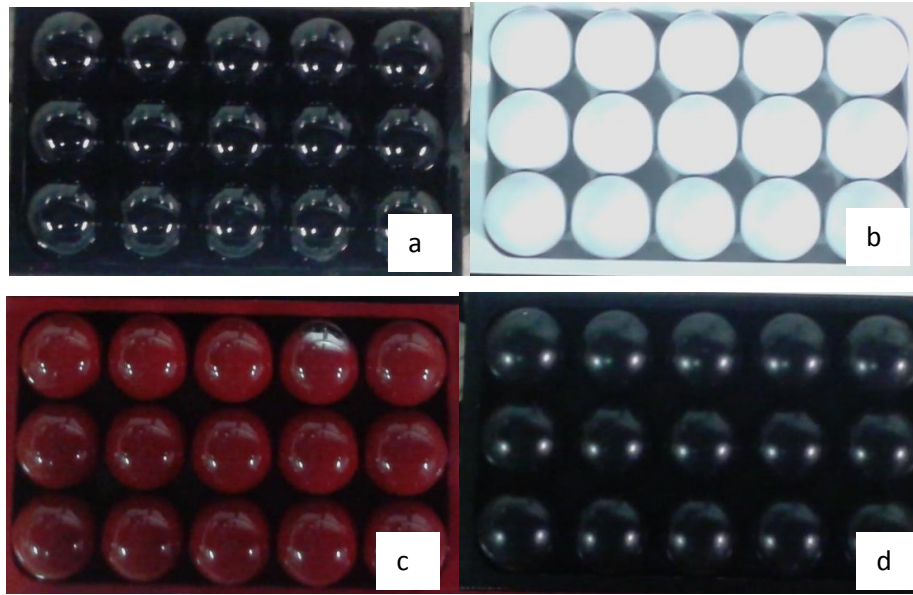
Figure 3-4. The spherical beds painted: a) black polished b) white opaque, c) red polished and d) black opaque
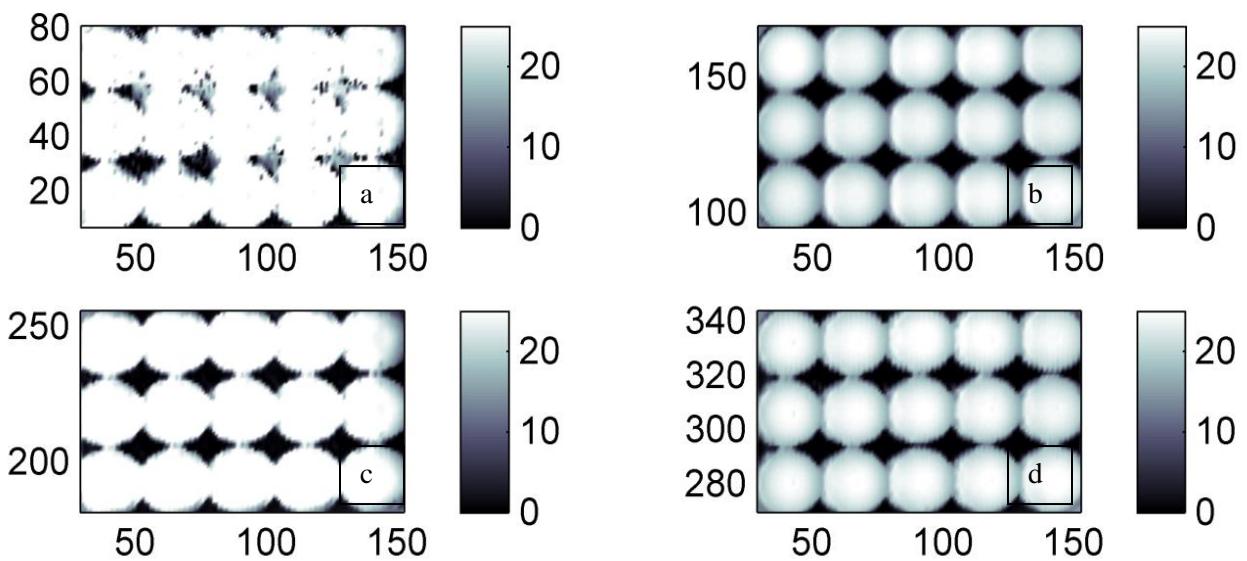
Figure 3-5. Measured surface elevation data of the four spherical beds: a) black polished, b) white opaque, c) red polished and d) black opaque

The theoretical surface elevation data of the spheres was also calculated as three-dimensional data using sphere formula of known diameter (in this case 25 mm), thus the true surface elevation of the bed is known a priori (Figure 3-6). The theoretical surface elevation data was used as a reference data to evaluate the elevation errors of PSD measurements. The corresponding surface elevation data acquired

by, for sphere bed painted white opaque, PSD laser scanner is shown in Figure 3-7. The elevation errors are evident on curved surface, mainly in y direction, of the spheres (the blue box in Figure 3-7).
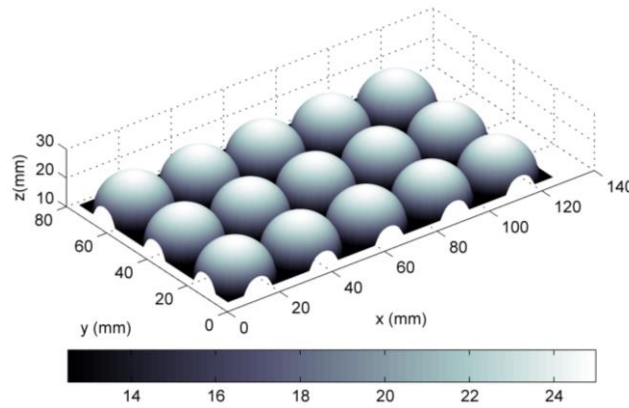
Figure 3-6. Theoretical surface elevation data (model) of sphere bed that was constructed by using sphere equation
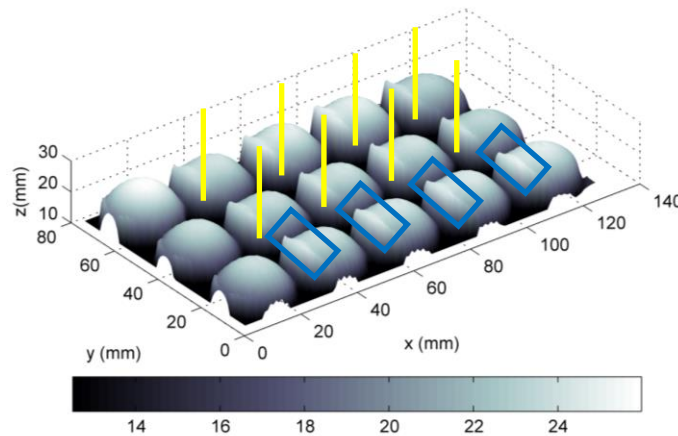
Figure 3-7. Measured bed surface elevations of sphere bed (white opaque spheres)

The measured surface elevation data is referenced to have zero elevation at the bottom of the spheres so as to compare with theoretical surface elevation data. This was accomplished by first interpolating the elevation points that correspond to the bottom of the spheres or the level of the plate (shown in yellow vertical lines in Figure 3-7) and then by subtracting it from the   surface elevation data. Finally surface elevation data with a minimum of zero and maximum of 25mm (the crest elevation of the spheres) was obtained.

3.5.3.   Gravel bed materials and acquired data

The gravel bed materials were prepared to investigate elevation errors of gravel surface elevation data acquired by PSD laser scanner and afterwards to characterize its roughness. The entire flume was first

filled with immobile coarse gravel particles to a thickness of 20 cm (Figure 3-8). The coarse gravel particles in the flume bed were prepared by screeding manually from upstream to downstream (in flow direction) in order to avoid gravel clustering. This procedure allows creating a gravel bed similar to water worked beds as reported in Aberle and Nikora (2006). The particle size distribution of the gravel bed material is shown in Figure 3-9. The particles are characterized by d_{50} = 24.9mm, d_{90} = 30.44mm, d_{84} = 29.54mm, d_{16} = 19.64mm, σ_g =1.227 and C_u =0.42. The gravel particles can be considered uniform and well-graded with coefficient of uniformity (C_u) less than 3 and geometric standard deviation (surface sorting) (σ_g) less than 3 (Tigrek and Aras, 2011). Figure 3-10 (top) shows the gravel bed material at the test (control) section (painted white) that comprises gravel particles in 180 mm x 180 mm area which is located 7.8 m downstream of the flume entrance (flume layout is plotted in Chapter 4) and surface elevation data acquired by PSD laser scanner. The acquired data is characterized by unusual spikes (erroneous surface elevations) that are related to the intrinsic limitation of PSD sensor which is used in the laser scanning of the gravel bed (Figure 3-10). The sensor seems to have limited capacity in capturing returning signal from gravel particles whose edges are laid opposite to sensor returning direction.
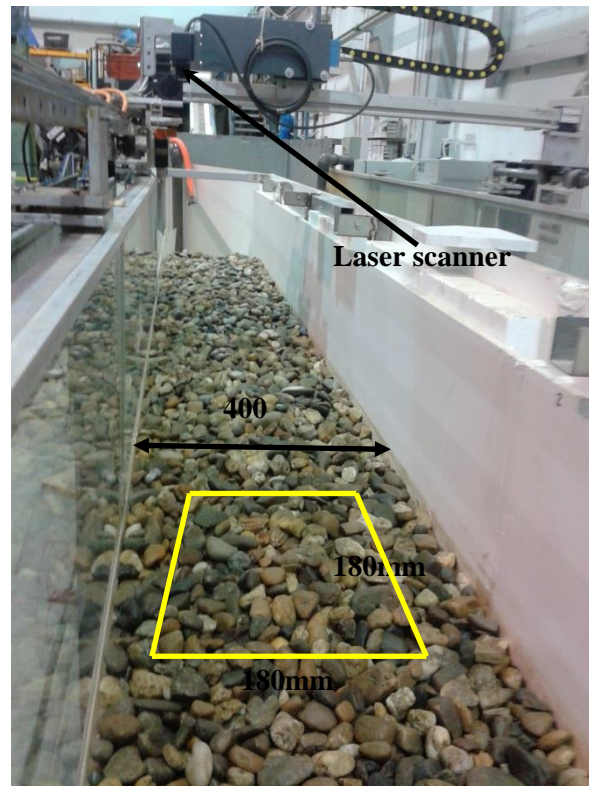
Figure 3-8. Gravel bed materials filled in the laboratory flume and test section (yellow box)
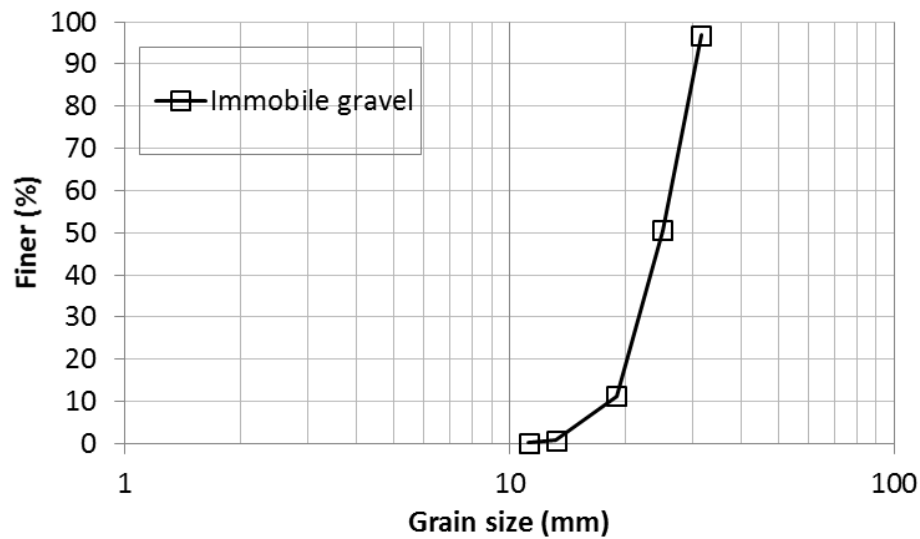
Figure 3-9. Grain size distribution of gravel bed material used in laboratory flume

Most of the erroneous elevation data are observed at the edges of the gravel facing downstream; surface elevation spikes shown with white dots (Figure 3-10, bottom). The erroneous data elements (surface elevation spikes) in the gravel surface elevation data have an elevation up to a maximum of 200 mm. The erroneous data should be filtered before subsequent analysis for roughness characterization. In the following sections the development of filter methods that aim to reduce the elevation errors are developed and tested.
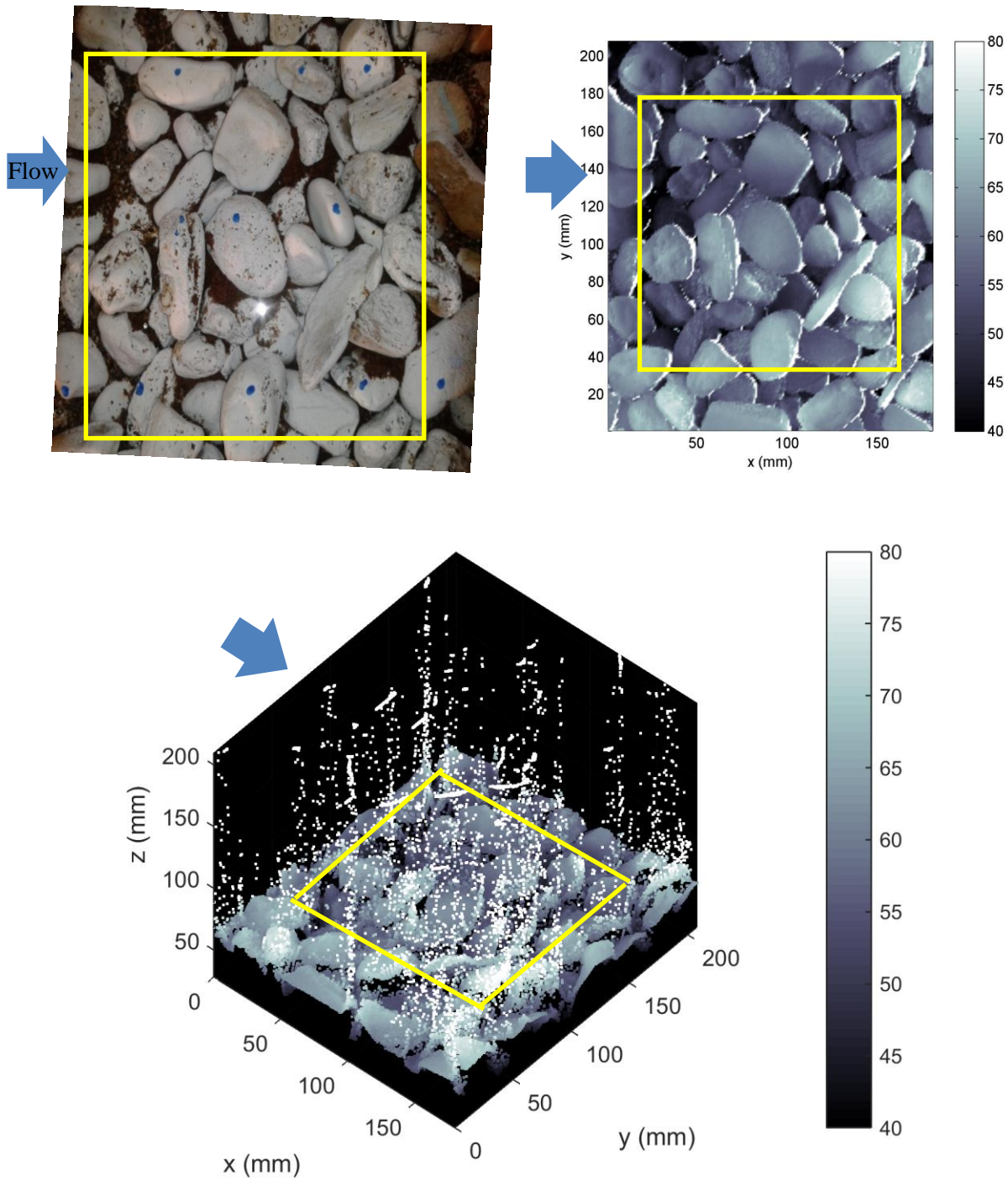
Figure 3-10. The gravel bed materials at the test section and the raw gravel surface elevation data acquired by PSD laser scanner (yellow box shows area of interest for further analysis)

3.5.4.   Development of methods to reduce elevation errors

In the present study two filter methods that use a threshold to detect erroneous data elements in the surface elevation data are devised and tested. The proposed methods are Adaptive Mean Filter (AMNF) and Normalized Adaptive Median Filter (nAMDF). Consider an elevation value in gridded data denoted by Z_0, its n x n –neighbourhood data, denoted by $\{Z_1, Z_2, ..., Z_{n^2-1}\}$, and $\langle Z \rangle$ and Z_m as the mean and median of $\{Z_1, Z_2, ..., Z_{n^2-1}\}$ (note that Z_0 is excluded) respectively where n is filter window size. In AMNF if a residual β, defined as: $\beta = Z_0 - \langle Z \rangle$ is larger than a user define threshold value (c) then that cell is identified as erroneous and removed. In this manner, AMNF identifies erroneous peaks surrounded by lower elevation points in the neighbourhood. A similar procedure is applied in Hodge et al. (2009) to remove erroneous peaks in gravel surface elevation data acquired by Terrestrial Laser Scanner (TLS). The normalized adaptive median filter is similar to AMNF filter however in this approach a more generalized or narrow range of threshold values is designed to detect the erroneous peak elevation elements. The approach is similar to the work of Westerweel and Scarano (2005) in which a universal optimal range of threshold value and optimal size of filter window was developed to detect and remove spurious data in Particle Imaging Velocimetry (PIV). In nAMDF a residual, r_i defined as: $r_i = |Z_i - Z_m|$ is determined for each grid data in the neighbourhood $\{Z_i \,|\, i = 1, ..., n^2 - 1\}$, and the median r_m of $\{r_1, r_2, ..., r_{n^2-1}\}$ is used to compute a dimensionless residual β of Z_0 as:

$$\beta = \frac{Z_0 - Z_m}{\varepsilon + r_m} \tag{3-1}$$

which is used to detect erroneous peaks (data elements). A minimum normalization level ε is introduced to correct β when $r_m = 0$ in cases of similar elevation values in the filter window. If β is larger than an optimal threshold value, c that cell is identified as erroneous and removed. In both AMNF and nAMDF methods the removed cells are replaced by interpolation of the neighbouring data elements instead of replacing with the mean or median value evaluated within the filter window unlike Hodge et al. (2009) and Westerweel and Scarano (2005). This allows eliminating any contribution from erroneous data elements as the use of mean or median value of the filter window (neighbourhood grid values) still will contain elevation errors. In this manner the procedure is applied to all the cells in the data. The interpolation of removed cells is completed by applying the Inverse Distance Weighting interpolation technique where the neighbouring un-removed and relatively error free cells are used. The procedure is applied and tested for various radii and thresholds until an optimal radius and threshold value that reduces

the error significantly is obtained. The advantage of nAMDF over AMNF is that it gives very small range of threshold that does not vary significantly among grid points of surface elevation data to detect spurious elevation measurements.

3.6. RESULTS AND DISCUSSIONS

3.6.1. Analysis of Surface Elevation Data of Sphere beds

3.6.1.1.Characteristics of Elevation Errors in Sphere bed

First, the statistical distributions of measured surface elevation data of sphere beds painted with different colour and surface finishes are investigated (Figure 3-11). Figure 3-11 shows that the mean, maximum and minimum elevations of BP and BO data are extremely affected by elevation errors and the elevations at the top of the sphere are the most affected ones. This shows that the surface elevation data acquired by PSD laser scanner contains elevation errors. The low reflectivity in combination with specular reflection from polished finish of the black painted spheres limits the performance of the PSD sensor. The white opaque and red polished spheres show very close agreement with the reference surface elevation data. The fact that red polished surface showing good measurement performance indicates that target colour is more important rather than the nature of surface finish (polished or opaque (matte)).
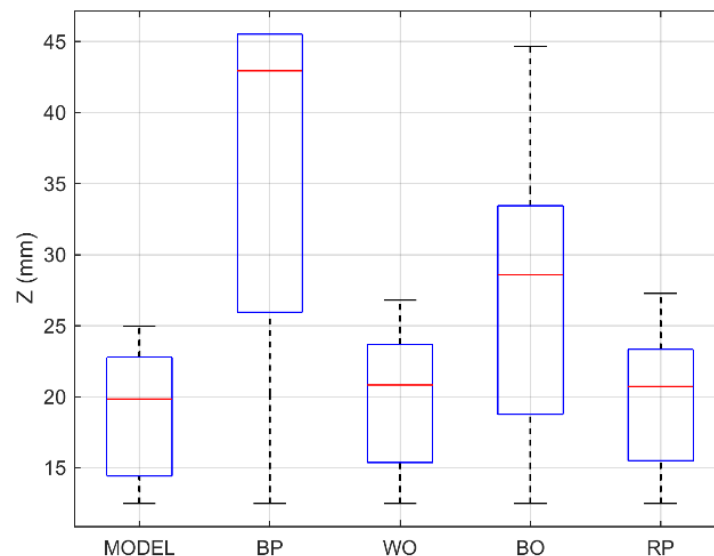
Figure 3-11.The distribution of surface elevation data of the reference theoretical bed (model) and the four sphere beds

Figure 3-12 shows the elevation profiles taken along the crest of the test spheres and black opaque (solid line with square) and black polished (solid line) beds are extremely erroneous. The profiles of sphere bed

painted white opaque (broken line) and red polished (solid with star) are in close agreement with the reference (model) (dashed line). Nevertheless, there are directional elevation errors shown in blue boxes in Figure 3-12 and Figure 3-7. These erroneous regions of the data are due to target tilt and laser beam obstruction caused by target shape. These areas are sphere regions whose surface curvature facing opposite to the returning laser beam received by PSD detector as shown in Figure 3-3 (left).
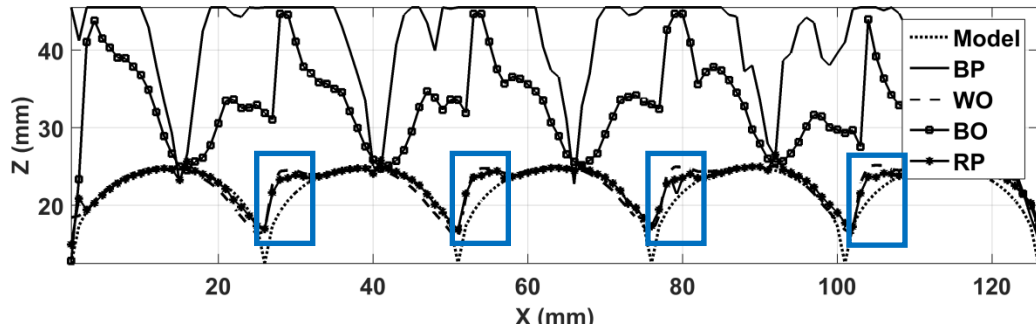
Figure 3-12. Elevation profile taken along the crest of the central five test spheres of surface elevation data of the spherical beds in Figure 3-5

3.6.1.2. Performance of Proposed Filter Methods

The datasets of black opaque and polished are discarded in this analysis since the entire elevation data was erroneous mainly due to target colour. The focus is to evaluate the performance of the filter methods to detect and remove the erroneous elevation grid points caused by mainly target shape. The sphere bed painted in white opaque spheres is selected since the elevation error is mainly due to target shape, which is a major cause of errors in gravel surface elevation data, rather than target colour. The proposed filter methods highlighted in Section 3.5.4 are tested to remove the directional erroneous peak elevations that are dominant on sphere curvature that lies opposite to returning laser beam (refer Figure 3-12). The sphere model plotted in Figure 3-6 is used as a reference data to evaluate the performance of each filter based on Root Mean Square Error (RMSE) and visual inspections.

I.   The AMNF Method

The AMNF filter is applied and tested for various filter radii and threshold taking into account the anticipated elevation differences among neighbouring pixels. In this manner, high elevation values surrounded by lower ones in the neighbouring grids can be magnified by identifying points with high deviation from the mean local elevation within the filter window. The choice of a proper filter window and a threshold parameter is essential to avoid data smoothing (especially at lower threshold) and to remove erroneous or peak elevations selectively from the data (e.g. Hodge et al., 2009).
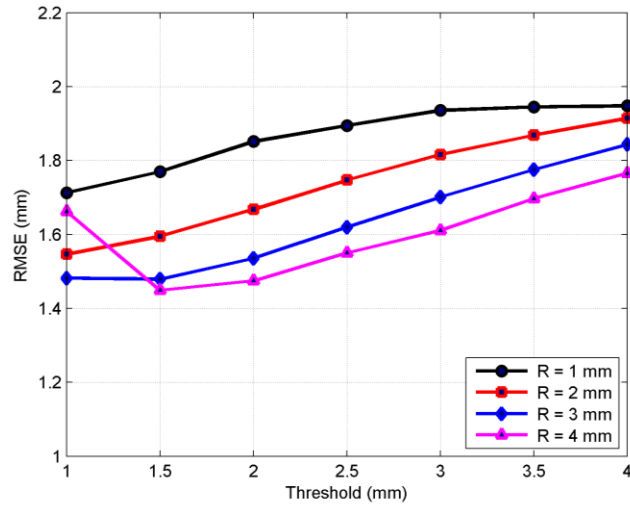
Figure 3-13. The RMSE of AMNF filtered surface elevation data for various thresholds and R=1-4mm

Figure 3-13 shows RMSE of AMNF filtered data calculated using theoretical bed as a reference. It shows that a large threshold with small filter window and a small threshold with large filter window give better filter performance. A threshold of c = 2.0 mm and filter window, R = 4 mm significantly removed the erroneous data in surface elevation data of the spheres by AMNF (see Figure 3-14). Figure A-1 (in Appendix A) shows the distribution (histogram) of the filter parameter (β) which is used to identify the optimal threshold, c = 2 mm. The negative values of β are excluded since they do not indicate erroneous data elements that are characterize by unusual elevation peaks.
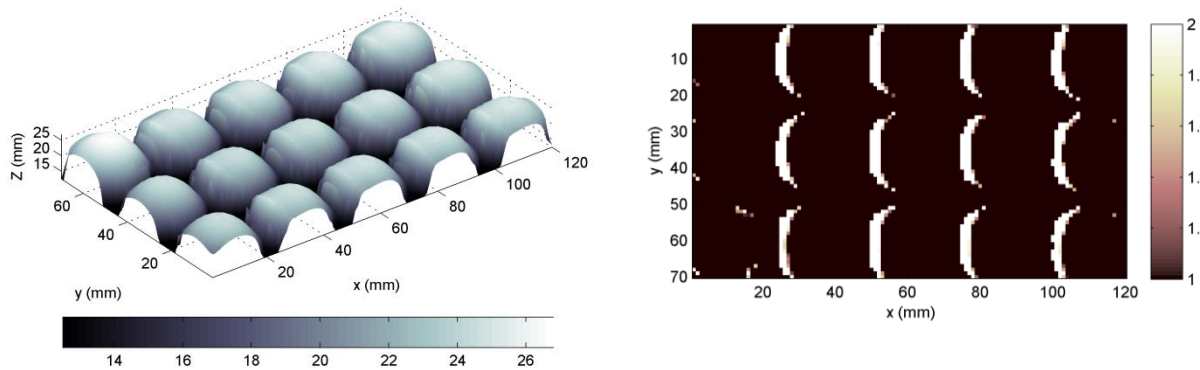
Figure 3-14. Filtered surface elevation data by AMNF: peak removed (left) and the difference between unfiltered and filtered (right)

The residuals (Figure 3-14, right) are calculated by subtracting filtered data from the raw data. Most of the modified surface elevation data elements are in the region of erroneous data elements (sphere curvature that lies opposite to returning laser beam) observed in the raw data. However, the use of AMNF

has some limitations since it needs trial and error to find an optimal threshold and filter window size. There is no any anticipated range of values for threshold parameter and the optimal threshold varies from data to data which makes the use of an optimal threshold of one data for another set of data problematic.

II. The nAMDF Method

The nAMDF method is applied after evaluating an appropriate ε, c and R. The selection of an optimal ε and R affects the estimate of the filter parameter β and identifying the erroneous data elements. Figure 3-15 (right) shows the filter parameter (β) distribution for ε = 0.5mm and for radius of the filter (R = 1.0 - 5.0 mm). The value of β comprises both negative and positive numbers and the positive values are those relevant to detect the erroneous peaks. It is important to note that there is not that much dependence of β on R especially when the value of ε is large. However the selection of optimal c based on statistical distribution of β should be with caution when the filter is evaluated for various R values. Figure 3-15 (left) shows the distribution of β for various normalization levels (ε = 0 - 0.5) and for R = 4.0 mm. As the normalization level (ε) increases the range of β gets narrow and this simplifies the choice of an optimal threshold for peak detection and removal compared to AMNF. The sensitivity of β with filter radius decreases with an increase in ε. For instance, when ε was increased to 0.5 the distribution of β remained similar for various radii (Figure 3-15, right). Over all the choice of an optimal c should be conducted with caution although the filter method establishes a narrow range of β distribution.
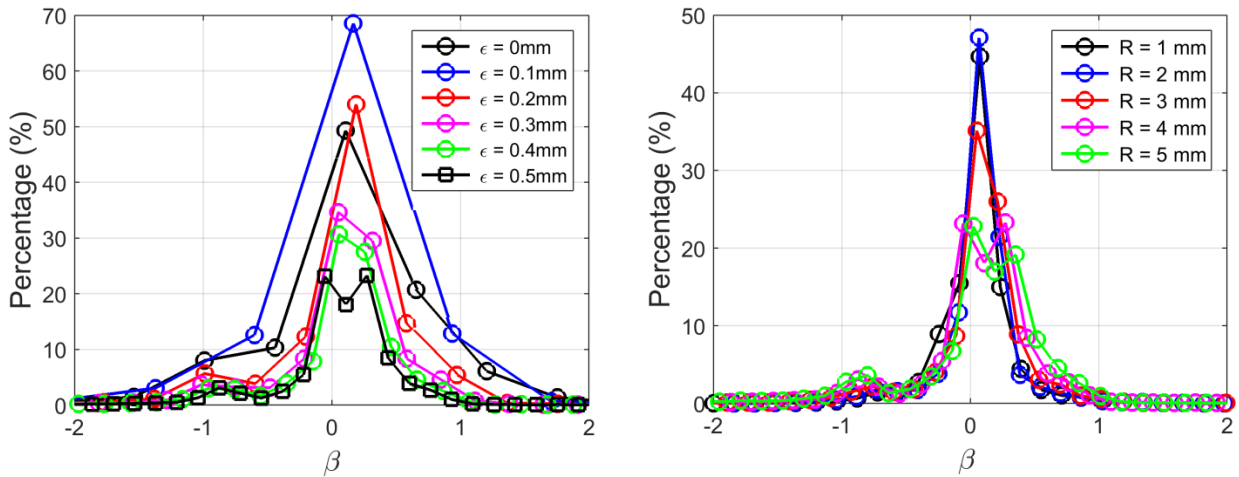
Figure 3-15. The distribution of β of nAMDF for various ε (R = 4mm) (left) and R (ε = 0.5mm) (right)
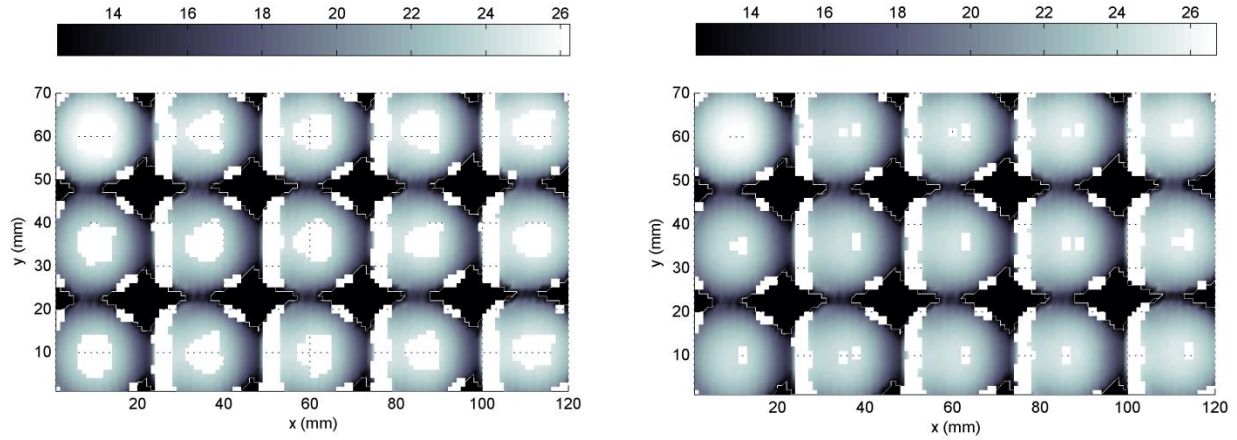
Figure 3-16. The erroneous data elements (white areas) identified and removed for ε = 0 mm (left) and ε = 0.5 mm (right) where R = 4 mm and c = 0.5

The selection of a very small or near zero ε tends to identify non erroneous data as erroneous (Figure 3-16, left). Especially at the top of the sphere bed the effect of small ε is significant in incorrectly identifying erroneous data elements (Figure 3-16, left). But with relatively larger ε solely erroneous elements of the data are identified (Figure 3-16 , right). Figure 3-17 shows the RMSE evaluated based on reference data for nAMND filter applied for various thresholds of selected filter windows (R). The parameters ε = 0.5 mm, R = 4 mm and c = 0.4 give the smallest RMSE and are optimal set of filter parameters that give best filter performance.
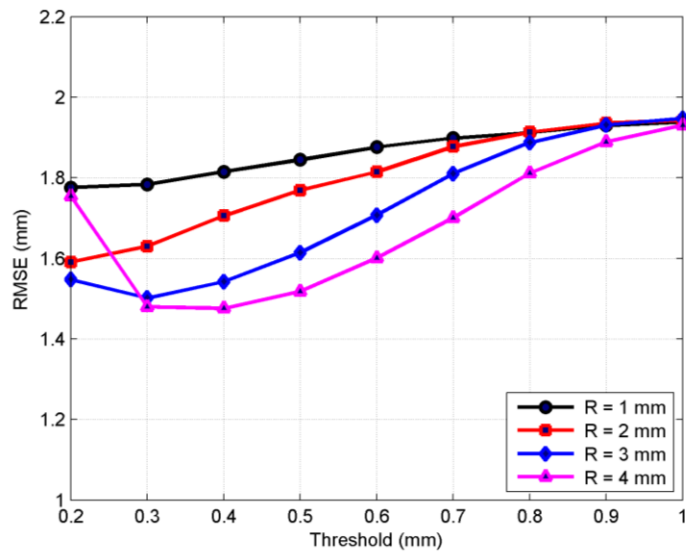
Figure 3-17. The RMSE of nAMDF filtered surface elevation data for various thresholds and R = 1-4mm

Figure 3-18 (left) shows surface elevation data of the sphere bed filtered using the optimal set of parameters of nAMDF. The erroneous peak elevations are effectively removed while preserving most of non-erroneous elements. Figure 3-18 (right) shows the difference between the raw and filtered data and it also shows that the errors are effectively removed. The percentage of elevation difference larger than 1 mm between reference and filtered data by AMNF and nAMDF are 12.60 % and 13.00% respectively. The percentage of elevation differences that are larger than 1 mm between the reference and the raw data is 28.20%. Figure 3-19 shows longitudinal (along y = 38.0 mm) and transversal (along x = 51.0 mm) profiles along filtered (AMANF and nAMDF) and raw surface elevation data of the sphere bed.
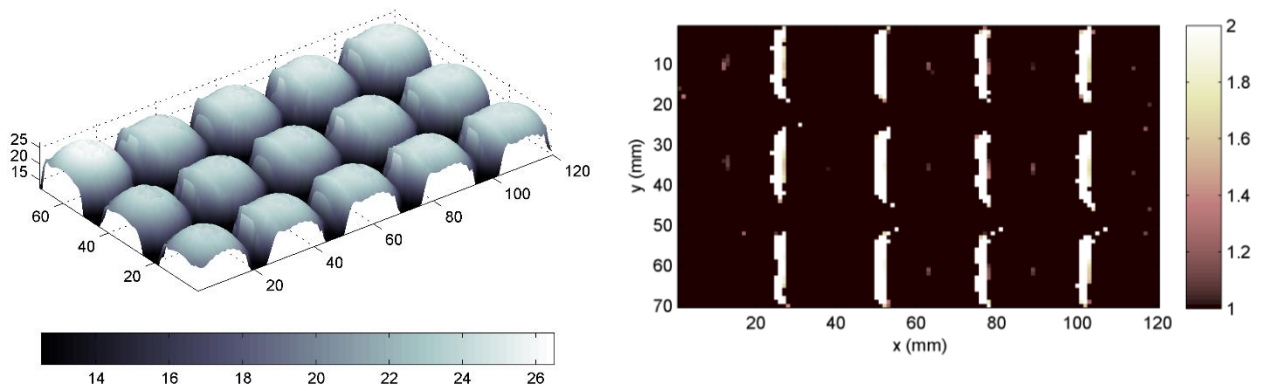
Figure 3-18.Filtered surface elevation data by nAMDF (left) and the difference with raw data (right)

The longitudinal profiles in Figure 3-19 (top) show that erroneous elevation peaks are effectively removed by AMNF (circle) and nAMDF (black dot) and the elevation values at the edges of the spheres match well with the reference sphere profile (blue line). The transversal profile (Figure 3-19, bottom) also shows more clearly the elevation error as large as 10 mm is effectively removed. Both AMNF and nAMDF remove the erroneous surface elevation data elements with efficiency however AMNF need trial and error to identify optimal window and threshold parameter while nAMDF can easily overcome this limitation as the range of optimal threshold is very narrow. However, slight changes in normalization level could significantly change the distribution of β thus cautious evaluation is required. AMNF tends to smoothen the edges of the spheres but nAMDF preserves the edges and detects solely the erroneous elevations.
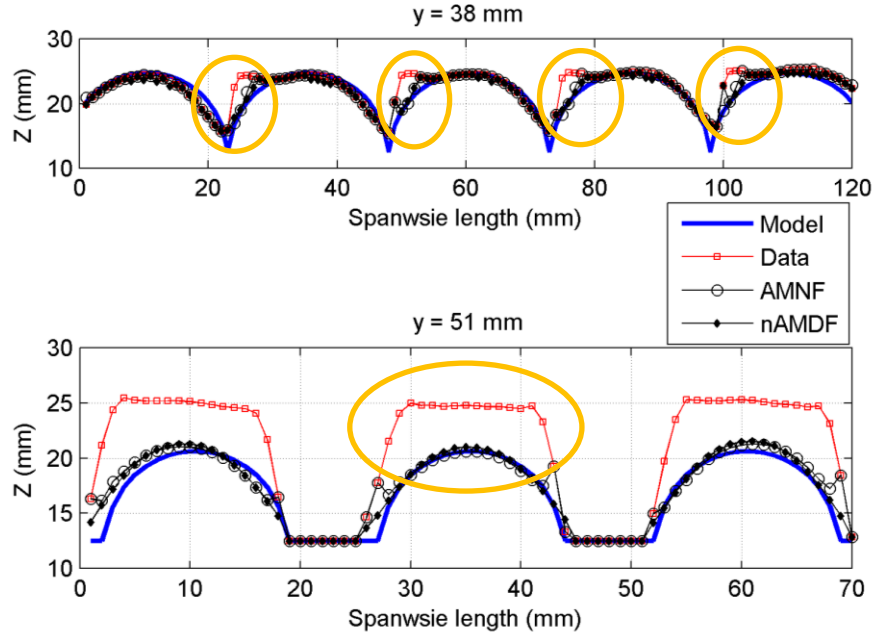
Figure 3-19. Elevation profile taken along y = 51.0 mm and x = 38.0 mm for unfiltered and filtered surface elevation data (green circles show regions of erroneous data)

Table 3-2.The statistical parameters of the reference (MODEL), raw (DATA) and filtered (AMNF and nAMDF) surface elevation data

	MODEL	DATA	AMNF	nAMDF
RMSE	0.00	1.95	1.44	1.43
μ_Z	19.58	20.15	19.83	19.80
σ_Z	4.15	4.44	4.35	4.30
k	12.48	14.29	14.29	13.99
S	-0.59	-0.65	-0.54	-0.57
K	2.02	2.00	1.94	1.94

μ_Z-mean surface elevation (mm)
σ_Z-standard deviation of surface elevation (mm)
k-geometric roughness height;
S-Skewness; K-Kurtosis

Table 3-2 shows the statistical comparison between the reference data, raw data, and filtered data for optimal radius (R) and threshold parameters (β) as well as normalization level (ε). The RMSE, mean and standard deviations of the surface elevations data filtered by AMNF and nAMDF are quite similar. The mean and standard deviation of the raw data is not very different from the model (reference data) however

the geometric roughness height is overestimated by raw data. In the next sections the filters developed for sphere surface elevation data are applied on gravel surface elevation data that was acquired at the same spatial resolution and environmental conditions.

3.6.2.   Analysis of Surface Elevation Data of Gravel bed

3.6.2.1. Filtering Errors in Gravel bed Surface Elevation Data

The filters that were developed based on elevation errors of sphere beds are further tested and applied to overcome the elevation errors noticed in gravel surface elevation data. This will improve bed roughness characterization based on random field approach. The AMNF and nAMDF filters were applied directly to gravel data based on the range of threshold and filter window (AMNF: c = 2 mm and R = 4mm and nAMDF: ε = 0.5 mm, R = 4 mm and c = 0.4) optimal for the sphere datasets as a first step. But with a slight adjustment of optimal parameters (c = 2.5 mm and R = 4 mm) of sphere datasets, the elevation errors (spikes) in gravel surface elevation data were effectively removed by AMNF preserving most of error free data elements (Figure 3-20). In Figure A-2 (in Appendix A) the distribution of the filter parameter (β) which is used to identify the optimal threshold for gravel surface elevation data is presented. The negative values of β are excluded since they do not indicate erroneous data elements that are characterized by unusual peaks or spikes. The difference between the filtered and unfiltered data (Figure 3-20, right) shows there are still some regions around gravel edges where error free regions are also removed to some extent. Both visual and qualitative evaluation of regions of erroneous data elements indicate the erroneous regions are removed.
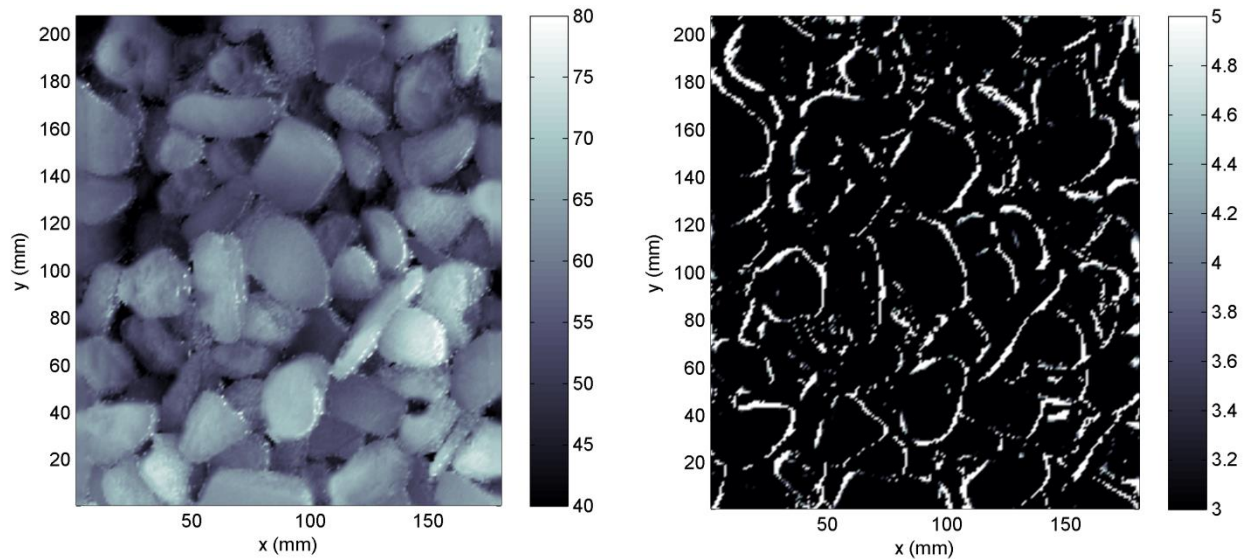
Figure 3-20. Gravel surface elevation data filtered by AMNF (left) and the difference with the unfiltered data (right)

Quantitatively the distribution (histogram) of elevation difference between the unfiltered and filtered data is evaluated and it shows negative differences which are caused by data smoothing by AMNF filter (Figure 3-22, left). A very small smoothing of edges is evident in the longitudinal profile taken along y = 94 mm (Figure 3-23). The filter performance is also evaluated based on the distribution of mean elevation difference parameter which is designed to identify local discontinuities in the surface (Hodge et al., 2009). The mean elevation difference parameter (E_Z) is calculated for each surface grid cell of AMNF filtered data using a three by three moving window. Large absolute values of E_Z indicates a large difference in elevation between the central cell and the surrounding cells, hence rapid changes in elevation over 1 mm distances, which are unlikely to occur in gravel surfaces, hence probably represent the presence of erroneous data points (Hodge et al., 2009). Figure 3-22 (right) shows that the frequency of E_Z larger than 1mm has reduced dramatically by the filter. The percentage of E_Z larger than 1mm has reduced from 39.20% to 29.50% after AMNF filter is applied.
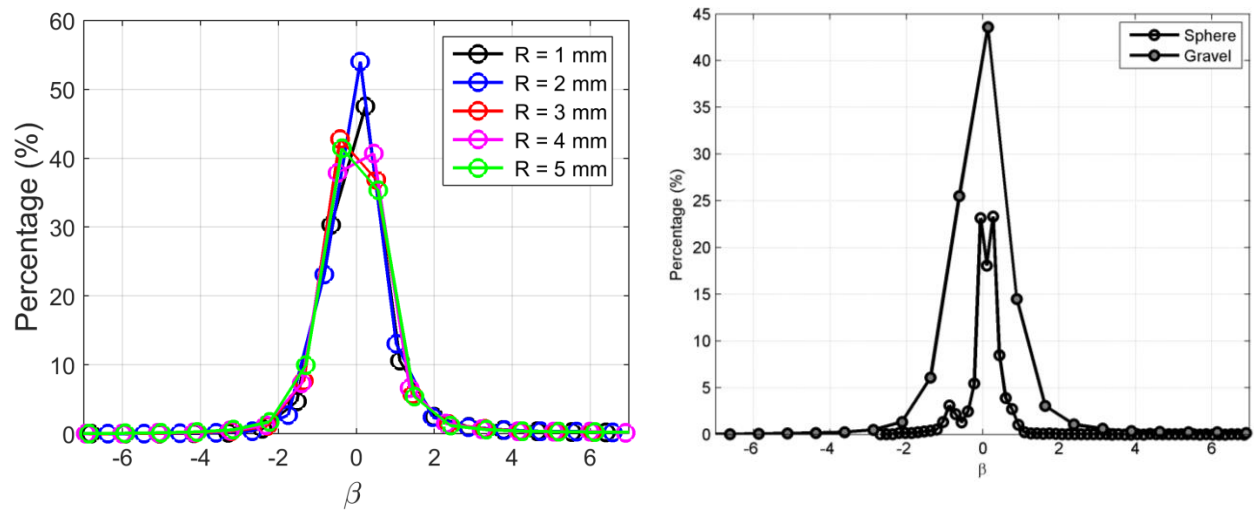
Figure 3-21. Threshold parameter (β) for ε = 0.5 and R = 1-5 mm (left) and R = 4mm (right)

The nAMDF filter is applied after appropriate normalization level ε, optimal radius R and threshold c are identified. Figure 23 (right) shows the range of β for both sphere and gravel are narrow and similar which could allow the transfer of the filter parameters from the sphere data. The distribution of the threshold parameter (β) for various filter radii and a given normalization level (ε = 0.5) does not vary as large as observed in the sphere data (Figure 3-15, right) instead it remains very similar over the range of radius (Figure 23, left). As the normalization level increases, the range of β shrinks thus simplifying the choice of a threshold for peak detection and removal (Figure 3-15, left and Figure A-2 in Appendix A). Increasing ε also decreases the sensitivity of β to filter radius thus β remains similar for various radii as the ε value increases. Nevertheless even though the distribution of β is similar for small and larger radius,

the same threshold applied at larger radius may not be more effective in detecting and removing the erroneous data elements.
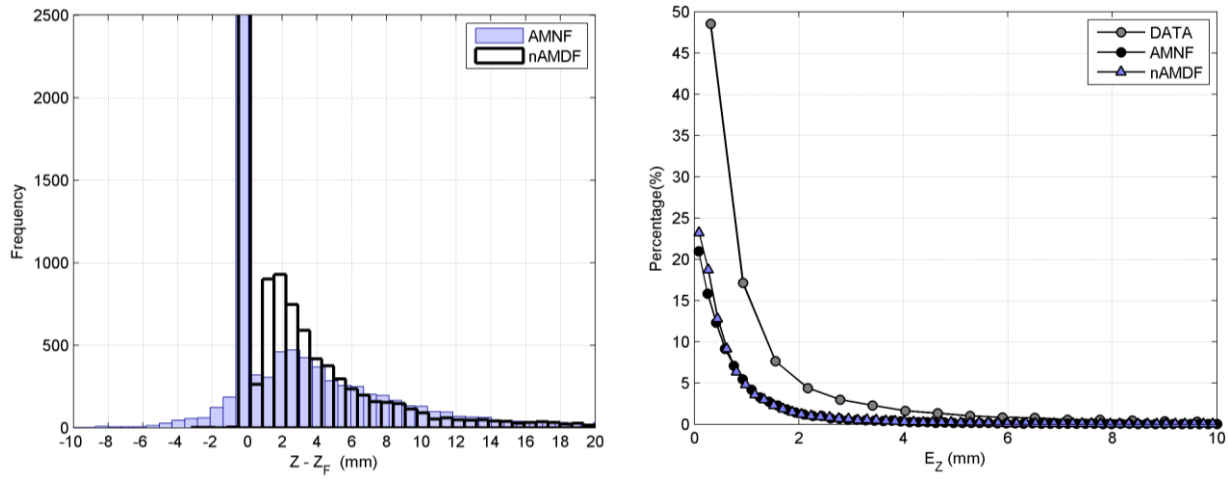
Figure 3-22. Distribution of the difference between the raw and filtered gravel surface elevation data (left) and elevation difference parameter (E_Z)
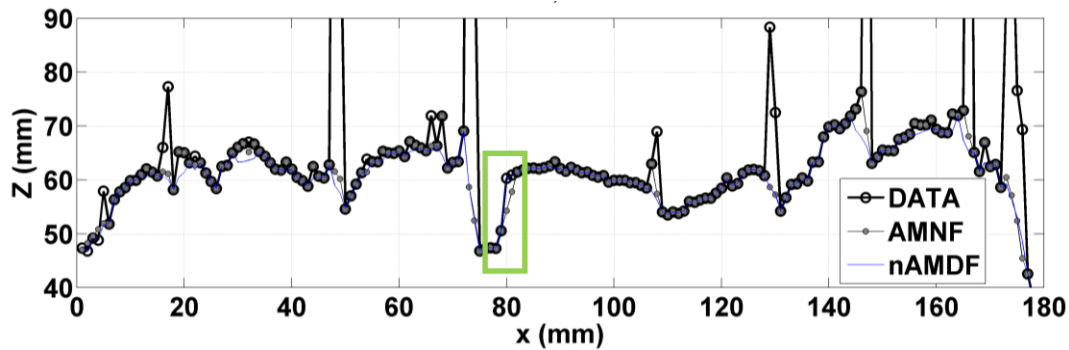
Figure 3-23. Elevation profile taken along y = 94mm for unfiltered and filtered gravel surface elevation data

Figure 3-24 shows nAMDF filtered surface elevation data and the difference with the unfiltered (raw) data for optimal filter parameters: $\varepsilon = 0.5$mm, R= 4 mm and c = 0.5 which are parameters used for sphere data. The erroneous elevations (spikes) are effectively removed by preserving most of error free data elements. The important observation is the optimal filter parameters of the sphere bed are directly applied and are able to effectively remove the errors in gravel surface data. There are no negative residuals (calculated as filtered data subtracted from the raw) evident in the histogram or distribution of surface elevation data after nAMDF is applied. This is due to no significant smoothing by the nAMDF filter

unlike AMNF filter (Figure 3-22). Figure 3-23 (green box) also indicates that the edges are not modified by nAMDF filter and solely the erroneous data elements are removed. The percentage of E_Z larger than 1.0 mm has also reduced from 39.20% to 26.80 % after nAMDF filter is applied.
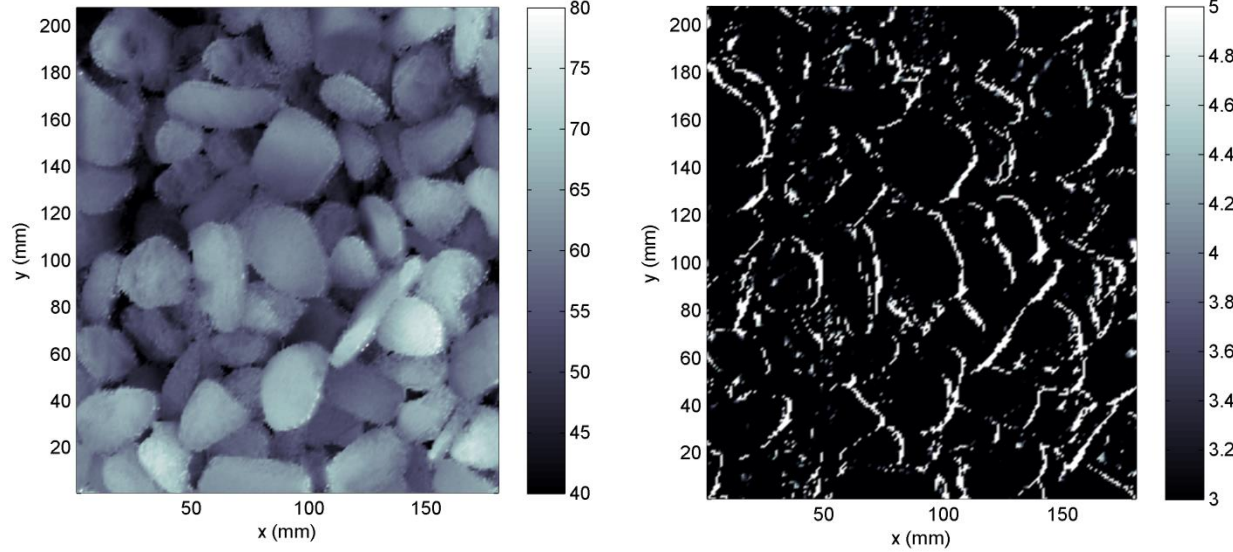
Figure 3-24. Gravel surface elevation data filtered by nAMDF (left) and the difference with the raw data (right)

3.6.2.2. Statistical Analysis of Gravel bed Surface Elevation Data

The main aims of the statistical analysis are to identify the distribution of the bed, estimate vertical roughness scale, and assess its similarity with water worked bed and to compare with literature values. It also enables to assess the effect of the elevation measurement errors on estimated roughness characteristics. Before statistical analysis of the gravel surface elevation data a de-trending procedure is applied. A planar trend is removed from the data using least square fitting procedure that de-trended the data both in span-wise and stream-wise directions. The de-trending allows to remove large scale trends (e.g. bed slopes) which could obscure the data properties and bias grain roughness statistics (e.g. Goring et al., 1999; Bertin and Friedrich, 2013). The probability distribution function (PDF) of gravel surface elevation data allows comparison of gravel texture parameters such as statistical moments and bed properties. The first four moments of bed elevation distribution, mean (μ_z), standard deviation (σ_z), skewness (S), kurtosis (K) are calculated. The standard deviation of bed elevations ($\sigma_{z)}$ is the characteristic vertical roughness scale (Nikora et al., 1998; Aberle and Nikora, 2006) and describes the variability in bed surface elevation. It is a measure of the range between high and low surface elevations with in a specific area (Curran and Waters, 2014). The skewness coefficient (S) quantifies the asymmetry of the PDF relative to the symmetrical normal distribution, $S = 0$, in order to describe the general form of the

bed surface. Figure 3-25 shows the probability distribution function (PDF) of raw (in diamonds) and filtered (in circles) gravel surface elevation data.
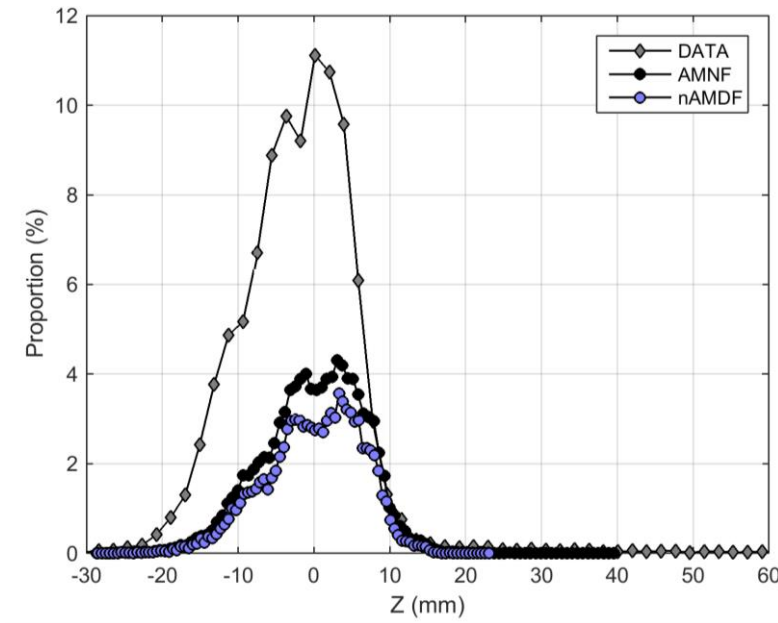
Figure 3-25. Statistical distribution of filtered and unfiltered (raw) gravel surface elevation data

The bed surface elevation distribution of the filtered datasets have a small negative skewness, $S = -0.44$ (nAMDF) and $S = -0.31$ (AMNF) (Table 3-3) and Kolmogrov-Smirnov test fails at the 0.05 significance level for null hypothesis for normality which indicates a non-normal distribution. The distribution of water worked beds are positively skewed (Nikora et al.,1998; Aberle and Nikora, 2006) due to the coarsening of the gravel bed surface with accumulation of coarse grains of higher elevation with respect to mean bed level. The large and positive skewness, $S = 6.04$ in the raw data though is rather due to spikes of erroneous data. The geometric roughness, $k = Z_{max} - Z_{min}$ is also significantly affected by elevation spikes in the raw data. The skewness of the filtered datasets (nAMDF and AMNF) agrees well with literature values (e.g. Mohajeri, 2014) for screed bed. The elevation errors in the raw data over-estimate the vertical roughness scale σ_z by three folds compared to filtered datasets (Table 3-3).

Table 3-3. The statistical characteristics of de-trended raw and filtered gravel surface elevation data

	H_x	H_y	μ_z	σ_z	k	S	K	L_{xo}	L_{yo}	L_{xo}/d_{50}	L_{yo}/d_{50}
Data	0.24	0.35	60.69	18.27	190.11	6.04	46.94	3.11	4.29	0.12	0.17
AMNF	0.47	0.49	57.50	6.58	68.87	-0.31	3.23	13.52	13.00	0.54	0.52
nAMDF	0.53	0.52	57.43	6.39	53.32	-0.44	3.04	12.00	12.00	0.48	0.48

$L_{xo,yo}$ – longitudinal (x) and transversal(y) horizontal roughness length scales

$H_{x,y}$ – longitudinal(x) and transversal (y)horizontal scaling exponents

3.6.2.3. Gravel bed Spatial Structure

The spatial bed surface particle orientation is found to be very important in characterizing bed roughness in open channel flow dominated by gravel beds (Cooper et al., 2008). The degree of surface particle organization or the spatial complexity of bed surface structures is usually assed by the generalized two-dimensional (2-D) second order structure function (Goring et al., 1999). It provides measure of the correlations between bed surface elevations over a range of spatial scales and directions. It has been widely used to identify surface particle orientations (directions) and sources of bed roughness in gravel bed rivers (e.g. Marion et al., 2003; Aberle and Nikora, 2006; Mohajeri, 2014). The 2-D second order structure function, γ, of gravel surface elevation is calculated by using Equation (3-2) as indicated in Aberle and Nikora (2006) with a maximum spatial lag values (l_x and l_y) of 90 mm not larger than one half of the dimensions (180 mm) in either the x or the y direction of the data.

$$\gamma(l_x, l_y) = \frac{1}{(N-n)(M-m)}\sum_{i=1}^{N-n}\sum_{j=1}^{M-m}\{|Z(x_i + n\delta x, y_j + m\delta y) - Z(x_i, y_j)|\}^2 \qquad (3\text{-}2)$$

where $l_x = n\delta x$, $l_y = m\delta y$, δx and δy are the sampling intervals (1.0 mm), N and M are the total numbers of measuring (grid) points of bed surface elevations in x and y direction. Nikora et al. (1998) showed that at very large lags l_x and l_y the data are spatially uncorrelated and γ tends to be equal to $2\sigma_z^2$ of the data and the corresponding lags l_x and l_y at which $\gamma \approx 2\sigma_z^2$ can be used to derive characteristic stream-wise and span-wise length scales. The normalized 2-D second order structure function is obtained when γ is divided by $2\sigma_z^2$.

The contour line plots in Figure 3-26 to Figure 3-28 show the 2-D second order structure function of raw and filtered gravel surface elevation datasets computed by Equation (3-2). There is no any clear spatial pattern in Figure 3-26 and this due to the erroneous data that obscure the actual grain scale surface elevation variations and pattern. The contour lines in Figure 3-27 and to Figure 3-28 are characterized by an elliptical shape in lag ranges of 0.5d_{50} to d_{50}. Geometrically, the elliptical shape of the contour lines

reflects the elliptical form of the dominant bed particles and the anisotropic surface structure of the bed. The gravel particles are somehow rotated during manual screeding to align their longest axis along the direction of screeding, which is downstream in flow direction. The contour pattern in Figure 3-27 and Figure 3-28 also shows that the major axes of the elliptical contours are aligned in the x-direction with an increasing l_x. This indicates that majority of the particles tend to rest on the bed with their longer axis along the x direction though the magnitude of inclination towards stream-wise direction may not be as large as water-worked beds. The ratio of the length of major to minor radii of the ellipse for AMNF and nAMDF are 1.58 and 1.40 and are similar with literature values of gravel bed created by screeding (e.g. Mohajeri, 2014).
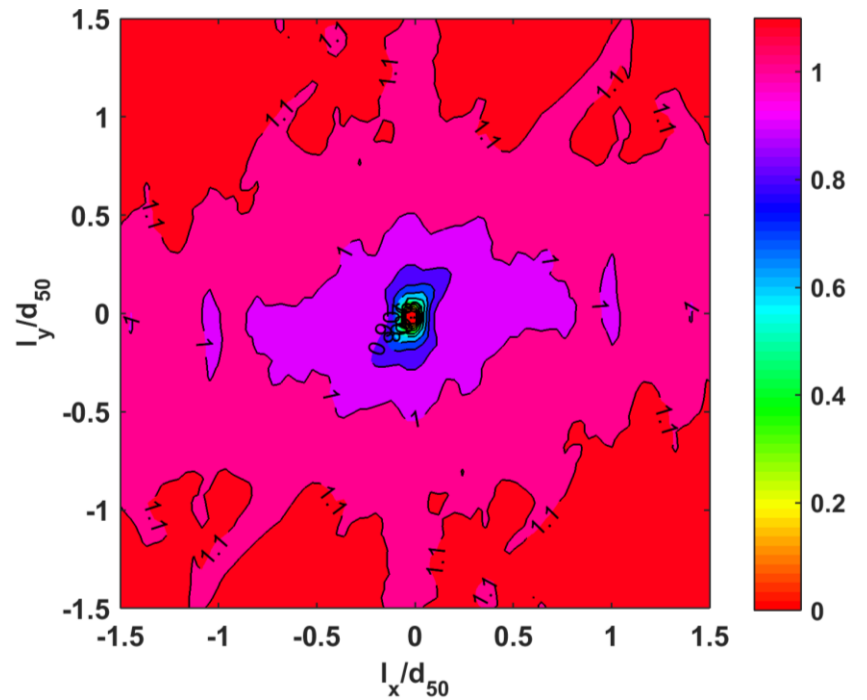
Figure 3-26. The contour plot of normalized second order structure function of gravel surface elevation data (raw)
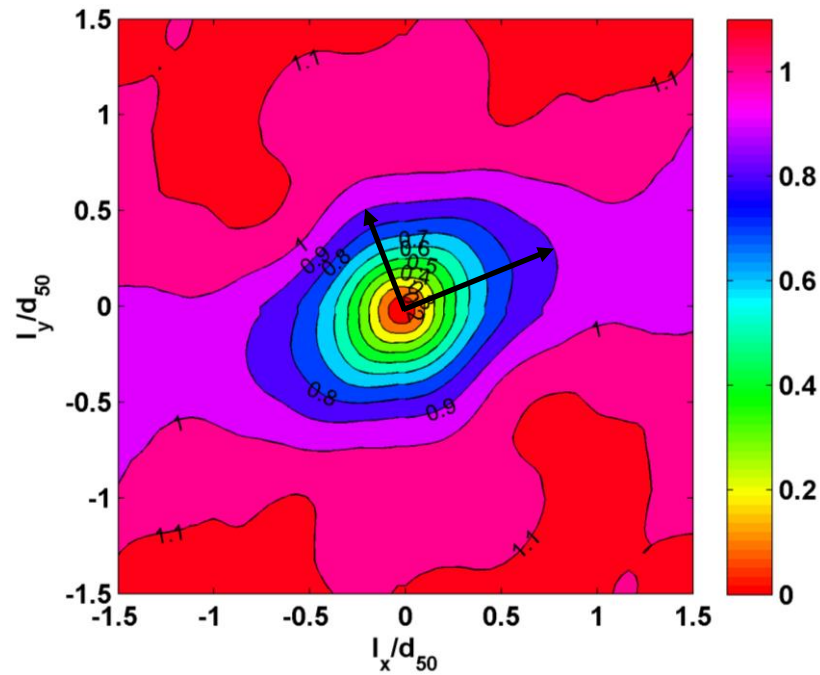
Figure 3-27. The contour plot of normalized second order structure function of gravel surface elevation data (AMNF filtered)
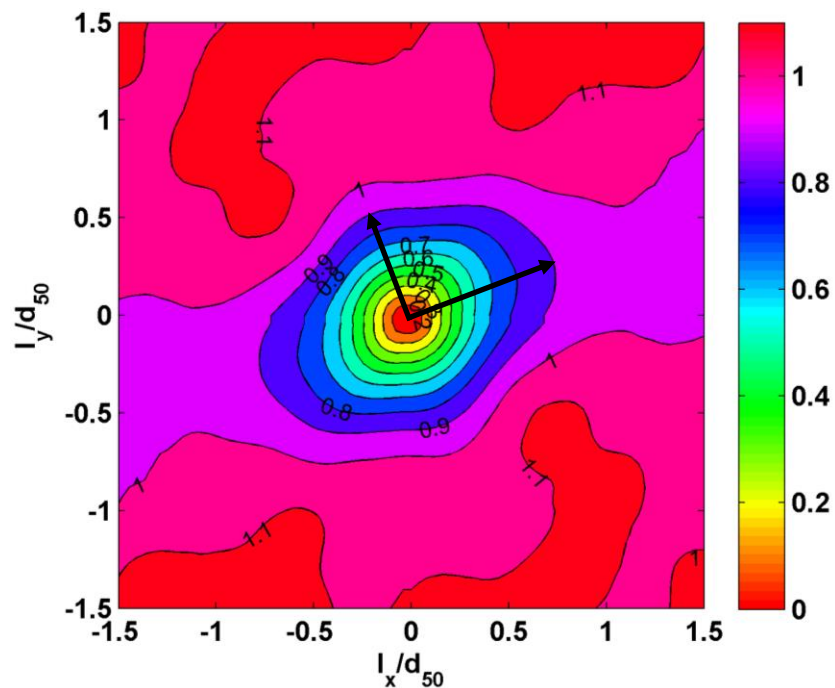
Figure 3-28. The contour plot of normalized second order structure function of gravel surface elevation data (nAMDF filtered)
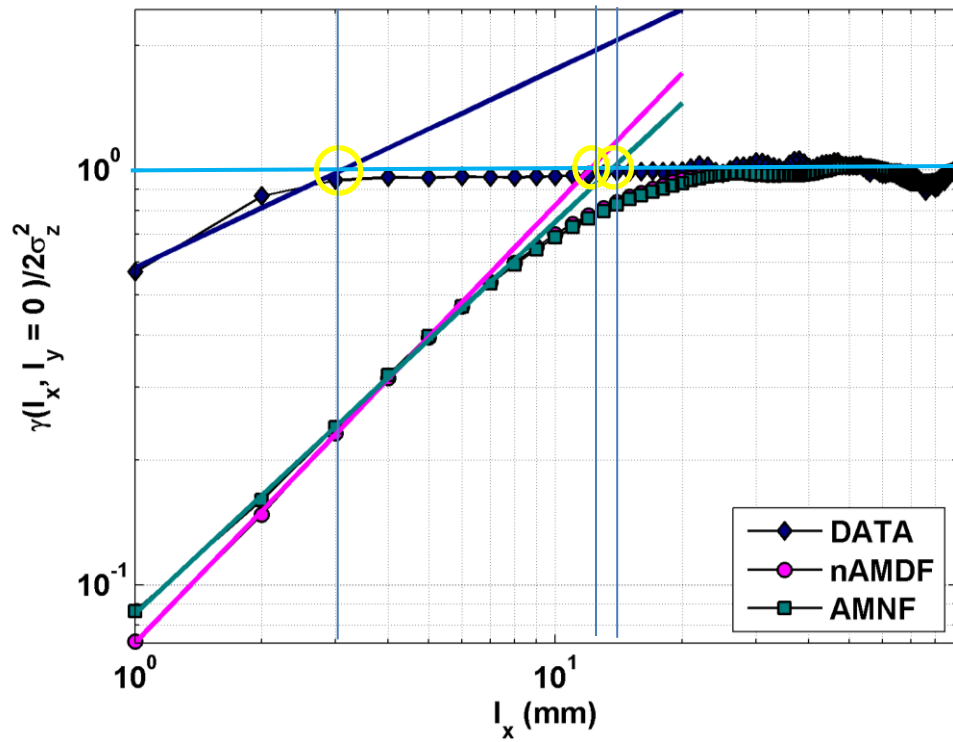
Figure 3-29. The stream-wise second order structure function of gravel surface elevation data
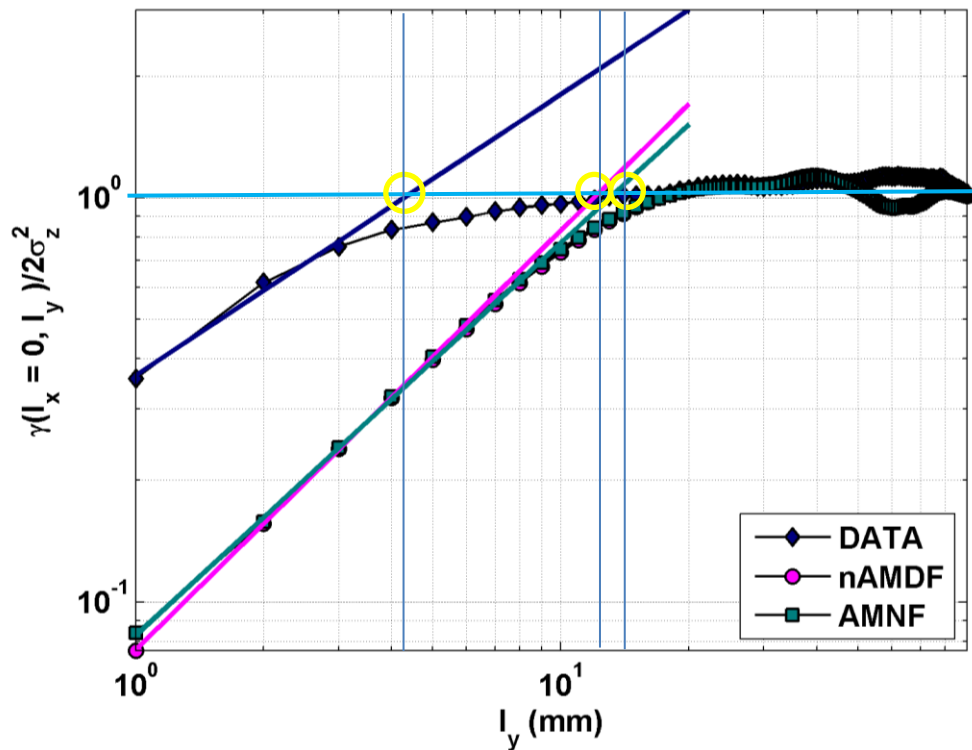
Figure 3-30. The span-wise second order structure function of gravel surface elevation data

According to Nikora et al. (1998) γ (l_x, l_y) is a popular tool for investigating the scaling properties of various types of rough surfaces such as gravel surface elevation data. The longitudinal γ $(l_x, l_y = 0)$ and transverse γ $(l_x = 0, l_y)$ structure functions are found to have three distinct regions depending on the spatial lags, namely, scaling region, transition region and saturation region (Nikora et al., 1998). At small lags there is a scaling region where the structure functions can be approximated by the power function γ $(l_x, l_y = 0)/2\sigma_z^2 \sim l_x^{2Hx}$ and γ $(l_x = 0, l_y)/2\sigma_z^2 \sim l_x^{2Hy}$. The scaling exponents H_x and H_y (Hurst exponents) and the characteristic spatial scales (also called horizontal roughness scales) L_{xo} and L_{yo} that separate the scaling and saturation regions are estimated from the power relations (Nikora et al., 1998). The horizontal roughness scales are calculated as the lag distance at which the extrapolation of the linear relation in the scaling region and a line of $\gamma = 2\sigma_z^2$ intersect (yellow circles in Figure 3-29 and Figure 3-30) as proposed by Nikora et al. (1998). The results are reported in Table 3-3 and Figure 3-29 and 32. The stream-wise (longitudinal) horizontal roughness scales estimated from filtered data, Table 3-3, are similar to corresponding span-wise (transverse) roughness scale. Such behaviour is reported by Nikora et al. (1998) for manually created beds in laboratory flumes while larger longitudinal scales in water-worked beds. However, the estimated horizontal roughness length scales of the raw data are small and are not similar to literature values. This is due to the erroneous data that obscure the actual grain scale surface elevation variations and spatial pattern. The vertical roughness length scale of natural water worked gravel-bed is less than half of the horizontal roughness scales (Nikora et al., 1998). The estimated horizontal roughness scales from the filtered data are within the upper limit of scaling region which is defined by $0.5d_{50}$ (Nikora et al., 1998; Aberle and Nikora, 2006) (Table 3-3). The scaling exponents of filtered datasets in (Table 3-3) are also within the range reported in Nikora et al. (1998) in field and flume studies. Nikora et al. (1998) reported that scaling exponent (H) is found to be universal where H = 0.79±0.04 for streams and H = 0.5± 0.07 for flumes. The similarity between H_x and H_y of the filtered data shows the bed is isotropic which agrees with Nikora et al. (1998) observation for both natural water worked and manually created gravel beds. The similarity between horizontal roughness scales (L_{x0} and L_{y0}) of filtered data (nAMDF) however shows isotropic ($L_{x0} = L_{y0}$) property of the random field of elevations, Z(x, y). But the AMNF filtered data shows a little difference between the L_{x0} and L_{y0} which shows anisotropic property could exist as shown in the 2-D contour plot (Figure 3-27). Nikora et al. (1998) reported that manually created gravel beds in laboratory scale showed isotropic ($L_{x0} = L_{y0}$) bed property unlike natural gravel beds ($L_{x0} \neq L_{y0}$). It is very useful to note that the estimation of horizontal roughness scales are prone (sensitive) to elevation errors looking at the estimates from AMNF and nAMDF filtered data. The ratio of vertical roughness length scales σ_z = 6.40 mm (nAMDF) and σ_z = 6.58 mm (AMNF) to horizontal length scales are in the range of 0.48 to 0.53 (Table 3-3) which are within the reach of the average value

of 0.44 reported for natural streams (e.g. Nikora et al.,1998). The estimates for the raw data are 4.3 and 5.87 which are way above literature values and show the significant effect of the elevation errors.

3.6.2.4. Gravel bed Porosity Characterization

The gravel bed porosity is estimated by applying two approaches: water displacement method and statistical analysis of gravel surface elevation data. The porosity of the gravel is calculated using a square tank filled with gravel materials, by measuring   depth of water displacement by gravel particles, as indicated in the Figure 3-31. The direct measurement of porosity in this way allows identifying the bottom of the interfacial sublayer. The measurement setup has three main components: the measuring cylinder, the square tank containing the gravel and the water level measurement meter (a calliper). The measuring cylinder, is attached to the side of the tank, has a cross-sectional area of 14.03cm^2 with a diameter of 4.23 cm. The square tank has a cross-sectional area of 784 cm^2 (L = 28 cm, W = 28 cm and H = 50 cm). Each incremental water level in the cylinder, which also means the water level in the tank for each added volume of water, is measured by the calliper manually. In order to estimate porosity two main measurements are conducted: the water level in the cylinder and the volume and mass of water that is added to the cylinder at every step.
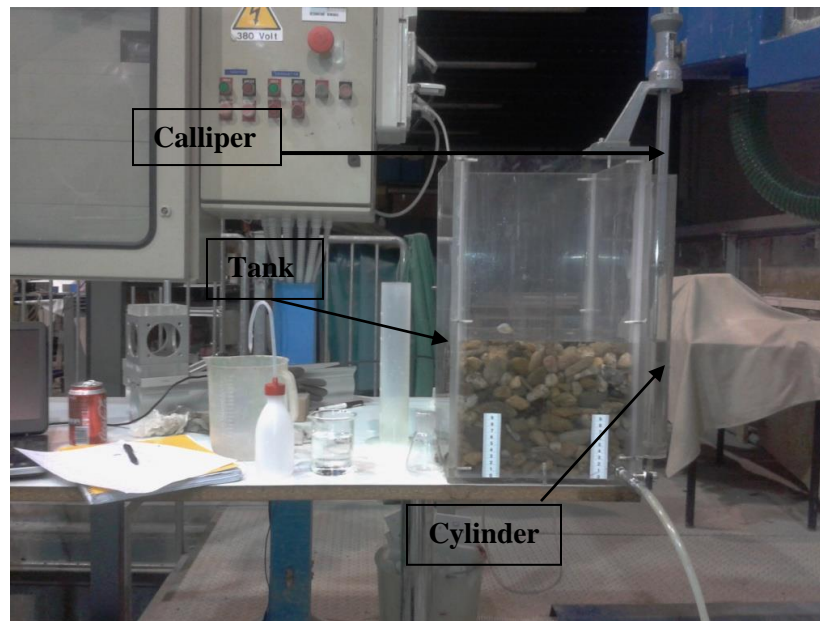
Figure 3-31. Porosity device for in-situ measurement of porosity profile of gravel material used in laboratory flume

In the procedure first a known mass of water is added to a cylinder. The volume of the added water (V_0) is estimated using the density of the water. The density of water is estimated based on known mass and

volume of water estimated before measurement of porosity since it depends on temperature of the water: 999.73 kg/m^3. To estimate the density of water the mass of 50 ml (measured by a pipette shown in Figure 3-32) of water is determined by weighing it on the digital balance (Figure 3-32). The density is obtained by dividing the measured mass with the known volume of water. The mass of water is measured by digital balance whose accuracy is 0.001 g for measurements less than 10 g and 0.01 g for measurements up to 400 g.
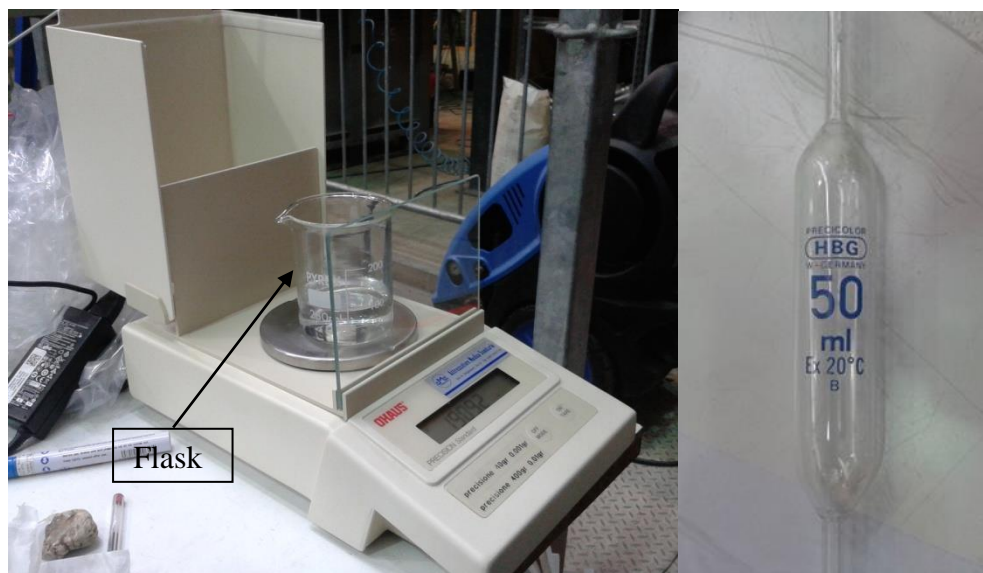
Figure 3-32. Digital balance (left) and pipette (right) for measurement of weight and volume of water respectively

For each added mass of water the change in the water level in the cylinder is recorded. To estimate the porosity at each level in the gravel the volume of water occupying the void has to be known. Thus, the volume of water that enters the tank is obtained by subtracting the volume of water in the cylinder from the volume of water added to the cylinder each step. Since the cross-sectional area (A) of the tank varies with different water level in the tank, for each water level the cross-sectional area (A (Z) where Z is the water level) was calculated. First, water was filled progressively in the tank to estimate the tank cross-sectional area at various water levels, before the gravel particles were filled in the tank for porosity measurement. The area was calculated by dividing a known amount of changes in the volume of water (ΔV_w) in the tank for any change in the water level (ΔZ) recorded in the cylinder. Figure 3-33 shows the area of the tank at varies along various sections of the tank around the mean (= 786.50cm^2). Here the zero level is level at which maximum porosity is observed and corresponds to level of gravel crest in the tank.

The level at which the areas are measured do not correspond exactly to the water level measurement for porosity calculation, therefore the mean of pairs of area were used. Finally the porosity (Φ) is calculated as the change in volume of water in the tank divided by the product of change in the water level in the cylinder and the cross-sectional area of the tank at that water level: $\phi(Z) = \Delta V_w / A(Z)\Delta Z$ where $A(Z) = \Delta V_w / \Delta Z$ and $Z =$ water level in the tank. The calculated porosity (Figure 3-34) shows increasing trend in the porosity at the top layer of the gravel which is in the last 17.0 mm of the upper gravel layer while it oscillates between 0.30 and 0.40 at lower gravel layer.
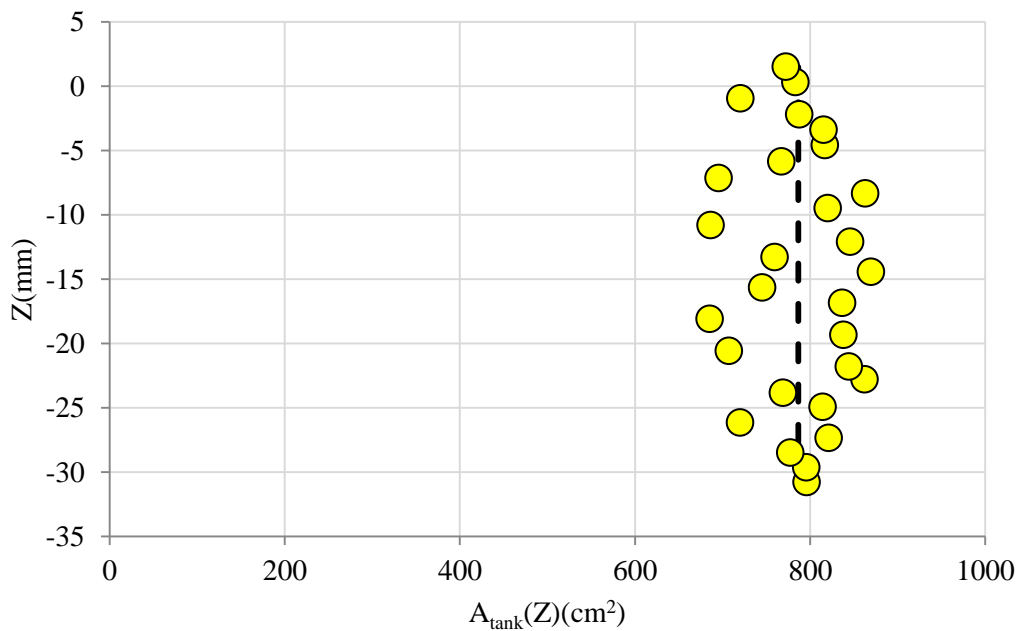
Figure 3-33. Variations in the area of the tank with water level in the measurement region of the tank height.
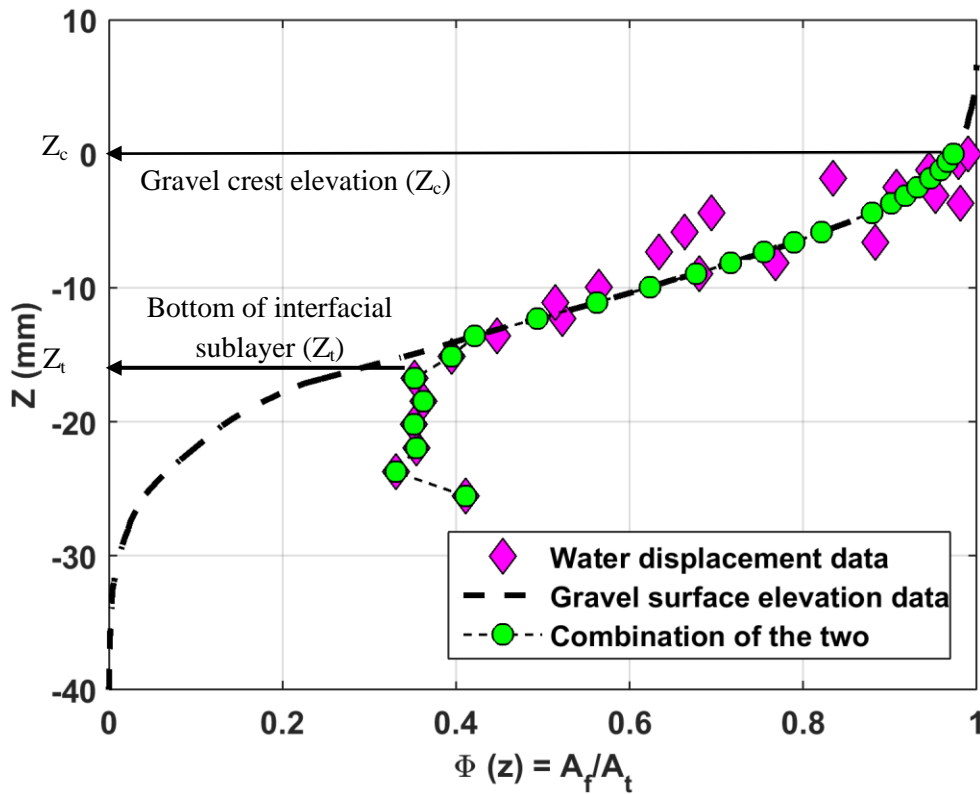
Figure 3-34. Porosity profile estimated from gravel surface elevation data and by water displacement method that show the gravel bed material porosity at various depths below gravel crest

The porosity of gravel can also be estimated based on statistical analysis of gravel surface elevation data (e.g. Aberle, 2007, Nikora et al., 1998). The cumulative probability distribution function (CPDF) of gravel surface elevation data is widely used to estimate gravel bed porosity (Figure 3-34 , broken line). Nevertheless it predicts bed porosity mainly in the upper 70 % of gravel layer (e.g. Aberle, 2007) since gravel surface elevation data cannot capture surface elevations below certain depths from the crest of gravel. Figure 3-34 shows that porosity profile estimated by water displacement method (yellow circles) agrees well with the estimate from gravel surface elevation data in the upper 60%. The estimate by water displacement method captures the bed porosity in the upper and subsurface layer of the gravel bed (Figure 3-34) which allows identifying the bottom of the interfacial sublayer which is not possible with CPDF.
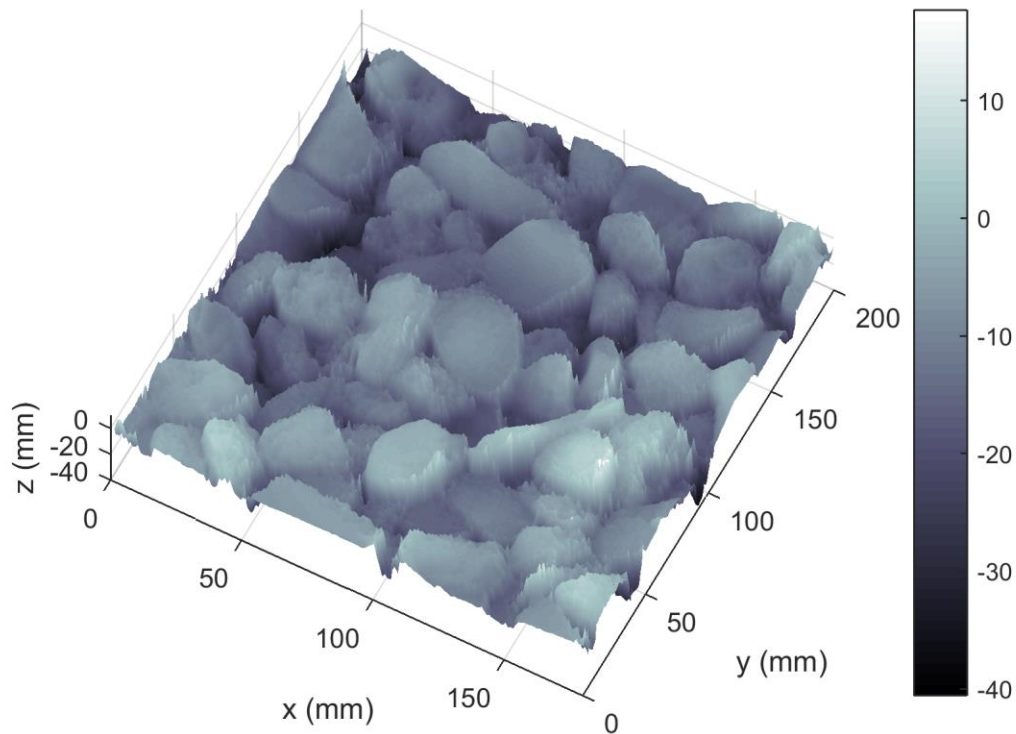
Figure 3-35. The 3-D view of nAMDF filtered surface elevation of data used for estimating geometric roughness function (porosity): the elevation values are with reference to crest elevation $Z_c = 0$

The crest level of the gravel bed Z_c = 69.23 mm is often computed as the elevation at 99 % of CPDF of gravel surface elevation data (Figure 3-35). The gravel crest elevation can bed set to zero by subtraction Z_c from the surface elevation data (Figure 3-34). The region of increasing porosity in Figure 3-34 is the thickness of the interfacial sublayer and its bottom is the top of the subsurface layer (e.g. Nikora et al., 2001). The bottom of the roughness layer Z_t is obtained from porosity profile by water displacement method where the bed level below which porosity remains constant or the interface between interfacial and subsurface layer. The porosity in the subsurface regions does not go less than 0.2 - 0.3 (Nikora et al., 2001). The bottom elevation of the interfacial sublayer in gravel surface elevation data is $Z_t = -17$ mm and the porosity is 0.35.

3.6.2.5. Gravel bed Roughness Density Characterization
The total drag force exerted by flow on rough permeable bed is an important phenomenon in gravel bed or rough bed hydrodynamics since it affects the transfer of momentum between the free-surface flow and turbulent flow within the underlying permeable layer (Pokrajac and Manes, 2008). Flows in vegetated

channels and gravel beds are also affected by the drag force or flow resistance imposed by gravel particles or submerged vegetation (e.g. Poggi et al., 2004). The total drag force such bed conditions is generally described by the conventional quadratic drag parameterization (e.g. Poggi et al., 2004; Nikora et al.,2004) which involves roughness density, here after described as 'a', flow velocity and drag coefficient. The estimation of roughness density of gravel beds is very relevant in estimation of drag coefficient in gravel bed flows and to characterize total drag force in the interfacial sublayer or within the permeable layer. In two dimensional flows in rough permeable bed the roughness density is described as the frontal area of roughness elements per fluid volume and is given as the total frontal area of all the roughness elements intersected by the thin section within the averaging window divided by the fluid volume in the thin section (e.g. Nikora et al., 2004). Mathematically it can be simplified as shown in Equation (3-3).

A new procedure is developed to estimate roughness density from gravel surface elevation data (shown in Figure 3-36). First images are extracted every 1mm for a depth up to 25 mm below the gravel crest. The localized frontal area or solid interface of each gravel particle at particular depth is estimated as blob width. The width of each gravel particle at particular z is estimated by taking the blob widths (blue box in Figure 3-36) in longitudinal (x) and transverse (y) directions. The total width, W (z), of frontal solid segment of the thin section of gravels is estimated as the sum of the widths of all blobs for each image below the gravel crest. The local roughness density (a (z)) is finally estimated as

$$a\,(z) = \frac{W(z)}{A_o \Phi(z)}$$
(3-3)

where A_o = the total surface area of each image and $\Phi(z)$ = gravel bed porosity.

The roughness density of various bed configurations of selected theoretical roughness bed elements (Figure 3-37) which are often used in laboratory experiment of fine sediment transport (e.g. Grams and Wilcock, 2013) and rough bed hydrodynamics (Pokrajac and Manes, 2009; Seddighi et al., 2015) are also estimated to compare with gravel roughness density and to develop a theoretical relation.
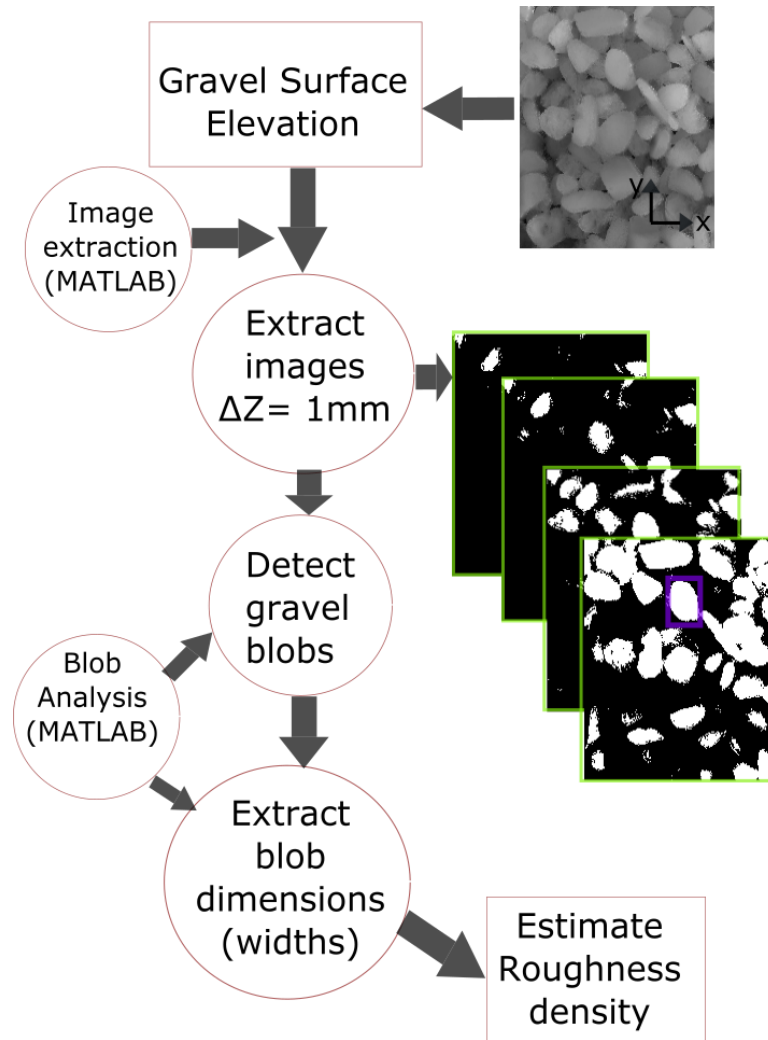
Figure 3-36. Procedures followed to estimate roughness density from gravel surface elevation data

Figure 3-38 shows the computed porosity profile for each bed where that of the gravel is estimated as indicated in Section 3.6.2.4. Generally the level of compactness in bed arrangement describes the porosity where only packed hemispheres (*tetrahedral packing*) show good resemblance to gravel beds unlike pyramids and loosely packed hemispheres (*cubical packing*) which show some similarity among themselves. The porosity for all theoretical beds seems to be described as a function of the horizontal and vertical length scales of the roughness elements (R, b and h) except for gravel bed which is given as CPDF of log-normal distribution. The vertical (l_z) and horizontal (l_x) length scales for each bed is summarized in Table 3-4.
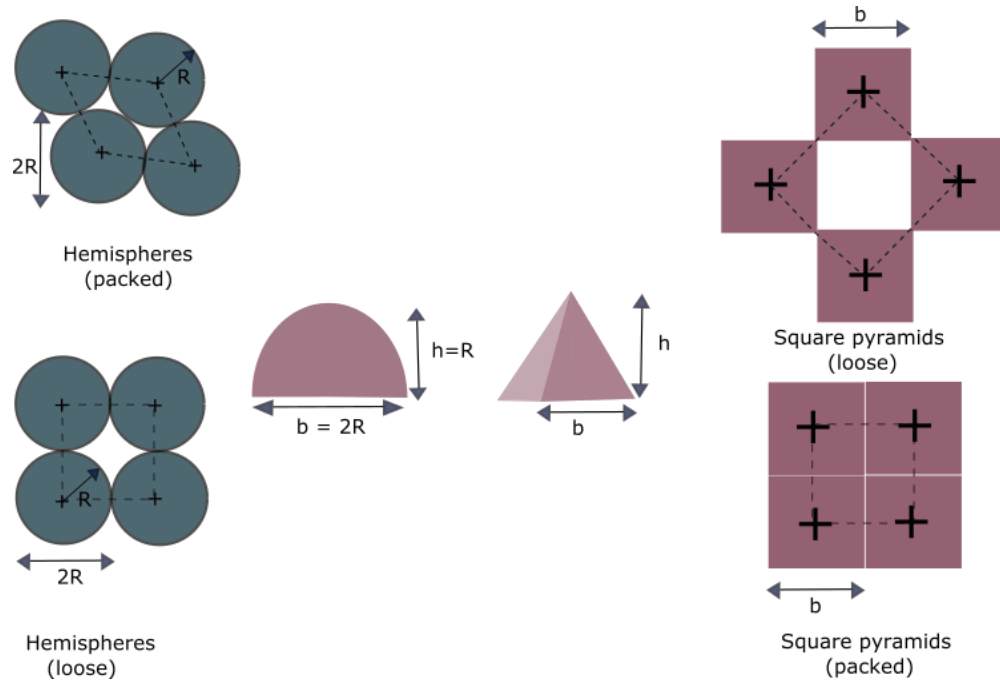
Figure 3-37. The spatial arrangement of the selected theoretical bed roughness elements
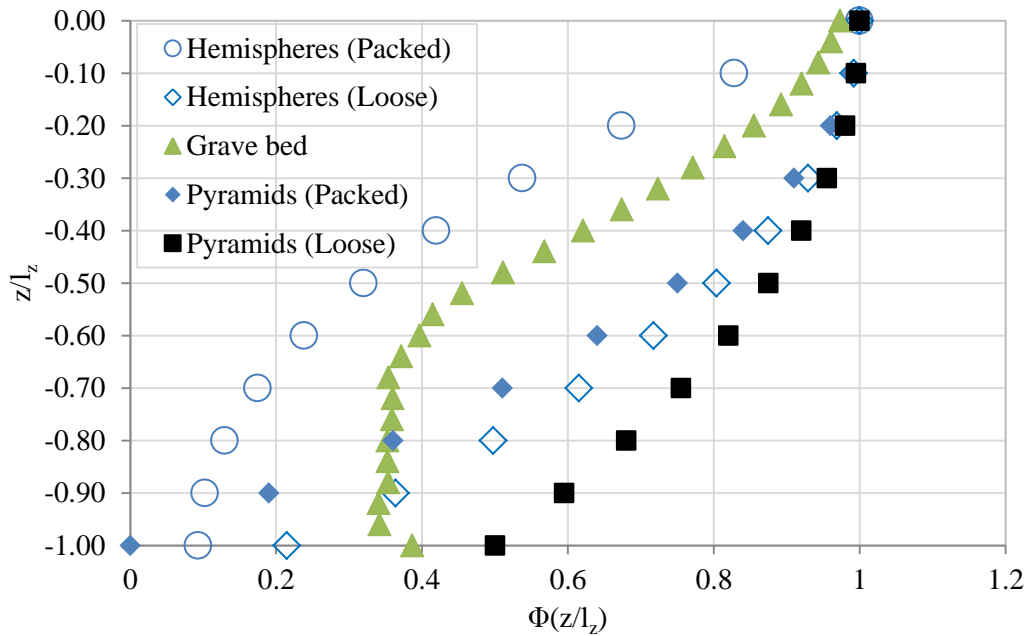
Figure 3-38. Bed porosity Φ (z) for the different arrangements of selected theoretical bed roughness elements and gravel bed

The roughness density of gravel bed is computed following procedure indicated in Figure 3-36 and shown in Figure 3-39 (square and diamond plots). The estimates of the roughness density 10 mm below the gravel crest becomes a zero and this due to the incapability of the blob extraction method to resolve blobs below this depth. So only roughness density estimate up to z = -10 mm (~0.5d_g) is taken to compare with the theoretical bed estimates. In Figure 3-39 a_x (z) and a_y (z) are the estimated roughness density based on total width of blobs in x (circles) and y directions (diamonds) respectively and they are equal which shows that the frontal areas per unit volume of fluid in longitudinal and transverse directions are similar (in screed gravel bed) in gravel bed flow. Figure 3-40 shows the roughness density for theoretical beds (hemisphere and pyramid geometries). Here gravel bed, loose hemisphere bed and packed pyramid bed show some similarity in the upper portion of the roughness layer while high and low roughness density are observed in packed hemisphere and loose pyramid bed arrangements respectively. In all cases the roughness density increases from top to bottom of the roughness layer or interfacial sublayer.
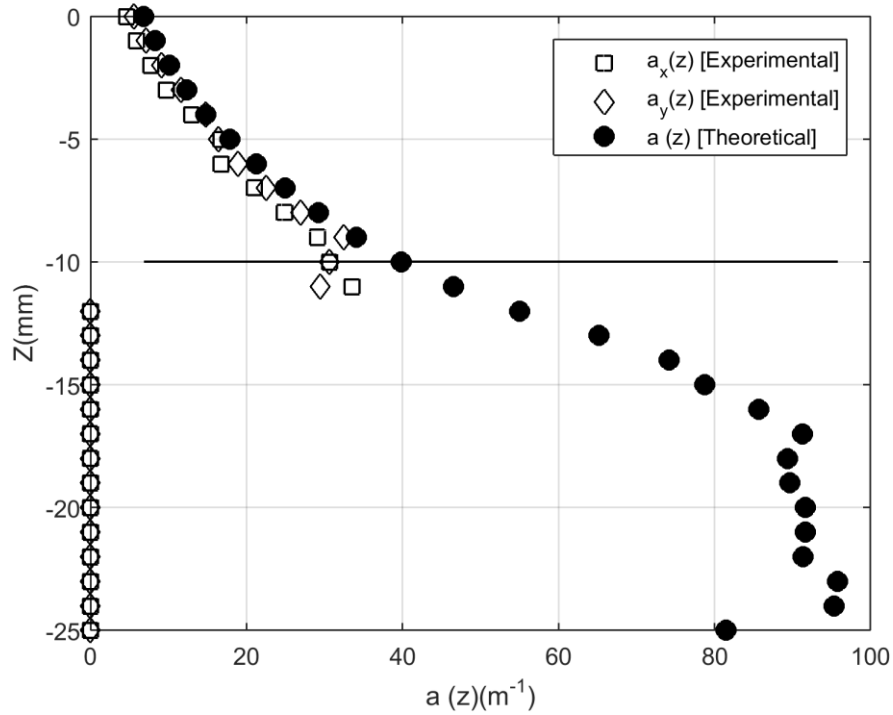
Figure 3-39. Localized roughness density a (z) of gravel bed computed theoretically (shaded circles) and extracted from gravel surface elevation data (unshaded squares& diamonds)
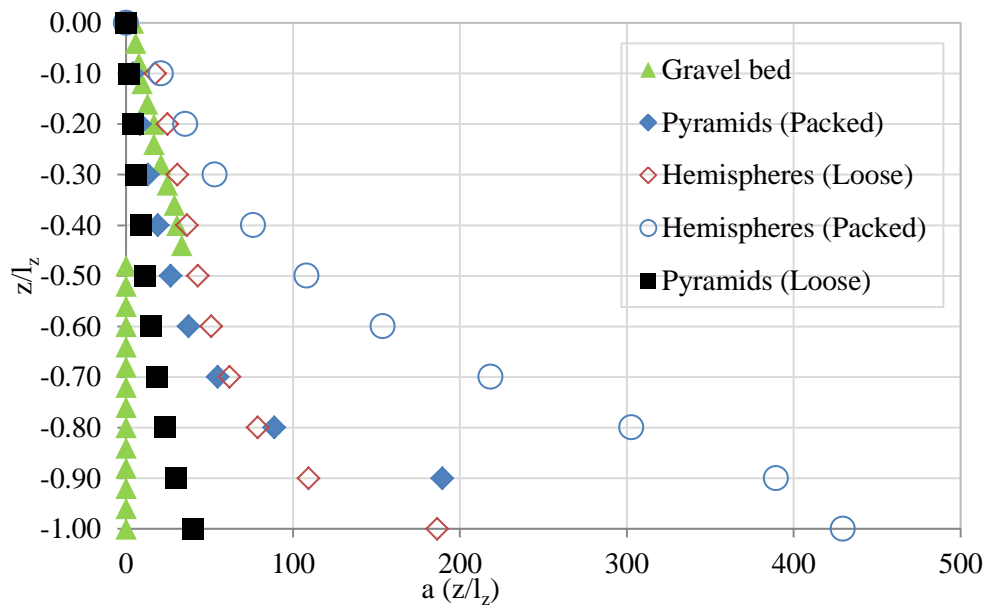
Figure 3-40. Localized roughness density a (z) for the different arrangements of selected theoretical bed roughness elements and gravel bed
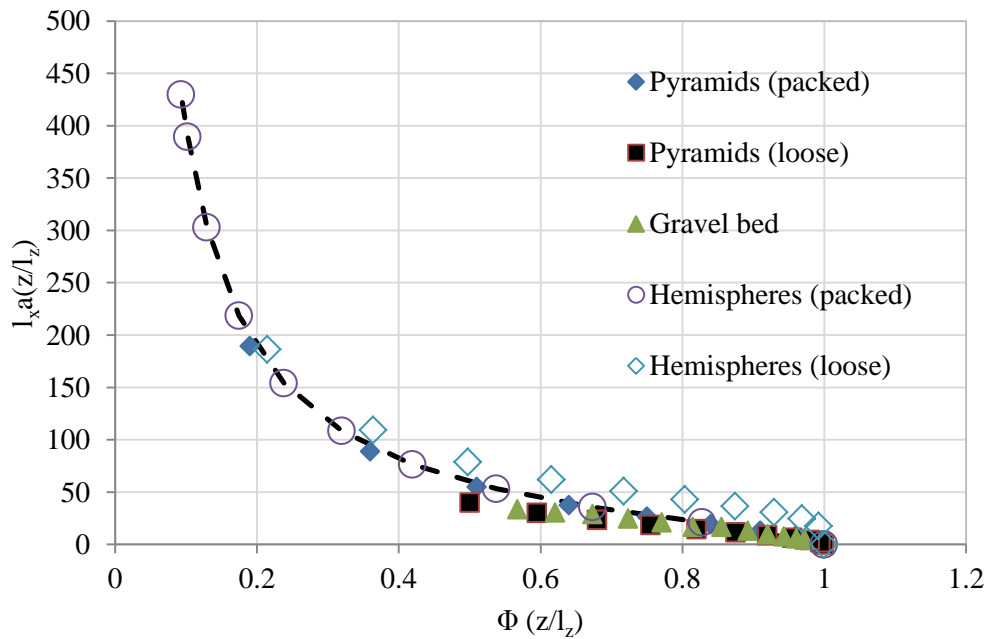
Figure 3-41. Dimensionless localized roughness density $l_x a$ (z) for the different arrangements of selected theoretical bed roughness elements and gravel bed

A collapse of dimensionless roughness density against bed porosity is also observed for all bed arrangements including gravel bed (shown in broken line in Figure 3-41). Thus a theoretical relation (in Table 3-4) as a function of geometrical properties of the roughness elements, i.e. bed porosity and horizontal roughness length scales (summarized in Table 3-4) can describe roughness density a (z). When the theoretical relation of roughness density of gravel is applied to gravel porosity data the estimated roughness density agreed well with the experimental estimates of roughness density (Figure 3-39). When the theoretical relation is applied to porosity data of other experiments (e.g. Dey and Das, 2012; Mignot et al., 2009) and made dimensionless by the respective horizontal roughness length scales (d_{50} = 40 mm and d_{50} = 20 mm respectively) the plots collapse (Figure 3-42). The most important observation is that the roughness density of any rough bed can be described as function of geometrical properties of the roughness elements and the theoretical relation proposed here is validated based on roughness density measured from gravel surface elevation data.

Table 3-4. The geometric characterization of the roughness density (a) and porosity (Φ) of gravel bed (Figure 3-35) and selected theoretical beds (Figure 3-37). The function Φ (z) for gravel bed has been represented by a CPDF of a log-normal distribution (shown in Section 3.6.2.4) of rough bed elevations with μ_z and σ_z the mean and the standard deviation of the log-transformed bed elevation Z.

	Hemispheres (packed)	Hemispheres (loose)	Pyramids (packed)	Pyramids (loose)	Gravel bed
l_x	2R	2R	b	b	d_{50}
l_z	R	R	h	h	$1.5d_{50}$[1]
$\Phi(z)$	$1 - \frac{\pi}{2\sqrt{3}}\left(1 - \left[\frac{z}{R}\right]^2\right)$	$1 - \frac{\pi}{4}\left(1 - \left[\frac{z}{R}\right]^2\right)$	$1 - \left[1 - \frac{z}{R}\right]^2$	$1 - \frac{1}{2}\left[1 - \frac{z}{R}\right]^2$	$\frac{1}{2}erfc\left[-\left(\frac{\ln(z) - \mu_b}{\sqrt{2\sigma_b{}^2}}\right)\right]$
a(z)	$\frac{(1 - \Phi(z))^{0.5}}{\Phi(z)R}$	$\frac{(1 - \Phi(z))^{0.5}}{\Phi(z)R}$	$\frac{(1 - \Phi(z))^{0.5}}{\Phi(z)b}$	$\frac{(1 - \Phi(z))^{0.5}}{\Phi(z)b}$	$\frac{(1 - \Phi(z))^{0.5}}{\Phi(z)d_{50}}$

[1]Nikora et al. (2001)
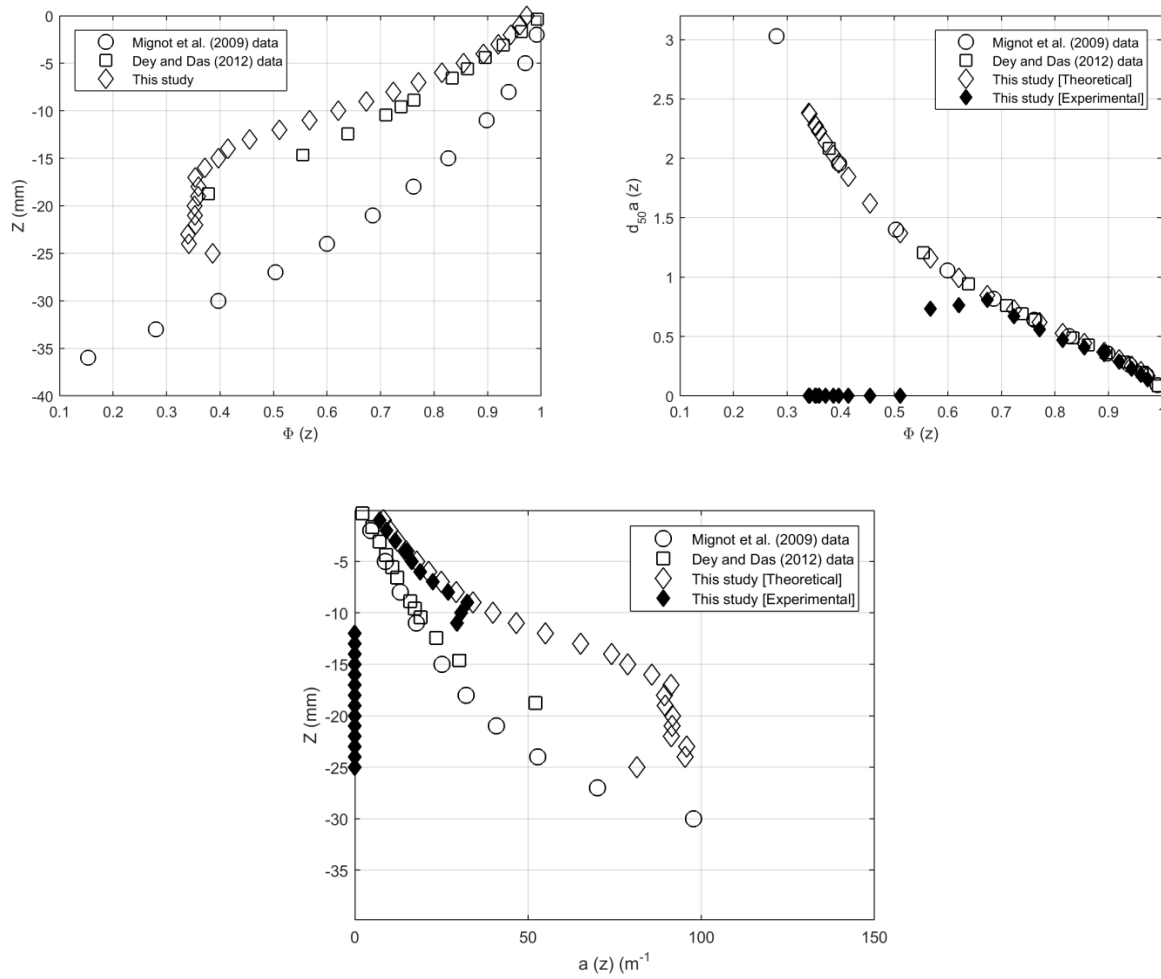
Figure 3-42. The porosity of different gravel beds (top left), the relationship between theoretically computed dimensionless roughness density and bed porosity (top right) and theoretically computed roughness density with the porosity of gravel beds (bottom)

3.7.   CONCLUSIONS

Surface elevation data of gravel bed acquired by PSD laser sensor contains elevation errors that are caused by target shapes and orientations. The elevation errors can also be caused by surface colour which is noticed in surface elevation data of painted sphere beds. This study characterized the elevation errors of PSD laser scanner based on sphere beds and developed methods to reduce the errors and applied the results to gravel surface elevation data. Two filter methods (AMNF and nAMDF) are developed to remove the elevation errors and were well tested and verified based on reference data. The nAMDF filter method is very effective in reducing elevation errors and the narrow range of filter parameters allows

selecting optimal values rather simple. It offers better alternative than local high point filter proposed by Hodge et al. (2009) which is the AMNF filter in the present study. The local high filter (Hodge et al., 2009) and AMNF need trial and error procedures to obtain optimal filter parameters which is sometimes problematic. Although nAMDF optimal parameters of sphere bed were able to effectively remove errors in gravel surface elevation data their use for similar datasets cannot be generalized.

The elevation errors in gravel surface elevation data showed significant effects on estimated gravel roughness scales (horizontal and vertical length scales) and 2-D second order structure function which characterizes spatial structure of the bed (gravel particle orientations). The errors obscure the isotropic characteristics of the scaling regions and anisotropy of the random field of surface elevations. The vertical length scale and geometric roughness of the bed were highly overestimated. The bred roughness parameters estimated from the filtered data agreed with literature values of screed gravel bed.   The bed porosity obtained from CPDF of filtered data also agreed well with the estimate based on water displacement especially in the upper 60% of gravel bed layer. Nevertheless, perfect agreement was not noted since particle orientation, spatial organization and level of compactness of gravel particles in the porosity tank could be slightly different from the laboratory flume. The porosity data obtained from water displacement method, though, was very useful to identify the bottom of interfacial sublayer.

The roughness density of various bed roughness elements showed dependence on horizontal length scales and bed porosity. This allowed developing a theoretical relation to predict roughness density as the function of geometrical properties of the bed, i.e. bed particle grain size and porosity. The development of the theoretical relation of vertical profile of roughness density is very useful to characterize drag force and drag coefficient in interfacial sub-layer of rough bed flows. It is often difficult to measure drag force directly especially in the interfacial sublayer. However, the measurement of flow velocity can be conducted with better accuracy, for example using PIV, thus the knowledge of roughness density will allow characterizing drag force. Finally, proper quality check and post-processing of gravel surface elevation data acquired by PSD laser scanner is very essential before extracting geometrical properties, roughness scales and roughness density of the bed.

4. FINE SEDIMENT EROSION RATE AND DYNAMICS IN IMMOBILE GRAVEL BED: METHODOLOGY

Summary

A new approach for measurement of fine sediment erosion rate in coarse immobile bed in laboratory experiment is presented. The method uses single laser line, video camera and a reflective mirror. It allows a non-intrusive, fast and accurate measurement of erosion rate in non-equilibrium transport under flowing water condition. The measurement method was conducted for flow depth that ranges from 3.0 cm to 8.0 cm. The procedures to extract laser lines from series of images and estimate rapid evolution of the erosion are presented and results show the effectiveness of the proposed methodology. The use of a mirror allowed measurement of depth of erosion with sub-millimetre (350µm) resolution. This study reports the first work of application of laser line technique to estimate erosion rate of fine sediments in interfacial sublayer of gravel bed dominated by suspended transport. This technique is very useful to acquire experimental datasets that could be used to describe the vertical profile of non-equilibrium erosion rate of fine sediments, its spatial heterogeneity and formulation of erosion rate relations in immobile gravel bed.

4.1. INTRODUCTION

The interaction between loose bed and flow field is an important process that controls the formation of bed forms and morphological evolutions. In this regards, the exchanges of sediment particles, especially suspended sediments, with the loose bed due to gravitational action and turbulent flow derive evolution of bed configurations. Laboratory experiments have been used successfully to reproduce and visualize sediment-flow interactions and bed morphology (e.g. Lajeunesse et al., 2010). A laboratory experiment allows conducting measurements of the interactions between the water stream and the movable boundary under controlled conditions. It also eliminates the variations in external forcing thus allowing one to characterize real environments and model processes that evolve over much longer time scales than possible in the field (Limare et al., 2011; Visconti et al., 2010).

There are currently several well tested techniques of laboratory measurements of flow characteristics as well as evolving bed morphology. For instance particle image velocimetry (PIV), acoustic Doppler velocimetry (ADV), ultrasonic doppler velocity profiler (UVP) are widely used in measurement of flow field. There are also methods to measure bed profiles in movable bed such as miniature echo sounder (e.g. Kantoush et al., 2006), joint use of triangulation laser sensor and an ultrasonic level transmitter (e.g.

Visconti et al., 2012), laser sheet technology (e.g. Huang et al., 2010; Soares-Frazão et al., 2007), moire method (Limare et al., 2011) and acoustic profilers and scanners (e.g. Lanzoni, 2000). The choice of the appropriate method is essential since the quality of data gathered from mobile bed experiments depends on the reliability and accuracy of the adopted measuring systems (Visconti et al., 2010). On the other hand, most and widely applied methods for bed profiling are stop and run approaches where water has to bed drained before bed acquisitions (e.g. Bertoldi and Tubino, 2005). Such measurement approaches are usually not applicable to monitor or acquire rapid evolution of bed morphology in the presence of water such as dike breach experiments and bed evolutions in non-equilibriums suspended transport. Though devices such as acoustic profilers and acoustic scanners allow bed profiling in the presence of water overlying the bed (e.g. Lanzoni, 2000; Thorne and Hanes, 2002), they cause undesirable morphological alterations such as local scour since instruments should be placed inside water (Visconti et al., 2010). Moreover, time lapse acquisitions of change of bed evolution may not be possible and similarly sufficient spatial resolution is required to depict spatial heterogeneities of the bed and small scale changes during erosion.

In recent years many developments have become available that allows one to measure bed evolution as a function of time in running water at laboratory scale (e.g. Abad and Garcia, 2009; Huang et al., 2010; Soares-Frazão et al., 2007; Visconti et al., 2010). Huang et al., (2010) proposed a non-intrusive method that couples a colour camera and a laser stripe to record water flow mixed with a fluorescent dye. By this method bed topography and water depth are reconstructed simultaneously from the colour images with high accuracy (0.6 mm) though the method is still to be tested at large scale. Soares-Frazão et al. (2007) applied laser sheet and a camera to reproduce the geomorphic evolution (changes in the cross-section) of a channel under dam-break flow conditions with an accuracy of 2.0 mm. In this method image of bed profile is taken by a digital camera while laser-sheet lights up a given cross-section. Then the two-dimensional (2D) pixel coordinates of the laser profile is transformed to three-dimensional (3D) metric coordinates by a calibration procedure that defines affine transformation (Spinewine et al., 2003). Abad and Garcia (2009) also applied similar bed profiling technique where a laser sheet is projected through water and the intersection of the laser sheet with bed is captured by a camera. The digital images are processed to reconstruct the bed profile in meandering experiment at laboratory scale. Some photogrammetric techniques are recently developed for quasi-simultaneous measurements of bed topography and water depth (e.g. Limare et al., 2011).

Suspended transport is the dominant mode of transport in the lower reaches of rivers, in tidal rivers, and along sandy beaches (van Rijn et al., 2007). In some occasions large quantity of fine sediments can be released during dam removal or sediment flushing operations where sediments are transported in

suspension in immobile coarse bed downstream of a dam (Wren et al., 2011). The exchange of the suspended particles in the flows with the bed is usually difficult predict (Wren et al., 2011) and direct measurement of the erosion rate in running water conditions will be useful to understand the processes. The direct measurement of the rate of fine sediment entrainment into suspension is however a challenging task and most studies focused on measurement of the near bed sediment concentration in equilibrium transport conditions to estimate rate of sediment entrainment by suspension flow (e.g. Garcia and Parker, 1991; Cao , 1999; Rijn, 1984a; Grams and Wilcock, 2007). The near-bed concentrations are measured by in-situ sampling and analysis of the concentration in sediment laden flow (e.g. Garcia and Parker, 1991; Grams and Wilcock, 2007). Most of these experiments are conducted in sand bed conditions of uniform bed materials while few studies conducted measurements in coarse immobile beds (e.g. Grams and Wilcock, 2007; Khunle et al., 2013; Wren et al., 2013). van Rijn (1984b) conducted direct measurement of sediment entrainment (sediment pick up) into suspension flow in non-equilibrium transport condition. The sediment pick-up rate is measured directly by using a mechanical sediment lift by which sediment particles can be pushed upward at constant rate through a circular opening in the flume bottom filled with running water. The pick-up rate is estimated as the mass of sediment particles per unit area of the movable surface of the lift over measurement period.

Due to the increasing ecological and environmental concerns of fine sediments in immobile beds, especially downstream of dams, laboratory based studies are emerging, in recent years, to understand fine sediment erosion and entrainment processes in immobile coarse beds (e.g. Wren et al., 2011; Kuhnle et al., 2013; Wren et al., 2013; Grams and Wilcock, 2007).   Nevertheless measurement of fine sediment bed evolution and entrainment in the immobile bed matrix is found to be difficult. For instance, Grams and Wilcock (2007) and Kuhnle et al. (2013) measured changes in bed profile due to suspension transport by manual profiling using point gauges. Despite many developments to estimate bed evolution in morphodynamic laboratory experiments, the measurement of fine sediment erosion rates in immobile coarse beds is extremely lacking. On the one hand, existing measurements of fine sediment transport rate in immobile bed are based on surrogate variables such as measurement of suspended sediment concentrations (Khunle et al., 2013; Wren et al., 2013).on the other hand, measurement of bed evolution by suspended transport is conducted by stop and run procedure (e.g. Grams and Wilcock, 2007) which does not allow continuous monitoring of erosion rate and bed evolution.

In this study a new non-intrusive methodology is developed to estimate evolution of bed topography and erosion rate of fine sediments in immobile coarse bed characterized by moving water in depth range of 3.0 cm to 8.0 cm. The methodology has been successfully applied to measure longitudinal distribution of erosion rate and bed profile due to suspension transport in immobile gravel bed in non-equilibrium

transport conditions. The proposed technique couples a single line laser sensor, a digital video camera and reflective mirror. The method is non-intrusive, fast, simple and cheap technique to monitor bed evolution and erosion rate measurement in laboratory experiment. Measurements of bed elevation and depth of erosion can be conducted at a resolution of 350µm with low resolution camera by using manually adjustable reflective mirror. First the experimental facilities and experimental setup for erosion experiment and laser line measurement principle and setup are described in Section 4.2 and 4.3. Secondly, image acquisition and processing as well as methods developed for laser line extraction are presented and results are discussed in Section 4.4. In Section 4.5 and 4.7 estimation of erosion rate and fine sediment bed evolution in the immobile gravel bed are presented and the results are discussed. The validation of the method is also presented.

4.2. LABORATORY FLUME FACILITIES

The experiments were conducted in tilting water circulating experimental flume whose length, width and depth are 16m, 0.4m and 0.7m respectively. The slope of the channel can be adjusted electronically from the horizontal plane to a value up to $i_b = 10\%$. These ranges of values allow a large range of flow conditions, very useful for obtaining a wide distribution of results. The optical level used in electronic device, used to measure slope, is able to evaluate the elevation of a point with a precision of 0.1 mm. The flume has a recirculation pump (maximum capacity of 13.33 l/min) and a water storage tank (maximum water storage of 15 m^3) to deliver water to the flume inlet (refer Figure 4-1, top). The right lateral flume wall is glass supported by steel structure and the left lateral wall is plastic, both can be considered smooth. The water discharge is controlled by a gate valve and measured by an electromagnetic flow-meter connected to the inlet pipe, which has a maximum error in measurement of 0.005Q, where Q is the water discharge. The flume has manually adjustable outlet gate which is used to maintain uniform flow conditions. The flume is equipped with PSD laser scanner for surface elevation measurement. The coordinate x-, y- and z-axis show the stream-wise, span-wise and vertical coordinates respectively used in the description of experimental datasets.
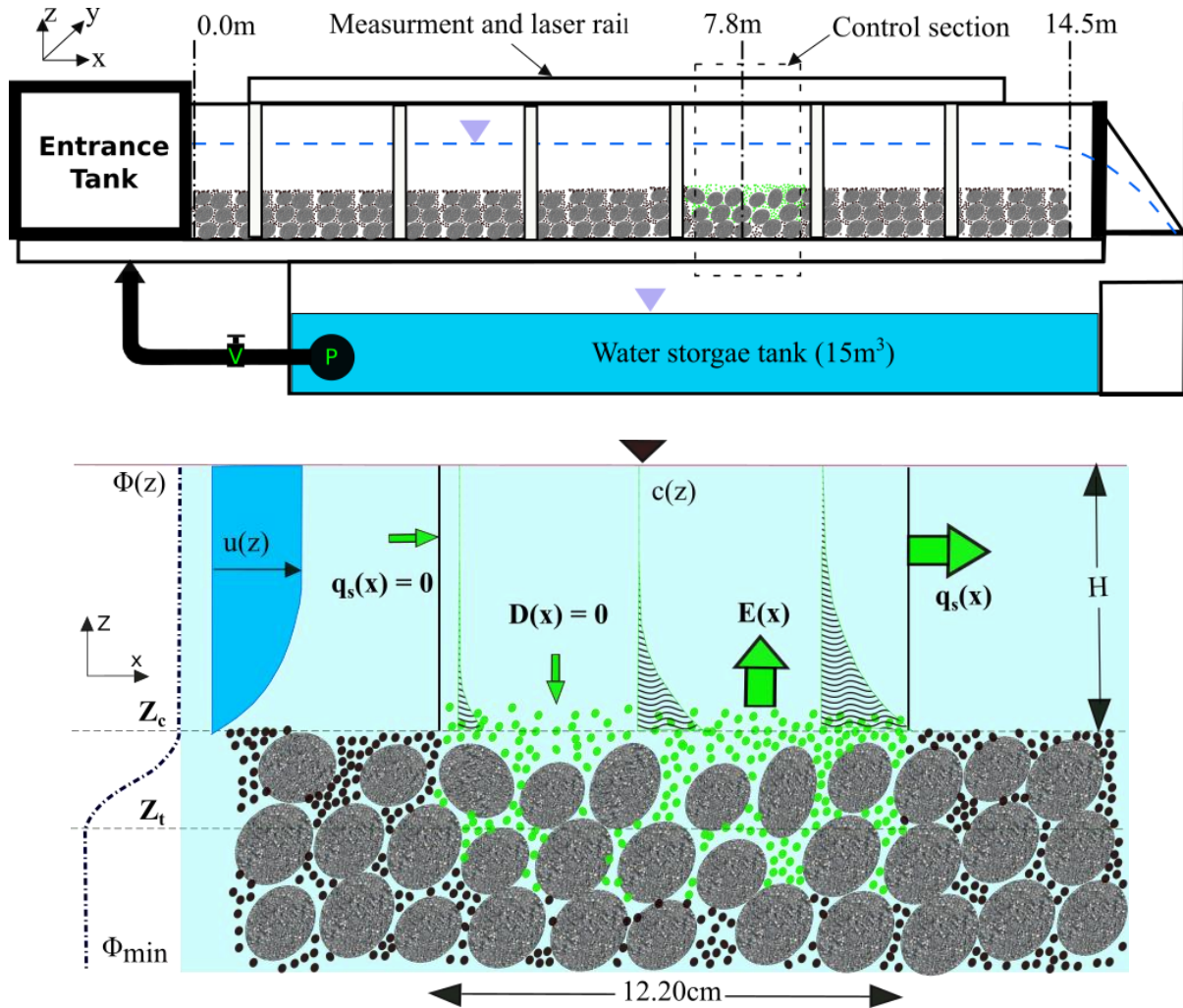
Figure 4-1. The schematic layout of the laboratory flume and bed sediment materials (fine particles & immobile bed materials (natural sand and gravels) used in erosion experiments (top) and the control section and experimental setup (bottom) where E = erosion; D = deposition; q_s= sediment load; Φ = gravel porosity; c = concentration; u=velocity; Z_c= crest elevation; Z_t= bottom of interfacial sublayer

4.3. MEASUREMENT APPROACH

4.3.1. Fine sediment erosion experimental setup

The hydraulic conditions of the experiments are indicated in Table 4-1 where Run IX is selected to describe the method developed for erosion rate measurement. The erosion measurement is conducted in a control section (measurement section) of the flume at 7.8 m from the flume entrance where fully developed boundary layer is reached (Figure 4-1, top). The dimensions of the control section are 20.00

cm in span-wise and 12.20 cm in stream-wise directions as shown in Figure 4-1(bottom). The flume bed is initially filled with relatively uniform immobile gravel particles of median diameter (d_g = 25.89 mm) with the standard deviation of bed surface elevations (σ_z) = 7.2 mm. Upstream and downstream of the control section natural sand materials (d_{50} = 1.25mm) (black dots in Figure 4-1, bottom), that are immobile, are filled in the roughness elements of the gravel bed up to the crest level (Z_c in Figure 4-1, bottom) except in the test section where this was made below the bottom of the interfacial sublayer (Z_t in Figure 4-1, bottom). The fine sediments (green dots in Figure 4-1, bottom) used in all experimental runs were Bakelite (phenol formaldehyde resin) particles of uniform grain size (d_s = 425 µm and 500µm) crushed out of Bakelite plate whose specific gravity is 1.553. Bakelite particles are widely used materials for sediment transport experiment (e.g. Nnadi and Wilson, 1995; Nnadi and Wilson, 1992). The mode of transport of the fine sediments was by suspension where u_*/w_s was larger than 1.0 (van Rijn, 1984a).

Table 4-1. Hydraulic conditions of the experiment for erosion measurements

Run	I	II	III	IV	V	VI	VII	VIII	IX	X
d_s (µm)					425					500
w_s (m/s)					0.0232					0.0284
H (m)	0.050	0.060	0.070	0.080	0.030	0.040	0.050	0.030	0.050	0.030
So	0.0014	0.0014	0.0014	0.0014	0.0024	0.0024	0.0024	0.0034	0.0024	0.0034
Fr	0.400	0.395	0.385	0.375	0.563	0.532	0.502	0.655	0.502	0.655
Re	13990	16558	18958	20672	7971	11111	14066	9275	14066	9275
B/H	8.00	6.67	5.71	5.00	13.33	10.00	8.00	13.33	8.000	13.333
Q (l/s)	5.608	7.275	8.942	10.617	3.667	5.333	7.033	4.267	7.033	4.267
U (m/s)	0.280	0.303	0.319	0.332	0.306	0.333	0.352	0.356	0.352	0.356
u_*	0.0251	0.0273	0.0294	0.0313	0.0257	0.0296	0.0329	0.0307	0.033	0.031
k_s (mm)	7.31	9.12	11.72	15.00	3.22	5.62	9.08	3.66	9.077	3.661
k_s^+	183	248.94	344	469	82.9	166.1	299	112.2	299	112.2
L_d (m)	1.69	2.02	2.31	2.57	1.08	1.37	1.62	1.05	1.618	1.054
u_*/w_s	1.080	1.176	1.264	1.347	1.107	1.273	1.418	1.320	1.160	1.079

d_s = median diameter of fine sediments (Bakelite particles); w_s = settling velocity (m/s); H = flow depth (m); S_o = gravel bed slope (m/m); $Fr = U/\sqrt{gH}$ = Froude number; Re = UH/ ν = Reynolds number; B/H = aspect ratio; Q = flow discharge; U = flow velocity (m/s); u_* = shear velocity (m/s); k_s = equivalent roughness (mm); k_s^+ = dimensionless Nikuradse sand equivalent roughness ; L_d = length of fully developed boundary layer (m); $u*/w_s$ = suspension parameter.

When shear velocity is higher than settling velocity suspended sediment transport is initiated (e.g. Bagnold, 1966; van Rijn, 1984a; Leeder et al., 2005). The fine sediments (Bakelite particles) were filled

in the gravel matrix before running the experiment. Each experimental run was conducted under uniform flow condition where this was maintained by gradual and simultaneous adjustment of upstream valve for controlling inflow discharge and downstream gate level to control water level. Nevertheless, an additional amount of fine sediments were put above the crest level of the gravels up to two-third of the flow depth (Figure 4-3). By this it is possible to avoid erosion of the fine sediments from the gravel matrix before uniform flow condition is achieved. Each erosion measurement was conducted once the uniform flow condition is achieved and fine sediment level is above the gravel crest. In Table 4-1, the dimensionless Nikuradse sand equivalent roughness $k_s^+ = $ u*k_s/ν shows that the present flows are in hydraulically rough condition (Nezu and Nakagawa, 1993). Equivalent roughness, k_s is estimated based on stage-discharge measurements using Colebrook and White (1937) formula, where ν is the water kinematic viscosity. The aspect ratio (B/H where B is channel width) shows measurements can be classified as wide open channels (Nezu and Nakagawa, 1993). The shear velocity (u_*) is computed as: $u_* = \sqrt{gR_bS_o}$ where the hydraulic radius related to the bed (R_b) is calculated using the relation of Vanoni and Brooks (1957) as modified by Chiew and Parker (1994). The length of fully developed boundary layer is estimated by using Kirkgoz and Ardichoglu (1997) formula (e.g. Nikora et al. 1998) as shown in Table 4-1. Further, it is verified by measurements of vertical velocity profiles (acquired by UVP-Ultrasonic Doppler velocity profiler (Metflow, 2000)) taken at five selected sections from flume entrance (see Figure 4-2).
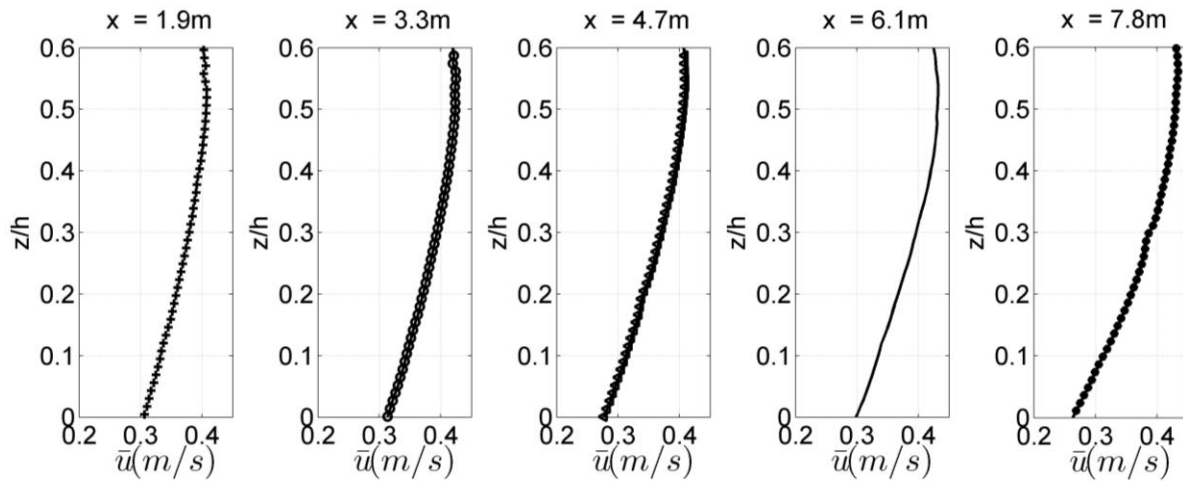
Figure 4-2. Span-wise averaged stream-wise velocity profiles at selected sections along the flume

The settling velocity of fine sediments is estimated by using Cheng (1997) formula:

$$w_s = \frac{v}{d_s}\left[\sqrt{\frac{1}{4}\left(\frac{A}{B}\right)^{2/m} + \left(\frac{4}{3}\frac{d_*}{B}\right)^{1/m}} - \frac{1}{2}\left(\frac{A}{B}\right)^{1/m}\right]^m \qquad (4\text{-}1)$$

where A, B and m are coefficients which are given by $A = 32.0$, $B = 1.0$ and $m = 1.5$. The dimensionless particle diameter (d_*) is given by: $d_* = (\rho_s - \rho)g d_s / \rho v^2$ where ρ_s and ρ are fine sediment and water densities. The experimental hydraulic conditions are selected to insure hydraulically rough flow ($k_s^+ > 70$), subcritical flow ($F_r < 1.0$) and insure dominant mode of transport as suspension ($u_*/w_s > 1.0$).
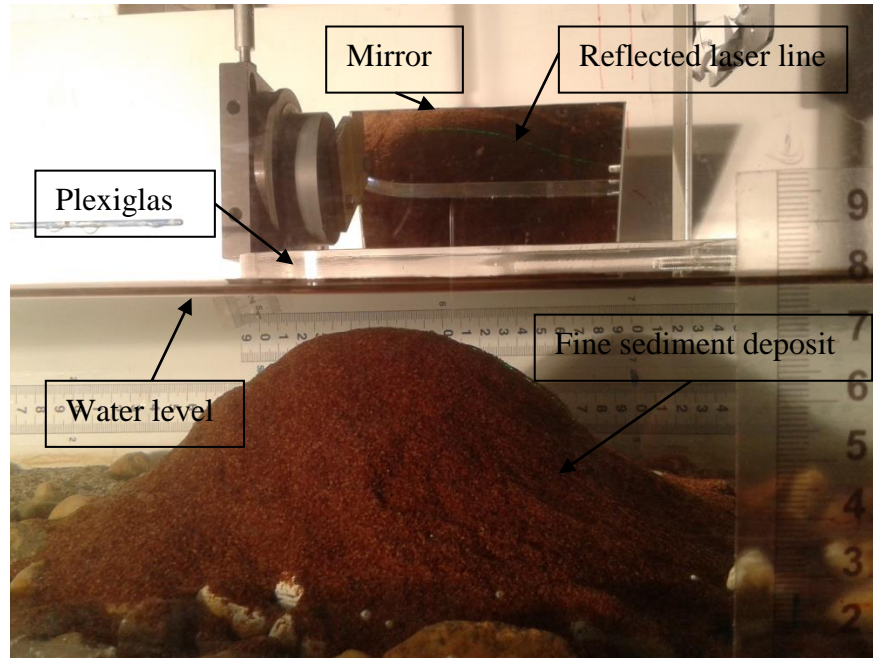
Figure 4-3. Initial deposit of fine sediments filled in still water at the control section before the experiment is run

4.3.2. Set-up for the laser-line measurement technique

The overall measurement principle involves laser light sheet, video camera and reflective mirror (Figure 4-4). The method applies a single line laser sheet to enlighten a given longitudinal cross-section (shown in Figure 4-3 and Figure 4-4 in green). The trace of the laser line is imprinted onto digital images of a high speed video camera through the surface of the flowing water. A green laser line is used since it has better contrast with respect to the background fine sediment particles and was within the camera light sensitivity range. The laser module is a FLEXPOINT® line laser type FP-53/4F-O30-HOM, wavelength 532nm with output power of 10mW and fan angle of 30^0. FLEXPOINT® line lasers have a Gaussian profile in that the power distribution along the line is extremely homogeneous.
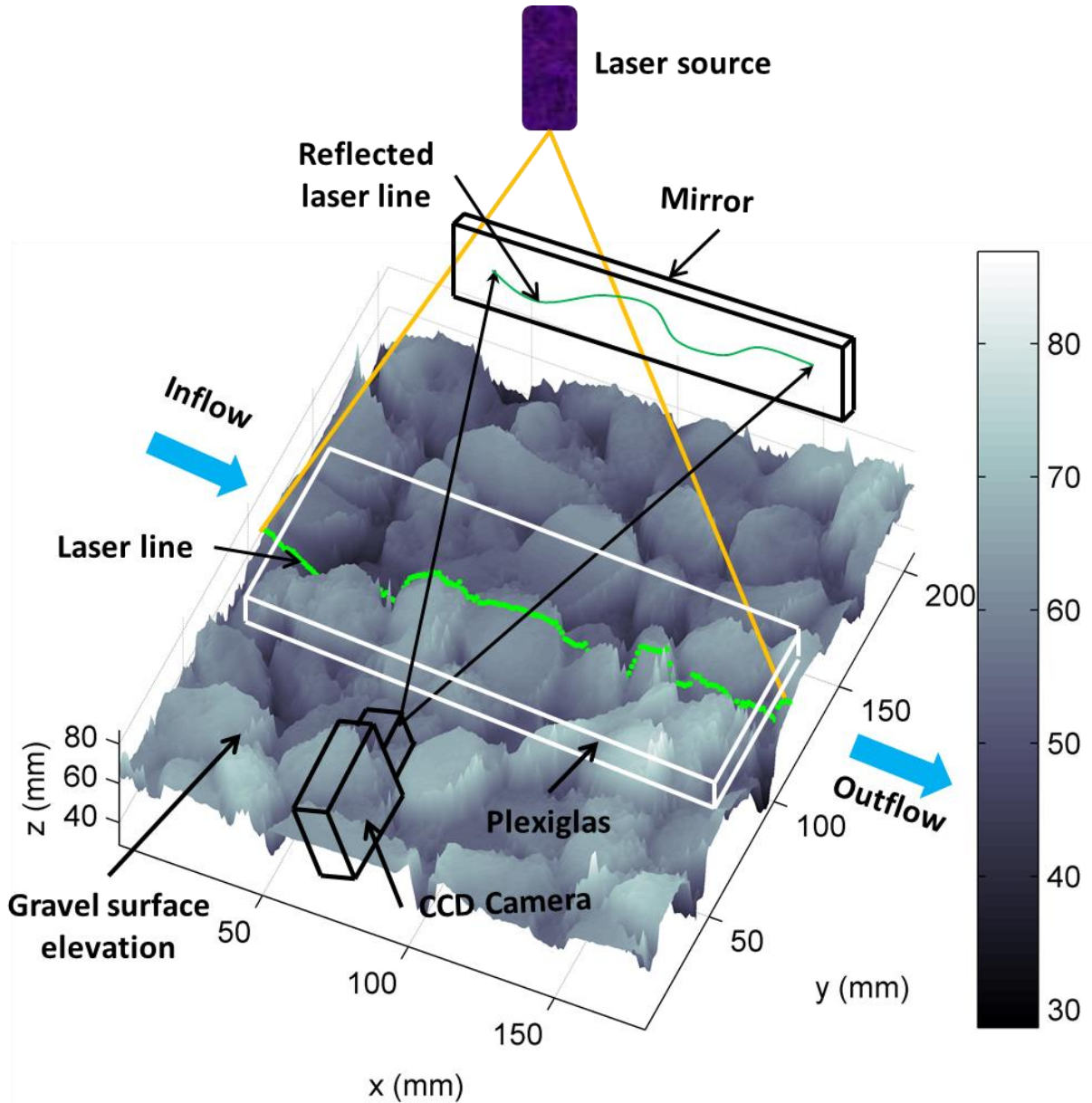
Figure 4-4. Set-up for the laser-line measuring technique for erosion rate. The green projected laser line on the gravel surface elevation shows a vertical plane (Plane 1) where fine sediment erosion is monitored. Another plane (Plane 2) was also selected for additional measurement which is discussed in later sections.

The true shape of the laser line could be distorted by light refraction along air –water interface (Huang et al., 2010) and measurement of true bed morphology and flow depth in running water is problematic unless corrections for refraction are applied. To avoid such complexities images of the bed and the laser line in this experiment are captured by placing a transparent Plexiglas at the surface of the running water. The transparent Plexiglas was efficient to reduce the effect of surface turbulence and refraction on the true

shape of the captured laser lines. The images are captured in video format from a mirror where the true reflection of the laser and the fine sediment bed were projected through the Plexiglas (see Figure 4-3 and Figure 4-4). Details of the use of the reflective mirror are presented in Section 4.3.3. The exact position of the laser line captures the rapid morphological evolution of the eroding fine sediments deposited in gravel matrix as a function of time.

4.3.3. Principle of laser line measurement of erosion rate and bed evolution

The principle behind the measurement of erosion rate by laser line is based on the assumption that the evolving shape of the laser line is a surrogate for bed evolution by sediment erosion. If there is no change in shape and position of the laser line in the image it shows that there is no erosion. Thus between any instant in time the shape changes can be reconstructed to estimate the depth of erosion along the projected laser line on the eroding bed. A series of digital images of laser line projected on immobile gravel bed filled with fine sediments was acquired during the experimental run until all the fine sediment materials were eroded. The position of the pixels of the images is indexed by two-dimensional column and row coordinates, L (c, r) where L = image. The laser line position and shape evolves depending on the vertical position of the fine sediments in the immobile gravel matrix. The displacement of the laser line between a pair of images taken at different instant of time indicates the depth of sediment that is eroded. To compute erosion rate the laser lines in image coordinates should be converted into fine sediment bed level by applying calibration factors and referencing to known elevation of the gravel surface elevation data. Therefore, the true vertical coordinate of the fine sediment bed level was thus computed based on known reference point in the image whose image coordinate is matched to the corresponding elevation value in the gravel surface elevation data (shown in Figure 4-4, top). In this manner all image coordinates along the laser line were assigned a true bed level (in mm) in reference to gravel surface elevation. Finally, the erosion (pick-up) rate (E, mm/s) of the fine sediments along the measurement section is calculated as the displacement in mean fine sediment bed level divided by the time interval between two acquisitions Δt and corrected for porosity (e.g. Okayasu et al., 2011). The mean of fine sediment bed level along the entire measurement length was estimated by averaging the individual fine sediment bed levels along the length of the measurement section except in regions where the laser line and the gravel bed intersect. The estimation of E and bed evolution from the images involves pre-processing of the images and these include extracting centreline of the laser lines, calibrating the images and referencing the extracted data to true vertical coordinates (details are in Section 4.4 and Section 4.5).

4.4. IMAGE ACQUISITION AND PROCESSING

4.4.1.   Image characteristics

The successive evolution of the shape and position of the laser line as erosion of the fine sediments progresses in the gravel matrix were recorded by a single colour camera in video format. A Sony DCR-VX2000 DV charge-coupled device (CCD) video camera (hereafter SONY camera) that captures images at 25 frames per second (fps) and with a resolution of 768 x 576 pixels and Chameleon 1.3 MP Color USB 2.0 video camera (hereafter Chameleon camera) that captures 15 frames per second (fps) at a resolution of 1280 x 960 were used. The cameras are mounted on a tripod to view the sand filled bed reflected on a mirror (Figure 4-3) with no angle of inclination from the horizontal. The mirror is useful to enhance the vertical resolution of the measurement and exposure of the laser line in the gravel matrix which are not possible when the camera was positioned to capture the bed directly.
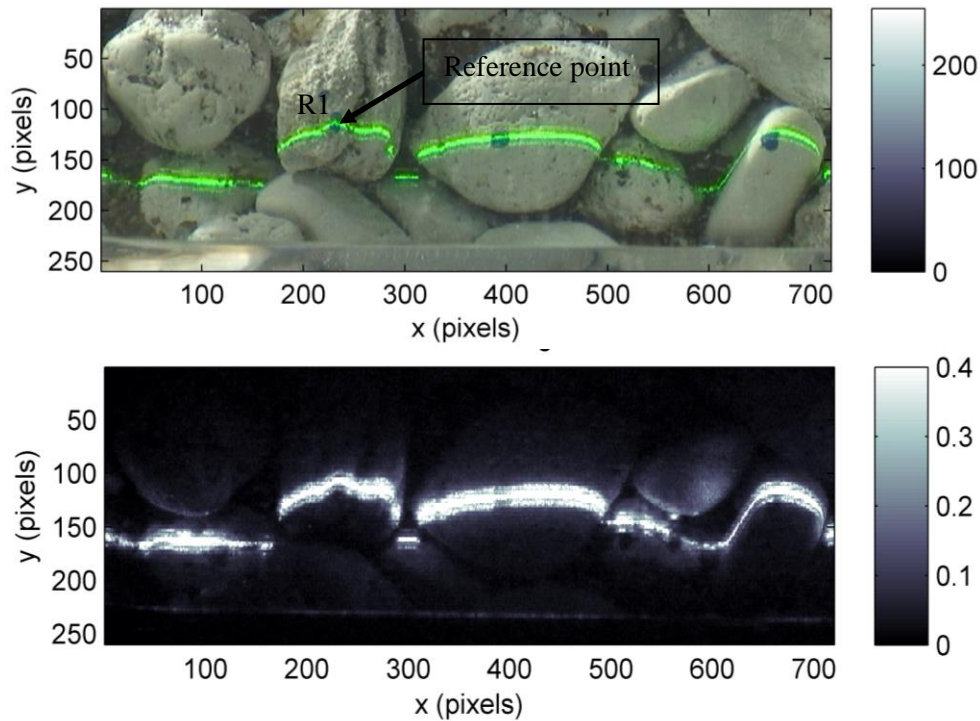
Figure 4-5. RGB (top) and extracted green component (bottom) images of the projected laser line on gravel bed when the fine sediment bed level is negligible

By adjusting the mirror in a vertical plane and moving it towards and away from the target as necessary enhances the exposure of the laser line in the gravel matrix. The videos were recorded in progressive mode in Mini DV cassettes using SONY camera but with Chameleon camera videos were recorded in AVI format. During the imaging process the target background was kept dark and the video camera

shutter was made narrow so that the laser light is intensified and the background is suppressed. The video from Mini DV cassettes were extracted in uncompressed format by using Window Movie Maker® to preserve the quality of the measurement. Finally image frames were extracted from the video in bitmap format using MATLAB®. Figure 4-5 (top) show one example of a colour image of the green laser line on gravel surface extracted from the video captured by SONY camera. Each of extracted colour images were coded as an MxNx3 array of intensity values for red, green and blue components. In subsequent processing of the images the green laser component was enhanced by extracting the green band of the colour images (Figure 4-5, bottom). The images described in this chapter are for Run IX and are acquired by SONY camera.

4.4.2. Image calibration

The images extracted from the videos were in pixel coordinates, $L(c, r)$. The erosion rate as well as gravel surface elevation data should be quantified in mm. Since the measured erosion process was in in the gravel matrix as thick as the mean diameter of the gravel, accurate vertical scales within this region were essential. The conversion from pixels to mm is also a measure of the resolution of measurement. By adjusting the position of the mirror, the vertical resolution of the measurement was improved. It enabled to capture a single grain size of the eroding particles (fine sediments) by more than a pixel. Since each image was captured from mirror reflection of the target through the water and Plexiglas interface, images used for calibration were also taken under the same condition. The vertical scale is estimated based two images that capture a 10mm vertical shift of a calibration rod in the gravel matrix through running depth of water for which the erosion experiment was conducted (see Figure 4-6). The movement from P_1 to P_2 was 28 pixels when estimated manually from the acquired images. Figure 4-6 show two images extracted from the video when the calibration rod was moved by 10mm from P_1 to P_2. The length (dark solid lines in Figure 4-6) of the calibration rod (length of rod painted in blue) is 104 mm and the number of pixels along this length is 612. Thus, the vertical scale (S_v) and the horizontal scale (S_h) are 0.36 mm per pixel and 0.17 mm per pixel respectively. The vertical scale shows that a single fine sediment particle is represented by more than a pixel.
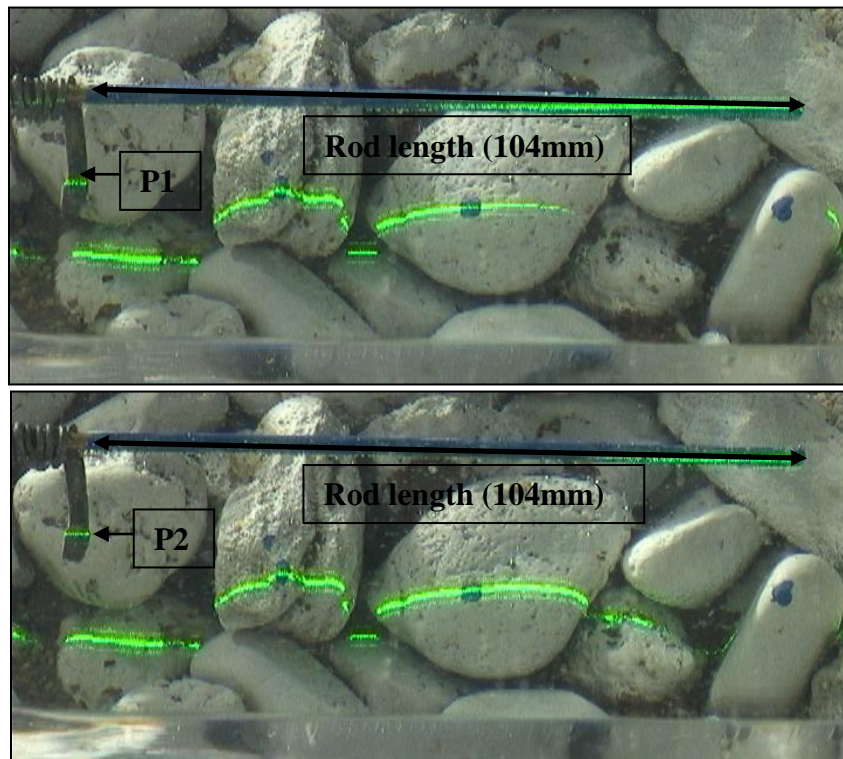
Figure 4-6. The images used for vertical and horizontal calibration

4.4.3. Image pre-processing

The detection of the exact position laser line in the images was one of the challenging tasks. This is mainly due to background noises, the effect of entrained particles moving through the laser sheet, the refraction due to the thickness of the Plexiglas, the hiding of laser line by the gravel particles and also low contrast of the laser line with respect the background immobile gravel bed (painted white) when the fine sediments level is below the gravel crest. Thus, pre-processing of the images was essential to detect and extract the position and the centreline of the laser line. To overcome these intrinsic problems systematically designed spatial filters and sampling procedures were developed. In Figure 4-7 the developed image filtering procedures are presented and the details of each filter are described in sub-sections. The arrows show each filter is tested for different values of filter parameters until the targeted noise removal at each step is achieved before moving to the next step.
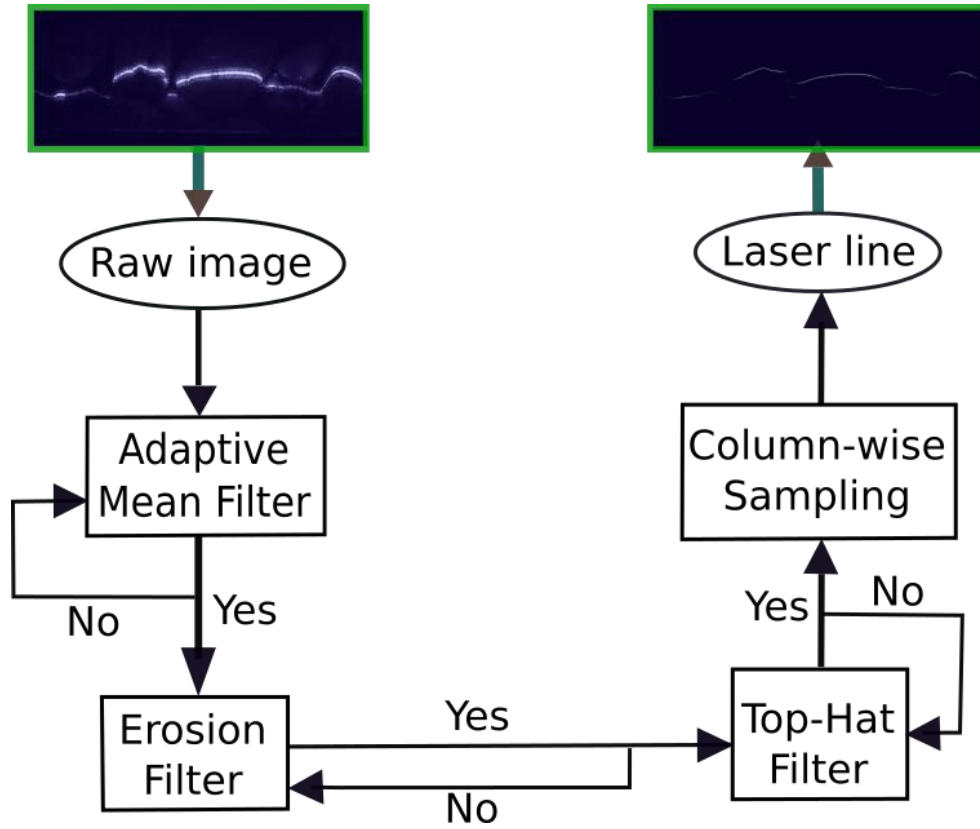
Figure 4-7. The sequence of techniques applied in laser line extraction from raw images

4.4.3.1. Adaptive Mean Filter

First, an adaptive mean filter (AMF) with a user-defined mask was developed and applied (Equation (4-2)) (e.g. Sung et al., 2009). The mask in the filter is designed to reduce background noise, intensify the laser line and interpolate regions where there was no clear imprint of the laser line by using solely pixel values from the neighbouring laser line. Considering a raw digital image $L(c, r)$ where c = 1 to N and r = 1 to M, Equation (4-2) is the mathematical description of AMF, where 2n+1 and 2m+1 indicate the pixel number within the mask in x and y directions respectively.

$$L_m = \frac{\sum_{c=t-n}^{t+n} \sum_{r=h-m}^{h+m} L(c,r)}{(2n+1)(2m+1)} \tag{4-2}$$

where L = the raw image intensity in the image coordinate (c, r), L_m = the image that is intensified after adaptive mean filtering, t = n to (N-n), and h = m to (M-m) .
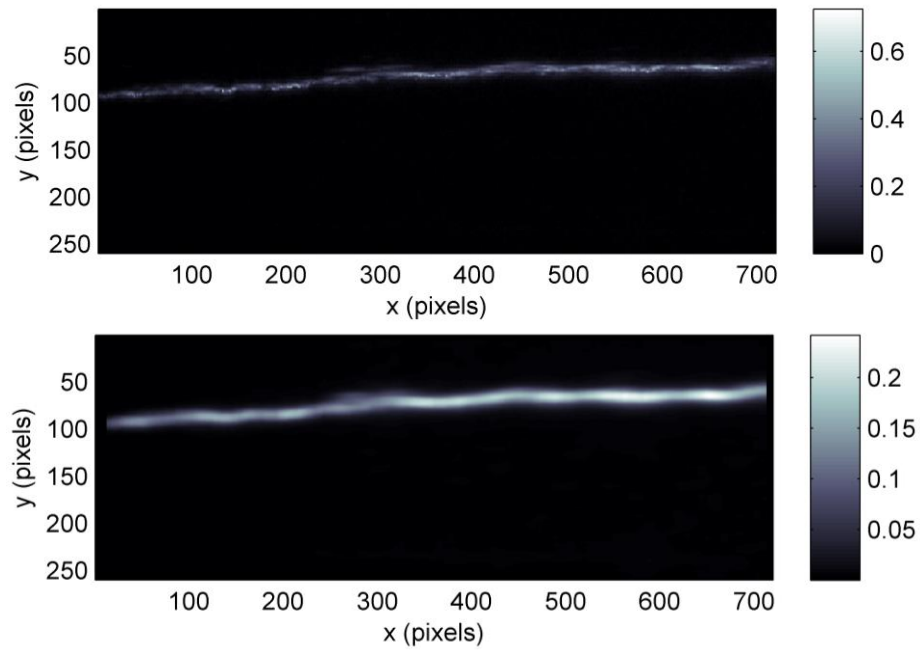
Figure 4-8.Unfiltered (top) and AMF filtered (bottom) images of laser line when fine sediment bed level is above gravel crest
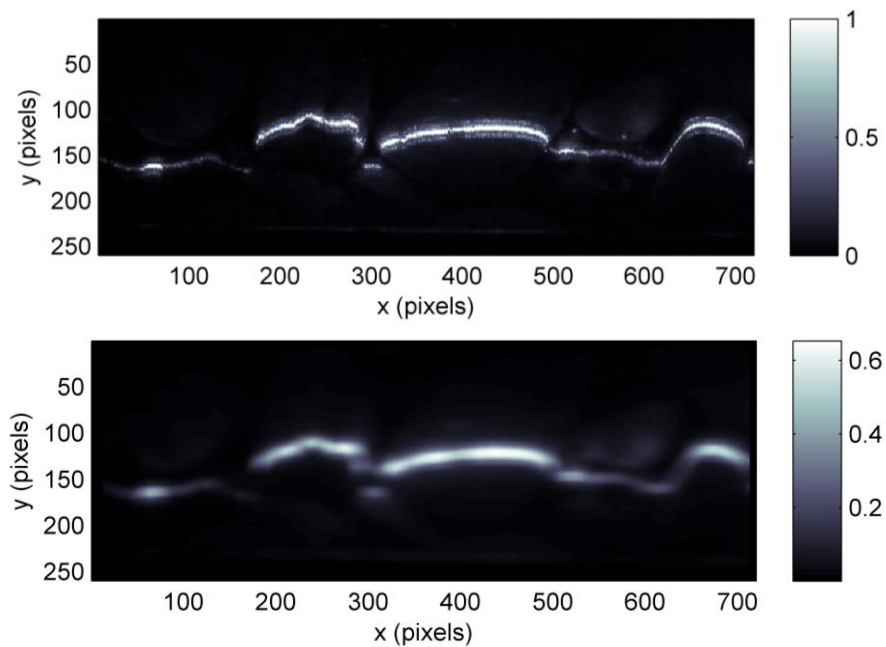
Figure 4-9. Unfiltered (top) and AMF filtered (bottom) images of laser line when fine sediment bed level is below gravel crest

AMF filter was used to remove unnecessary background noises and intensify relatively low-intensity pixels along the laser lines. The dimensions of the filter mask, n and m were selected based on the orientation of the laser line and the thickness (number of pixels a single laser line is imprinted) of the laser line in the raw image. The selection of larger n = 13 along the laser line and an m = 5 value as large as the thickness of the laser line were found to be effective. Figure 4-8(top) and Figure 4-9(top) show the position of the laser line in the raw images and Figure 4-8 (bottom) and Figure 4-9 (bottom) show after the AMF filter was applied.

4.4.3.2. Morphological erosion filter

A morphological erosion filter (EF) shrinks or thins objects in a grey scale image (e.g. Gonzalez et al., 2004). In this type of filter the manner and extent of shrinking or thinning is controlled by the structuring element.
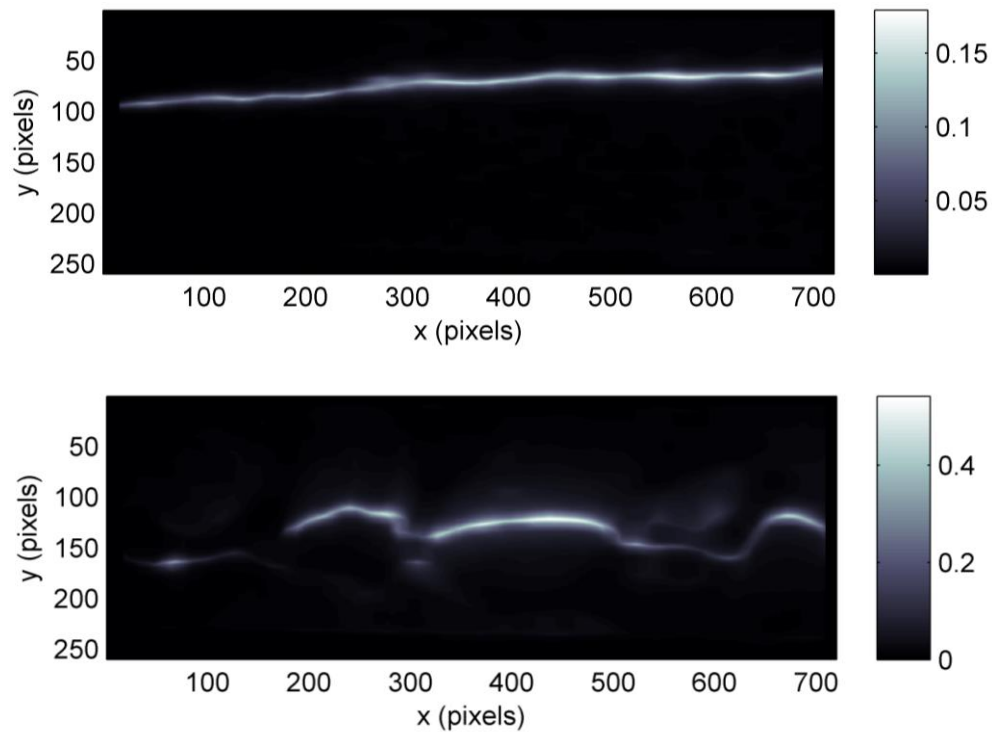
Figure 4-10. EF filtered images of laser line when fine sediment bed level is above (top) and below (bottom) gravel

Mathematically a morphological erosion filter of L by structuring element S can be described in Equation (4-3) where $S(x, y)$ for x = -X to X and y = -Y to Y and 2X and 2Y are dimensions of the filter mask.

$$L_{ef}(c,r) = \min\left(L(c-x,\ r-y) - S(x,\ y)\right)$$ (4-3)

EF was applied to the mean filtered image (L_m) to remove the remaining background noises and to strengthen the intensity of the laser line. A square structuring element of size 9 x 9 was found to be effective. Figure 4-10 (top) and (bottom) show that the image intensity along the laser line is enhanced and the background noises are well reduced.

4.4.3.3. Morphological Top-Hat Filter

A morphological top-hat filter (THF) is a commonly used for peak detection in image processing (e.g. Meyer, 1979).
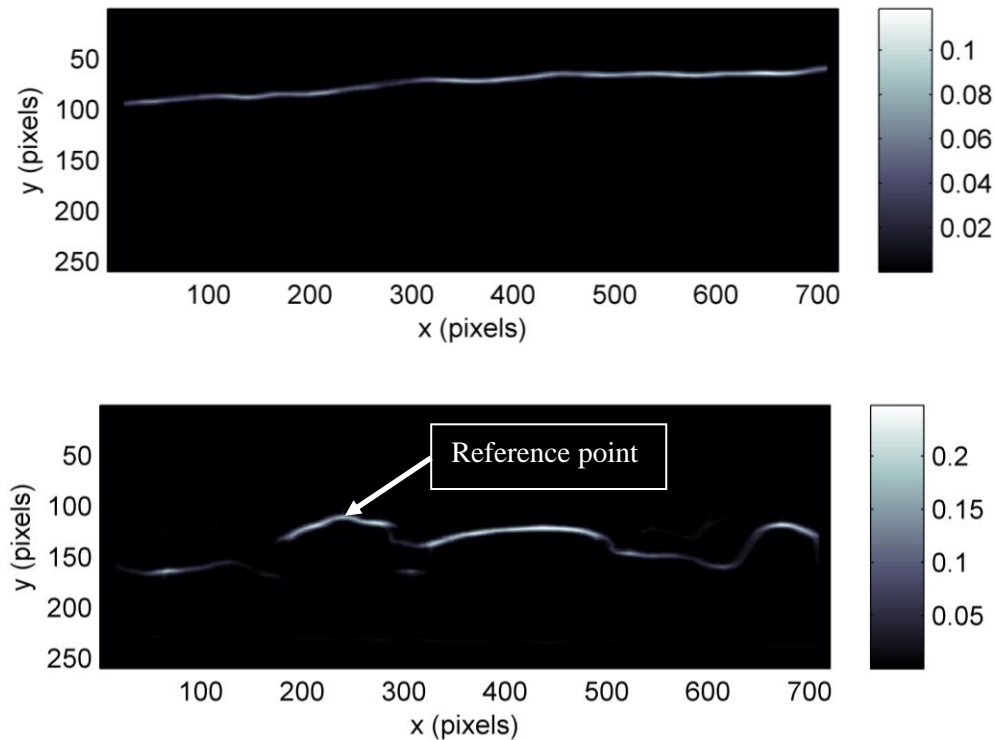
Figure 4-11. THF filtered images of laser line when fine sediment bed level is above (top) and below (bottom) gravel crest

Mathematically it is described as a function of erosion and dilation filters (Equation (4-4)). Dilation filter (DF) is obtained when the minimum is replaced by maximum in Equation (4-4). A top-hat filter preserves sharp peaks and eliminates other features, including image pixels with lesser contrast.

$$L_{thf}\left(c,\ r\right)=L\left(c,\ r\right)\ -DF\left(EF\left(L\left(c,\ r\right),S\left(x,\ y\right)\right),S\left(x,\ y\right)\right) \tag{4-4}$$

At the final stage of filtering, a THF with a square structuring element of size 9 x 9 was applied to AMF and EF filtered image (see Figure 4-11). At this stage of pre-processing the laser line become thinner and converges to high intensity pixels (Figure 4-11) which allowed identifying the location of the centreline of the laser imprint in the raw image.

4.4.4.   Extraction of laser centreline

Despite the image filtering resulted in thinned laser line (see Figure 4-11) the centreline of the laser must be precisely extracted. The centreline is assumed to be the pixel with the highest pixel intensity. The peak intensity and its position was extracted using column by column search of maximum pixel intensity along columns taken across the laser line. The peak intensity is the maximum intensity along each column. The procedure was applied for entire columns of the image and the output is an image of the centreline of the laser line (Figure 4-12).
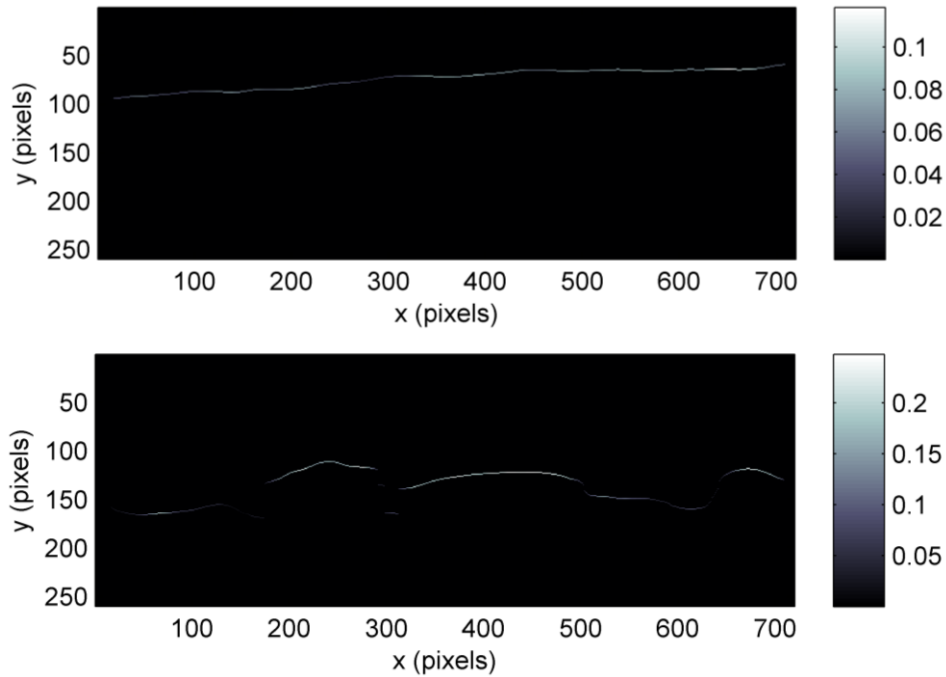
Figure 4-12. The centre line of extracted laser lines when fine sediment bed level is above (top) and below (bottom) gravel crest

The extracted centre line of the laser line, following this procedure, in images of fine sediment bed (fine sediment bed level above gravel crest) and gravel bed is shown in Figure 4-12 (top and bottom respectively). The general procedure for the extraction of the laser line is summarized in the flow chart shown in Figure 4-7. Figure 4-13 shows the profiles of pixel intensity taken across the laser line at each stage of image pre-processing of an image acquired for fine sediment bed (left) and gravel bed (right). The profile plot in black line is the raw data while in red, blue and green are AMF, EF and THF filtered profiles respectively. The intensity profile of image containing the extracted laser line is plotted in black dashed line. The figure shows that at each step the distribution of pixel intensity becomes narrower and narrower both in fine sediment bed and gravel bed showing the effectiveness of the filters under different surface conditions. Significant change in pixel intensity was noted when THF was applied.
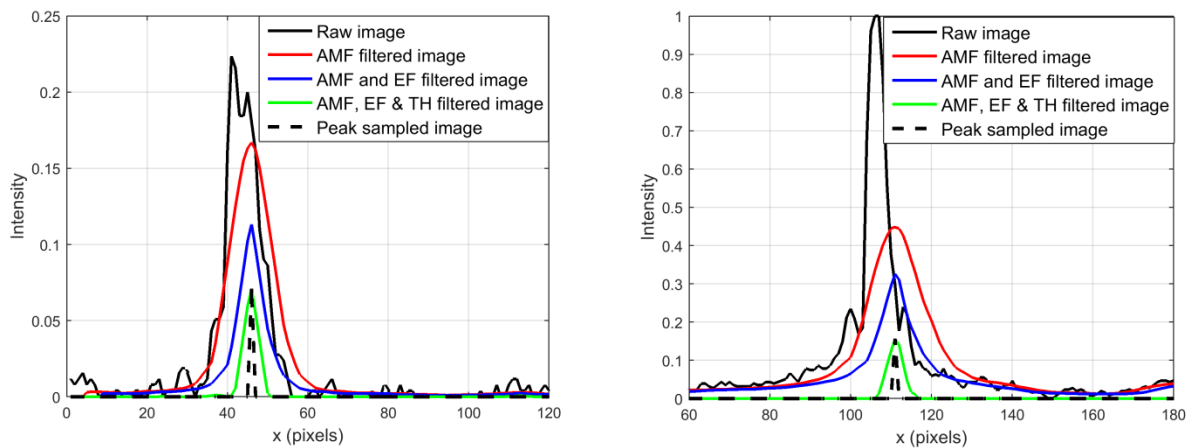
Figure 4-13. Profile of brightness intensity of pixels taken along image column at x = 232 pixels on fine sediment bed (left) and gravel bed (right)

The accuracy of the extracted laser centreline is evaluated by computing the difference between the pixel coordinates, at selected sections across the laser line (in Figure 4-12), of peak intensity of the laser line of the raw image and image of the extracted centreline (the difference of the coordinates of the peak of intensity profiles in black and green in Figure 4-13). Figure 4-14 and Figure 4-15 show the profile of pixel intensity taken across the laser line at selected sections in the raw image (in solid lines) and extracted laser line image (in broken lines). The accuracy is evaluated for condition when the fine sediment level is above gravel crest (fine sediment bed) (Figure 4-14) and when there is no fine sediment deposit (gravel bed) in the gravel (Figure 4-15).
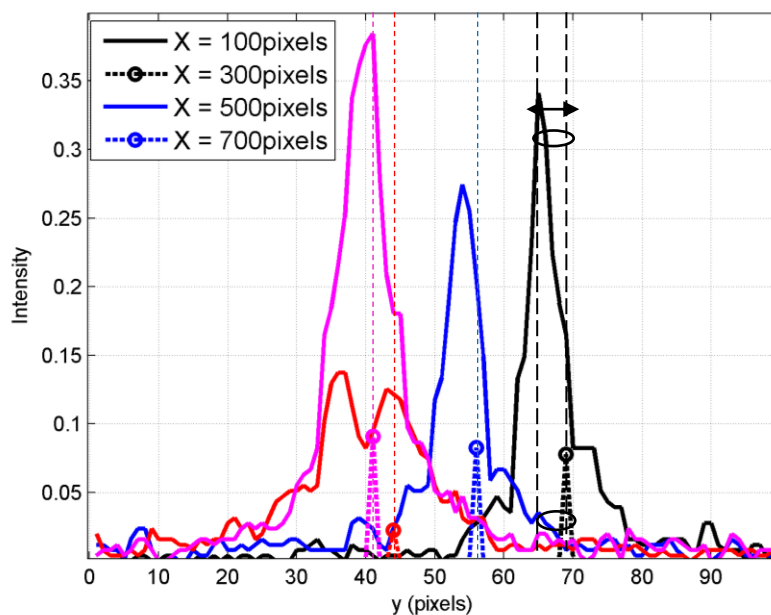
Figure 4-14. Intensity profiles of image pixels across laser line (Figure 4-11, top) on the fine sediment bed surface at selected sections along x (solid & broken lines show profiles of pixel intensity of raw image & extracted centreline respectively)
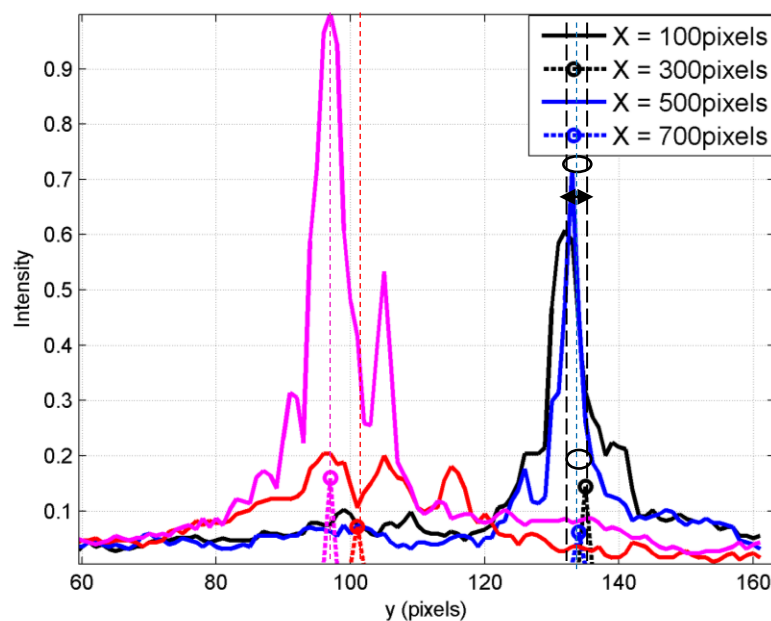
Figure 4-15. Intensity profiles of image pixels across the laser line (Figure 4-11, bottom) on gravel surface at selected sections along x (solid & broken lines show profiles of pixel intensity of raw image & extracted centreline respectively)

The actual position of the centreline of the laser line in the raw image of fine sediment covered bed is extracted with an accuracy of 1 - 2 pixels (0.36 - 0.72 mm) on average. While the evaluation of the extraction of the centreline of laser line on the gravel surfaces showed slightly different result and the accuracy varied between 2-3 pixels (0.72-1.08 mm) on average. This is due to the fact that the laser lines in the raw image of gravel surface have equal peak intensities in more than one pixel across the laser line (solid lines in Figure 4-15).

4.5. ESTIMATION OF FINE SEDIMENT BED LEVEL IN GRAVEL MATRIX

The fine sediment bed level in the roughness elements is used to estimate erosion rate and to describe the reference fine sediment bed level for vertical profile of erosion rate. First, a series of grey scale images containing laser lines are extracted from a video at time step (Δt) = 0.24 seconds thus a total of 551 images for a fine sediment bed level starting from above the crest level of gravel and within the interfacial sublayer of gravel bed. The images are selected in such a way that the first image is selected at time, t = 108 seconds (from the start of the experiment) when the position of the laser line is above the gravel crest and when there is no any net deposition. It is noticed that there is a net deposition in the region between 100 – 120 mm along x-direction for t = 0 to t = 20 seconds, t = 0 is the time at which the erosion experiment starts. The last image is selected at time, t = 240 seconds when there is no significant change in the position of the laser line (when it reaches the bottom of the interfacial sublayer). Figure 4-16 shows the extracted laser lines plotted in a single image and are used to estimate the fine sediment bed level along the laser lines.

The fine sediment bed level is the position of the laser line and is only described in pixel-wise coordinates as shown in Figure 4-16. Therefore, the pixel coordinates with reference to gravel surface elevation data of the roughness elements has to be established. In this manner, the absolute (true) values are estimated based on gravel surface elevation data where a reference point R_1 in the image coordinate is related to a known point whose elevation is known from measured surface elevation data of the gravels (Chapter 3, Figure 3-35). First, the image coordinate of R_1, (Figure 4-5, top) is identified in the raw image. The elevation of R1 and the local crest of the gravel bed are known from the gravel surface elevation data (see Figure 4-4). The elevation at R1 is 65.08 mm and each image coordinate in y - direction of the laser lines is referenced to this value.
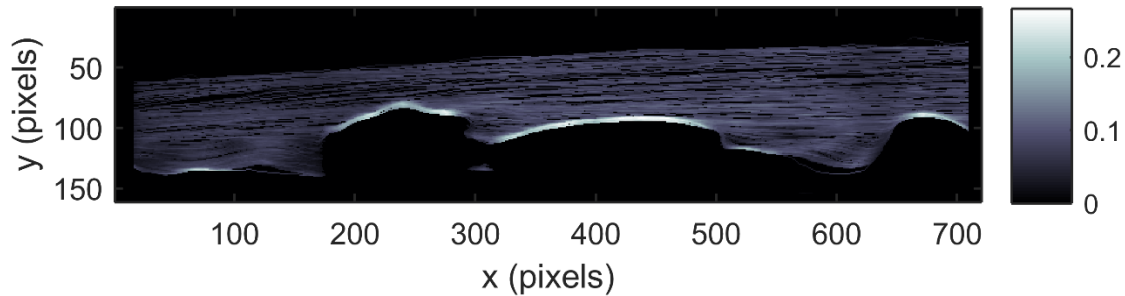
Figure 4-16. The positions of all laser lines (551) in image coordinate that are used to fine sediment bed level and erosion rates, Δt = 0.24s.

Figure 4-17 shows the temporal evolution of fine sediment bed level of the fine sediment deposit above and in the gravel roughness elements estimated based on the position of laser line positions extracted at Δt = 12 seconds for a duration of t = 0 -132 seconds. Figure 4-17 also shows that there is no any net deposition along the measurement section since no net increase in bed level is noticed. However, it is evident that the fine sediment bed level at the upstream end of the measurement section is lower than that of the level at the downstream section. This is due to the depletion of the fine sediment deposit at the upstream section by the water current coming from upstream before uniform flow condition is achieved.
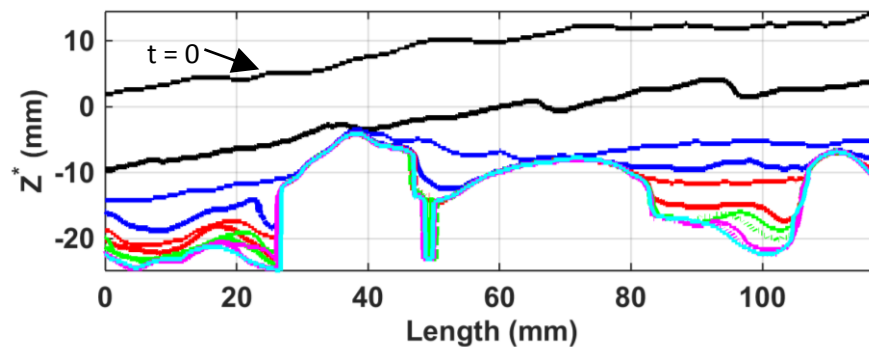
Figure 4-17. The temporal evolution of fine sediment bed level during the course of erosion (t = 0 - 132 seconds, Δt = 12s)

Thus the initial level of fine sediments along the measurement section is unequal when fine sediment bed level measurement commence. Figure 4-18 shows the fine sediment bed level measured at a selected section (at 104mm in the control section) along Plane 1, Δt = 6.0s, as fine sediment erosion progresses. A sub-millimetre change in fine sediment bed level can be captured and measurements can be acquired up to a depth below the bottom of the interfacial sublayer. This shows that the method is very efficient to

monitor small changes in fine sediment bed level and acquire erosion rate with in the gravel roughness elements.
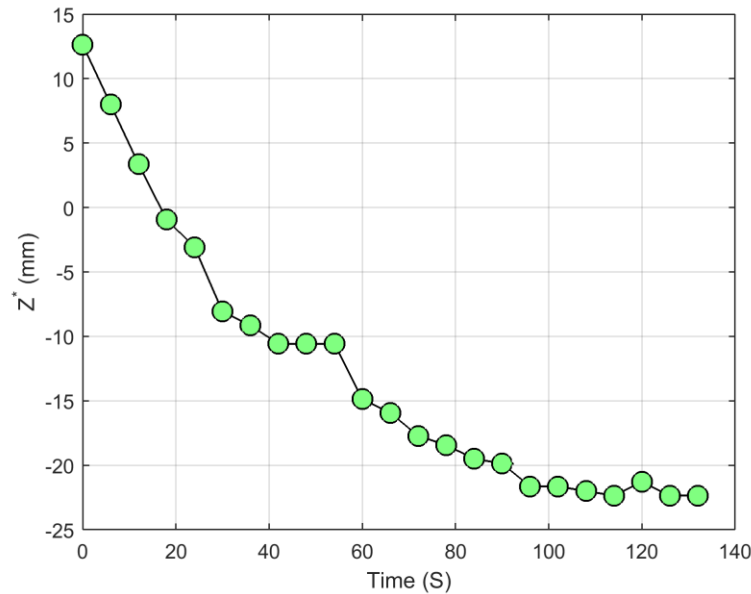
Figure 4-18. The temporal evolution of fine sediment bed level taken at section where length = 104 mm

4.6. VALIDATION OF THE METHOD

The accurate extraction of the laser line is essential to estimate the correct position of the fine sediment bed level within the roughness elements (gravel bed). Thus, it is important to verify whether the laser lines are precisely extracted and their positions are well reproduced with independent data. Gravel surface elevation data from the laser scanner (shown in Figure 3-35 and Figure 4-4) is available as an independent set of data whether elevation profiles of the laser line could reproduce the elevation variations among the roughness elements. Figure 4-19 shows the gravel surface elevation profile along Plane 1 extracted from the laser scanner gravel surface elevation data shown in Figure 4-4. A profile of the measurement section is extracted from image of the laser line taken when the fine sediment bed level in the roughness elements is negligible as shown in Figure 4-20. Estimating the vertical displacement between a known reference point R_1 (blue line) (Figure 4-20) and laser line projected on the surface of the gravel roughness elements (Figure 4-20) enables estimating the gravel surface elevation along the measurement section (in blue box, Figure 4-19). In Figure 4-21 shows a horizontal line through R_1, y = 111pixels is a reference line whose elevation is known (Z = 65.08mm) while the other line is the laser line extracted from the image shown in RGB (Figure 4-20). The elevation along the laser line in Figure 4-21 is computed by extracting the

vertical displacement between the reference line and the laser line. In Figure 4-22 an extracted vertical profile of laser scanned gravel surface elevation data (blue line) is compared with a vertical elevation profile extracted based on laser line method (black line). The root mean square error between the two profiles is 2.76mm. The laser line method captures very small details of gravel surface elevation profile due to high vertical and horizontal resolution. For instance, at x = 73 mm (x = 300 pixels) the depressions between two gravel particles are not captured by the laser scanner. However, the laser line method preserves small details that are not captured (e.g. depressions between gravels) by laser scanner profile.
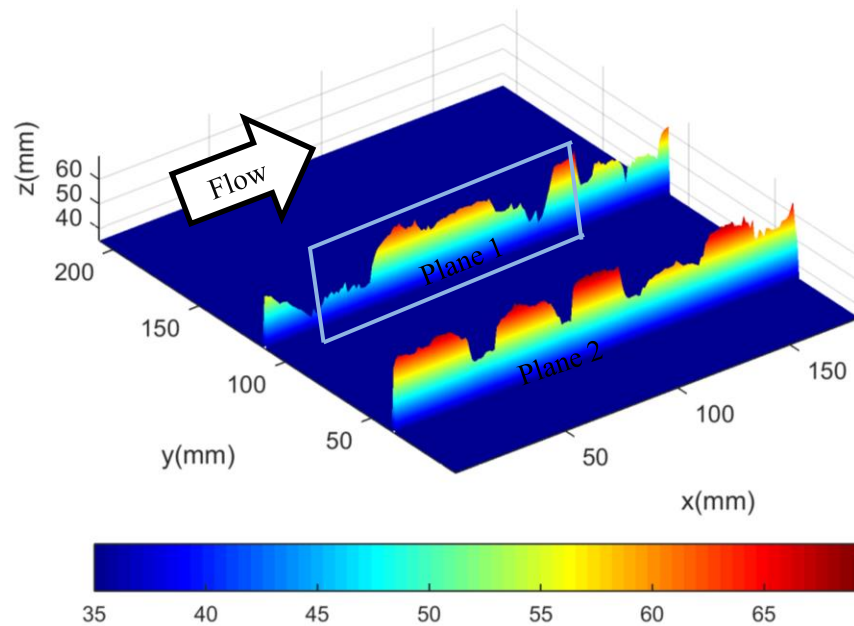
Figure 4-19. The 3-D view of laser scanned surface elevation profile of gravel along Plane 1 of the control section: Plane 2 is selected for additional fine sediment erosion measurements
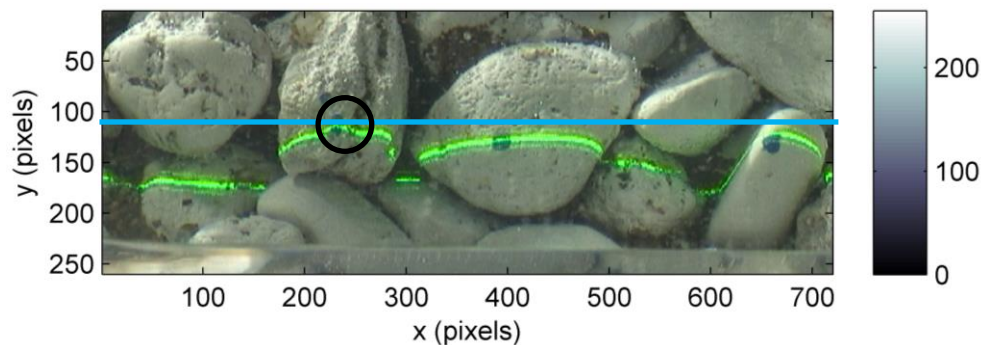
Figure 4-20. The image of projected laser line used to construct gravel surface elevation profile along Plane 1
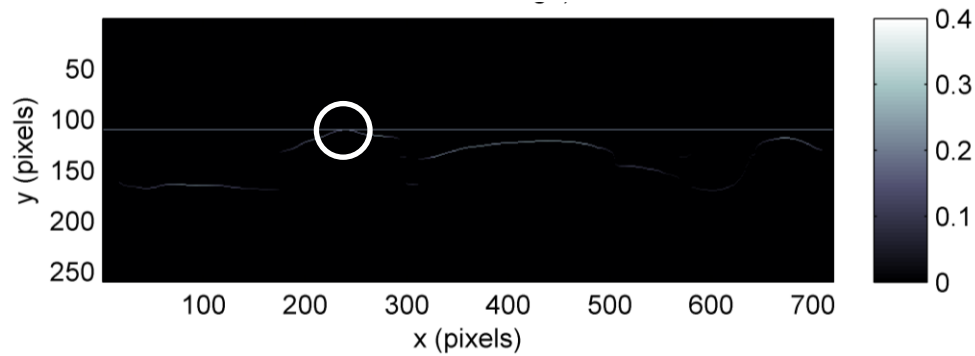
Figure 4-21. The extracted laser line of gravel surface elevation following the procedures in Figure 4-7
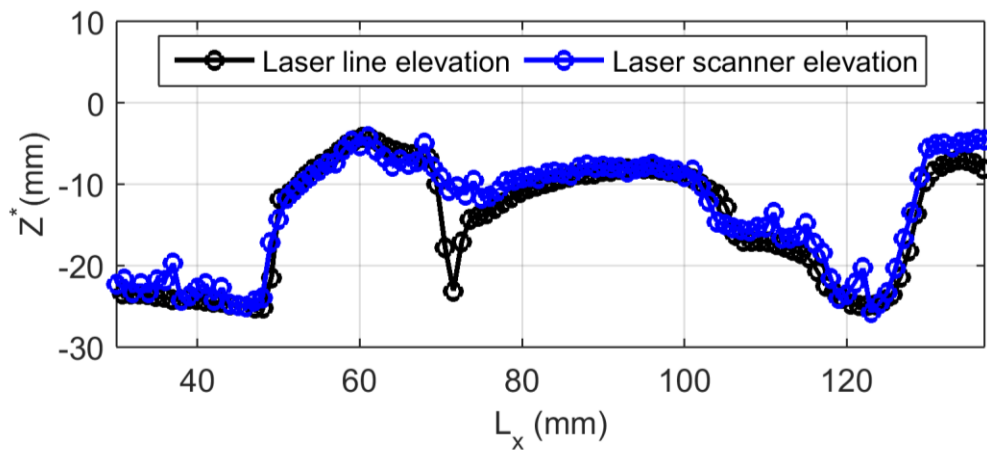
Figure 4-22. The comparison between surface elevation profiles by laser scanner and laser line method

4.7. ESTIMATION OF DEPTH AND RATE OF EROSION

4.7.1.   Estimation of depth of erosion in gravel roughness elements

In order to estimate the depth of erosion, first, the mean of fine sediment bed levels in the measurement section (estimates at each pixel along the laser line) was estimated (Figure 4-16). The result is mean fine sediment bed level referenced to gravel surface elevations given in mm (Figure 4-23). The mean fine sediment bed level is computed only by averaging fine sediment bed levels (pixel values along the laser line) where progressive changes in fine sediment bed level were observed. For instance, in situations when the laser line is below gravel crest averaging is done only in regions of fine sediment erosion thus regions of gravel protrusions are excluded in the averaging process. The regions of gravel surfaces along the laser line are identified using a simple approach. The image coordinates of the laser line along the gravel bed with no fine sediments is taken as a reference image (Figure B-3 and Figure B-4 in Appendix

B). If the difference in pixel coordinates along the laser lines of an image under consideration and the reference image is 0 or 1 or -1 that pixel is considered gravel surface. This procedure allows estimating the projected length of gravel and fine sediment bed along each laser line. The total projected length of the laser line is 117.76 mm i.e. the projected length of the measurement section. Figure 4-28 (green circles) shows the proportion of projected length of fine sediment deposit plotted at each mean fine sediment bed level (Δt = 6.00 seconds), which is indirectly the measure of the proportion of void spaces among the gravel roughness elements.
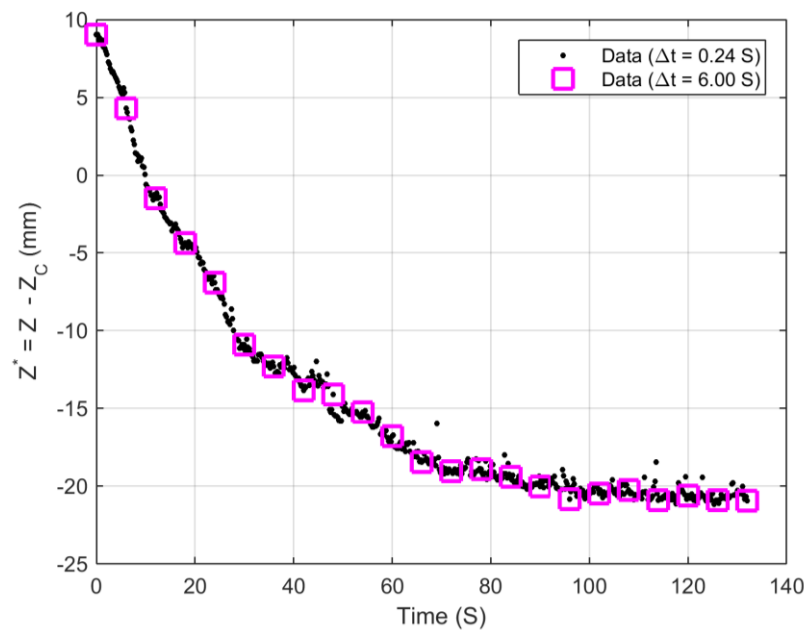
Figure 4-23. The temporal evolution of mean fine sediment bed level at different time steps for Δt = 0.24 and 6.00 seconds

The depth of erosion is estimated as the difference between pairs of mean fine sediment bed levels (shown in Figure 4-24) observed at 't' and 't + Δt'. In Figure 4-24 computed depth of erosion based on mean sand elevation measured at Δt = 0.24 (in green) seconds and Δt = 6 seconds (in black). There is no any significant trend in the depth of erosion estimated from data of mean fine sediment bed level for Δt= 0.24s and it shows very irregular pattern even though mean fine sediment bed level shows a decreasing trend in time (see Figure 4-23). The time resolution, Δt = 0.24s, is too small to capture any significant change in mean fine sediment bed level and thus the actual signal can be obscured due to measurement accuracy which is in the range of 0.36-1.1 mm.
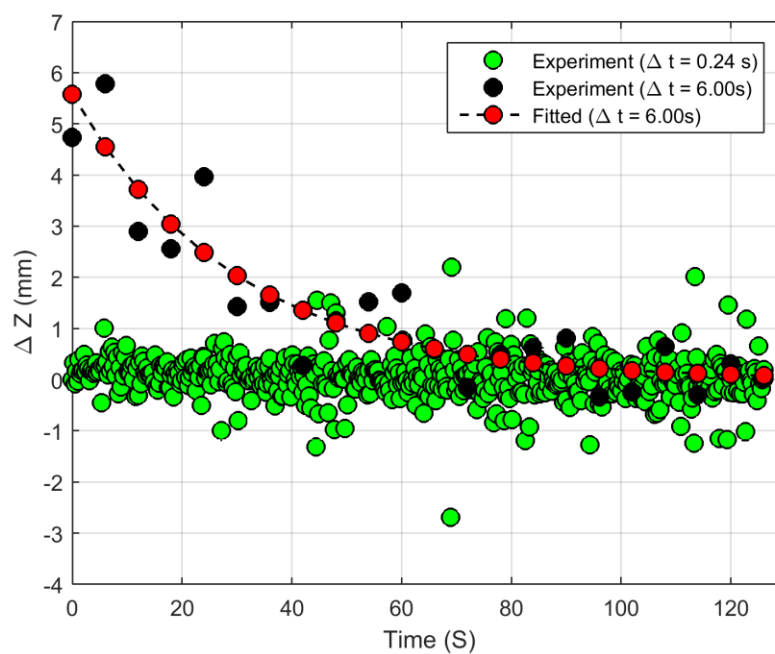
Figure 4-24. The temporal evolution of depth of erosion estimated by using mean fine sediment bed level (black and green circles) and estimated based on exponentially fitted fine sediment bed level (broken line)
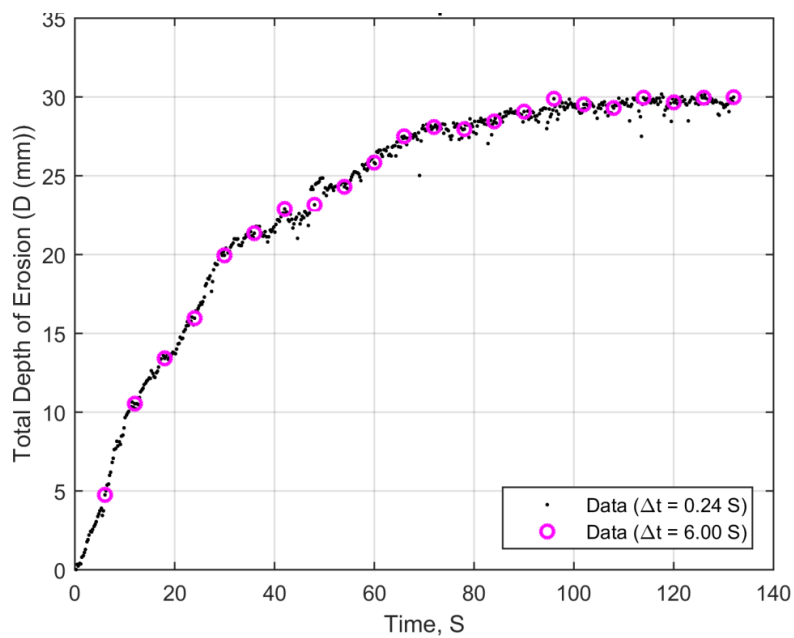
Figure 4-25. The temporal evolution of cumulative depth of erosion estimated by using mean fine sediment bed level that shows the maximum depth of erosion

Theoretically the depth of erosion should decrease as the mean fine sediment bed level goes below the gravel crest. However, when mean fine sediment bed level sampled at $\Delta t = 6s$ was used (shown in black circles Figure 4-24) the irregularity diminished and a clear decreasing trend of erosion depth is observed. Lest, some measurement details of the erosion depth may also be lost although assumed negligible in this case. To avoid the irregularity of the estimated depth of erosion a realistic empirical relation can also be fitted to the measured mean fine sediment bed level. However, finding a physically sound mathematical function is not very simple. An exponential function is widely used to predict the time evolution of scour phenomena at bed sills (e.g. Gaudio and Marion, 2003) which is a physical process that resembles the erosion of fine sediments in the present study.

The cumulative or total depth of erosion is also calculated by summation of the estimated erosion depths. Figure 4-25 shows the total depth of erosion observed over time (t = 0 to 132 seconds) estimated from mean sand level data of $\Delta t = 0.24$ (in black) and $\Delta t = 6.0$ (in pink). It indicates the maximum depth of erosion at the end of the experimental run where no change in fine sediment bed level is noticed after t =100s. The total depth of erosion below gravel crest is $D_{max} = 19.45$ mm (computed from t = 18 to 132 seconds) which is somehow correlated well, although is a bit larger, with the thickness of the interfacial sub-layer, 17mm.

4.7.2.   Estimation of erosion rate in gravel roughness elements

The erosion rate (E, mm/s) is estimated as the ratio of the difference between a pair of mean fine sediment bed level (ΔZ) multiplied by (1- λ) where λ = sand porosity and the time step (Δt) which has to be described at a reference fine sediment bed level and is computed as the average of the pairs. This approach to estimate erosion or pickup rate is reliable (e.g. Okayasu et al., 2011). In the present study, since the depth of erosion estimated based mean fine sediment bed level is scattered (Figure 4-24) , it is decided to fit the mean sand level data with a mathematical relation before computing E. An exponential function has been implemented after normalizing the mean fine sediment bed level by Z_{min} (minimum mean fine sediment bed level) and d_g. The exponential function takes a form: $z = ae^{bt}$ where $z = (Z^* - Z_{min})/d_g$ and *a (=1.06)* and *b (= -0.03)*. Figure 4-26 shows the raw and fitted data of mean fine sediment bed level sampled at $\Delta t = 0.24s$ and 6.0s. The exponential function fits both datasets with large $R^2 = 0.98$ thus capturing the temporal trend. The fitted data of $\Delta t = 6.0s$ is then used to estimate the erosion rate. Figure 4-24 shows the depth of erosion estimate based on raw experimental data (black circles) and fitted data (red circles) of mean fine sediment bed level. The plot with a broken line shows the depth of erosion estimated based on fitted data and captures the estimate form the raw data (black

circles). The plot also shows that the depth of erosion decreases from starting above the gravel crest to the bottom of the interfacial sub-layer.
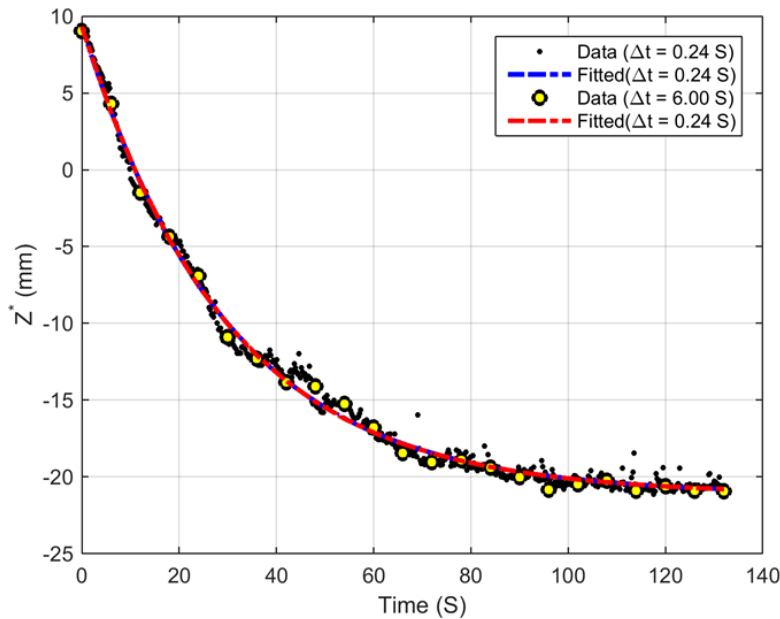
Figure 4-26. The plot of experimental and exponentially fitted temporal evolution of mean fine sediment bed level data

Figure 4-27 shows the vertical profile of erosion rate computed using raw (green) and fitted (yellow) mean fine sediment bed level. The erosion rate decreases from the gravel crest to the bottom of the interfacial sublayer linearly. Figure 4-28 shows the roughness geometric function Φ (z) (black diamonds) and the proportion of length of fine sediment deposit (green circles) at each mean fine sediment bed level. The decrease in the proportion of projected length of fine sediments follows the porosity profile until it reaches the bottom of the roughness layer. No change in the proportion of the projected length of the fine sediment deposit is noticed and remains at a value of 0.312 and $\Phi = 0.3243$ (blue arrow in Figure 4-28). This shows that the proportion of the projected length of fine sediment deposit could predict the vertical profile of gravel porosity as well as the bottom of interfacial sublayer and can be considered alternative way of validating the measurement method. Nevertheless, the spatial heterogeneity of porosity cannot be strictly predicted by this approach. In later sections, repeated measurement of erosion rate at another control section is presented.
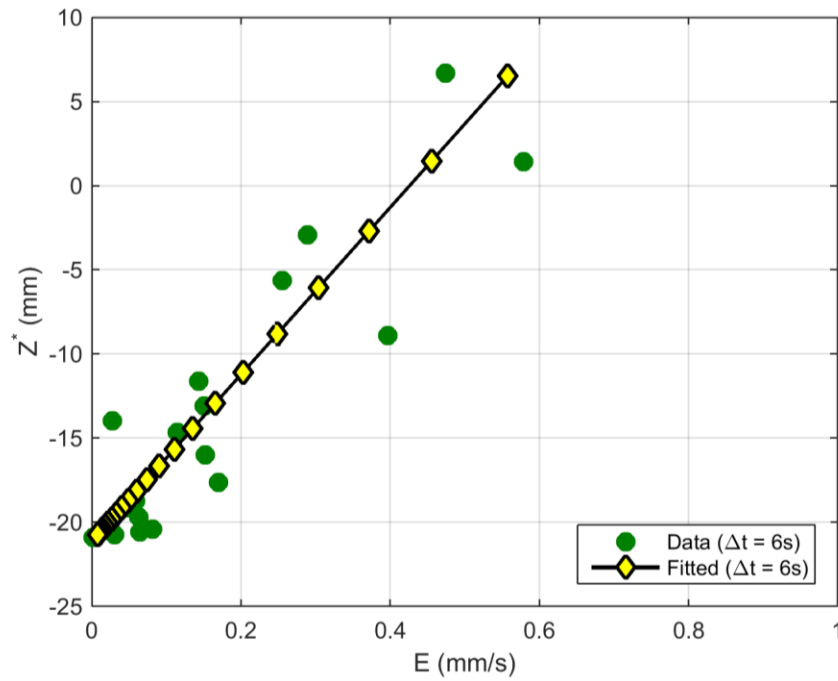
Figure 4-27. The vertical profile of erosion rate, *E* in the interfacial layer of the gravel bed
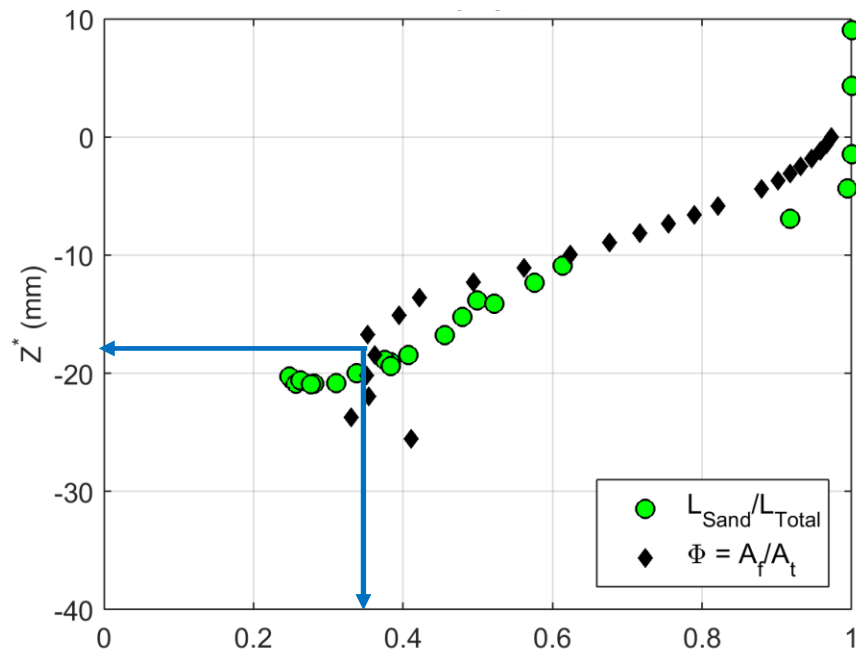
Figure 4-28. The proportion of the projected length of fine sediment deposit and bed porosity (roughness geometric function) computed at mean fine sediment bed level

4.7.3. Estimating spatially averaged Erosion Rate in gravel roughness elements

In order to capture the spatial heterogeneity of erosion rate additional measurement of fine sediment erosion was conducted at Plane 2 at y = 37 mm, as large as *3d$_g$* away from Plane 1(see Figure 4-19). The measurement of erosion rate at Plane 2 is observed for duration of 32 seconds as the fine sediments depleted in very short period of time. The images are sampled every Δt = 0.27 seconds and the mean fine sediment bed level is computed following procedures described for Plane1. The erosion depth calculated using mean fine sediment bed level data acquired at Δt = 0.27 seconds showed no distinct trend as in the case of Plane 1. Thus, erosion rate is estimated based on exponentially fitted mean fine sediment bed level extracted every Δt = 4.0 seconds where the exponential function fitted with coefficient of determination, R^2 = 0.87. Figure 4-29 shows the experimental and the fitted data of mean fine sediment bed level where the exponential function takes a form: $z = ae^{bt}$ where z = normalized mean fine sediment bed level and *a (= 0.67)* and *b (= -0.1)* are exponential coefficients.
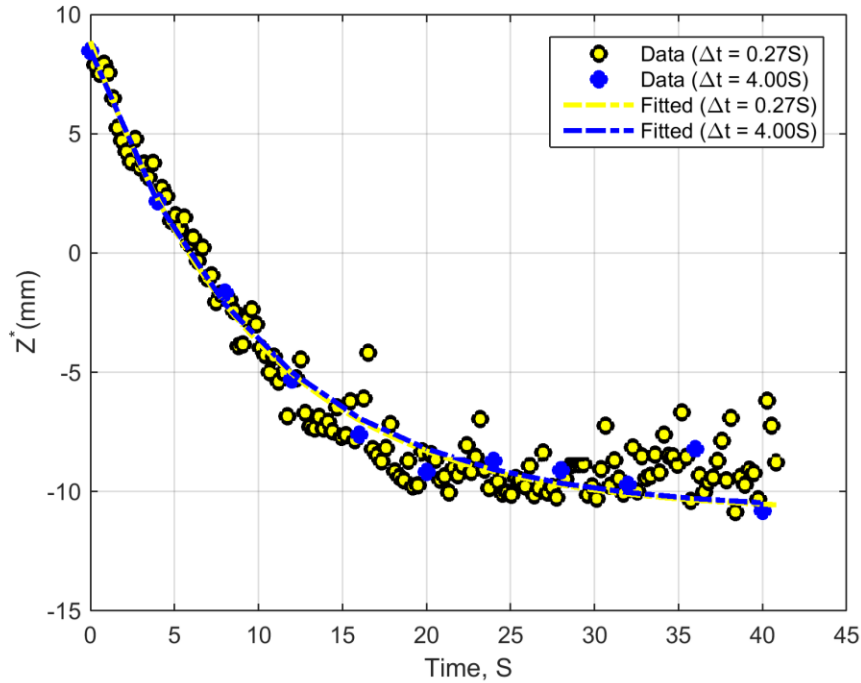
Figure 4-29. The plot of experimental and exponentially fitted temporal evolution of mean fine sediment bed level data (Plane 2)

Figure 4-30 (in circles) shows the vertical profile of erosion rate measured along Plane 2 where there is a clear linear decrease in estimated erosion rate with depth. The spatially averaged erosion rate above and below gravel crest were estimated by averaging the vertical profiles of erosion rate measured along P1 and P2 which correspond to the same mean fine sediment bed level. Figure 4-30 show the vertical profiles

of erosion rates measured at Plane 1, Plane 2 and the spatially averaged erosion profile estimated from fitted data of mean fines sediment bed level. The figure shows that high erosion rate is observed along Plane 2, both below and above gravel crest, which has relatively different gravel bed arrangement.
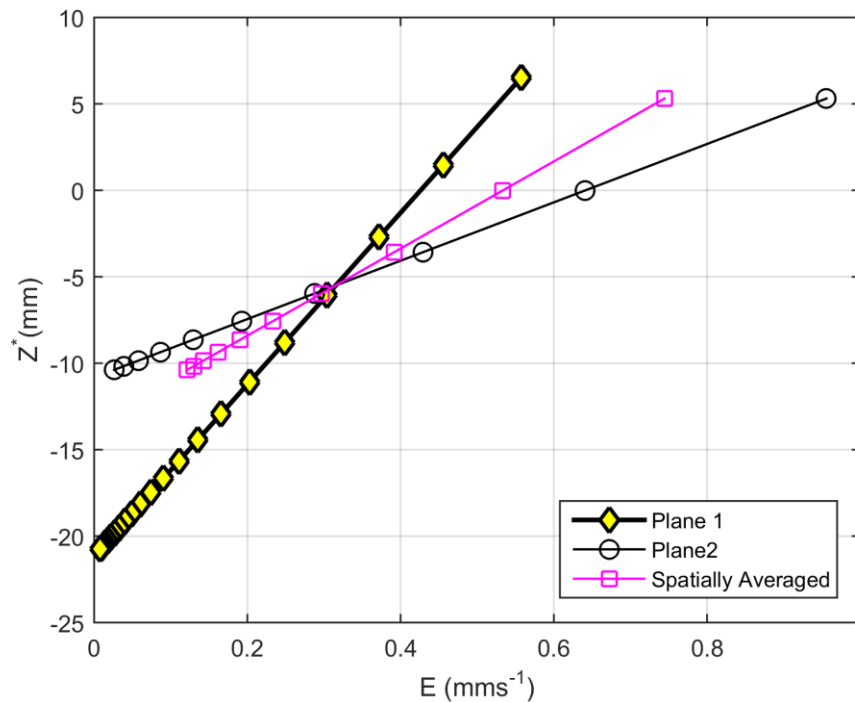
Figure 4-30. Spatially averaged erosion rate in the interfacial layer of the gravel bed estimated based on fitted fine sediment bed level data

4.8. CONCLUSIONS

In this chapter results from a development of a new method to measure fine sediment erosion rate and bed evolution in laboratory experiment of suspended transport in immobile coarse bed are presented. The method applies single laser light sensor, video camera and reflective mirror. Erosion rate and bed evolution by non-equilibrium suspended transport can be measured with a resolution lower than the grain size of particles eroded from the bed. The important advantage is that the measurement method can be used to monitor rapid fine sediment erosion under running water that avoids stop and run approach common in laboratory measurements of bed evolution. The method also enables direct monitoring the rate of fine sediment erosion at various fine sediment bed level within the interfacial sublayer of the immobile roughness elements. The method can be of significant use to monitor rapid bed evolution such as dam-break analysis at laboratory scale. Many studies focused on equilibrium transport of suspended sediment

where measurement of near bed sediment concentration is widely used to estimate erosion rate. The present method allows direct measurement of fine sediment erosion rate in immobile bed by suspended transport. The method is validated based on surface elevation data obtained by laser scanner and superior agreement was noted between laser scanner data and the proposed method. The present methodology can be used, at lowest cost, to collect accurate, non-intrusive and continuous measurements of bed evolution and fine sediment erosion rate. The use of multi-line laser sensors is expected to improve the estimation of, especially, spatially averaged rate of sediment erosion in immobile coarse bed conditions. The image processing procedures developed to extract the laser lines are very efficient for complex target surface geometry and could have application beyond the present study. The method can be easily applied for multi-line laser configurations which could improve the spatial coverage of measurements.

5. FINE SEDIMENT EROSION RATE AND DYNAMICS IN IMMOBILE GRAVEL BED: EXPERIMENTAL RESULTS

Summary

The transport of fine sediments in coarse immobile bed condition is a common phenomenon in many rivers under natural conditions and also downstream of dams during activities such as sediment flushing, dam removal and sediment bypassing. The entrainment, transport and deposition of fine sediments (suspended) in immobile coarse bed are very crucial for the stability of channel morphology and habitats of aquatic life. Thus, proper understanding of the dynamics of fine sediment erosion and entrainment in immobile coarse bed is essential for planning management activities. Particularly, the erosion or entrainment of fine sediments in non-equilibrium suspended transport condition is poorly understood although such transport conditions could often occur during sediment flushing operations. A series of experiments are conducted to characterize fine sediment erosion in immobile gravel bed in non-equilibrium suspension transport. The results from erosion rate measurements are applied to describe profile of erosion rate and its spatial heterogeneity in immobile gravel bed. The effect of fine sediment level in the gravel roughness elements on fine sediment erosion rate and its relation with gravel bed flow structure is discussed. The erosion rate measurements are also used to develop a new relation for fine sediment erosion rate in immobile gravel bed to be used. The development of such relations is useful for the developing a numerical model to study fine sediment dynamics of sediment flushing.

5.1. INTRODUCTION

The transport of fine sediments in fluvial systems is an important component of the morphological and ecological states of many rivers. The largest components of total sediment transported by many rivers are fine sediments (Meade et al., 1990) and the supply of fine of sediments in rivers, especially in Alpine rivers, is even expected to increase significantly (Asselman et al., 2003). The transport of fine sediments is not limited only in alluvial rivers with sand beds but also in many of gravel and cobble bed rivers particularly in the form of suspension. For instance, in natural rivers such as mountain and Canyon Rivers whose bed consists of coarse bed (e.g. Wohl, 2000) that are transported in rare events and most of the sediments passing trough are fine sediments (Grams and Wilcock, 2014). Moreover, in many rivers the sediment load comprises largely fine sediments and a decrease in fine sediment supply relative to transport capacity could lead to parts of underlying bed substrate become exposed and transport occurs over a bed that consists partially of fine sediment and partially of large immobile particles (e.g. Kleinhans et al., 2002). During flushing operations, sediment-bypassing and dam removal large quantity of fine

grained sediments are also introduced downstream. In such occasions the released fine sediments are also transported in the immobile coarse bed (e.g. Wren et al., 2011) since the channel bed downstream of dams are usually deprived of sediment supply and suffers from continuous erosion of the channel bed that leaves only coarser and immobile beds, which is often called an armoured bed (Kondolf, 1997). The transport, entrainment and deposition of fine sediments in immobile coarse bed such as gravel bed are also important for the stability of habitats and survival of aquatic species such as salmonid fisheries (e.g. Nelson et al., 1987; Lisle and Lewis, 1992). Therefore, there is a need, for better understanding of fine sediment transport processes in immobile bed and relations that could be implemented in numerical models to predict fine sediment transport in coarse immobile beds. Many of existing relations and theories of fine sediment transport are developed for conditions in which the bed material and the transported load are the same which are not usually applicable and cannot be easily transferable to cases where fine sediments are transported in coarse immobile beds (e.g. Grams and Wilcock, 2013). In recent years few studies have been reported that focused on understanding the flow hydrodynamics and transport processes in immobile coarse beds (e.g. Kuhnle et al., 2013; Grams and Wilcock, 2007; Grams and Wilcock, 2013; Wren et al., 2014; Wren et al., 2011). However, the dynamics of fine sediment erosion and entrainment in immobile coarse bed yet lack full understanding and need detailed studies. Particularly, the erosion or entrainment of fine sediments in non-equilibrium suspended transport condition is poorly understood although such transport conditions could often occur during sediment flushing operations. The main aims in this study are to describe series of laboratory experiments that were conducted to investigate non-equilibrium fine sediment erosion rate in immobile gravel bed and develop a pick-up type erosion rate formula from the experimental datasets and analysis of flow characteristics in gravel bed.

5.2. THEORY OF FINE SEDIMENT EROSION/ENTRAINMENT

The mechanism of fine sediment erosion, entrainment and transport in immobile coarse beds such as gravels has become a subject of study in the last few years (e.g. Grams and Wilcock, 2007; Pellachini, 2011). The entrainment of non-cohesive fine sediments in immobile coarse bed depends on the surface exposure of the fine sediments in the coarse bed (Grams and Wilcock, 2007; 2014), fraction (availability or abundance) of the fine sediments in the bed (Einstein and Chien ,1953;Grams and Wilcock, 2007; 2014), the elevation of the fine sediment layer relative to the elevation of the coarse immobile bed (Garcia and Parker, 1991; Grams and Wilcock, 2007, 2014), and the interactions of the flow, the fine sediments and the immobile coarse grains in the variable roughness bed (Kuhnle et al. 2013). In very recent works (e.g. Pellachini, 2011; Khunle et al., 2013 ; Wren et al., 2014) it is shown that the surface exposure of the fine sediments and the effective shear stress at a given sand elevation in the immobile bed roughness

elements could be scaled with its bed porosity. Figure 5-1 shows the different complex processes that derive fine sediment entrainment in immobile bed.
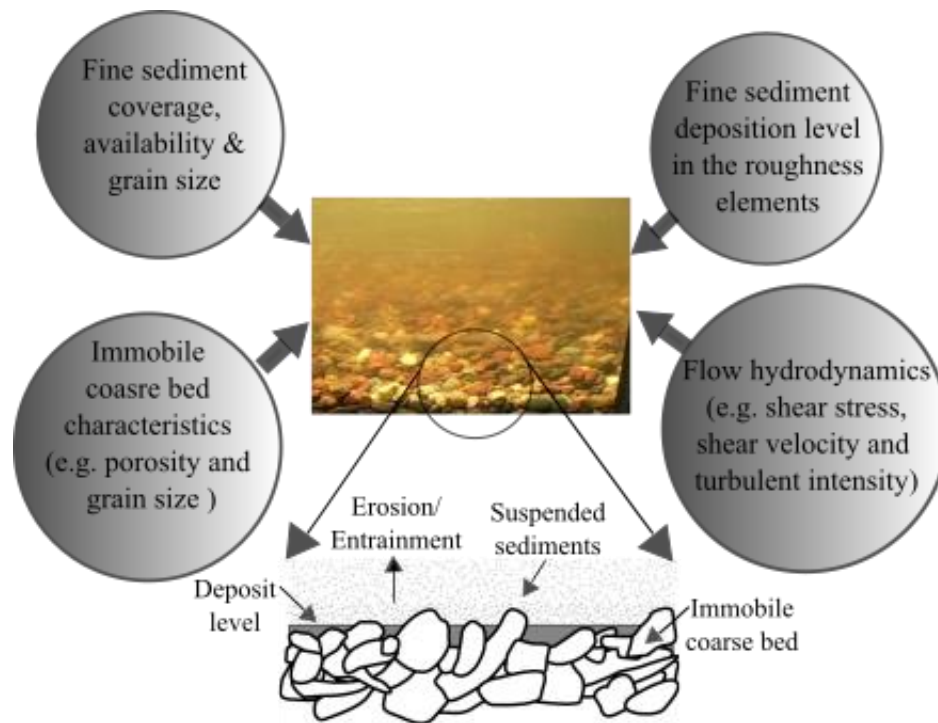
Figure 5-1. Drivers of fine sediment transport and entrainment in coarse immobile bed

In general, it is believed that, the entrainment (erosion) and transport of the fine sediments in the interstices of immobile coarse bed could be affected by two contrasting processes. While the fine sediments in the interstices of the gravel may be shielded from the shear stress of the flow (e.g. Kuhnle et al., 2013; Garcia and Parker, 1991), the local perturbations of the flow caused by the immobile gravel bed may also increase the shear stress on the interstitial fine sediments (e.g. Grams and Wilcock, 2007). On the one hand, the sand elevation with respect to the immobile coarse bed could reduce the entrainment or erosion rate by hiding effect exerted by the coarse immobile bed (e.g. Garcia and Parker, 1991). On the other hand, the turbulent wakes shed by the large coarse immobile bed could enhance local scour causing erosion of the fine sediments when flow separation occurs over the roughness elements. For instance, Nickling and McKenna Neuman (1995) reported enhanced entrainment in wind-tunnel experiments involving the emergence of large roughness elements in a deflating sand bed. The elevated transport rate was evident when the roughness elements were initially exposed and increased turbulence by emerging surface roughness. However, as the sand bed elevation continued to decrease a rapid transition from enhanced transport to extremely low transport rates was observed since all of the available bed shear stress was consumed by form drag on the bed roughness elements. Similar phenomena are reported in

open channel flows where emerging immobile bed roughness exert form drag that could result in reduction of shear stress available for fine sediment entrainment or erosion (e.g. Kuhnle et al., 2013; Wren et al., 2014; Papanicolaou et al., 2011).

5.3.FLOW CHARACTERISTICS IN GRAVEL BED

The flow structure in immobile rough bed is very important in modulating the entrainment and transport of fine sediments (Sambrook and Smith, 2005; Papanicolaeou et al.2011; Wren et al., 2011), mainly due to spatial variability of flow characteristics in near bed region and also due to secondary currents created by immobile obstacles (e.g. Nezu and Nakagawa, 1993). The turbulent bursting phenomenon is one of the factors that control sediment entrainment and the frequency of occurrence and magnitude of such events depends on the spatial organization of the roughness elements (Papanicolaou et al., 2001). Moreover, the erosion and transport of fine sediments in immobile gravel bed is further complicated by continuous modification of the bed geometry by the fine sediments in interstices of the immobile bed that eventually affect the flow structure and shear stress distribution (e.g. Kuhnle et al., 2013; Wren et al., 2011;Sambrook-Smith and Nicholas, 2005). The total drag force by the roughness elements controls the shear available for sediment erosion in the interstices of the roughness elements. Thus, as a first step, characterizing the shear stress profile in immobile clean gravel bed is essential to conceptualize the shear stress available for fine sediments below gravel crest. In this section, the theory of bed shear stress distribution and geometric properties of the roughness elements in gravel bed flow are discussed and some experimental datasets are presented and analysed to relate its implication for fine sediment erosion and transport. A case of two dimensional, steady, uniform and turbulent open channel flow conditions in immobile gravel bed is considered. For these flow conditions, the double averaged momentum equation in the stream-wise direction is given as (e.g. Nikora et al., 2007):

$$\rho g S_o \phi(z) + \frac{\partial \phi(z)\tau_t(z)}{\partial z} = \phi(z) f_d(z) \tag{5-1}$$

where

$$\tau_t(z) = \rho \left\langle \nu \frac{\partial \bar{u}}{\partial z} \right\rangle (z) - \rho \left\langle \overline{u'w'} \right\rangle (z) - \rho \left\langle \overline{\tilde{u}\tilde{w}} \right\rangle (z) \tag{5-2}$$

$$f_d(z) = \frac{1}{dV_f} \iint_S \overline{p} n_x dS \tag{5-3}$$

τ_t (z) = total fluid shear stress; and f_d (z) = total form drag force exerted on a unit fluid volume (dV_f= ΦdV_0) by gravel roughness elements (or by the fluid exerts on individual roughness elements) within the averaging domain; p = fluid pressure; and n_x is the unit vector normal to the surface S of the section of bed described by the area of the averaging domain (A_o). The total fluid shear stress comprises three components: viscous, turbulent, and form-induced (or dispersive) stresses respectively as in Equation (5-2). The form induced stresses are small at greater distance from the bed and increase slightly toward gravel crests (Aberle et al., 2008). The total drag force is zero above gravel crest and can be approximated by only the drag due to pressure forces considering the viscous forces negligible or very small. Equation (5-3) can be described by flow parameters and roughness element geometric characteristics in the interfacial sublayer. The net pressure drag force, dF_d, acting on the thin section of roughness elements of the total width W and thickness dz within the averaging domain at the vertical coordinate z can be described by using a conventional quadratic drag parameterization as $dF_d= 0.5\rho C_d W dz \langle u \rangle^2$ (Nikora et al., 2004). Thus drag force per unit fluid volume is given as:

$$f_d(z) = \frac{1}{A_f} \frac{dF_d}{dz} = 0.5\rho C_D \frac{Wdz}{A_f dz} \langle u \rangle^2 = 0.5\rho C_D(z) a(z) \langle u \rangle^2 (z) \tag{5-4}$$

where F_d = total drag force per unit area; C_D = drag coefficient depending on the roughness elements shape, density, and spatial arrangements; $\langle u \rangle$ = double averaged flow velocity; Wdz = total frontal area of all the roughness elements intersected by the thin section within the averaging domain; and a = $Wdz/A_f dz$ = $Wdz/\Phi A_o dz$ = local roughness density (i.e., roughness frontal area per fluid volume); A_f = fluid area of the averaging domain. The double averaged flow velocity distribution in interfacial sub-layer of gravel bed flow is known to be approximately linear profile (e.g. Mignot et al., 2009; Nikora et al., 2001, 2004a) and a polynomial profile is also reported (e.g. Dey and Das, 2012). Experimental datasets showed that the roughness density can be described as a function of roughness geometric function (bed porosity) and mean diameter of roughness elements and increases exponentially from top to bottom of interfacial sub-layer (see in Chapter 3).

The integration of Equation (5-1), neglecting viscous shear stress, gives the longitudinal total shear stress distribution as (e.g. McLean and Nikora, 2006; Nikora et al., 2001):

$$\tau(z) = \underbrace{\rho g H S_o + \rho g S_o \int_{z_t}^{z_c} \phi(z)dz}_{Momentum-supply} = \underbrace{-\rho\phi\left\langle\overline{u'w'}\right\rangle - \rho\phi\left\langle\overline{uw}\right\rangle}_{\tau_t(z)} + \underbrace{\int_{z_t}^{z_c} \phi(z)f_d(z)dz}_{F_d(z)}$$

(5-5)

It is evident from Equation (5-5) that, in clean gravel bed, the available effective shear stress in the interstices of the roughness elements can be estimated from momentum supply if the drag force (F_d) is known and this assumption can be applied in immobile gravel bed with fine sediments which erode rapidly by suspended transport.
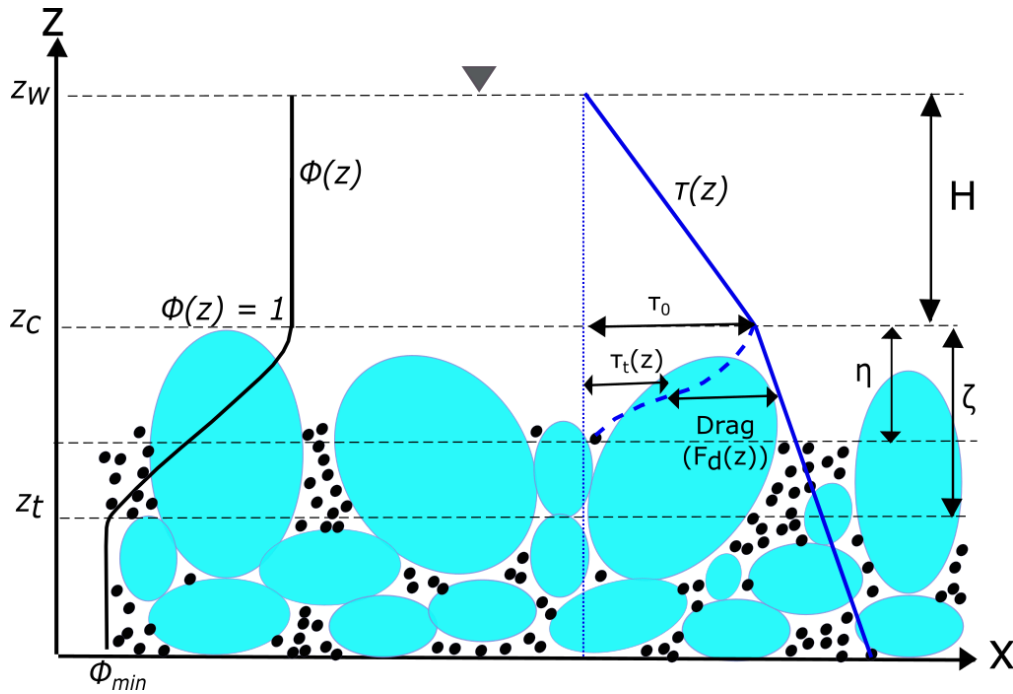
Figure 5-2. Conceptual diagram of momentum supply and fine sediment (black dots) erosion in immobile gravel bed

Figure 5-2 shows a conceptual diagram of longitudinal momentum supply between any z to free surface (z_w) (blue line), distribution of total shear stress, vertical profile of porosity Φ (roughness geometric function) and fine sediment deposition in coarse bed where η = fine sediment bed level below gravel crest and ζ = thickness of interfacial sub-layer. In the interfacial sublayer ($z_t < z < z_c$) the momentum supply is partially absorbed by the drag and partially transferred by the fluid shear stress (dashed blue line) where the momentum supply at the gravel crest is denoted by $\tau_0 = \rho g H S_o$. The shear stress responsible for fine sediment entrainment below gravel crest, $\tau_t(z)$, generally decreases from the top to the bottom of the interfacial sublayer (Figure 5-2). In contrast the total drag force (F_d) increases within the interfacial sublayer with little total shear stress left to entrain fine sediments from the coarse bed.

In this study the profiles of drag force (F_d) in the interfacial sublayer of clean immobile bed from experiments reported by Mohajeri (2014), Mignot et al. (2009) and Dey and Das (2012) are analysed. The aim is to characterize F_d based on experimental evidences and to scale shear stress in the interfacial sublayer. The reductions in bed shear stress are directly related to momentum sink by the drag force induced by roughness elements below gravel crests. Figure 5-3 shows the distribution of observed fluid shear stress, $\tau_t(z)$, and estimated total drag force, $F_d(z)$, within the interfacial sublayer of gravel bed of the three experiments. The total drag force is estimated taking the difference between the momentum supply and total fluid shear stresses. The shear stress generally shows a decreasing trend while the total drag increases and reaches to a point where it exhibits a relatively very gradual decrease and this is evident in the data of Mignot et al. (2009). It is worth nothing that the data points of the three experiments for shear stresses, in the interfacial sublayer, do not collapse but that of the total drag force do well (Figure 5-3, broken line). Moreover, despite a linear decrease in the vertical distribution of flow velocity (Figure C-8, Appendix C) in the interfacial sublayer the total drag force increases which shows that the roughness density partly derives the increasing pattern of the drag force. This study attempted to test the relationship between dimensionless drag force and the corresponding dimensionless roughness density for the three experimental runs (Figure 5-4).
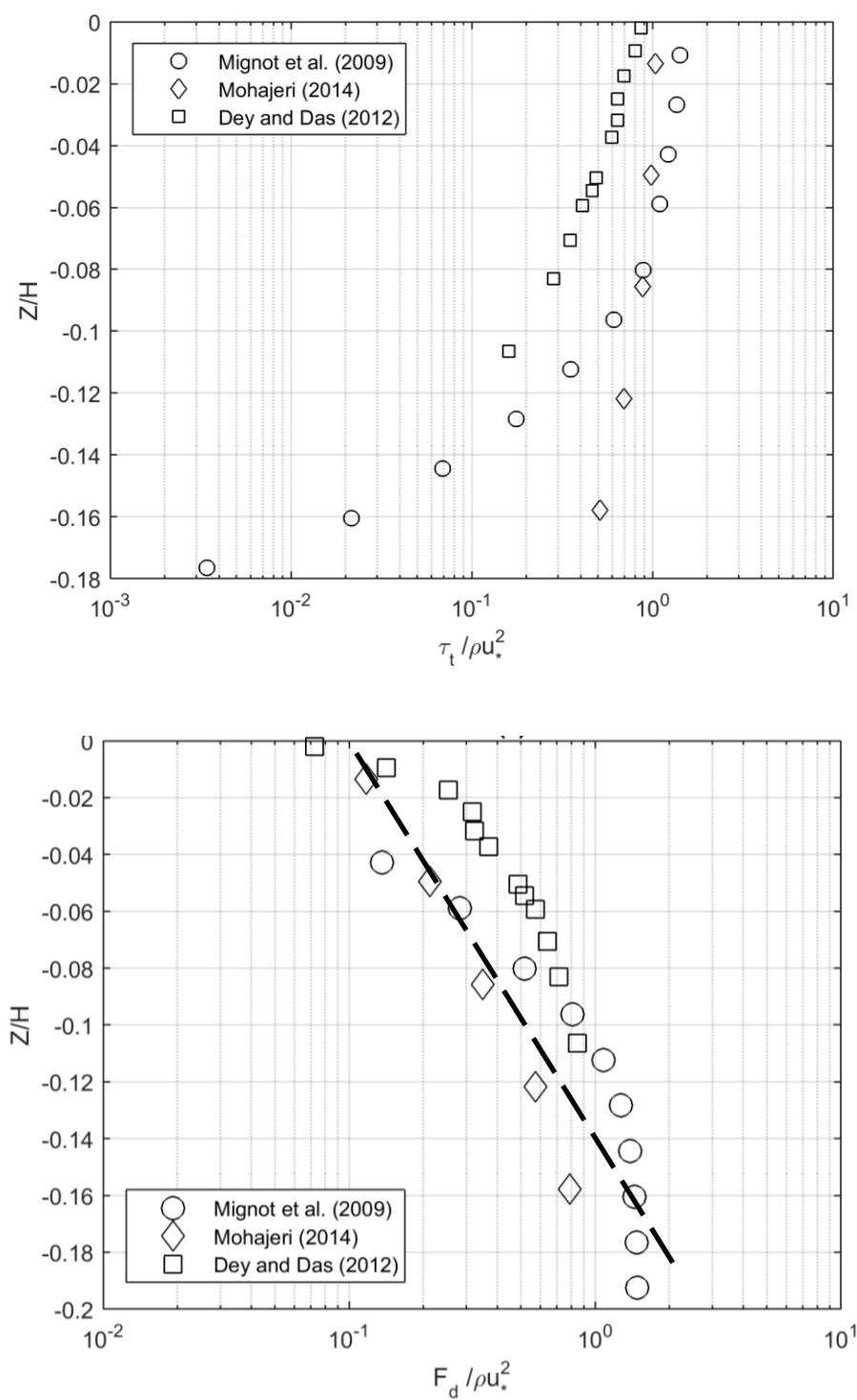
Figure 5-3. Dimensionless shear stress (top) and total drag force (bottom) distribution in roughness layer estimated from experimental data
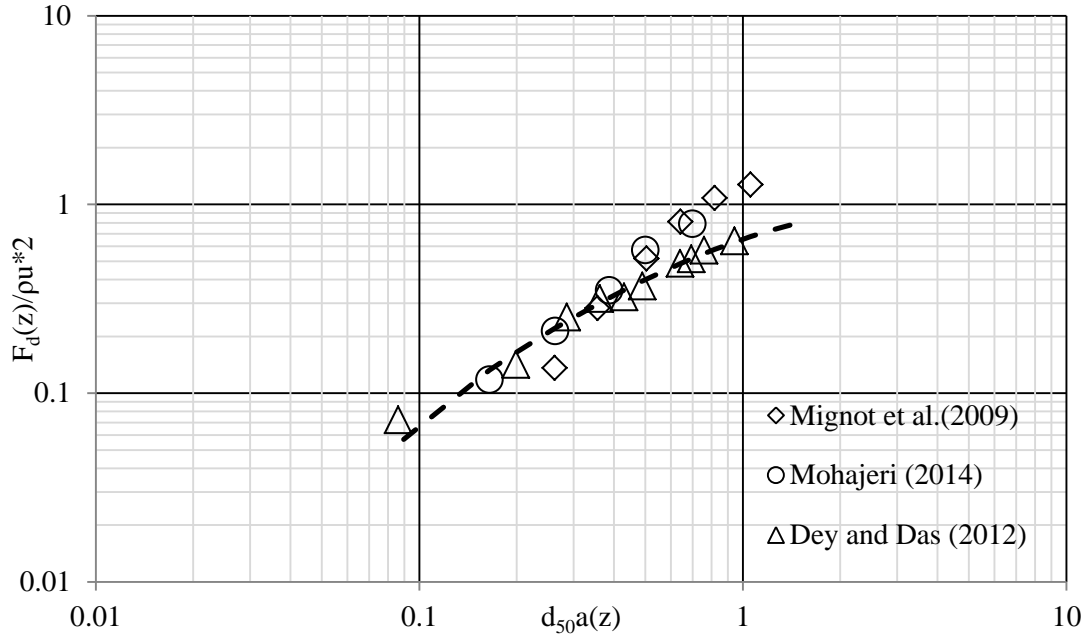
Figure 5-4. The relationship between dimensionless drag force and dimensionless roughness density below gravel crest for datasets of clean bed experiments of published research

It shows that most of the experimental data points of the three experiments collapse and thus it can be argued that a single empirical relationship can be used to scale the drag force. Thus, an empirical relation of the form shown in Equation (5-6), where c_o and c_1 are empirical coefficients, is obtained to be appropriate to scale the drag profile and by this the shear stress distribution. The broken solid line is the empirically fitted dimensionless drag force where the empirical coefficients are: $c_o = 1.014$ and $c_1 = -1.20$.

$$\frac{F_d(z)}{\rho u_*^{\,2}} = 1 - c_o e^{c_1 a(z)} \tag{5-6}$$

The effective shear stress, τ_e, available (for sediment entrainment) below gravel crest will be the difference between momentum supply minus total drag force, described by Equation (5-7), thus, given by:

$$\tau_e(z) = \tau(z) - \rho u_*^{\,2}(1 - c_o e^{c_1 a(z)}) \tag{5-7}$$
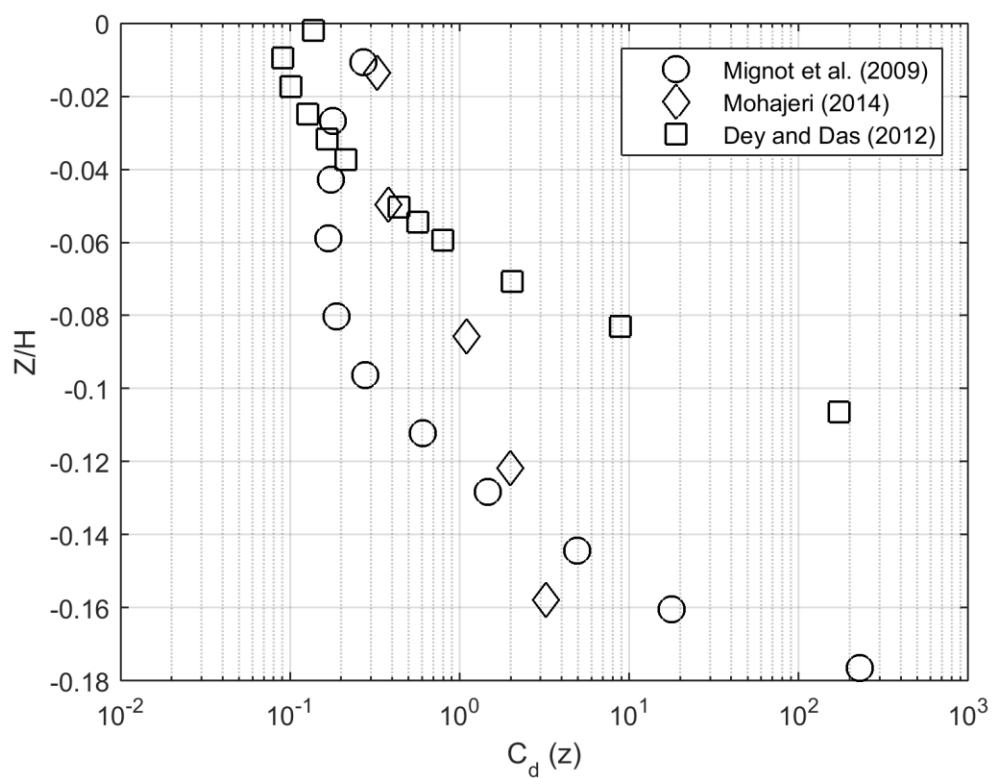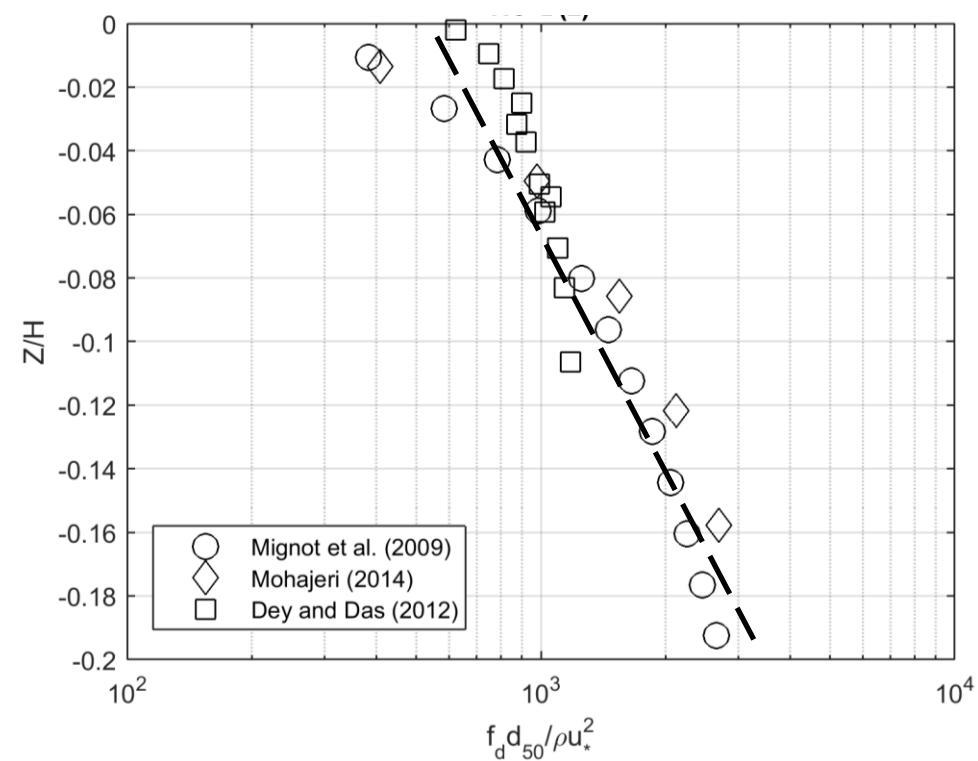
Figure 5-5. Drag force per unit volume (top) and drag coefficient (bottom) in interfacial sublayer

The drag coefficient (C_D) profile in the interfacial sublayer is also computed by solving Equation (5-4) since the total drag force, velocity profile (see Figure C-8, Appendix C) and roughness density (see Chapter 3) are known and obtained from the three experiments. First, the drag force per unit volume is computed and then the drag coefficient is estimated. Figure 5-5 (top) shows that the vertical profile of f_d, drag force per unit volume (not per fluid volume), shows decreasing trend and the estimates of each experiments collapse (along broken line) when made dimensionless (using horizontal length scale, d_{50} and ρu_*^2). The C_D also increases in the interfacial sublayer and most of the estimated values are within the experimental ranges of C_D estimated for rough beds (e.g. Schmeeckle et al., 2007). It is worth to recognize that the increasing pattern in drag force in the interfacial sublayer is not influenced by the decreasing trend of velocity profile and rather is related to the increase in the roughness density and C_D.
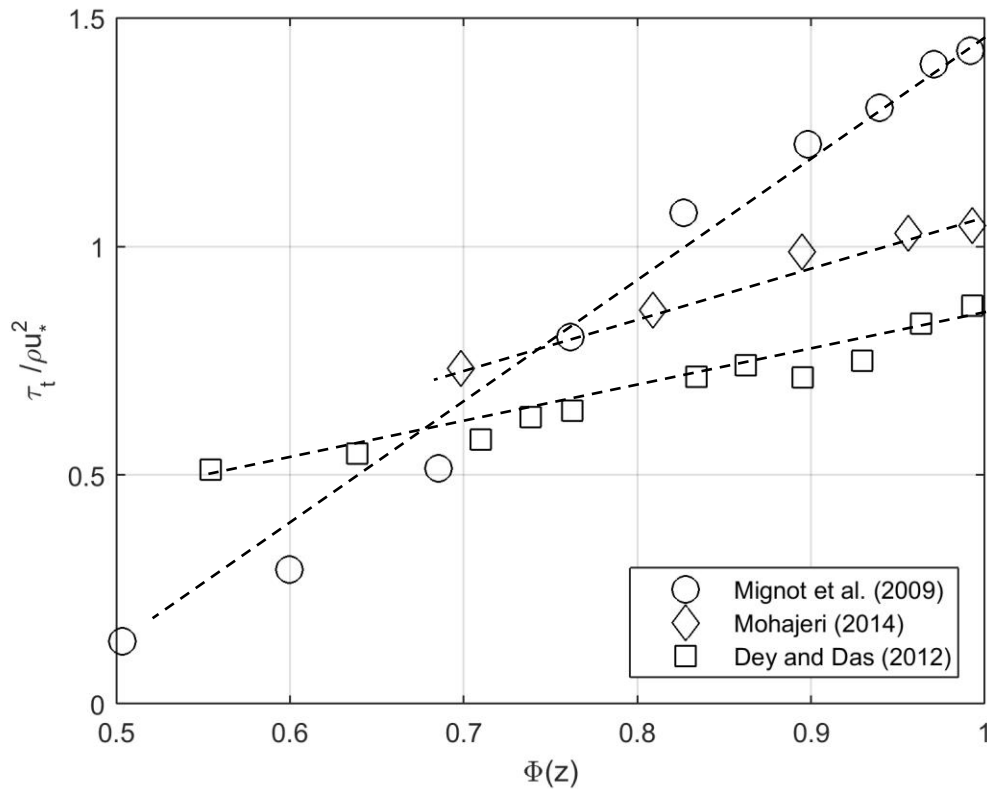
Figure 5-6. The relationship between fluid shear stress and bed porosity, Φ in interfacial sublayer

Figure 5-6 shows there is no unique relationship between porosity and fluid shear stress, in all the three experiments, although the dimensionless shear stress shows a linear increases with an increase in bed porosity. It is also worth to note that the relationship between shear stress and bed porosity seems to be

different from one experiment to another while the relationship between drag force and roughness density does not vary in the region of the interfacial sublayer. This shows that dimensionless drag force distribution from different experiments can be described by a single empirical equation.

5.4. SPATIAL CHARACTERISTICS OF FINE SEDIMENT EROSION

The hydrodynamics of gravel bed flows are strongly influenced by the spatial heterogeneity of the bed topography caused by spatial arrangement and orientations of gravel particles (Sarkar and Dey, 2010; Papanicolaou et al., 2001; Nikora et al., 2004). The spatial heterogeneity of the bed topography results in spatial heterogeneity in the flow quantities such as shear stress, flow velocity, and turbulent intensity, which control the transport of fine sediments in-among the roughness elements and/or in the interfacial sublayer. The heterogeneity in turbulence structure and characteristics could lead to heterogeneity in entrainment or erosion of fine sediments from gravel roughness elements. Here the spatial pattern of the vertical profile of erosion rate is investigated based on experimental datasets of Run IX to understand the spatial heterogeneity of erosion rate and its relation with the bed configurations of the roughness elements. In order to capture the spatial heterogeneity of erosion rate measurements were conducted along two planes (Plane 1 and 2).The vertical profiles of erosion rate are extracted at the stoss and lee side of the roughness elements at Plane1 and Plane 2. Figure 5-7 shows the sections (blue lines) at which the erosion profiles are extracted. In Figure 5-8 the temporal evolution of fine sediment bed level (left) and the estimates of the vertical profile of erosion rates (right) at C1 (stoss), C2 (lee) and C3 (stoss) of Plane 1 are plotted. In similar manner Figure 5-9 shows the temporal evolution of fine sediment bed level (left) and the estimates of the vertical profile of erosion rates (right) at C4 (stoss), C5 (intermediate), C6 (lee) and C7 (stoss) of Plane 2. The erosion rate in the roughness layer at the stoss side (C1, C3, C4 and C7) of the gravel particles is generally larger in both cases (Plane1 and Plane 2) than the estimates at the lee side (C2 and C6). The estimates of erosion rate between closely packed gravel particles (C5) shows larger erosion rate than the lee side.
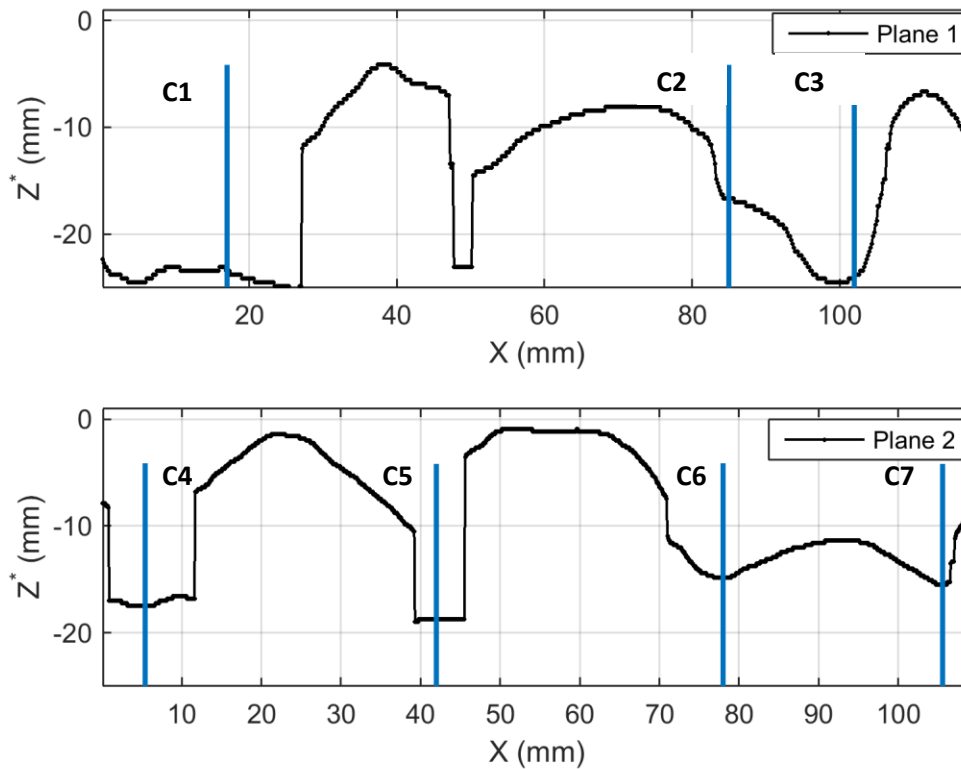
Figure 5-7. Sections (Plane 1 and Plane 2) at which erosion profiles are estimated for evaluation of spatial heterogeneity
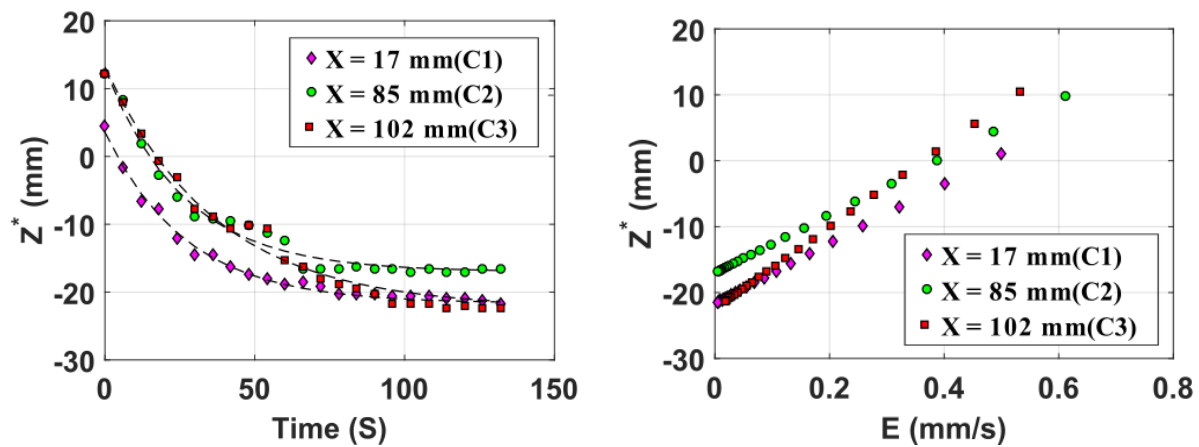
Figure 5-8. Temporal evolution of fine sediment bed level (fitted data in broken lines) (left) and erosion profiles (right) extracted at Plane 1 along the sections in Figure 5-7 (top)
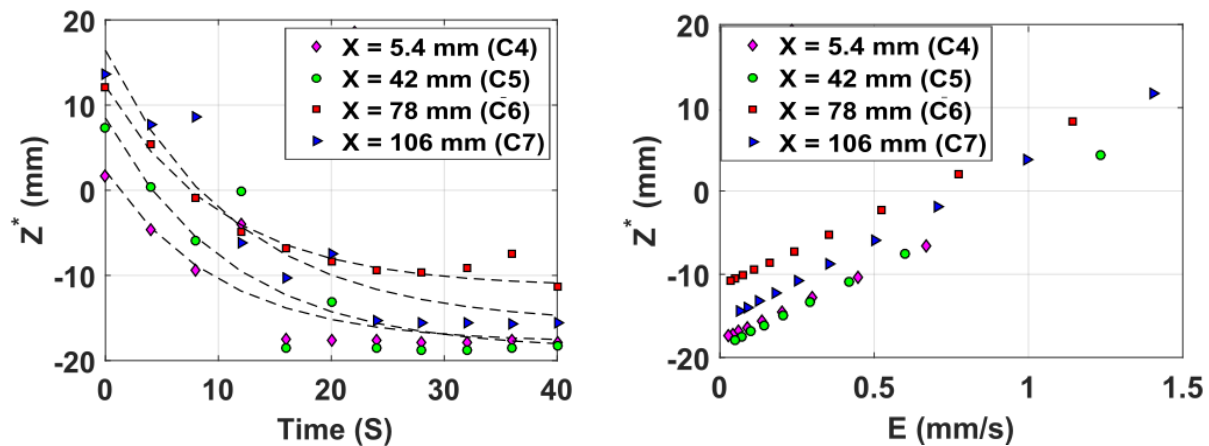
Figure 5-9. Temporal evolution of fine sediment bed level (fitted data in broken lines) (left) and erosion profiles extracted at Plane 2 along the sections in Figure 5-7 (bottom)

Previously published research shows that near-bed flow structure is affected by bed topography (Sarkar and Dey, 2010; Papanicolaou et al., 2001; Sambrook Smith and Nicholas, 2005). This is dictated by the high proportion of upward flow that occurs in the stoss side while downward flow that occurs in the lee side. Mohajeri (2014) showed that sweep events are particularly common at downstream side of gravel crests (lee), while at upstream side of gravels (stoss) ejection events. Thus, the occurrence of upward flow in stoss side and downward flow in the lee side of gravels tend to entrain sediments from the lee side thus increasing the erosion rate in the vicinity while sweep dominated areas such as the lee side will have lesser erosion rate. Keshavarzi et al. (2012) reported similar observation in sand ripple experiments where they observed more entrainment in the upstream and more deposition in downstream side of sand ripples based on measurement of the number of particles deposited and entrained. They reported that the entrainment and deposition characteristics were well correlated with the probability of occurrence of sweep and ejection events along the ripple. On the other hand, as the fine sediment bed level in roughness elements decreases the duration of high-magnitude turbulent events increases at the stoss side and the peak of the roughness elements and the effect is less substantial in gap between roughness elements (Sambrook Smith and Nicholas, 2005). This phenomenon may also lead accelerated erosion rate in the stoss side.

5.5. THE EFFECT OF GRAVEL BED ROUGHNESS ON EROSION RATE

For the purpose of investigating the effect of changes in the roughness of gravel bed roughness on erosion of the fine sediments, the immobile sand (natural) bed level (coverage) in the immobile grave bed upstream and downstream of the experimental control section was reduced manually.

Figure 5-10. The photo of the gravel bed upstream of the control section for full (left) and partial sand cover (right) conditions
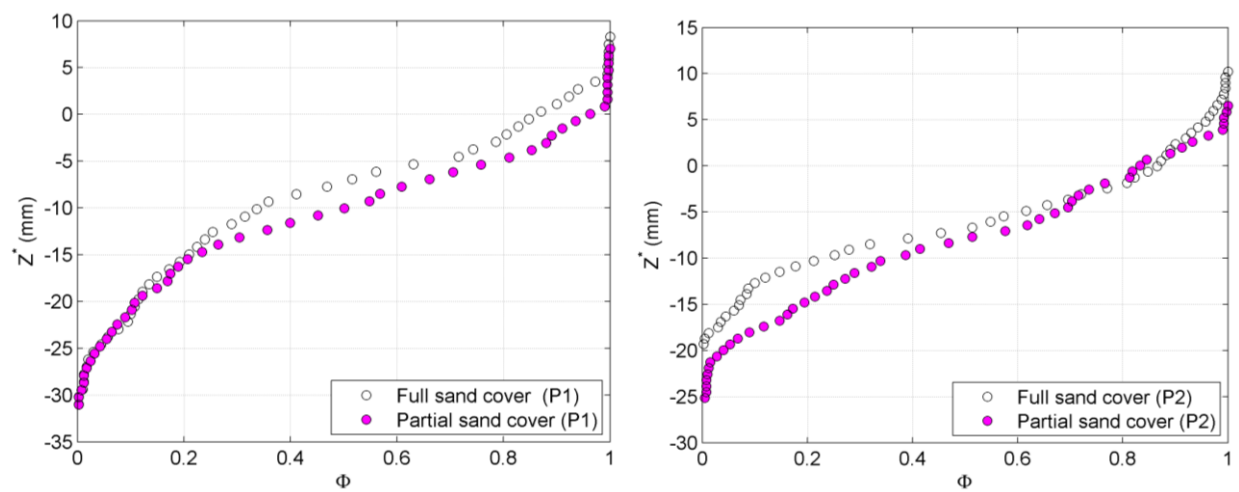
Figure 5-11. Roughness geometric function along measurement planes (P1 and P2) for full and reduced sand level (cover) over a total length of 40cm

The immobile sand particles coverage and level was reduced mechanically using a vacuum cleaner by a few millimetres (~10 mm) for a length on average 1.5 m upstream and 0.5 m downstream of the control section. This allows studying the effect of changes in equivalent roughness height on the rate of erosion of fine sediments in the gravel matrix. The immobile sand level is reduced for a length of 1.5 m upstream to reach enough length of flow to adapt to the local bed roughness as sand is filled from the inlet of the flume down to the control section. Figure 5-10 shows the images of the part of gravel bed upstream of the control section taken before (left) and after (right) sand level is reduced. Figure 5-11 shows the roughness geometric function calculated for surface elevation of gravel along Plane 1 (left) and Plane 2 (right) before and after (shaded) sand level is reduced. The total length, along which the surface elevation profile is extracted, was 40cm with 25cm upstream and 13.2cm downstream of the control section. The standard deviation of elevation (σ_z) of the gravel surface elevation which is a measure of vertical roughness length scale along Plane 2 before and after sand bed level reduction is 5.72 mm and 6.97 mm respectively. For Plane 1 σ_z is 7.9 mm and there is no significant change when sand level is reduced. Nevertheless, as shown in Figure 5-11, when sand bed level is reduced more void spaces are observed for elevation larger than -15mm along Plane 1 while it is below gravel crest for Plane 2, thus increasing the roughness at the bed.

The characteristics of flow velocity in response to changes in equivalent roughness height (due to reduction in immobile sand from the gravel matrix) of the immobile gravel bed are investigated. The vertical profiles of stream-wise velocity were measured (using UVP) before and after the immobile sand fill were reduced in the gravel matrix. The velocity measurements were conducted at six verticals in span-wise direction with spacing between the verticals set 42 mm, the first and last verticals are 92 mm from the flume wall. Three measurement sections in the stream-wise direction are selected which are at 6.11, 6.36 and 6.61 m from the flume entrance. The velocity profiles are measured for flow depth, $h = 0.05$m, discharge, $Q = 5.6$ l/s, bed slope, $S_o = 0.0014$. Figure 5-12 shows the span-wise averaged velocity profiles at the three cross-sections (circle, diamond and square markers) for full sand (shaded plots) and partial sand (unshaded plots) conditions. As the sand level reduces the flow resistance increases and there is a general trend in which the velocity measured at each flow depth is slightly less than full sand cover condition at all measurement sections (Figure 5-12).
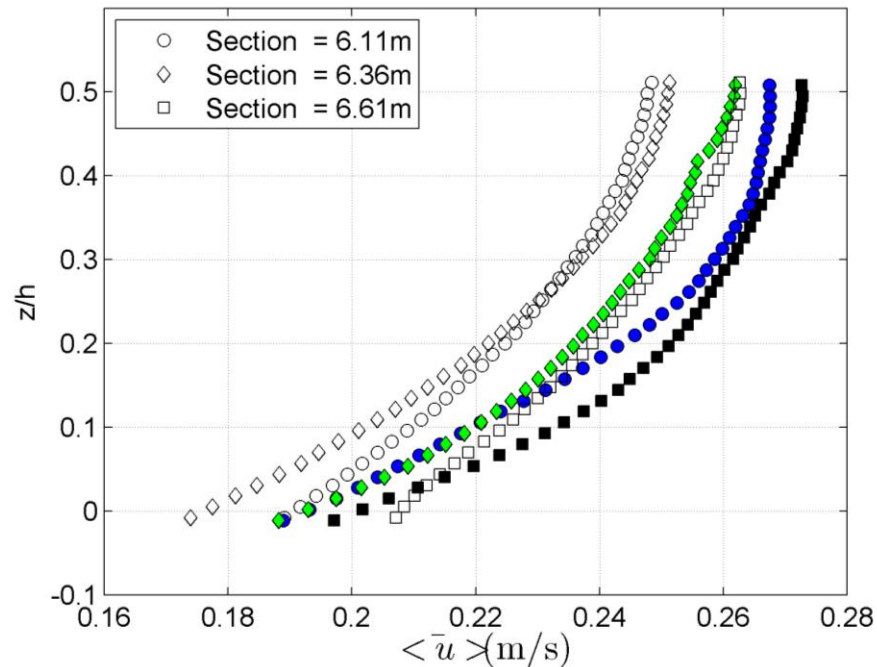
Figure 5-12. The span-wise averaged velocity profiles at the selected sections where shaded plots are for full sand cover condition

In Figure 5-13 the spatially averaged velocity (average of the three measurement sections) profiles for partial and full sand cover is indicated. It shows that the velocity profile along the flow depth for partial sand cover condition is lower compared to full sand cover. In Figure 5-14 the percentage reduction, compared to full sand condition, in velocity at each flow depth is plotted. It clearly indicates that the difference is very small (3.0 - 5.0 %) near the bed (z/h < 0.1) and near free water surface (z/h > 0.3) with the largest (7.0 %) difference observed at z/h = 0.2. Since the percentage reduction, in general, is relatively small, i.e., 3.0 - 7.0 %, it shows that the effect of the reduction in the sand level, in this experiment, on the velocity profile is not very significant. Wren et al. (2011) conducted measurement of velocity profiles for incremental sand level in gravel bed (relative submergence, $h/d_g = 6$) and observed stream-wise velocity was insensitive and there was no clear trend for the ranges of roughness investigated despite they observed increment in Reynolds shear stress profile as the sand level reduced. In other study Sambrook Smith and Nicholas (2005) conducted experiment on the effect of sand addition to roughness elements on coherent structures and they observed a general trend of increment in near bed stream-wise velocity as the sand fill in effective roughness increases.
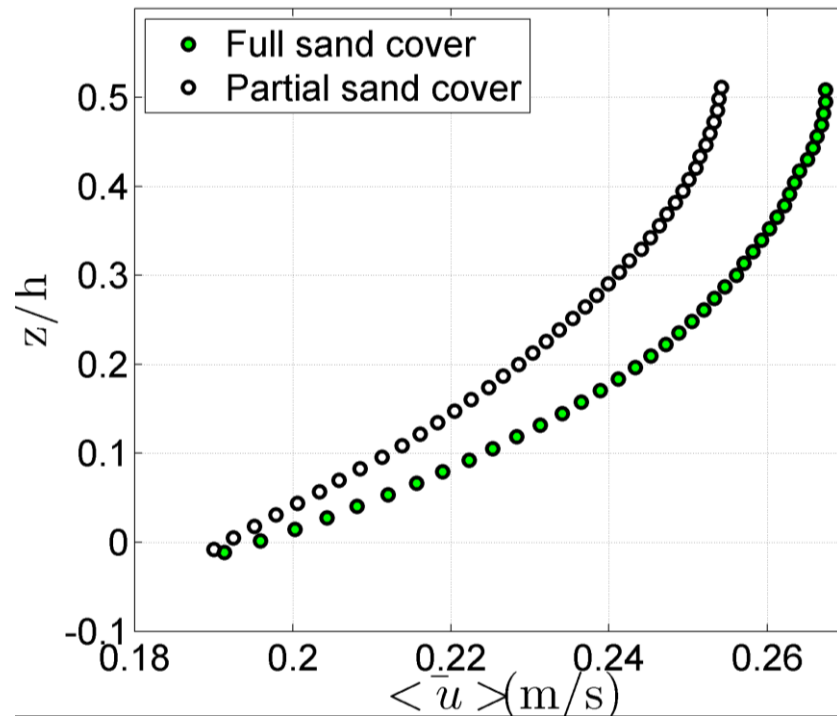
Figure 5-13 . The spatially averaged (of 3 sections) velocity profiles for full and partial sand cover conditions
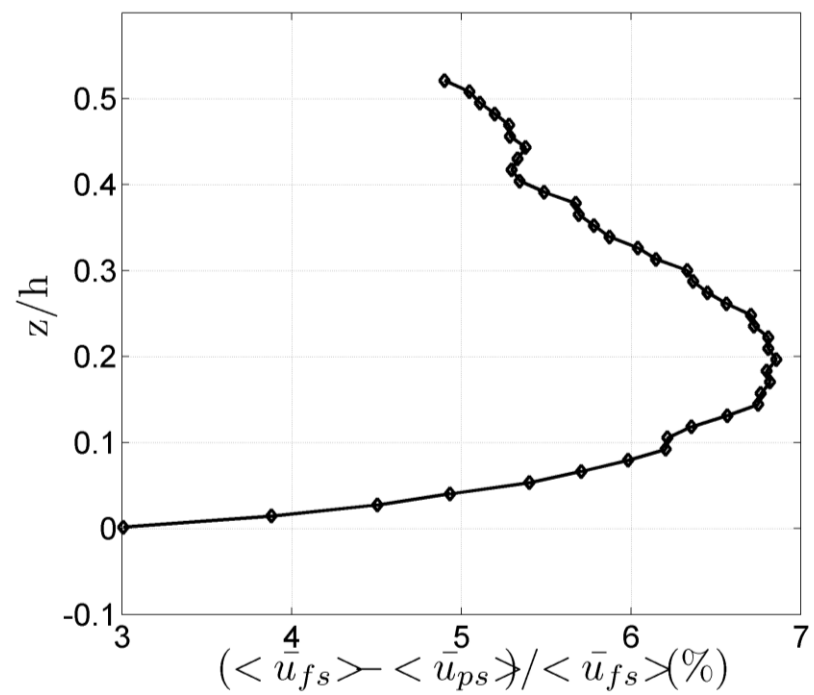
Figure 5-14. Percentage reduction in spatially averaged velocity due to reduction in sand level (cover)

A near constant velocity in near bed region (Figure 5-15) is observed for both partial and full sand condition and this might be due to occurrence of larger scales of turbulence that are able to mix the near - bed region, creating a zone of near constant velocity. The regions of near constant velocity is observed for $z/h < 0.031$ which shows similarity with Grams and Wilcock (2007) experiment for $h/d_g = 4$. Wren et al. (2011) showed that such near constant velocity region was not observed for large relative submergence (e.g. $h/d_g = 6$) as there is small scale roughness in such flow conditions.
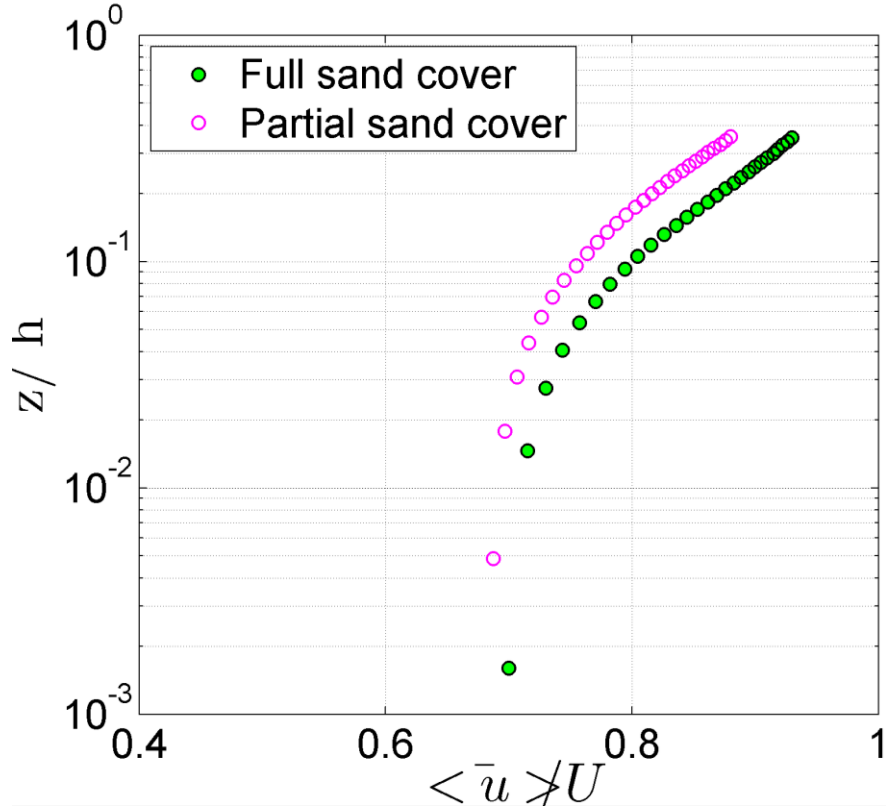
Figure 5-15. Profiles of normalized spatially averaged stream-wise velocity for partial and full sand cover conditions

Although changes in sand coverage observed to affect spatially averaged velocity profile slightly, the effect on estimated erosion rate is worth explanation. Figure 5-16 (top) shows the vertical profile of erosion rate of fine sediments in the control section for partial and full sand cover condition at Plane 1. There is generally larger erosion rate in the interfacial sub-layer for partial sand cover (increase in immobile bed roughness). As shown in Figure 5-16 (bottom) the reduction in sand level (increase in immobile bed roughness) has significant effect on erosion rate of fine sediments near the last one-third of the interfacial sub-layer, up to 1.5-2.0 fold increase in erosion rate at Plane 1 where E_{PS} and E_{FS} denote erosion rate for partial sand and full sand conditions respectively.
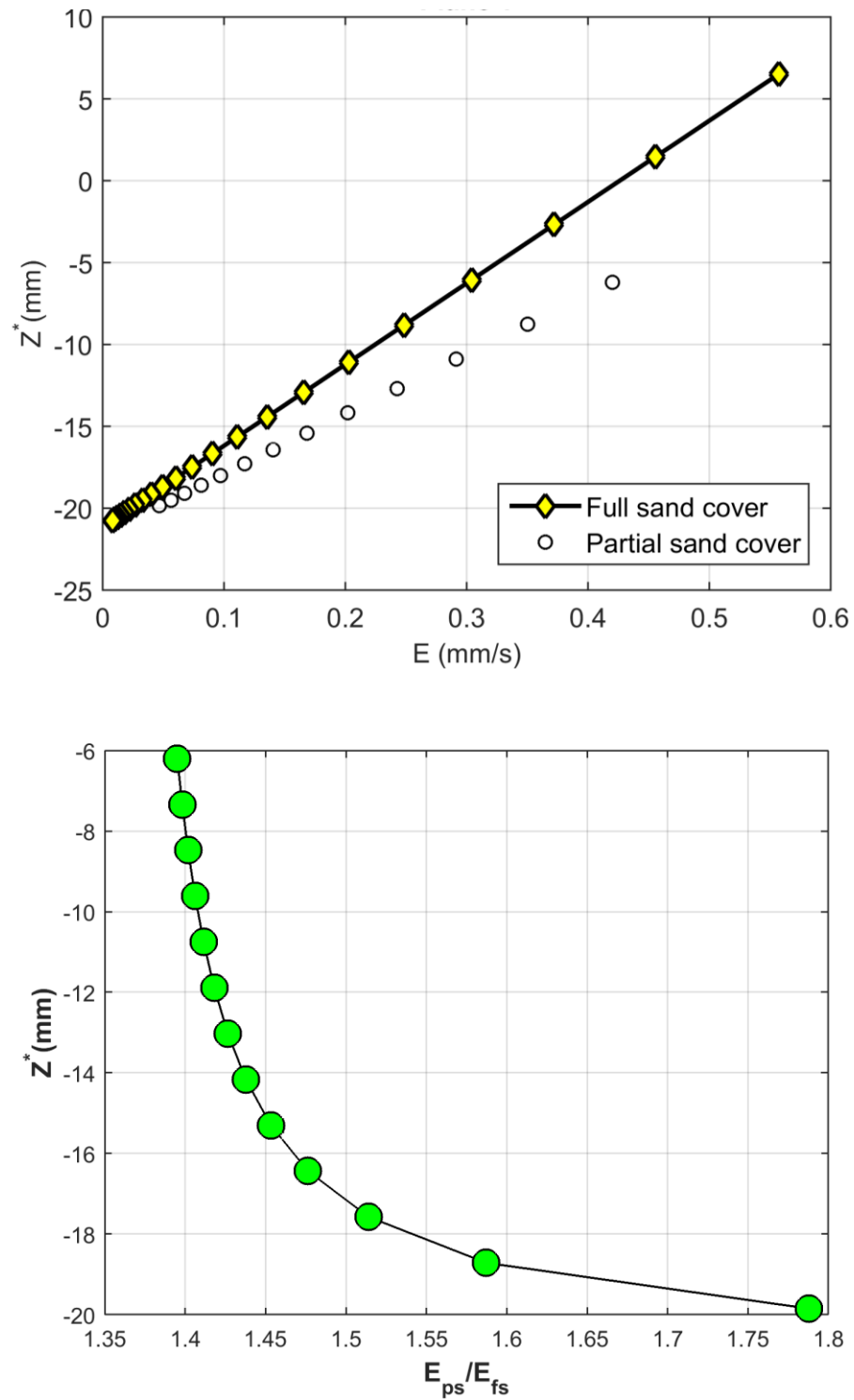
Figure 5-16. Effect of sand level (cover) on estimated vertical profile of erosion rate (Plane 1): erosion rate (top) and ratio of erosion rate (bottom) under partial to full sand condition

Near the gravel crest, upper two third of the roughness layer of Plane 1, the increase in erosion rate of fine sediments due to sand level reduction, is in the range of 1.4-1.45 folds. When the sand level decreases in the gravel bed upstream and downstream of the control section the effective roughness of the gravel bed increases. This results in increased turbulent intensity, Reynolds shear stress and increment in total duration of high magnitude turbulent events (Sambrook Smith and Nicholas, 2005) that could lead to increased sediment entrainment.

5.6. DEVELOPMENT OF EROSION RATE FORMULATION

5.6.1. Theoretical background

The component of turbulent flux of suspended sediments near a flat and erodible bed that is directed upward normal to the bed is often termed as rate of erosion or more accurately, entrainment of bed into suspension per unit bed area per unit time (Garcia, 2008). It is described as a function of turbulent fluctuations of concentration and vertical flow velocity averaged over turbulence (Garcia, 2008) since it is predominantly controlled by turbulent bursting (Sutherland, 1967). The determination of the entrainment flux is one of the pivotal components of modelling suspended sediment transport and morphological evolution (Celik and Rodi, 1988; Cao et al., 2004). In equilibrium steady uniform suspension, there is neither net erosion nor deposition from the bed, the dimensionless rate of entrainment (volume of entrained sediment per unit bed area per unit time) can be assumed equal to near bed sediment concentration or rate of deposition is equal to the rate of erosion or entrainment (Parker, 1978). This assumption has been fundamental basis for development of many erosion/entrainment relations although not applicable for non-equilibrium conditions. In steady flow and non-equilibrium transport condition, the sediment entrainment and deposition are rather considered independent processes (van Rijn, 1984b).

There are many empirical and semi-empirical formulations have been developed to predict the entrainment rate of fine sediments in uniform grained sand beds (e.g. Garcia and Parker, 1991; van Rijn, 1984a; Cao, 1999; Celik and Rodi, 1988; Zyserman and Fredsoe, 1994; Smith and McLean, 1977). Most of these models are developed empirically based on measurement of near bed sediment concentrations under equilibrium suspended sediment transport conditions conducted in laboratory flumes. These entrainment models are widely used in suspended sediment transport modelling from small scale to large scale modelling applications (e.g. van Rijn, 1984a; Smith and McLean, 1977; Zyserman and Fredsoe, 1994) where bed sediments are similar to particles in suspension. van Rijn (1984b) developed a pick-up (erosion) rate formula for non-equilibrium transport conditions that was valid for particle size ranges of

130-1500μm. It was found to be a reliable relation to predict fine sediment transport in rapid morphological evolutions (e.g. dam break) characterised by non-equilibrium transport (e.g. Iervolino et al., 2010). van Rijn (1984b) can also be used for unsteady flow conditions (e.g. Nielson, 1992). It can be argued that quite many entrainment or erosion rate formulations exist which offer alternatives for modelling transport of suspension in erodible fine sediment bed. Nevertheless, modelling suspension transport of fine sediments in immobile bed conditions has rather been more complicated. There are limited studies that have been conducted to predict fine sediment entrainment, erosion and transport rates in immobile coarse beds (e.g. Grams and Wilcock, 2007; Grams and Wilcock, 2007; Kuhnle et al., 2013; Grams and Wilcock, 2013; Wren et al., 2014).

There are only few studies that developed relations to predict fine sediment entrainment from immobile coarse bed although their limitations are yet to be tested. Grams and Wilcock (2007) developed a logistic function that corrects fine sediment entrainment rate of sand bed (Garcia and Parker, 1991) to predict entrainment rate for sand bed level in immobile coarse bed. The function is developed empirically by fitting an empirical relation to the data of the ratio of observed near bed sediment concentration for selected sand bed level in immobile bed to the entrainment rate by Garcia and Parker (1991). The immobile coarse bed used in the experiment was hemispheres of uniform diameters (10 cm) with cubical arrangements. The function applies no correction for sand bed level as large as half of the radius and this may lead to over-estimation of the entrainment (e.g. Kuhnle et al., 2013). Kuhnle et al. (2013) and Wren et al. (2014) developed empirical relations that predicted the total transport rate of fine sands (mainly bed load) in immobile gravel bed and cobble bed respectively. The sand transport rate was predicted as a function of effective shear stress, sand bed elevation and bed porosity profile of gravel or cobble. The same relationship between bed shear stress, sand elevation (level), and sand transport rate was found to be valid for both gravel and cobble experiments. They scaled total bed shear stress by a porosity profile to estimate effective shear stress below gravel crest which is a crucial assumption which has to be verified. Since their relationships are developed for total fine sediment transport their application for suspended transport prediction is limited. Cui et al. (2008) proposed a simple roughness and partial sand coverage correction to adjust sand transport rate relation by Brownlie (1982) for immobile bed condition. Since the relation calculates transport rate based on bed roughness of sand particles the roughness has to be corrected for transport over gravel the bed, which has higher roughness. In this manner the correction for roughness is introduced to adjust the overall roughness and partitioning the shear stress into that exerted on roughness elements of the immobile bed and that exerted for fine sediment transport. Moreover, since the relation was also developed for full sand bed condition a correction has to be applied when sand layer is thin enough exposing gravels. The corrections for bed roughness and partial sand coverage are

described as a function of roughness height of clean gravel bed (twice the mean diameter), roughness height of sand bed (twice the mean diameter) and thickness of sand deposit. The corrections are found to improve model prediction of sand pulse releases of dam removal (e.g. Cui et al., 2008; Stillwater Science, 2002). Despite few studies of fine sediment erosion or entrainment in immobile coarse bed, relations that could be useful to predict erosion rate in non-equilibrium and unsteady flow conditions remains lacking. Therefore, experimental studies that are conducted in non-equilibrium conditions would be very useful. In the following sections the experimental datasets are presented and are described and an alternative entrainment formulation is devised based on aforementioned theoretical backgrounds.

5.6.2. Description of vertical erosion profiles from experiments

As shown in Table 4-1 ten experimental runs (Run I-X) were carried out for flow depth that ranges from 3 cm to 7 cm. Figure 5-17 (top) shows the temporal evolution of raw data (scattered markers) and exponentially fitted data (broken lines) of the mean fine sediment bed level for each experimental runs sampled every $\Delta t = 6s$ from which the vertical profile of fine sediment erosion rates (Figure 5-17, bottom) are estimated. The raw mean fine sediment bed level of each run is fitted to an exponential function of type: $z = ae^{bt}$ where z = normalized mean fine sediment bed level and *a* and *b* are coefficients which varied among the different runs, as described in Section 4.7.2 of Chapter 4, before it was used in the estimation of erosion rate (broken lines in Figure 5-17 , top). In Figure 5-17 (bottom) the profiles of erosion rate estimated for each run (combinations of flow depth (*H*) (3-7cm), bed slope (*So*) (0.0104-0.0304) and fine sediment grain sizes (d_{50}) (425 and 500µm)) are presented. The figure is plotted for various ratios of shear velocity (u_*) to settling velocity (w_s) which are indicators of the mode of transport (e.g. Bagnold, 1966). The settling velocity is estimated by using Cheng (1997) formula indicated in Equation (4-1). Estimated erosion rate for $u_*/w_s = 1.42$ is the largest while the lowest erosion rate is observed for $u_*/w_s = 1.11$. The lowest u_*/w_s is not necessarily related to the lowest erosion rate while in the other case the same $u_*/w_s = 1.08$ resulted in different erosion rates, for instance, for $H = 3cm$, $S_0 = 0.0304$, $d_{50} = 500µm$ (green circle) and $H = 5cm$, $S_0 = 0.0104$, $d_{50} = 425µm$ (red circle) the erosion rates are quite different where the latter is larger. It is worth noting that the vertical profile of erosion rate for each experimental runs follow a linear trend with elevation below the gravel crest. Such trend is physically sound since the first derivative of the exponentially decaying mean fine sediment bed level is a function of the mean fine sediment bed level and an empirical constant ($\partial Z^*/\partial t = c(Z^* - Z_{min})$) where c = an empirical constant).
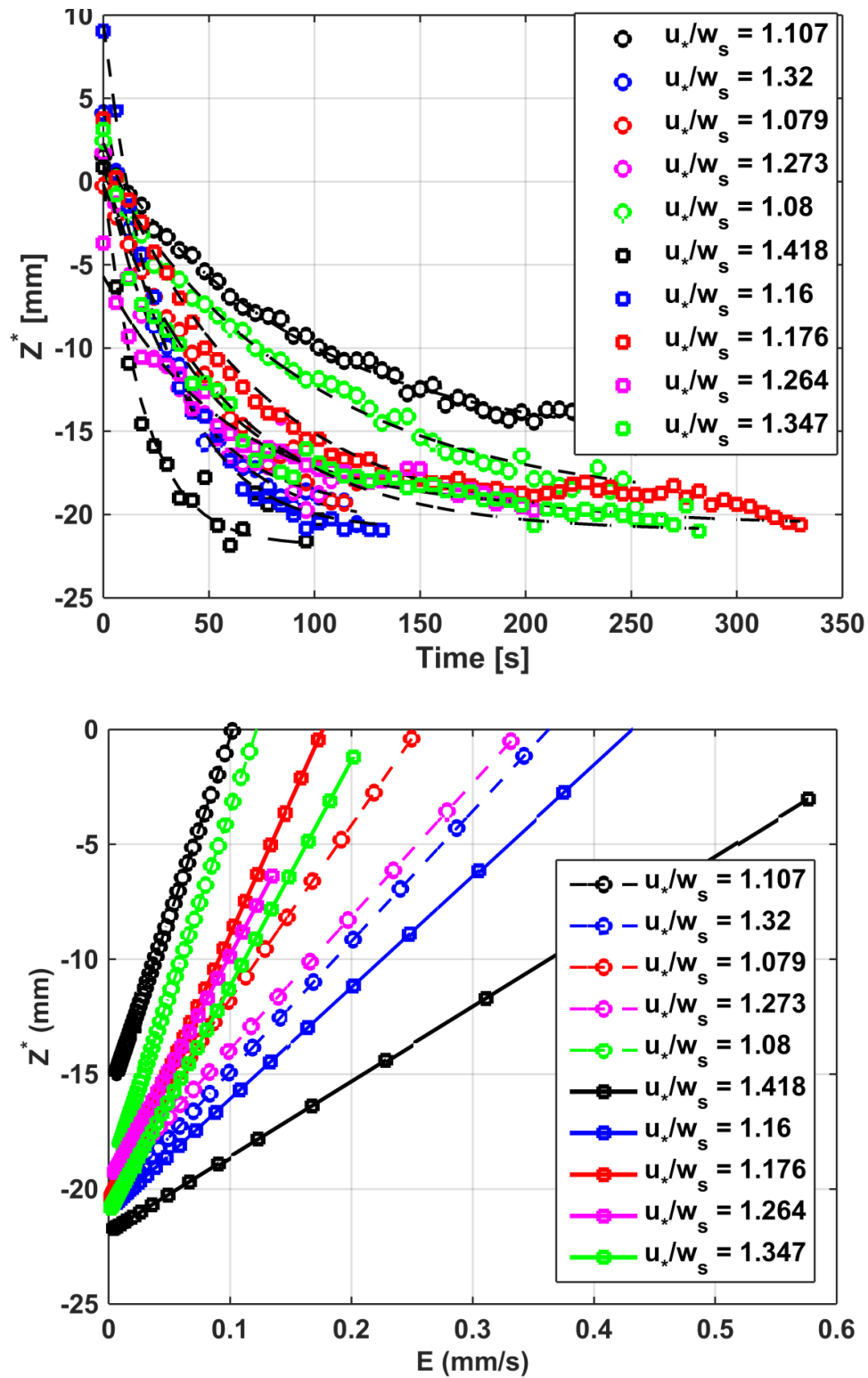
Figure 5-17. Temporal evolution of mean fine sediment bed level (top) and the vertical profiles of erosion rates (H = 3 - 7 cm and u$_*$/w$_s$ = 1.08 -1.42) (bottom)
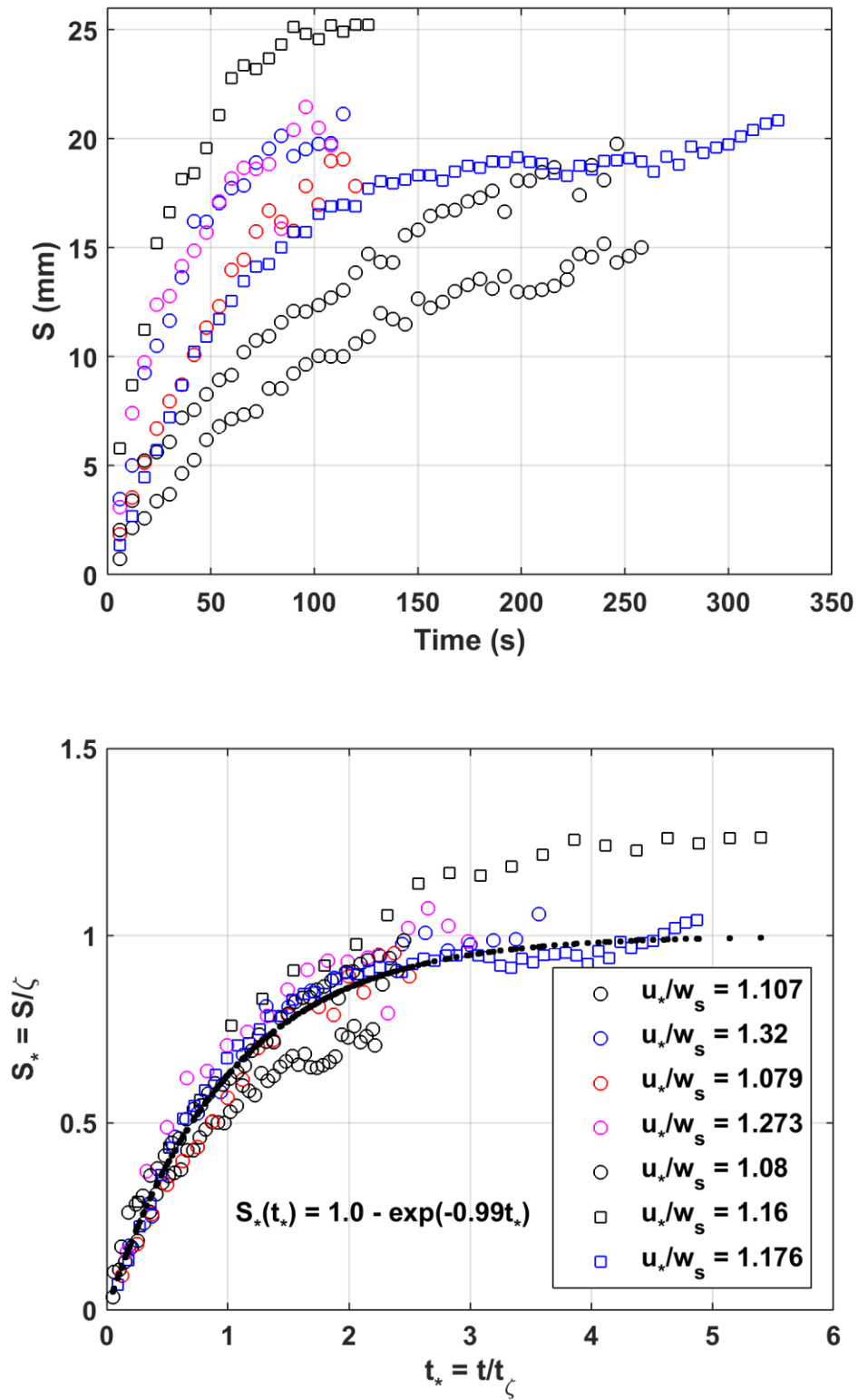
Figure 5-18. Temporal evolution of cumulative (total) depths of erosion from gravel crest to bottom of interfacial sublayer (top) and the dimensionless depth of erosion (bottom)

Figure 5-18 (top) shows the total depth of erosion below gravel crests for experimental Runs I, II, V, VI, VIII, IX, and X along Plane 1. The cumulative depth of erosion (S) for all these runs can be predicted by a single exponential function of time if it is made dimensionless. Thus, the cumulative depth of erosion is made dimensionless by the thickness of interfacial sub-layer (ζ) and the time is made dimensionless by the total time required to erode a total depth equivalent to ζ. Figure 5-18 (bottom) shows that the normalized total depth of erosion of all runs, when properly made dimensionless, seems to nearly collapse around a single exponential relation shown in black dots. The exponential equation takes the form: $S_* = 1.0 - e^{\alpha t}{}_*$ where $S_* = S/\zeta$ and $t_* = t/t_\zeta$ where t_ζ is the time scale required to erode ζ which is estimated based on above gravel crest erosion rate and α = empirical coefficient which in this case is $\alpha = -0.99$. It can be argued that if the thickness of interfacial sub-layer and rate of erosion above gravel crest is known the cumulative (total) depth of erosion and thus the mean fine sediment bed level can be reconstructed.

5.6.3. Description of experimental data and formulation of erosion rate relation

The erosion rate (E, m/s) computed for each experimental run could be related to hydraulic variables and sediment characteristics to derive an empirical relation for estimation of fine sediment erosion rate in immobile gravel bed. In many earlier studies (e.g. van Rijn 1981; van Rijn 1982; van Rijn,1984a) transport of bed material is described as a function of dimensionless bed material particle diameter (D_*) and dimensionless transport stage parameters (T) which is described as a function of bed shear stress and critical shear stress according to Shields. van Rijn (1984b) extended these approaches further to predict suspended sediment pick-up or erosion rates. This approach is conceptually robust in unsteady flow, since it does not make the assumption of instantaneous equilibrium between the bed shear stress and near-bed concentration. Many suspended sediment entrainment formulas are based on equilibrium transport assumptions (e.g. Garcia and Parker, 1991; Grams and Wilcock, 2007). van Rijn (1984b) is practically relevant especially to model sediment transport phenomenon downstream of dams during sediment flushing, since it is characterized by unsteady flow and non-equilibrium sediment transport conditions. The dimensionless erosion rate or pick up rate (in m/s) of sediments can be described as $E_* = \dfrac{E}{(\Delta g d_s)^{0.5}}$, where $\Delta = \rho_s/\rho - 1$ and g = gravitational acceleration, following Einstein (1950). The dimensionless erosion (pickup) rate in non-equilibrium transport of sand in fully sand covered bed can be described as follows according to van Rijn(1984b):

$$\frac{E}{(\Delta g d_s)^{0.5}} = \varepsilon D_*^{0.3} T^{1.5} \tag{5-8}$$

where

$$T = \frac{\theta - \theta_c}{\theta_c}$$

where θ = bed shear stress (= $u_*^2/\Delta g d_s$); θ_c = critical shear stress according to Shields; $\boldsymbol{\varepsilon}$ = empirical coefficient; D_* = dimensionless grain size (= $d_s (\Delta g/ \upsilon^2)^{1/3}$), where υ = kinematic viscosity of water = 10^{-6}.

In this study van Rijn(1984b) relation is evaluated with experiment datasets of seven runs measured in fine sediment bed condition, i.e. when the immobile bed was covered by the fine sediments (fine sediment bed level was above gravel crest) which represents erosion rate in fine sediment bed. First, the experimental data of erosion rate measured in fine sediment bed condition was related to bed material related parameter, D^* and bed shear stress related parameter, T following Equation (5-8) and the result is compared with calculated pickup rate formula of van Rijn (1984b). This enabled to evaluate whether the experimental data sets are within reasonable range of prediction by relations developed in similar conditions and also to obtain an empirical coefficient for the present study. A value of $\boldsymbol{\varepsilon}$ = 0.000169 was obtained which is smaller than   = 0.00033 of van Rijn (1984b) relation. This shows that the estimate of the erosion rate by van Rijn (1984b) formula is larger by nearly twice when compared to the experimental data of this study. However, it can be considered acceptable since such discrepancies are expected to exist and in all subsequent analysis of experimental results and formulations the empirical coefficient $\boldsymbol{\varepsilon}$ = 0.000169 is used.

Figure 5-19 shows above crest dimensionless erosion rate of the selected experimental runs (I, II, IV, V, VI, VIII, and IX) (diamonds) and estimated based on van Rijn (1984b) formula (circles) plotted in log-log scale. It shows that there is a linear relationship between above crest dimensionless erosion rate and $D_*^{0.3} T^{1.5}$. The error bar is computed considering measurement uncertainty of fine sediment bed level by 1 pixel (= 360μm) as described in Section 4.4.4. The above crest erosion rate for each experimental run is estimated by taking the slope of the mean fine sediment bed level time series (e.g. Figure 4-26) just above gravel crest.
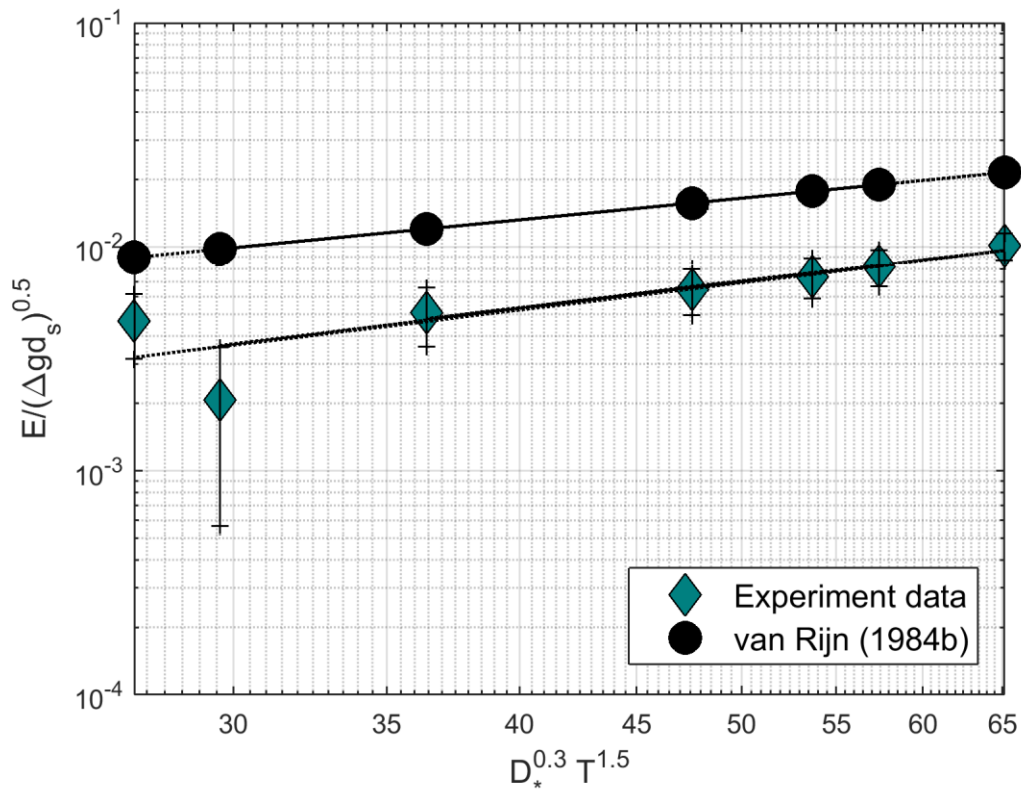
Figure 5-19. Dimensionless erosion rate as a function of transport stage parameter (T) and dimensionless grain size (D∗)

The prediction of the rate of erosion below gravel crest is difficult since it is controlled by many contrasting variables (Wren et al., 2014, 2011). The main factors that control the entrainment or erosion of fine sediments in immobile coarse bed include the fine sediment bed level below gravel crest (η), fraction of fine sediments available in the coarse bed, the net shear stress acting on the fine sediment below the gravel crest, the grain size of the fine sediments and immobile bed materials, and relative roughness (Grams and Wilcock, 2013; Kuhnle et al., 2013; Wren et al., 2014, 2011). Earlier studies (e.g. Kuhnle et al., 2013; Wren et al., 2011, 2014) argued that fraction of fine sediments   available in the coarse bed and the net shear stress acting on the fine sediment particles below the gravel crest can be well scaled at a given sand depth or level by roughness geometric function (Φ). In this study the total drag force is found to be well scaled (as discussed in Section 5.3) as a function of roughness density and thus the effective shear stress in the interfacial sublayer can be estimated from the momentum supply instead. This approach is conceptually superior and physically sound as the total drag force is theoretically described as a function of roughness density while there is no physical basis to scale shear stress with bed porosity.

The experimental observations of the erosion rate below gravel crest show a decrease in erosion rate with fine sediment bed level below gravel crest (see Figure 5-17) where θ $(\eta =0)$ = dimensionless Shields number at gravel crest, $\eta = 0$. The erosion rate below gravel crest decreases as a result of progressive decline in effective shear stress by drag force. The total bed shear stress observed at gravel crest is potentially partitioned between the shear on the immobile coarse bed and on the fine particles when fine sediment bed level goes below the gravel crest. Equation (5-8) can be directly applied to calculate shear stress based on measured erosion rates at selected fine sediment bed levels below gravel crest by assuming that the erosion rate from the fine sediment bed below the gravel crest is similar to a case of fully sand covered bed. The estimated shear stress is plotted with thick lines in Figure 5-20 and it decreases as the fine sediment bed level decreases. Nevertheless the estimate varies from run to run where high reduction in shears stress is evident for high velocity flow and less reduction in the cases of low velocity flow conditions (Figure 5-20). The result is physically sound since the drag force is high when the flow velocity is high leading to high reduction in shear stress.
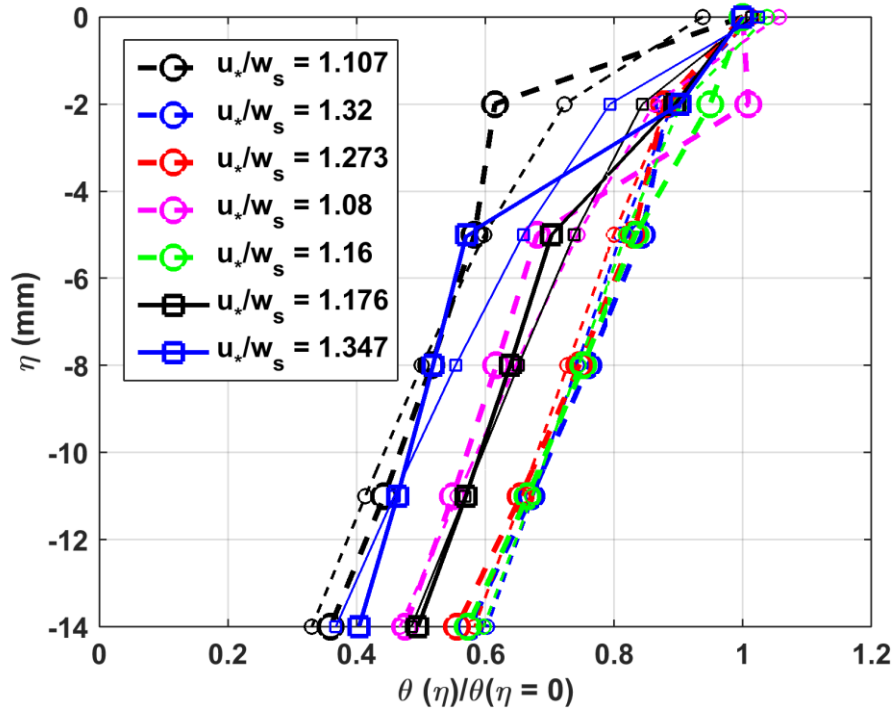
Figure 5-20. Shear stress profile computed using Equation (5-8) (thick line) based on measured erosion rates below gravel crest and estimated with Equation (5-7) (thin lines)
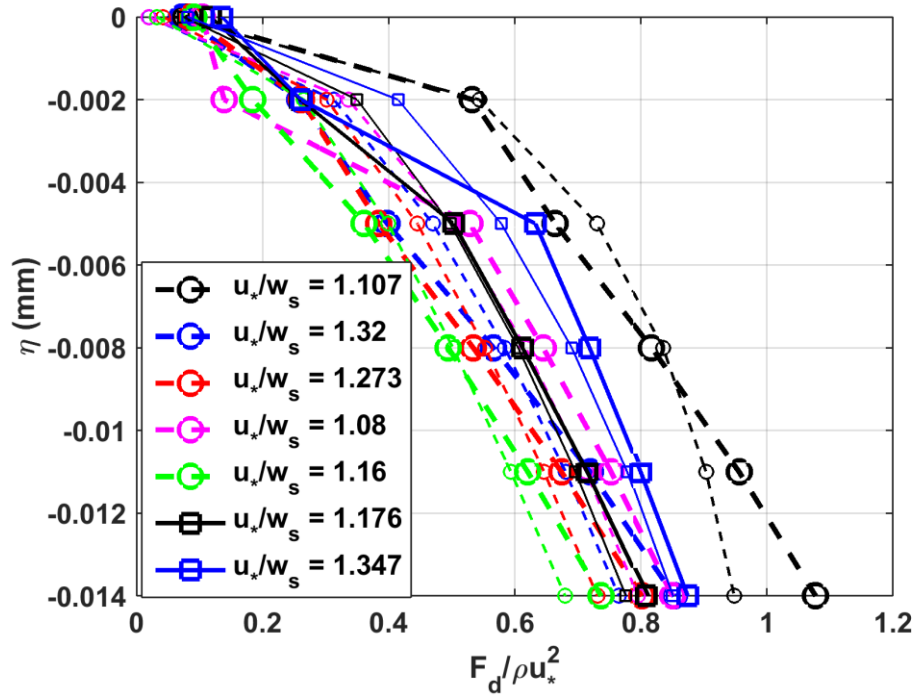
Figure 5-21. Dimensionless drag force estimated at selected fine sediment bed level: estimates from momentum balance (thick lines) and calculated based on Equation (5-6) (thin lines)

As shown in Equation (5-6) the drag force in clean gravel bed can be scaled as a function of the roughness density of the immobile gravel bed. In the present study the total drag force for the selected experimental runs at selected fine sediment bed level below gravel crest (η) is estimated as the difference between the momentum supply and shear stress estimates from erosion rate data (thick lines in Figure 5-20) and the result is presented in Figure 5-21 (thick lines). The dimensionless drag force of each experimental run is then plotted against the dimensionless roughness density and nearly all collapse along experimental datasets obtained in clean gravel bed (e.g. Dey and Das, 2012; Mignot et al., 2009) (see Figure 5-22). When the estimated total drag force of each run are fitted in Equation (5-6) the empirical coefficients $c_o =$ 1.01 and $c_1 = -0.80$ are obtained which are close to the estimates from the experiments in clean bed conditions shown in Figure 5-4. The broken line in Figure 5-22 shows the fitted dimensionless total drag force. It is worth noting that the values of the empirical coefficients (c_o and c_1) varied from run to run and the uncertainty of each empirical coefficient was calculated based on the uncertainty calculated for shear stress. The uncertainty of the shear stress is estimated based on uncertainty of fine sediment bed level measurements indicated in Section 5.6.3. The plots of the error bar for estimated empirical parameters are shows in Figure C-10 (Appendix C). Therefore, the values of the experimental coefficients ($c_o = 1.01$ and $c_1 = -0.80$) used in the prediction of below crest erosion rate are the mean of the empirical coefficients of

all experimental runs which lie within the uncertainty bands of all runs. Figure 5-21 (thin line) show the estimate of drag force with the empirical coefficients (c_o = 1.01 and c_1 = -0.80) which are close the estimate from momentum supply (the thick line). In Figure 5-20 the shear stress profiles estimated based on empirically fitted drag forces are plotted in thin lines. The estimates are closer to the shear stress calculated from below gravel erosion measurements (thicker lines in Figure 5-20).
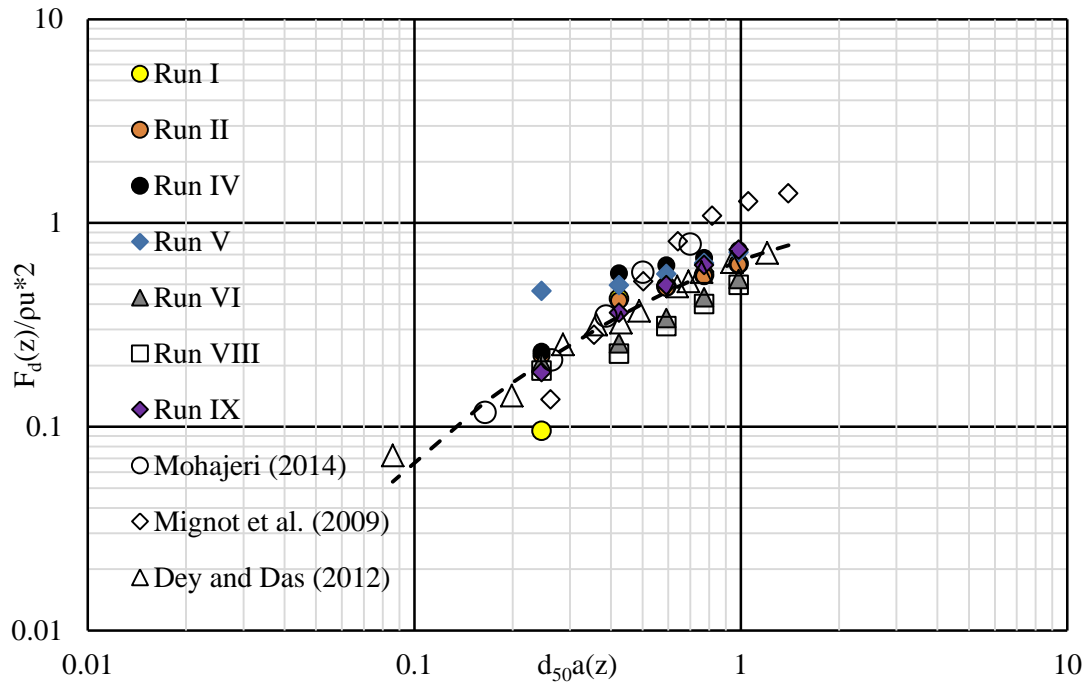
Figure 5-22. The relationship between dimensionless drag force and dimensionless roughness density below gravel crest for datasets of clean bed and this study show roughness density could be used to scale drag force

In this study it is assumed that if the shear stress below gravel crest is properly scaled, the erosion rate below gravel crest can be predicted with formulas developed for sand bed conditions. Thus the main purpose is to evaluate whether it is possible to predict below crest erosion rate by implementing predicted shear stress below gravel crest by Equation (5-7) in Equation (5-8). First, the relationship between observed (experimental) below crest dimensionless erosion rate and the dimensionless shear stress at gravel crest was evaluated as shown in Figure 5-23. This was conducted to evaluate if the linear relationship observed for above crest condition is valid also below crest as pointed out in Section 5.6.3. The dimensionless below crest erosion rates of the experimental runs at Plane 1 were extracted from

vertical profiles of erosion rates (at η = 5 mm, 10 mm and 15 mm) in Figure 5-17 and plotted against $D*^{0.3}T^{1.5}$ as shown in Figure 5-23. Figure 5-23 shows that the linear trend observed in Figure 5-19 is also valid below gravel crest.
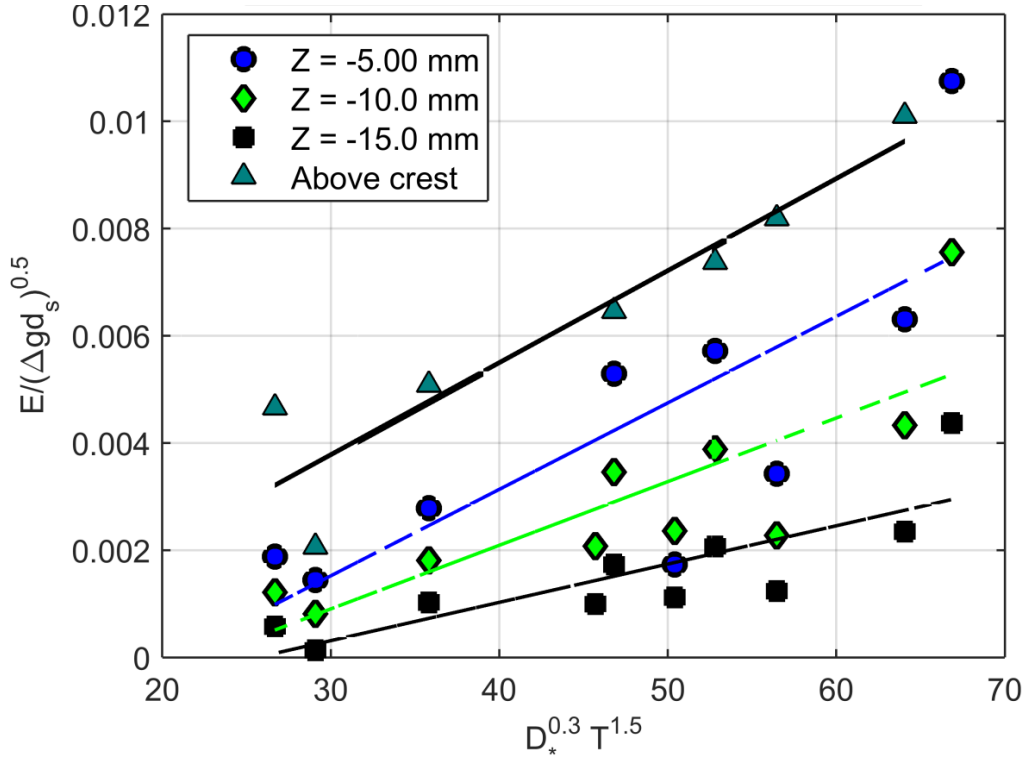
Figure 5-23. Dimensionless erosion rate above and below gravel crest where T estimated based on shear stress at gravel crest

When the bed shear stress in Equation (5-8) is replaced by $\tau_e(\eta)$ for η = 5 mm, η = 11 mm and η = 14 mm and compared to observed below crest erosion rates of the experimental runs a very good agreement is obtained (see Figure 5-24). In Figure 5-24 the plots in black, blue and red filled markers are the predicted erosion rate and are within the measurement uncertainty or error bands of observed erosion rate below gravel crest. The result shows that below gravel crest erosion rate, in non-equilibrium fine sediment transport in immobile bed, can be predicted by pickup rate formula of sand bed of van Rijn (1984b) provided that the shear stress below the immobile gravel crest is well scaled at each fine sediment bed level. Thus, the proposed new formulation reads as:

$$\frac{E(\eta)}{(\Delta gd_s)^{0.5}} = \varepsilon D_*^{0.3} \left[\frac{\tau_e(\eta) - \tau_c}{\tau_c} \right]^{1.5}$$

(5-9)

where

$\tau_e(\eta) = \tau(\eta) - \rho u_*^2 (1 - c_o e^{c_1 a(\eta)})$ and E (η) = erosion rate at fine sediment bed level η; τ_e (η) = effective shear stress at fine sediment bed level η and C_o = 1.01 and C_1 = -0.80; $\tau(\eta)$ = total momentum supply; τ_c = critical shear stress from Shields; and ε = 0.000169 is an empirical constant.

In Figure 5-25 the plot of the experimental data of dimensionless erosion rate against $D_*^{0.3}T^{1.5}$ estimated from predicted or scaled shear stress below gravel crest at selected fine sediment bed level (η = 5 mm, 10 mm and 15 mm). The experimental data points of above and below gravel crest erosion rates seem to overlap along a line depicting the strong relationship between dimensionless erosion rate and $D*^{0.3}T^{1.5}$. The plots in diamond are those measured above gravel crest (i.e. a condition similar to sand bed). A similar plot of dimensionless erosion rate against $D_*^{0.3}T^{1.5}$ estimated from momentum supply (τ) is indicated in Figure C-11 (Appendix C). In this case no any clear relationship is evident.
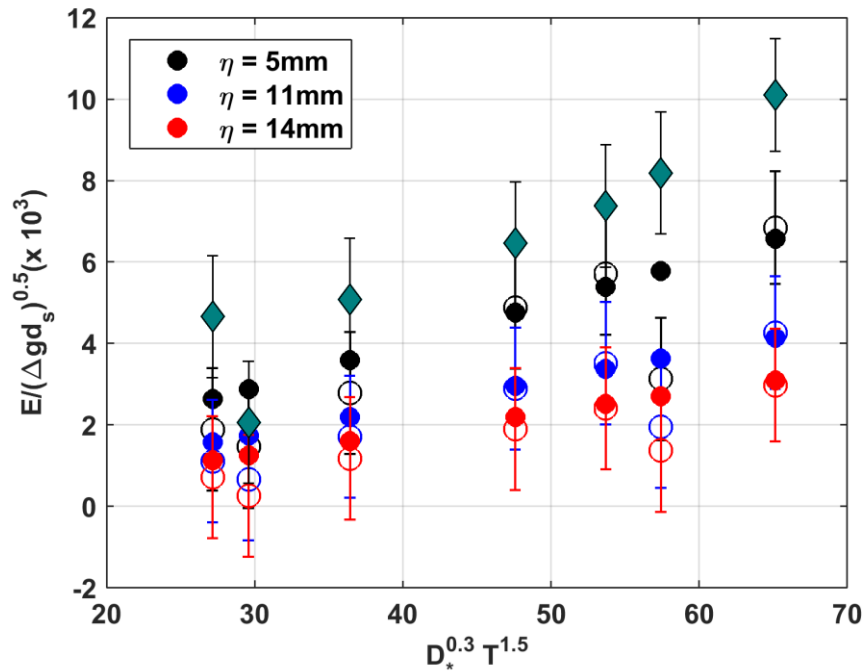
Figure 5-24. Predicted dimensionless erosion rate below gravel crest plotted against T estimated from shear stress at gravel crest
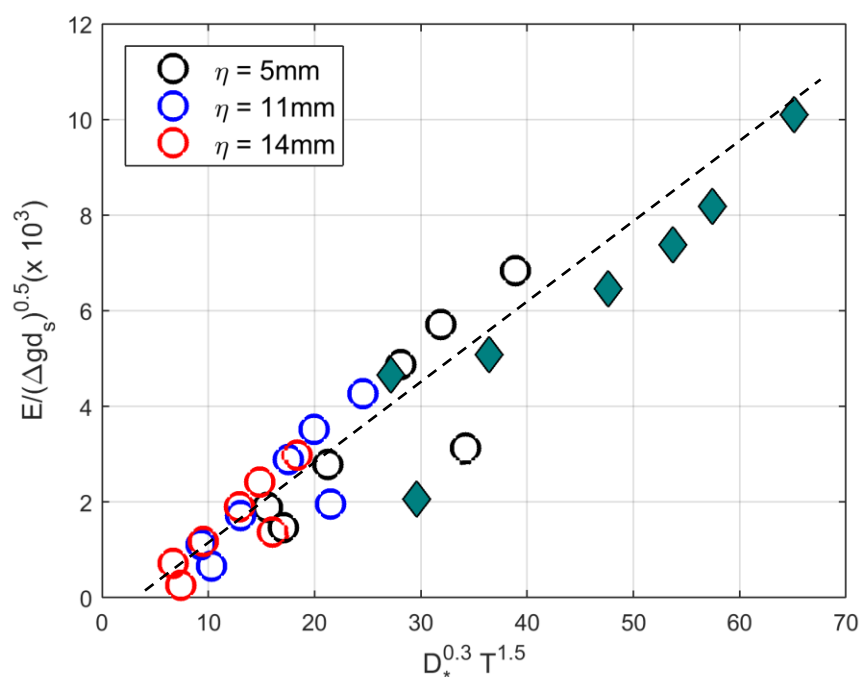
Figure 5-25. Observed dimensionless erosion rate plotted against T estimated from shear stress calculated below gravel crest (circles) and shear stress at gravel crest (diamond)
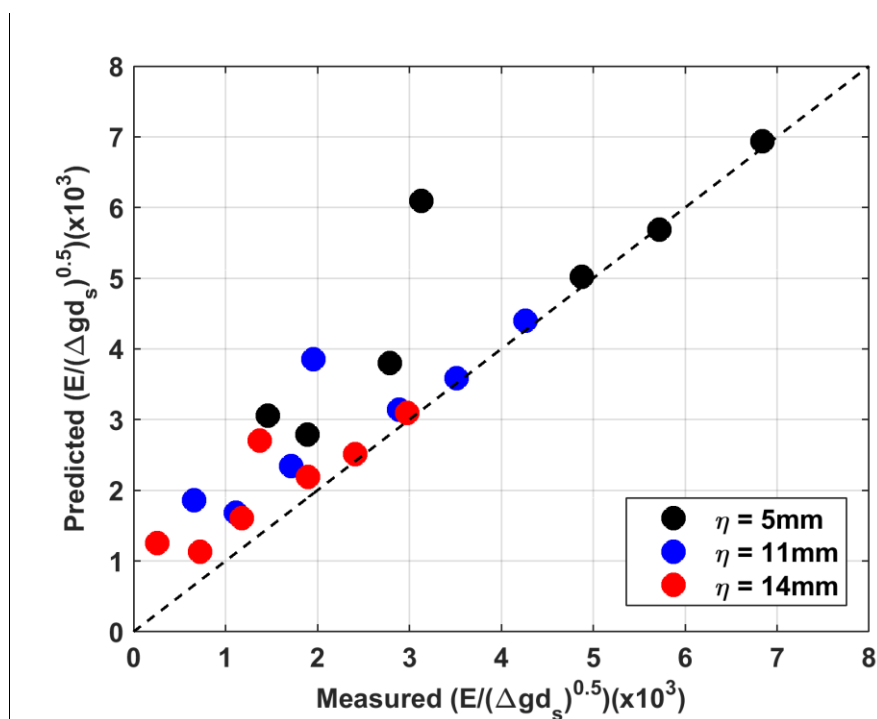
Figure 5-26. Measure of goodness of fit: the predicted versus measured below crest erosion rates

Figure 5-26 shows that the predicted erosion rate for selected fine sediment bed level below gravel crest (η = 5, 11 and 14 mm) show good agreement for larger estimates of erosion rate but a bit of over prediction for smaller estimates.

5.6.4. Characteristics of erosion in partial sand cover condition

The characteristics of erosion profile and rate when the immobile sand level (coverage) is reduced upstream and downstream of the control section (refer Section 5.5) is presented based on data collected along Plane 1 for reduced immobile sand bed level. The experimental runs for partial sand cover are sampled at higher temporal time scale (Δt = 0.24 s) but no clear trend in erosion rate was evident due to the reason discussed in Section 4.7.2. Thus the mean fine sediment bed level was re-sampled every Δt = 4.8s (shaded circles in Figure 5-27) and fitted (broken lines in Figure 5-27) to an exponential function (as discussed in Section 4.7.2 of Chapter 4) before it was used in the estimation of the erosion profile (Figure 5-27).
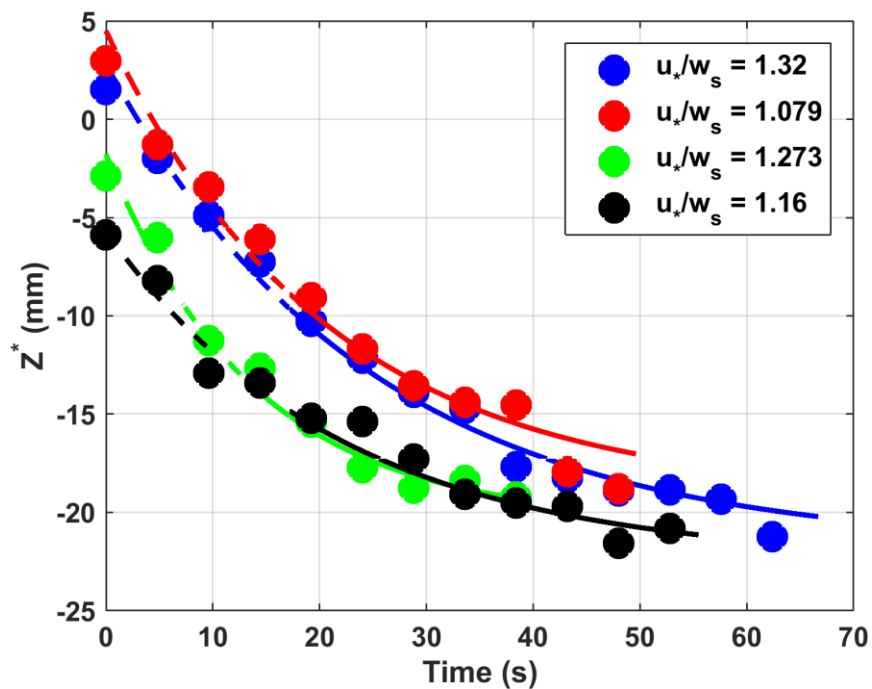
Figure 5-27. Temporal evolution of mean fine sediment bed level for Run VI, VIII, IX and X for partial sand cover condition

Figure 5-27 shows the mean fine sediment bed level of experimental runs (Run VI, VIII, IX and X) along Plane 1. The mean fine sediment bed level data show relatively large gradient indicating high erosion rate compared to full sand condition (Figure 5-17, top). In Figure 5-28 the vertical profile of erosion rates for

partial and full sand conditions for Run VI, VIII, IX and X are plotted where lines with diamond markers indicate the partial sand cover condition. Note that the vertical profiles of erosion rates are computed from the fitted mean fine sediment bed level data. The erosion rate below the gravel crest for experiments conducted in partial sand condition are larger than that of full sand for the same shear stress or suspension parameters (Figure 5-28). Such behaviour of the erosion profile can be directly related to the increase in effective roughness height of the immobile gravel bed since the sand level is low in the immobile gravel bed upstream and downstream of the control section. As highlighted in Section 5.5 the increase in effective roughness height in increases turbulent intensity, Reynolds shear stress and also the total duration of high magnitude turbulent events (Sambrook Smith and Nicholas, 2005) and this could lead to increased sediment entrainment or erosion.
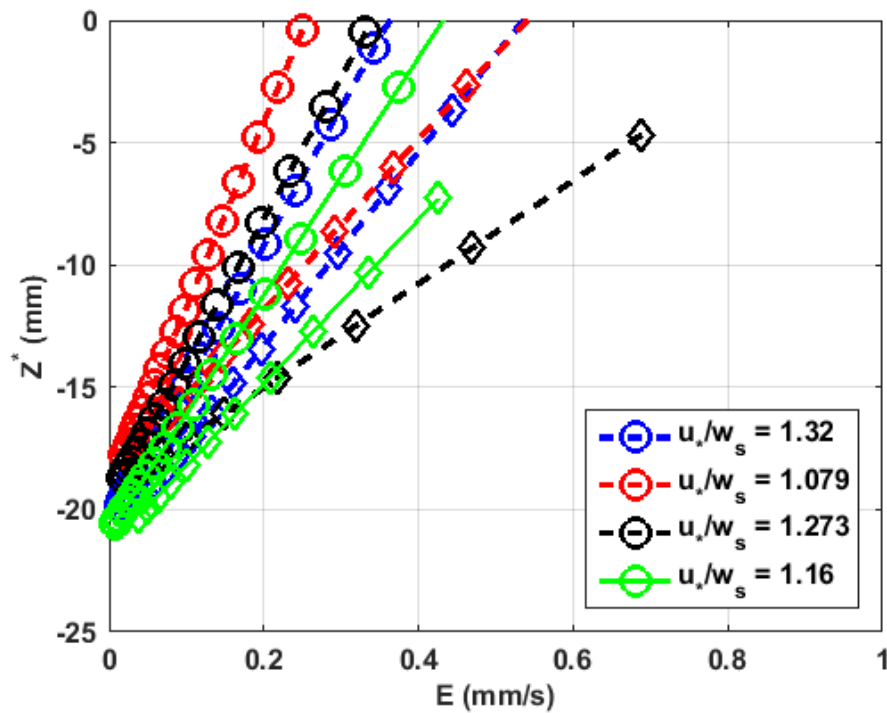
Figure 5-28. Comparison of vertical profiles of erosion rates for full (circles) and partial (diamonds) sand conditions

Figure 5-29 shows dimensionless erosion rate plotted against the dimensionless shear stress as described in Equation (5-8) for each experimental runs of full (unshaded square markers) and partial (shaded square markers) sand cover conditions. The figure shows the dimensionless erosion rates at selected depths below gravel crest for partial sand cover are related to above crest shear stress. The broken lines are linear regression fitted lines to the scattered data points. There is a linear relationship between

dimensionless erosion rate (E_*) and above crest transport stage parameters ($D_*^{0.3}T^{1.5}$) which is observed in full sand cover condition (Figure 5-29). The same relation is also valid for partial sand condition despite limited number of observations. The erosion rate for the same dimensionless shear stress applied under partial sand cover condition is observed to be as large as 1.5 to 3 folds of full sand condition.
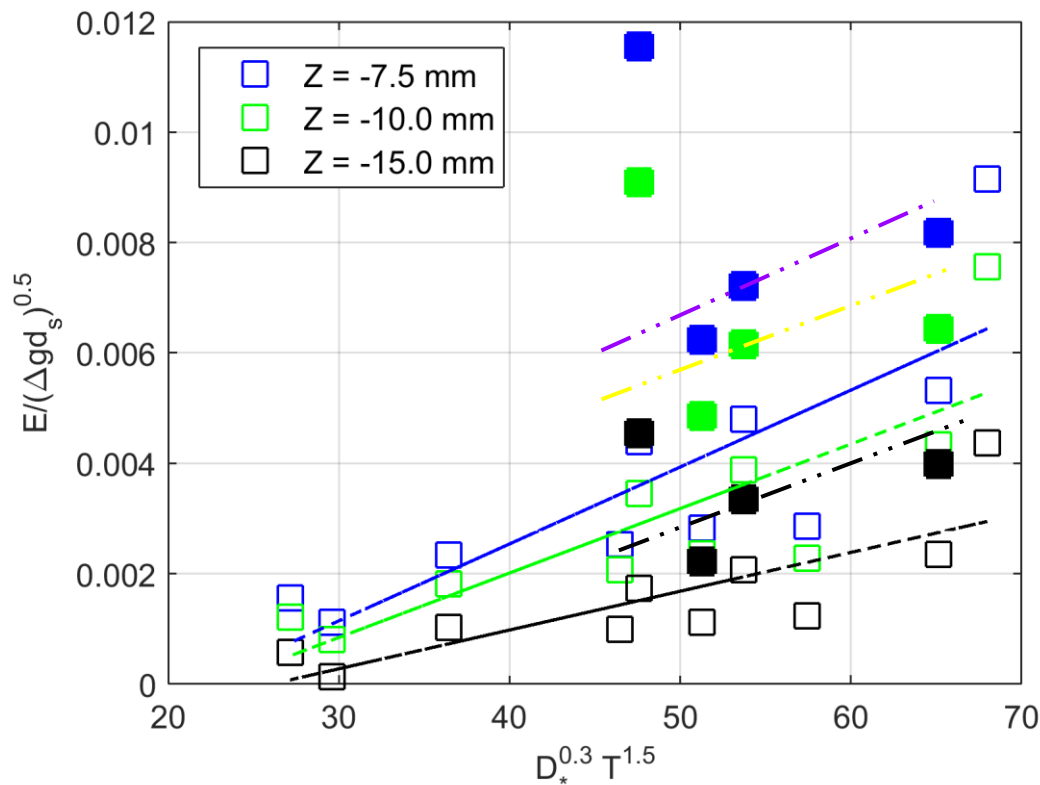
Figure 5-29. Dimensionless erosion rate of fine sediments as a function of T (estimated based on shear stress at gravel crest) and D_* for full (unshaded squares) and partial (shaded squares) sand conditions

5.7. CONCLUSIONS

In this study the characteristics of fine sediment erosion by suspension flow in immobile gravel bed are presented. An alternative non-equilibrium fine sediment erosion (pick-up) rate relation is proposed from the analysis of the experimental data and data of flow hydrodynamics in gravel bed. The most important observations from this study include the spatial dependence of erosion rate on the immobile bed topography, the effect of immobile bed roughness on flow velocity and fine sediment erosion rate,   and the link between drag force and roughness density and the relevance to estimate effective shear stress for fine sediment erosion in interfacial sublayer.

The experimental datasets showed that the temporal evolution of mean fine sediment bed level of eroding fine sediments in the immobile bed roughness elements generally showed an exponentially decaying pattern, which is expected as the fine sediment deposit among the roughness elements continuously erode. The estimates of the vertical profiles of erosion rate in the interfacial sub-layer are found to follow a linear trend with the depth of fine sediments in the layer. The spatial pattern of erosion rate varied significantly with larger erosion observed in the stoss side while smaller erosion in the lee side of gravel particles which agrees with literature evidences of turbulent flow structures in gravel bed flows. The changes in bed roughness of the gravel particles upstream and downstream of the experimental control section is found to affect the erosion rate where increase in equivalent roughness (by reducing the deposited level of immobile sand in gravel matrix) of the gravel bed intensified the erosion rate significantly. Measured stream-wise velocity profiles were also observed to be affected although not very significant. In fact, the effect of changes in roughness (immobile sand level in gravel matrix) on velocity may also depend on the relative submergence of the flow (e.g. Grams and Wilcock, 2007).

The analysis of drag force estimates from datasets obtained from three different published experimental studies showed that it can be scaled properly in the interfacial sublayer with roughness density of the immobile coarse bed. Thus, the effective (below crest) shear stress can be formulated as a function of momentum supply and drag force. This allowed developing an erosion rate formula for fine sediment transport in immobile gravel bed based on properly scaled shear stress (effective shear stress) implemented in van Rijn (1984b) non-equilibrium fine sediment transport formula. It can be argued that formulas such as van Rijn (1984b), developed for sand bed condition, can be directly applied if the effective shear stress at each fine sediment bed level below the gravel crest is properly predicted. The comparison of the predicted erosion rate and the estimates based on scaled shear stresses at each bed level of fine sediments indicated good agreement. The result revealed that proper scaling of shear stresses below gravel crest could be sufficient to predict erosion rate below crest level of immobile roughness elements with erosion formulas developed for sand bed conditions, which in this case applies for non-equilibrium transport conditions. This approach is conceptually superior and physically sound when compared to Grams and Wilcock (2013) approaches where above crest erosion rate is directly scaled empirically to predict the erosion rate when fine sediment bed level goes below gravel crest. Moreover, Grams and Wilcock (2013) relation was developed from experiments that were conducted in artificial bed with relatively simple geometry (hemispheres) which does fully represent the complex bed roughness characteristics in natural gravels. Moreover, over-prediction of entrainment rate was also noticed in Grams and Wilcock (2013) relation especially for small fine sediment bed level below immobile bed crest. Although some studies (e.g. Kuhnle et al., 2013; Pellachini, 2011) argued that below crest effective

shear stress can be scaled with the bed porosity but the analysis in this study indicated that the drag force is found to be scaled properly for the experiments under consideration. The observed dimensionless shear stress data points in the interfacial sublayer, however, were found to be rather scattered and when plotted against porosity the relationship varied from experiment to experiment (see Figure C-9 , Appendix C).

Finally, the predictive capability of the developed erosion rate relation is tested by applying it in 1-D numerical model developed to study sediment wave dynamics of reservoir sediment flushing and the results are discussed in Chapter 6.

6. MODELLING SUSPENDED SEDIMENT WAVE DYNAMICS OF RESERVOIR FLUSHING

Summary

Flushing of fine sediments from reservoirs is one of the most effective techniques to reduce reservoir sedimentation, but the sudden release of high suspended sediment concentration can have adverse effects on the receiving water body. Field observations of sediment flushing operations have shown that the released volume of water and sediments propagate downstream through different types of waves. In particular the hydrodynamic signal travels faster than the sediment signal resulting in the splitting of the two waves. Since the sediment wave lags behind, deposition is enhanced in the tail of the hydrodynamic wave, where velocity decreases and cannot sustain the sediment in suspension: the separation phase of the two waves controls the deposition process of the released suspended sediments. Thus, in this study a one-dimensional numerical model is developed to evaluate the interaction between the two waves and the spatial and temporal patterns of sediment deposition. The mathematical model accounts for the reduction of the depth-averaged sediment transport velocity as a function of Rouse number, which was neglected in most of the models. This study focused on a very simple case, considering a channel with rectangular cross-section, constant slope and width, and assuming that the bed is initially composed of non-erodible (immobile) coarse material. In this framework, the present study isolated the process of transport and deposition of the released fine sediments only. The study showed that the correction factor for sediment wave celerity enhances the deposition because of the anticipated separation from the hydrodynamic wave. The peak-to-base flow and intermittence of flushing release also play an important role in determining the length and volume of the deposited material. More in general, a series of feedbacks can be highlighted, the most important being the reduction of bed roughness in the regions of deposition of fine sediments. This work represents the first step toward the understanding of the dynamics of the waves originated by flushing operations, and hence toward strategies that may reduce downstream negative impacts.

6.1. INTRODUCTION

Reservoir sedimentation has become one of the most challenging problems of the current generation of dams with annual worldwide loss rate of storage capacity by 0.5 - 1.9% (White, 2001). Among the various methods developed up to date to tackle the problem, sediment flushing (release of deposited sediments through bottom outlets of dams) is the most effective, economic and fast method (Liu et al., 2004a). However it may often have significant effects on downstream river reaches due to the high flows

induced by the sudden release of water and high concentration of fine sediments (Espa et al., 2013; Crosa et al., 2010; Downs et al., 2009). The concentration can be extremely high, exceeding 100 g/l and in some cases even up to 1000 g/l (Morris and Fan, 2010), and fine sediments after flushing operation could infiltrate to significant depths in the river bed especially in gravel-bed interstices (Camenen et al., 2013). This may impact the downstream aquatic environment by, for instance, modifying fish survival conditions due to clogging of interstices, altering the channel morphology and destroying habitats type and stability (Wohl and Rathburn, 2003) or affecting the vegetation dynamics (Asaeda and Rashid, 2012; Camenen et al., 2013). The high concentration can reduce sediment deposition by hindered settling especially in condition when the flow is hyperconcentrated (concentration larger than 200 - 300 g/l) (van Maren et al., 2009).

Therefore, sediment flushing operations should be designed so as to safeguard the riverine ecosystems and at the same time reduce loss of storage of reservoirs. Many studies have given increasing attention to the downstream impacts of reservoirs. These studies focused on downstream morphological changes and environmental impacts due to sediment depletion and altered seasonal hydrograph (Wohl and Rathburn, 2003) with fewer studies concerning the impacts of sediment releases from reservoirs by flushing operations. Some field studies reported on the erosion and depositional processes that occur in downstream river during flushing operations (e.g. Brandt and Swenning, 1999; Camenen et al., 2013; Espa et al., 2013; Wohl and Cenderelli, 2000), and flume experiments were conducted to examine coarse and fine sediment releases (Cui et al., 2008). Numerical models are crucial to evaluate the effects of different operations on the morphological and ecological quality of downstream rivers (e.g. Liu et al., 2004a; Rathburn and Wohl, 2001).

During sediment flushing operations two pulses are typically released in the downstream reach: a larger liquid discharge and a considerable amount of solids. These two pulses can be seen as waves travelling with their own celerities. The first wave transports the signal of a hydrodynamic variable (depth, discharge or velocity) with the celerity of flood waves, thus higher than the cross-sectional averaged flow velocity (e.g. Toffolon et al., 2010). The second wave is associated with the concentration of suspended sediments or dissolved substances, water temperature, etc. Since its celerity is equal, or smaller as in the case of suspended sediments, than the flow velocity, the two waves travel with different speeds and tend to separate. For instance, this behaviour is noticeable downstream of hydropeaking releases characterized by different temperatures (Toffolon et al., 2010; Zolezzi et al., 2011).

Field investigations downstream of reservoirs similarly show that there is a time lag between the signals

of suspended solid and liquid discharge. Measurements are available for the Cachí reservoir in Costa Rica (Brandt and Swenning, 1999; Brandt, 2005) showing that the phase lag in- creases as the two waves travel in the downstream river: at three stations (10, 30 and 70 km) there exists a time lag of 2, 5 and 7 hours between sediment and discharge peaks, respectively. This time lag in the suspended sediment trans- port and its interaction with the hydrodynamic wave control the depositional pattern of the suspended sediment carried by the release. Since the sediment wave lags behind, deposition is enhanced in the tail of the hydrodynamic wave, where velocity decreases and cannot sustain the sediment in suspension: the separation phase of the two waves controls the deposition process of the released fine sediments. Nevertheless, no attempts have been made to understand the mechanism how the temporal and spatial pattern of the deposition is controlled by the interaction between the two waves. Previous studies (e.g. Rathburn and Wohl, 2001; Gallerano and Cannata, 2011; Liu et al., 2004a) focused mainly on the study of morphological evolution and suspended sediment concentration after sediment flushing. Moreover, the celerity of sediment waves is assumed equal to the depth averaged flow velocity in many models, but this assumption might be misleading in modelling suspended sediment transport that are mostly transported near the bed, where the velocity is smaller.

On the other hand, channel beds downstream of a dam is usually deprived of sediment supply and suffers from continuous erosion of the channel bed (Kondolf, 1997) and this leaves only coarser and immobile beds, which is often called a degraded and armoured bed (Kondolf, 1997). Thus, the fine sediments released during flushing operations are transported in the immobile coarse bed (e.g. Wren et al., 2011). Similar phenomenon is also common in natural rivers such as mountain and canyon rivers whose bed consist of coarse bed that are transported in rare events and most of the sediments transported are fine sediments (Grams and Wilcock, 2014). This study aims to characterize sediment flushing wave dynamics in immobile coarse bed composed by gravel, where bed roughness is controlled by the fine sediment deposition within the gravel matrix also when the deposition level does not exceed the top of the coarse material. In this situation, the entrainment of fine sediments is also hindered because of the reduction of the shear stress. The porosity of coarse immobile bed also plays important role in the deposition and entrainment of fine sediments in the matrix of immobile coarse bed. Thus understanding the deposition characteristics of the released sediments in such bed conditions when porosity is taken into account is important to design the discharge required to clean up the sediments clogging the immobile matrix. Model based studies of characterizing flushing wave dynamics and the implication on deposition of released sediments are lacking. Thus, this study attempted to reveal the relevance of coarse immobile bed porosity, bed roughness changes, celerity factor and hindered settling velocity in predicting the deposition pattern of suspended sediments of flushing releases.

First, in Section 6.2 the development of the numerical model and the key processes included are briefly presented. An approach to describe sediment flux in immobile bed is presented and implemented in the numerical model. Selected entrainment relations for sediment transport in immobile bed are also discussed. The description of bed porosity and the effect on characteristics of sediment deposition are also presented. Second, sediment wave dynamics for different celerity formulation and bed roughness parameterization are presented. In connection to this sediment deposition patterns for selected flushing release scenarios are evaluated. Selected entrainment relations for fine sediment transport in uniform sand bed are implemented in the model and their predictions are evaluated. Finally, in Section 6.4 conclusions and directions for further works are highlighted.

6.2. FORMULATION OF THE MODEL

6.2.1.   Simplified case study

In this study, the focus is on a very simple case in order to highlight only some selected features of the complex processes occurring during sediment flushing operations. In particular, the river bed is assumed to be initially composed by coarse sediments only. This initial bed is not erodible, as in the case of a gravel-bed river subject to a relatively low discharge that is not able to move the coarse sediment matrix. During flushing operations a given amount of water and fine sediments is released in a limited time period, producing two waves traveling downstream. The fine sediments are transported by the flood wave, but the initially high concentration can produce deposition. Part of these deposits can be slowly eroded and possibly deposited again in a downstream region. The aim of this work is to study the dynamics of these depositional patterns in order to have a clear description of the role of some different factors. Among the most important processes, this study analyses: the dynamics of the separation of the flood wave from the sediment wave; the role of the bed roughness that changes depending on the type of sediments in the bed surface layer (either fine or coarse); the sensitivity of the results with different formulations of the fine sediment erosion.

6.2.2.   Governing Equations

This study focuses on the large-scale dynamics of sediment transport and, as a first approximation, with no consideration for any lateral distribution of the variables along the cross-section. Thus, a one-dimensional (1-D) description of the system is adopted. The variables introduced include Q for the water discharge, A for the cross-section area, and B for the top width. Thus $U = Q/A$ is the cross-sectional averaged velocity, $h = A/B$ is the averaged depth and $q = Q/B$ is discharge per unit width. Moreover, the cross-section is assumed as rectangular and wide enough to approximate the hydraulic radius by means of

the flow depth. This approximation can be easily relaxed in further studies dealing with the local distribution of depositional patterns.

The hydrodynamic wave can be described by the usual 1-D Saint-Venant shallow water equations

$$\frac{\partial A}{\partial t} + \frac{\partial Q}{\partial x} = 0 \tag{6-1}$$

$$\frac{\partial Q}{\partial t} + \frac{\partial}{\partial x}\left(\beta\frac{Q}{A} + gI_1\right) = gI_2 + gA(S_0 - S_f) \tag{6-2}$$

where t = time, x = the longitudinal spatial co-ordinate, β = the coefficient accounting for the deviation of local values of momentum from its cross-sectional average, g the gravitational acceleration, S_0 = the local bottom slope, S_f = the local energy slope, I_1 = the hydrostatic pressure force term, I_2 = the pressure forces in a volume of constant depth due to longitudinal variations (e.g. Siviglia and Toro, 2009).

The transport of suspended sediment is governed by the continuity equation of the solid phase

$$\frac{\partial CA}{\partial t} + \frac{\partial}{\partial x}\left(\alpha CQ\right) = \frac{\partial}{\partial x}\left(KA\frac{\partial C}{\partial x}\right) + B(E - D) \tag{6-3}$$

where C = the depth-averaged volumetric sediment concentration, α = the correction factor for sediment wave celerity, K = the longitudinal diffusion/dispersion coefficient, E and D = sediment entrainment and deposition from/on the bed respectively. The sediment exchange E - D with the bottom layer is evaluated at the interface between the mobile bed and the water column where the near bed suspended sediment concentration is estimated. The net flux of sediment across such an interface can produce a variation of the volume of sediment deposition which is a measure of bed elevation

$$\frac{\partial \xi}{\partial t} = \frac{(D - E)}{1 - p} \tag{6-4}$$

where ξ is the volume of sediment deposit per unit surface area and p is the porosity of bed fine sediments. For sake of simplicity, the effect of bed load in the Exner Equation (6-4) is neglected.

The unknown variables in the governing equations are A, Q, C and ξ, while the terms S_f , E, D are determined by means of empirical closure relationships, which are discussed in the following sections. The estimate of the diffusion/dispersion coefficient K depends on the distance from the release point (e.g. Rutherford, 1994). In the intermediate field it can be estimated by Elder (1959) formula, while in the far field the Fischer's relationship (Fischer et al., 1979) is typically used. In this work Fischer's relationship given by: $K = 0.011B^2U^2/hu_*$ is used.

6.2.3.   Flow resistance and bottom shear stress

Flow resistance in mobile-bed conditions depends on two main factors: the so-called skin friction, which represents the drag force exerted by the single sediment grains of the bed surface, and the resistance due to bed forms of different sizes (mainly ripples and dunes in sand-bed river; for the cross-section averaged effect of alternate bars see Francalanci et al. (2012)). While the total resistance determines the flow conditions, the skin friction is important for sediment transport because sediment movement depends on the force acting on individual grains (e.g. van Rijn, 2007). This study introduces the dimensionless Chézy coefficient $\chi = U/u^*$, where u* is the friction velocity ($=\sqrt{ghS_0}$ in uniform flow conditions).

Two bed roughness parameterizations are considered: when fine sediment in bed (deposited) and transported are similar and when fine sediments are transported in immobile coarse bed. For the latter, this study considered a transport condition when fine sediments are released from impoundments (dams) and transported in riverbed composed of relatively less mobile (immobile bed) coarse gravel. Such transport and flow conditions are common phenomena downstream of dams during sediment flushing operations and dam removals (e.g. Wren et al., 2011; Cui et al., 2008; Grams and Wilcock, 2014). The immobile coarse gravel material can be characterized by a fixed bed roughness coefficient (determined by χ_g, where χ_g stands for Chézy coefficient of clean gravel bed), and considering that bed form resistance is not present for gravel-bed conditions. The fixed roughness is estimated by means of the Strickler coefficient based on Meyer-Peter and Müller (1948) formula and converted to Chézy coefficient, which solely depends on the mean grain size of gravel particle, d_g (= mean diameter of immobile gravel bed materials). Moreover, this study assumes that a single characteristic grain size d_s (= mean diameter of fine sediment materials) can be used to describe the fine sediment transport, for which bed forms increasing flow resistance can develop.

In order to estimate the bed form resistance when the bed comprises purely fine sediments (or when fine sediments are deposited over the immobile bed), the approach proposed by Wright and Parker (2004) is adopted, where the total shear stress $\tau = \tau_s + \tau_f$ is the sum of the shear stress acting on the sediments, $\tau_s = \rho g S_0 h_s$, and that due to bed forms, τ_f . The skin-related flow depth h_s is determined through the relationship

$$\chi = \frac{U}{\sqrt{gh_s S_0}} = 8.32 \left(\frac{h_s}{k_s} \right)^{1/6} \tag{6-5}$$

where $k_s = 3d_{90}$ is the grain equivalent roughness (van Rijn,1984a). Wright and Parker (2004) propose the following relationship,

$$\theta_s = 0.05 + 0.7 \left(\theta F_r^{0.7} \right)^{0.8} \tag{6-6}$$

between the Shields number related to the skin friction, $\theta_s = \tau_s /(\rho g(s-1)d_s)$, and the total, $\theta = \tau /[\rho g(s-1)d_s]$. Here $F_r = U/\sqrt{gh}$ is the Froude number and $s = 2.65$ is the relative density of sediments with respect to water. The total Chézy coefficient is then calculated as

$$\chi = \frac{U}{u_*} = 18 \log \left(12 \frac{h}{k_s} \right) \tag{6-7}$$

This approach allows for an implementation of changes in bed roughness that takes into account the changes in bed forms with the flow conditions, i.e. a feedback between the hydrodynamics and the morphodynamics is established. Villaret et al. (2013) show that the use of a constant bed roughness leads to an overall reduction in the sediment transport rates. The friction slope S_f is finally calculated as

$$S_f = \frac{Q^2}{gA^2 \chi^2 R} \tag{6-8}$$

where R = hydraulic radius, which can be approximated by flow depth h exploiting the assumption of wide rectangular cross-section.

Figure 6-1 shows the conceptual framework of fine sediment transport (deposition and entrainment or

erosion) in immobile gravel matrix and the parameters used for bed roughness characterization where η = the thickness of fine sediment deposit in the coarse immobile gravel bed. When the thickness of fine sediment (sand) deposit decreases enough, it goes below the immobile gravel crest level resulting in emergence of gravel protrusions. As a result the bed roughness changes creating a rougher bed, and this change in roughness is purely due to level of deposit in the coarse immobile bed. Thus, the bed roughness for hydrodynamic computation is estimated as a function of the sand level below the gravel crest, the roughness of clean gravel bed and pure fine sediment bed, and the thickness of interfacial sub-layer of the immobile gravel bed. The thickness of the interfacial sub-layer is approximated by $\zeta = 1.5d_g$ (e.g. Nikora et al., 2001). The flow resistance or bed roughness when the fine sediment bed level is within the interfacial sublayer is expressed as a simplified linear function of the depth (thickness) of fine sediments (η) and Chézy coefficient of a sand bed (χ) and gravel bed (χ_g) (after Mignot et al. (2009)) and given as: $\chi_g + \eta(\chi - \chi_g)/\zeta$. The vertical variability of the dimensionless Chézy coefficient with fine sediment bed level inside the gravel framework occurs between a value of 0.3 and 0.6 (Mignot et al., 2009; Pellachini, 2011). The full description of the formulation is discussed in Pellachini (2011).
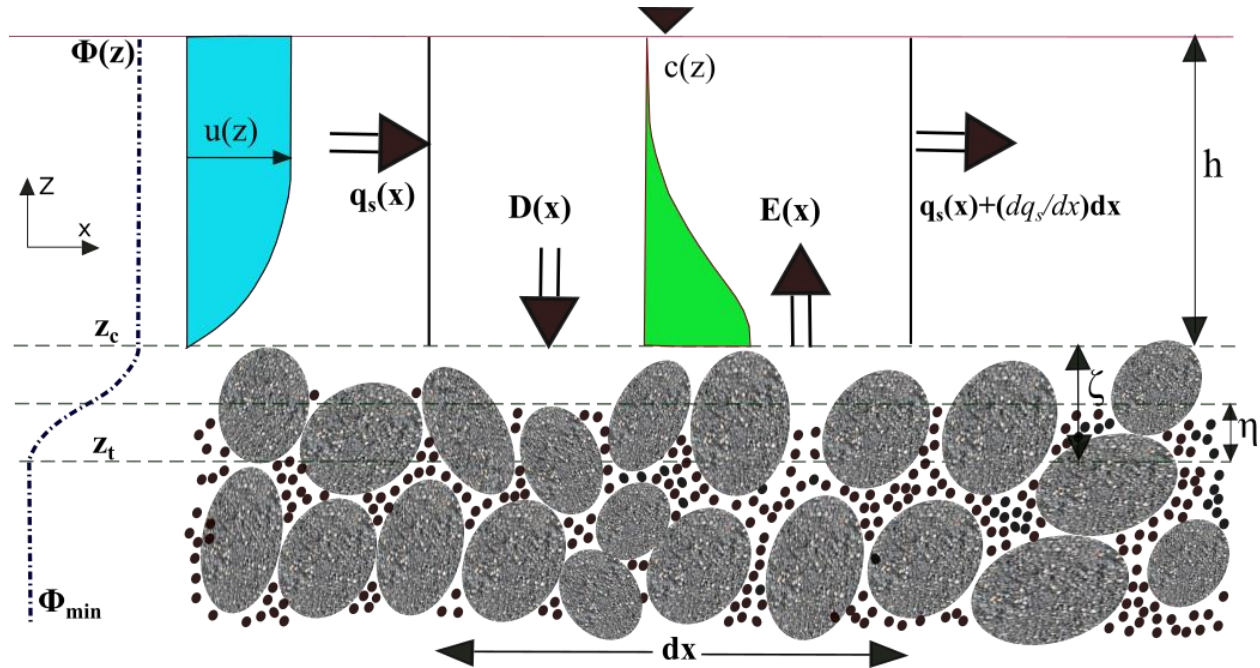
Figure 6-1. Conceptual diagram of water column, fine sediment erosion (E) and deposition (D) in the gravel matrix which depict variations in bed roughness with fine sediment bed (sand) (black dots) level where q_s = sediment load per unit width; c and u = profiles of concentration and flow velocity; Z_c = gravel crest; Z_t = bottom of roughness layer; Φ = gravel porosity

It is important to take into account that two conditions affect the fine sediment transport in the immobile bed: 1) the partition of the total bed shear stress on gravel particles and fine sediment particles and; 2) the surface (area) coverage of the fine sediments in the gravel bed or gravel matrix. The gravel protrusions decrease as the sand elevation (bed level) in the gravel increases, thus decreasing the turbulent fluid shear stress (Kuhnle et al., 2012). When the sand elevation is above the gravel crest (Z_c) the channel bed becomes a purely sand bed condition. This study assumes that the reference point for sand elevation in the gravel roughness elements is taken as the elevation below the gravel crest where sand entrainment is very small. This point can be considered as the bottom of the roughness sublayer (Z_t), where fluid (turbulent) shear stresses are nearly negligible. In Figure 6-1the vertical profile of the immobile gravel bed porosity is denoted by Φ.

6.2.4.   Sediment flux at the bed

Deposition and entrainment fluxes of fine sediments at the bed are estimated by empirical relationships. The deposition flux can be readily calculated as (Richardson and Zaki, 1954)

$$D = wC_b \tag{6-9}$$

where w is the effective settling velocity of a single particle settling and velocity C_b is the near bed concentration. The effective settling velocity is calculated as $w = w_0(1-C)^m$ (after Richardson and Zaki, 1954) to account for the effect of sediment concentration on settling velocity. The hindering factor m indicates the effects of high sediment concentration for particle sizes of 50-500 μm (van Rijn, 1984a); this study assumes a value $m = 4.45R_p^{0.1}$, where $R_p = w_0 ds/\nu$ is the particle Reynolds velocity and ν the kinematic viscosity of water. In a sediment-laden turbulent flow in vigorous conditions, for instance in sediment flushing operations, high concentrations (c > 0.01, c = local concentration) could occur in the near-bed layer. In such situations 'hindered' settling occurs, thus the settling velocity of a grain in isolation needs to be corrected to take account of both grain-grain and grain-fluid interactions (Li and Davies, 2001).

The settling velocity in quiescent water w_0 is calculated following Dietrich (1982) relation: $w_0 / \sqrt{(s-1)gd_s} = \exp\left\{-b_1 + b_2 \ln(R_{ep}) - b_3 [\ln(R_{ep})]^2 - b_4 [\ln(R_{ep})]^3 - b_5 [\ln(R_{ep})]^4\right\}$ where $R_{ep} = d_s \sqrt{(s-1)gd_s} / \nu$ is the particle Reynolds number and $b_1 = 2.891394$, $b_2 = 0.95296$, $b_3 = 0.056835$, $b_4 = 0.002892$ and $b_5 = 0.000245$. The near bed concentration is related to the depth-averaged concentration C through the relation $C_b = \gamma C$, where γ is an empirical adaptation coefficient of suspended load (Wu and Wang, 2007). The estimate of γ can be obtained by depth integration of Rouse profile, Equation (6-17), as

shown in Equation (6-20). However, following Cao et al. (2004), Cao et al. (2006), and Wu and Wang (2007), this study adopts a minimum value of $\gamma = 2$ as necessary.

The entrainment flux E, which describes the erosion of sediments from the bed, is a function of the hydrodynamics and of the sediment characteristics. In order to describe the process in a simpler way, this study introduces the concept of dynamic equilibrium concentration whereby deposition of sediments equals erosion (Cao and Carling, 2002; Celik and Rodi, 1988), and hence introduce the equilibrium near-bed concentration $C_b = C_e$ for which

$$D = wC_e = E \tag{6-10}$$

There are a wide variety of empirical and semi-empirical formulations to estimate sediment entrainment from channel bed materials composed of mainly uniform fine sediments. Four widely used entrainment relationships are tested to estimate entrainment flux: van Rijn (1984a) (hereafter indicated as VR), Smith and McLean (1977) (SM), Garcia and Parker (1991) (GP) and Zyserman and Fredsoe (1994) (ZF). The reference level at which the entrainment flux estimates vary among level (Zr) at which the different relations and it is given as 0.05H, $2d_{50}$, max(k_s,0.01H), and $26.3(\theta - \theta_c)d_{50} + k_s$ for GP, ZF, VR and SM, respectively.

The relationships can be cast in a common form,

$$C_e = \frac{aT^n}{b} \tag{6-11}$$

where a and n are constants. The values of the constants is reported in Table 6-1, where θ_s = skin-related Shields number, θ_c = the critical value sediment motion, Z_r = the near-bed reference level, and T = dimensionless transport variable that is a function of shear stress (θ and θ_c).

Table 6-1. Parameters used in Equation (6-11)

Authors	a	T	b	n
SM	γ_0	$(\theta - \theta_c)/\theta_c$	$1+aT$	1.00
GP	1.3×10^{-7}	$u_* R_{ep}^{0.6}/w$	$1+3.33aT$	5.00
ZF	0.331	$\theta - \theta_c$	$1+2.17aT$	1.75
VR	0.015	$(\theta - \theta_c)/\theta_c$	$Z_r R_{ep}^{0.6}/d_{50}$	1.50

Since we assume that the bed is not erodible and that only the fine sediments are transported and eventually deposited, a limit exists for the amount of entrained material. Referring to Equation (6-4), the maximum erosion rate is determined by the already deposited material. Thus, in a computational time step Δt, the actual erosion is

$$E = \min\left\{ E_0; D + \frac{(1-p)\xi}{\Delta t} \right\} \tag{6-12}$$

where E_0 is the theoretical value determined by Equation (6-10).

The entrainment rate or erosion rate or pick up rate of fine sediments in immobile coarse bed cannot be predicted by formulas described in Table 6-1. Thus, formulations that are specifically developed to predict entrainment or erosion rate must be used. The present study considered entrainment relations by Grams and Wilcock (2014), Cui et al. (2008) and the erosion rate formula proposed in Chapter 5. Grams and Wilcock (2014) formula corrects the entrainment rate formula of sand bed condition by Garcia and Parker (1991) when the fine sediments are within the interfacial sublayer. The correction function is given by: $E(\eta)/E(0) = \left(1 + e^{-9.3(\eta/\zeta - 0.13)}\right)^{-2.8}$ for $\eta/\zeta < 1$ where $\zeta = R$ for hemispherical bed. While the formulation by Cui et al. (2008) is not specifically developed for fine sediment entrainment in immobile bed. Nevertheless, Cui et al. (2008) developed a simple correction function, to estimate transport rate of fine sediments in immobile coarse bed, by considering the roughness differences between a gravel bed and sand bed at grain size scale, and by this partitioning the total shear stress on sand and gravel particles. Cui et al. (2008) also included an additional correction that takes into account partial sand coverage in the coarse immobile bed. This correction function is given by: $E(\eta)/E(0) = \left(\eta/(\zeta - k_s)\right)\left(k_s/(\zeta - \eta)\right)^{7/20}$ for $\eta/(\zeta - k_s) < 1$ where $\zeta = 2d_g$ is roughness height of gravel and $k_s = 2d_s$ is roughness height of fine sediment. The derivation and mathematical description of the correction function is presented in Cui et al. (2008). This correction is applied on VR formula of fine sediment entrainment in sand bed condition to estimate entrainment rate in immobile coarse bed by suspension flow. The erosion rate formula developed

in Chapter 5 is also evaluated in the numerical model to predict sediment entrainment in immobile bed from experimental data obtained from Grams and Wilcock (2014). The plot of theoretically analysed erosion rates based on the correction functions of the three different formulations considering transport of fine sediments in hemispherical bed (from Grams and Wilcock (2014)) and coarse immobile gravel bed with flow rate, bed slope, and fine sediment grain sizes: q = 0.80m2/s, S_0 = 0.007, and d_{50} = 230μm and d_{90} = 320μm respectively is presented Figure 6-2. Figure 6-2 (in diamond) shows that the estimates of fine sediment erosion rate by Grams and Wilcock (2014) exhibit no difference with respect to the estimate in sand bed condition mid-way through the interfacial sublayer (> 0.5ζ, where ζ = R for hemispheres and ζ = d_g for gravels). It is also clear that erosion rate increases steadily in the lower part of the roughness layer. The estimates by the method presented in Chapter 5 and by Cui et al. (2008) show a different distribution of erosion rate in the interfacial sublayer as compared to Grams and Wilcock (2014). They show also a very similar trend especially in the upper part of the interfacial sublayer (in circle and square). Nevertheless, Cui et al. (2008) relation varies among η / ζ (refer Cui et al. (2008)), thus the good agreement with the relation in Chapter 5 may fail to agree for some values of η/ζ other than discussed here.
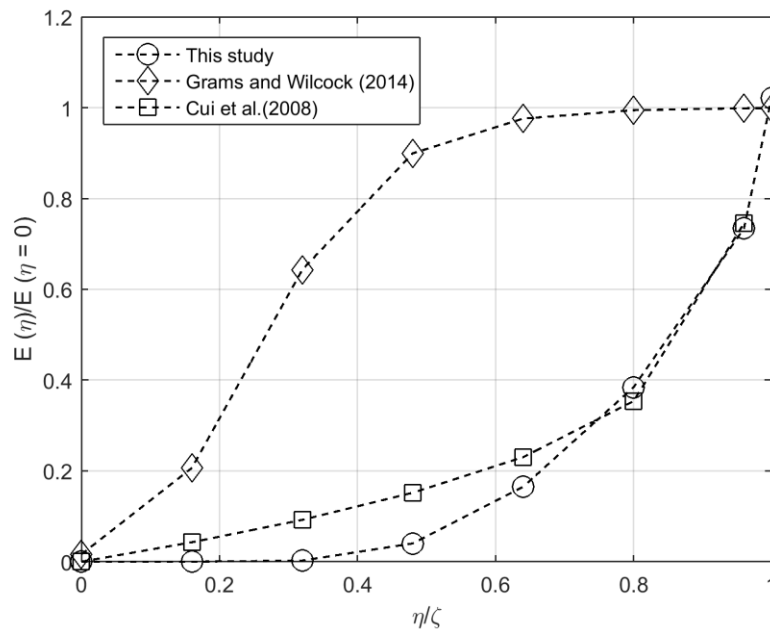
Figure 6-2. The ratio of erosion rates below gravel crest, E (η), and above or at crest of gravel, E (0), estimated by different relations

6.2.5.   Characterization of immobile gravel bed porosity

The transport of fine sediments in immobile bed is closely related to the porosity of the immobile bed. The bed porosity directly affects the bed permeability and bed permeability increases flow resistance and modifies spatial structure of the flow in the vicinity of roughness elements (Pokrajac and Manes, 2009). The flows in the interstices are strongly dominated by wakes shade by the immobile grains (Grams and Wilcock, 2014). The fine sediments occupying the porous interstices modifies the flow structure and intensity of the turbulent wakes affecting erosion and entrainment process of the fine sediments (Wren et al., 2013). The bed porosity also determines the proportion of fine sediments and effective fluid shear stress in the interfacial sublayer of the immobile gravel bed (Kuhnle et al., 2012). Overall, the quantity of fine sediments entrained during sediment transport over immobile bed depends on bed porosity and the flow required to clean up the fine sediments should be designed taking into account the effect of changing porosity in the immobile bed. The present study describes such process in the numerical model and evaluates the effect on thickness of sediment deposit and entrainment.

The thickness of sediment deposit is estimated considering immobile gravel bed that takes into account the thickness of the interfacial layer and the porosity function of the immobile bed (Φ). In Equation (6-4) the volume of fine sediment deposit per unit area is computed by the numerical model. When the channel bed is an immobile coarse bed, the volume of deposition per unit area changes because the area of deposition changes with the porosity of the immobile coarse bed. In this case the porosity function is used to estimate the thickness of sediment deposit (η) in the interfacial sublayer. The thickness of sediment deposit (η) is formulated for two conditions: when the volume of fine sediment deposit per unit area (ξ) is larger than the total void of the immobile bed per unit area (η_0) and when it is smaller than η_0. The relationships are given as: $\eta = f(\eta)$ for the former and $\eta = \xi - \eta_0 + \zeta$ for the latter where $\eta_0 = \int_0^\zeta \phi(z)dz$ and $f(\eta) = \left(\int_0^\eta \phi(z)dz \right) - \xi = 0$. The equation $\eta = f(\eta)$ can be solved by iterative procedure or analytically, depending on the equation describing the bed porosity, to compute the thickness of the sediment deposit in the interfacial sublayer. In the present study two types of bed condition are considered to model fine sediment transport dynamics: hemispherical bed (diameter 2R = 150 mm) and gravel bed (d_g = 35 mm). The porosity of the hemispherical bed and gravel bed are given as: $\phi(z) = 1 - (\pi/2\sqrt{3})\left(1 - (z/R)^2\right)$ and $\phi(z) = \phi(z_t) - (z/d_g)\left(1 - \phi(z_t)\right)$ respectively where the porosity of immobile gravel bed material is approximated by a linear relation in the interfacial sublayer.

6.2.6. Sediment wave celerity

Many suspended sediment transport models assume that advection occurs with the depth-averaged flow velocity U. However, since the vertical distribution of both longitudinal velocity and suspended sediment concentration is not uniform, the depth-integrated transport is

$$q_s = \int_{z_r}^{h} cudz = \alpha CUh \tag{6-13}$$

where u(z) and c(z) are the vertical profiles of velocity and concentration, respectively, z is the vertical coordinate with origin at the bed level, and α is the correction factor already introduced in Equation (6-3). Since velocity increases upward approximately following a logarithmic profile while the suspended sediment concentration is maximum toward the bottom, the overall transport is less that the product CUh that could be expected for a tracer uniformly distributed along the vertical. Thus it is important to estimate the value which contains the Einstein integrals (Einstein, 1950).

$$\alpha = h \frac{\int_{Z_r}^{h} cudz}{\int_{Z_r}^{h} udz \int_{Z_r}^{h} cdz} \tag{6-14}$$

In order to express the sediment wave celerity explicitly, Equation (6-3) can be rewritten as

$$\frac{\partial C}{\partial t} + \alpha U \frac{\partial C}{\partial x} = \frac{1}{A} \frac{\partial}{\partial x}\left(KA\frac{\partial C}{\partial x}\right) + \frac{E-D}{h} - (1-\alpha)\frac{\partial A}{\partial t} \tag{6-15}$$

where the longitudinal variation of α have been neglected. Two interesting features can be deduced from Equation (6-15). First, the sediment wave celerity is αU, which is in general slower than the depth-averaged velocity U (≤ 1 always); hence, the separation between the hydrodynamic wave and the sediment wave is enhanced. Second, an additional source term arises in Equation (6-15) when α ≠ 1. This term can increase the concentration in the falling phase of the hydrodynamic wave (∂A/∂t < 0) producing values higher than the previous maximum even without a net erosion from the bed (E - D > 0), an occurrence that is usually not possible in standard advection-diffusion problems.

In general, the value of α from Equation 22 cannot be calculated analytically. However, an approximate solution can be obtained by assuming logarithmic profile of velocity

$$u = \frac{u_*}{\kappa} \ln\left(\frac{z}{z_0}\right)$$

(6-16)

where $z_0 = 0{:}033k_s$; $u_* = $ bed-shear velocity; $\kappa = $ the von Karman constant; and $k_s = $ bed roughness. It is assumed that the bed roughness to be equal to grain roughness thus $k_s = 3d_{90}$ (van Rijn, 1984a) is adopted where $d_{90} = 90\%$ particle diameter of sediment material and the simplified Rouse profile for the suspended sediment concentration

$$c = C_b\left(\frac{z}{z_r}\right)^{-R_0}$$

(6-17)

based on a linear diffusivity profile, where $R_0 = w/\kappa u_*$ is the Rouse number. The reference level (z_r) is also taken as $k_s = 3d_{90}$. Huybrechts et al. (2010) propose a simplification of the Einstein integrals that provides the analytical solution

$$\alpha = -\left(\frac{I_2 - I_1 \ln\left(\frac{z_r^*}{30}\right)}{I_1 \ln\left(\frac{ez_r^*}{30}\right)}\right)$$

(6-18)

where $z_r^* = z_r/h$ and the two integrals read

$$I_1 = \begin{cases} -\ln z_r^* & , R_0 = 1 \\ \dfrac{1 - z_r^{*(1-R_0)}}{1 - R_0} & , R_0 \neq 1 \end{cases} \qquad \& \qquad I_2 = \begin{cases} -0.5\left(\ln z_r^*\right)^2 & , R_0 = 1 \\ \dfrac{I_1 + z_r^{*(1-R_0)} \ln z_r^*}{1 - R_0} & , R_0 \neq 1 \end{cases} \tag{6-19}$$

The depth-integration of the Rouse profile simplified as in Equation (6-17) gives an analytical relation between the mean (depth-averaged) concentration (C) and the reference concentration (C_b):

$$\gamma^{-1} = \begin{cases} -z_r^* \ln z_r^* & , R_0 = 1 \\ z_r^*\left(\dfrac{1 - z_r^{*(1-R_0)}}{1 - R_0}\right) & , R_0 \neq 1 \end{cases} \tag{6-20}$$

6.2.7. Numerical Solution

The mathematical model solves Equations (6-1), (6-2) and (6-3) in a fully coupled manner. Following Siviglia and Toro (2009), the operator splitting method for Advection-Reaction-Diffusion Splitting (ARDS) is used. First, the advection-reaction part is computed at each time step by the Weight Average Flux (WAF) scheme, which is second-order accurate in space and time. An explicit finite volume conservative discretization of advective-reactive is adopted, and the time step is chosen according to the Courant-Friedrich-Levy (CFL) condition in order to ensure stability to the numerical scheme. Then, the solution of the first step is used as initial condition to solve the advection-diffusion problem by means of a non-linear version of the Crank-Nicolson method (Crank and Nicolson, 1947), an unconditionally stable implicit second-order finite difference method. The conservative form of the system of the governing Equations (6-1), (6-2) and (6-3) is given as follows:

$$\frac{\partial \boldsymbol{U}}{\partial t} + \frac{\partial \boldsymbol{F(U\,)}}{\partial x} = \mathbf{S(U)} + \frac{\partial}{\partial x}\left[\boldsymbol{K}\left(\frac{\partial \boldsymbol{U}}{\partial x}\right)\right] \tag{6-21}$$

where $\mathbf{U}$ = vector of unknowns; $\mathbf{F(U)}$ = flux vector; $\mathbf{S}$ = source term vector; $\mathbf{K}$ = diffusive tensor.

$$U = \begin{bmatrix} A \\ Q \\ AC \end{bmatrix} ; S = \begin{bmatrix} 0 \\ gI_2 + gA(S_0 - S_f) \\ (E - D)B \vert_{z=\eta} \end{bmatrix} \tag{6-22}$$

$$F = \begin{bmatrix} Q \\ \beta \dfrac{Q^2}{A} + gI_1 \\ \alpha QC \end{bmatrix} ; K = \begin{bmatrix} 0 & 0 & 0 \\ 0 & 0 & 0 \\ D_x C & 0 & D_x \end{bmatrix} \tag{6-23}$$

The Jacobian matrix associated to the flux is as follows:

$$\dfrac{\partial F}{\partial U} = \begin{bmatrix} 0 & 1 & 0 \\ g\dfrac{A}{B} - \beta\left(\dfrac{Q}{A}\right)^2 & 2\beta\dfrac{Q}{A} & 0 \\ -\alpha\dfrac{QC}{A} & \alpha C & \alpha\dfrac{Q}{A} \end{bmatrix} \tag{6-24}$$

where β and B are taken as unity. The advective-reactive part is described by non-linear system of differential equations shown in Equation (6-25).

$$\dfrac{\partial U}{\partial t} + \dfrac{\partial F(U)}{\partial x} = S(U) \tag{6-25}$$

An explicit finite volume conservative discretization of advective-reactive gives

$$U_i^{k+1} = U_i^{k+1} + \dfrac{\Delta t}{\Delta x}\left(F_{i+1/2} - F_{i-1/2}\right) + \Delta t S_i \tag{6-26}$$

where Δt = time step; Δx = spatial step; i = spatial node; k = time step index; $F_{i+1/2}$ = numerical flux at x = $x_{i+1/2}$ and S_i = numerical source term. The weighted average state ($U^k_{i+1/2}$) is determined by TVD version of WAF scheme (Toro, 2001) as shown in Equation (6-27).

$$U^{k+1}_{i+1/2} = \frac{1}{2}\left(U^k_i + U^k_{i+1}\right) + \frac{1}{2}\sum_{j=1}^{3}\operatorname{sgn}(c_j)A^j_{i+1/2}\left(U^{j+1}_{i+1/2} - U^j_{i+1/2}\right) \tag{6-27}$$

where $c_j = S_j\Delta t/\Delta x$ = Courant number related to wave speed; S_j and A_j = WAF limiter function. The numerical flux, for WAF Scheme, is finally obtained as:

$$F_{i+1/2} = F\left(U_{i+1/2}\right) \tag{6-28}$$

The advective-diffusion problem is described by the following non-linear system of differential equations:

$$\frac{\partial CA}{\partial t} = \frac{\partial}{\partial x}\left(D_x A\frac{\partial C}{\partial x}\right) \tag{6-29}$$

6.3.   RESULTS AND DISCUSSION

6.3.1.   Model inputs and initial conditions

First, sediment concentration and bed elevation data from a series of flume experiments that were conducted by Grams and Wilcock (2014) for fine sediment transport by suspension in immobile hemispherical bed (diameter = 150 mm) were used in this modelling work. The immobile hemispheres were arranged in tetrahedral packing (e.g. Frings et al., 2008) and experiments were run in 84 m long flume for uniform flow depth = 60 cm, channel bed slope = 0.0005, channel width = 2.74 m. The data were collected in a test section of 40 m located 17 m from downstream end of the flume outlet. Non-uniform sediments, d_{50} = 130 µm were fed for 90 min and segments of experiments were run for a total duration of 661 min (see the details of Run 1 in Grams and Wilcock (2014)). The sediment feed rate were converted to volumetric concentration and used as an upstream boundary condition to test the numerical model developed in this study (see Figure 6-3). In the modelling exercise clean water and a uniform flow was imposed as an initial condition and no fine sediment deposit in the hemispherical bed. The modelling was conducted assuming the fine sediments are nearly uniform with d_{50} = 130µm and d_{90} = 200µm.

Second, although flushing operations are common practices, exhaustive information is usually not available for the input data, the calibration and the validation of a modelling exercise like the one this study is presenting. One of the most documented case studies is the Cachí Reservoir flushing in Costa Rica (Brandt, 2005). Therefore, most of the input variables are adopted from that case for sediment wave dynamics and transport characterization. The main model inputs are summarized in Table 6-2. For sake of simplicity, the upstream boundary conditions are defined in the form of a rectangular shaped hydrograph and sedimentograph and are plotted (in black) along with the observed discharge (in blue) and sediment concentration (in green) data at 10 km downstream of the dam (see Figure 6-4).

Initially, clean water ($C = 0$) and uniform flow are imposed along the whole river, whose slope is assumed constant. The channel cross-section is assumed rectangular and wide, so that just the discharge per unit width q = Q/B is considered. All sediment flushing modelling exercises presented in this study were conducted considering transport in immobile gravel bed, unless and otherwise stated, and the immobile coarse bed is assumed clean as an initial condition. The simulation domain length (L_d) is 500 km so as to observe the sediment wave dynamics over a long spatial scale.

Table 6-2.Input datasets used for modelling the sediment flushing of Cachí Reservoir

Model parameter	Value
Base unit discharge q_b	$0.62 \text{ m}^2\text{s}^{-1}$
Peak unit discharge q_p	$4.0 \text{ m}^2\text{s}^{-1}$
Release duration t_p	3 hr
Bed slope S_0	0.007
Base sediment concentration C_0	0 g l^{-1}
Peak sediment concentration C_p	344.5 g l^{-1}
Grain size of fine sediments d_s	230 μm
Grainsize of immobile gravel d_g	35 mm
Sand porosity p	0.40
Roughness of immobile gravel bed χ_g	$26/(3d_g)^{1/6}$
Simulation period	30 hr
Spatial steps Δx	50 m
Courant-Friedrich-Levy CFL	0.95
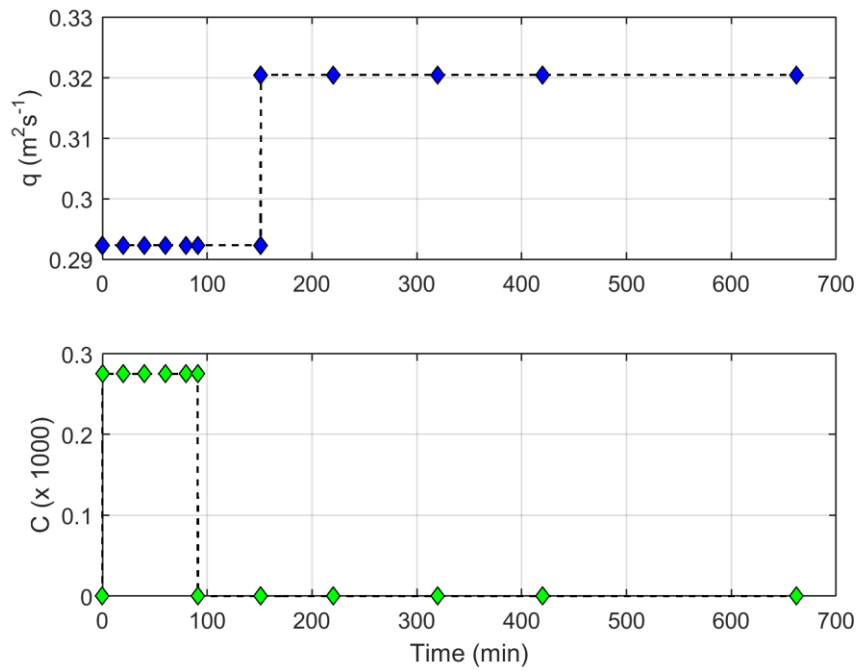
Figure 6-3. The flow and concentration boundary conditions of experiment (Run 1) of Grams and Wilcock (2014) conducted in immobile bed conditions and used in numerical model testing
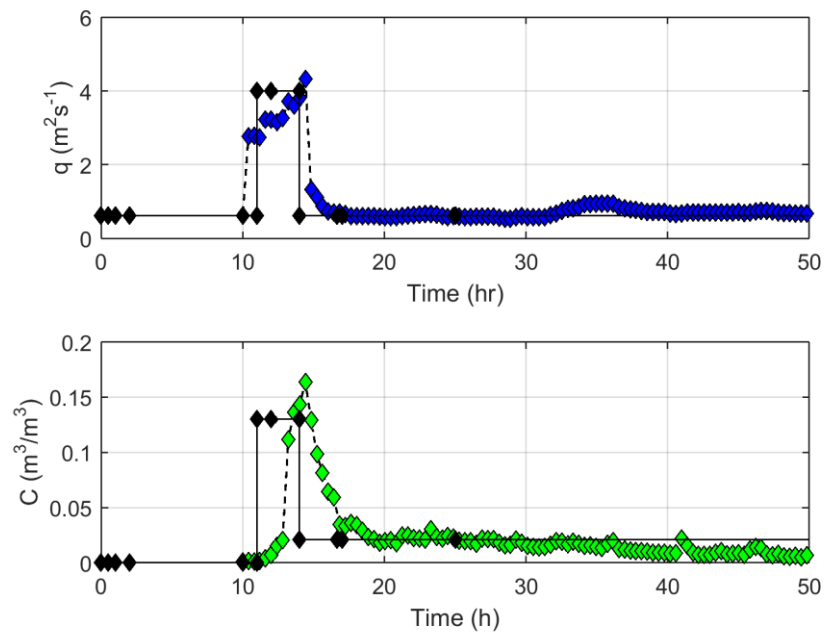
Figure 6-4. The flow and concentration boundary conditions used for sediment flushing modelling of Cachí Reservoir

6.3.2.   Model testing of fine sediment transport in immobile bed conditions

Here the comparisons of the numerical simulation of fine sediment transport in immobile hemispherical bed and the corresponding experimental observations of Grams and Wilcock (2014) are presented where the boundary conditions in Figure 6-3 were used as model inputs. The main aim is to test the model performance and fine sediment entrainment or erosion relations from previous research and developed in Chapter 5. Thus, three fine sediment erosion or entrainment relations (presented in Section 6.2.4) of immobile bed condition were implemented in the numerical model. Figure 6-5 shows the thickness of fine sediment deposit simulated by the numerical model at selected time steps t = 90, 150, 300 and 660 min and compared to experimentally observed deposit thickness (solid plots) obtained from Grams and Wilcock (2014). Though the main purpose here is not to validate the model prediction of bed sediment thickness it is evident that there is a good agreement qualitatively in the spatial pattern of simulated sediment thickness for the different entrainment relations used. The predicted thickness of fine sediments by Grams and Wilcock (2014) formula shows that the deposited sediment in the first quarter of the test section is subsequently eroded and at time steps t = 300 and 660 min nearly all sediments are re-suspended (no sediment deposit on the bed). While in the case of Cui et al. (2008) (diamonds) and formula developed in Chapter 5 (triangles) the simulated sediment deposit show higher thickness of deposit in the first quarter of the domain as observed in the data. But no sediment deposit is evident in the downstream three-fourth of the test section. It is worth noting that the model is not calibrated and the fine sediments are assumed uniform although the sediments fed during the experiments were non-uniform and so were the datasets used here. The transport of non-uniform sediments shows difference from uniform sediments even though the mean grain sizes are the same (Wu et al., 2000). This could be attributed to the hiding, exposure, and armouring among different size fractions and may significantly affect sediment transport and morphological changes (e.g. Wu et al., 2000). This indicates that the simulated sediment deposits may not be able to capture observations of non-uniform sediment experiments. Thus, direct comparison of the simulated and observed sediment deposits is not emphasized here. Nevertheless, the comparison of different entrainment relation is possible. The predictions by Cui et al. (2008) and formula developed in Chapter 5 show good agreements with the observations qualitatively and can be considered useful. Despite Grams and Wilcock (2014) relation was found to be reliable when applied in 2-D advection-diffusion model to predict non-uniform sediment transport (Grams and Wilcock, 2014), it is also worth noting that erosion rate could be over-predicted by Grams and Wilcock (2014) formula as discussed in Section 6.2.4. For instance for uniform sediment simulation conducted in this study less deposition was noticed as shown in Figure 6-5 and all deposited sediments, including sediment deep in the roughness elements, were entrained at the end of the simulation (refer to Figure 6-5 and Figure 6-6).

The description of variable gravel bed porosity as a function of sediment deposit or level in the immobile hemispherical bed is discussed. The bed porosity consideration allows estimation of sediment deposit thickness within the interstices of hemispherical bed. Two bed porosity parameterizations are considered to evaluate the effect: $\Phi < 1$ and $\Phi = 1$. In the latter case the bed porosity is assumed to be constant regardless of sediment depth but the entrainment is described as a function of depth of sediment deposit (thickness). In this consideration more storage volume (void) is available compared to $\Phi < 1$ where porosity varies with fine sediment deposit in the interfacial sublayer of the immobile hemispherical bed. The behaviour of sediment deposition is found to be different when the variation in gravel bed porosity with sediment deposition in the immobile bed matrix is taken in to account as described in Section 6.2.5. Figure 6-6 shows that the elevation of sediment deposit below crest increased in all cases (entrainment formulations) showing the deposit thickness has increased when porosity is considered. The thick solid line shows the bottom of hemispheres and $\eta - \zeta = 0$ indicates the crest. When porosity is considered a volume of sediment deposited in the case of constant porosity will have less deposit thickness than a similar volume deposited in the interstices. The consideration of porosity is important for two reasons: first it allows the entrainment relation use the actual depth of sediment deposit in the immobile layer to calculate entrainment rate, and second such consideration is also essential to model the clogged depth of sediment, which could be under-predicted when the porosity of immobile bed is not considered ($\Phi = 1$). It could be also useful to design flushing discharges. In Figure 6-7 simulated sediment concentrations are plotted for time steps t = 90,150,300 and 660 min. It shows that the sediment concentration remains higher compared to the case with constant immobile bed porosity considerations. This could be argued in such a way that as the sand thickness is higher the entrainment rate will be higher resulting more sediments in suspension as far as the entrainment rate is not high enough to remove large portion of the deposited fine sediments. The figure also shows that the peak of sediment concentration is attenuated and delay in response of concentration when $\Phi = 1$. This phenomenon is due to larger storage of fine sediments in the immobile bed matrix in the case of constant porosity ($\Phi = 1$). Similar characteristics of sediment concentration can be noticed in longitudinal dispersion of tracers in river channels with dead zone storages (Davis and Atkinson, 2000).
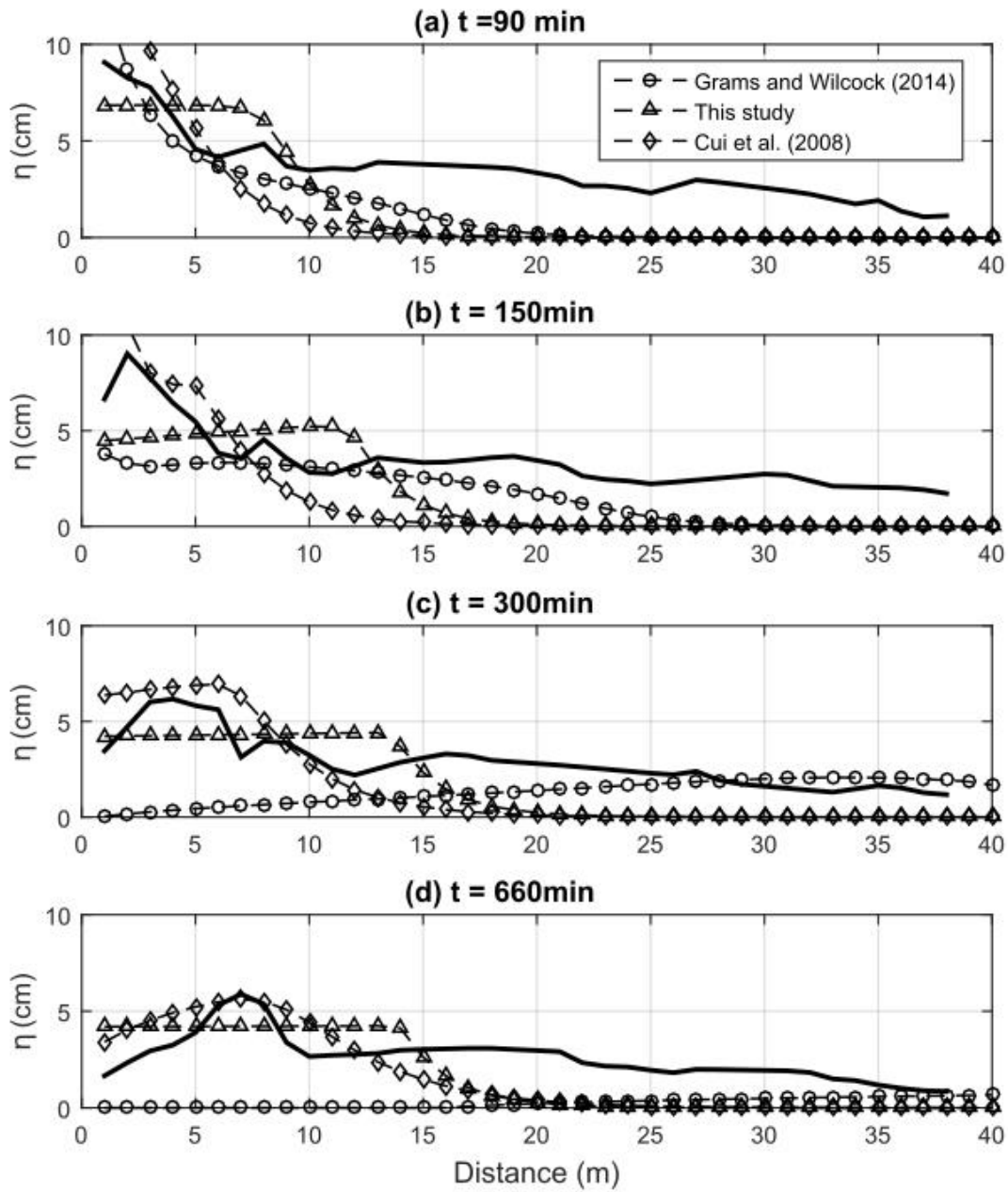
Figure 6-5. The observed (black solid) and simulated fine sediment bed level in immobile hemispherical bed for $\Phi = 1$.
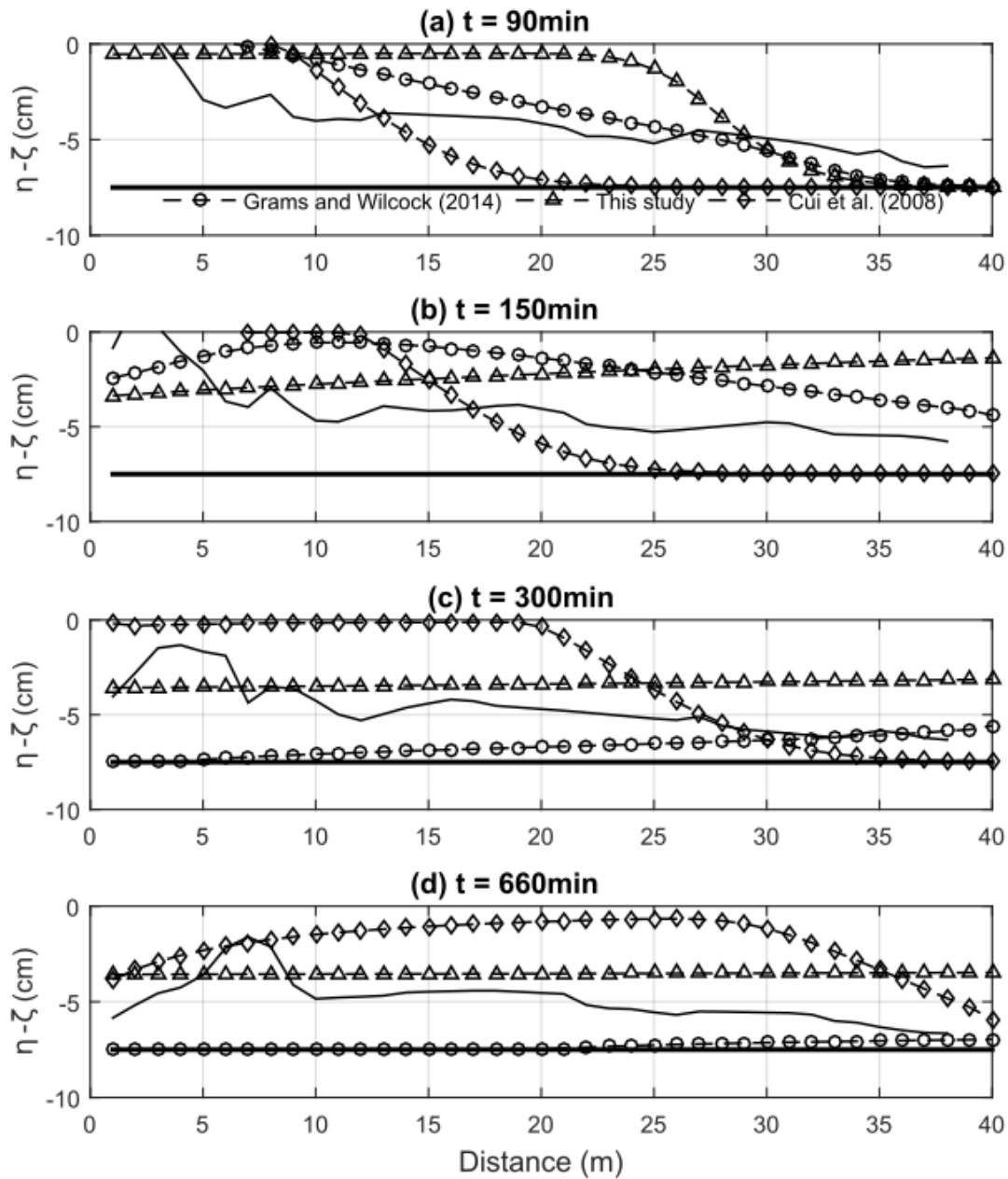
Figure 6-6. The observed (black solid) and simulated fine sediment bed level below the crest of immobile hemispherical bed considering immobile bed porosity ($\Phi < 1$)
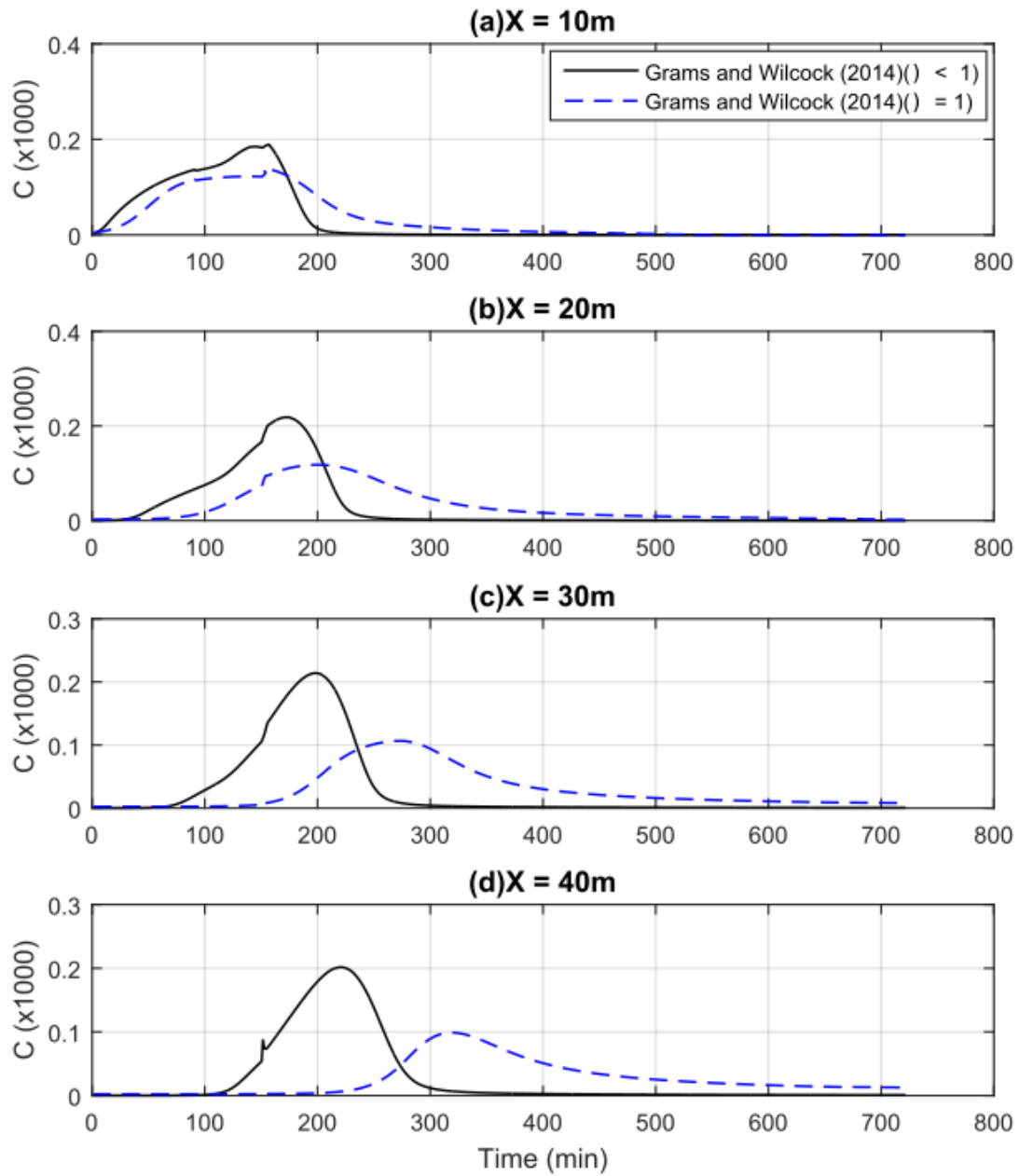
Figure 6-7. The simulated fine sediment concentration for conditions with immobile bed porosity ($\Phi < 1$) and $\Phi = 1$

6.3.3.   Modelling downstream sediment and hydrodynamic waves of flushing releases

This section focuses on presentations of the results of the numerical model simulations of sediment flushing of Cachí Reservoir as case study where the boundary conditions in Figure 6-4 and model parameters in Table 6-2 were used as model inputs. The results focus on characteristics of downstream hydrodynamic and sediment wave dynamics, characteristics of wave celerity and its effect on sediment deposition, the effects of gravel bed roughness and porosity on sediment deposition and evaluation of selected fine sediment entrainment relations. The results are presented in the following sub-sections.

6.3.3.1. Sediment and hydrodynamic waves

The characteristics of sediment waves and hydrodynamic waves are evaluated based on simulated profiles of sediment concentration and flow depth. Figure 6-8 shows the simulated longitudinal profiles of the waves of flow depth and suspended sediment concentration, highlighting the different phases. At the initial stage after the release the two waves are in phase (Figure 6-8 a). As the waves travel downstream, they start to separate (Figure 6-8 b and c) with the separation distance increasing further downstream, and finally they become completely separated (Figure 6-8 d). Brandt (2005) noted an increasing time lag between the liquid and solid discharges observed at selected downstream stations during sediment flushing operations of the Cachí Reservoir as the two waves travel further downstream. Such physical phenomenon could contribute significantly to the spatial lag observed in simulated spatial dynamics of flow depth and sediment concentrations. Figure 6-8 also shows that the thickness of simulated deposition enhanced as the waves separate. It is also evident that most of the deposition occurs at the tail of the hydrodynamic wave since the energy to carry the fine sediments declines. At the same time, the concentration wave decreases in the region where there is sediment deposition. It can be argued that spatial interaction between the two waves could control the spatial pattern of the deposition of released fine sediments. The temporal pattern of simulated flow depth, deposition thickness and concentration at different time steps (Figure 6-9) also indicate an increasing lag in time as we go further downstream from the release point (from 5 km to 150 km), this agrees qualitatively with Brandt (2005) field observations. The peak of the flow depth arrives earlier than the peak of sediment concentration and large concentration and sediment deposit are evident on the falling limb of the flow depth. In this particular case, the subsequent clean-up of the deposited sediments from the immobile coarse bed is quite evident since the base flow carries enough energy to entrain all the deposited sediments.
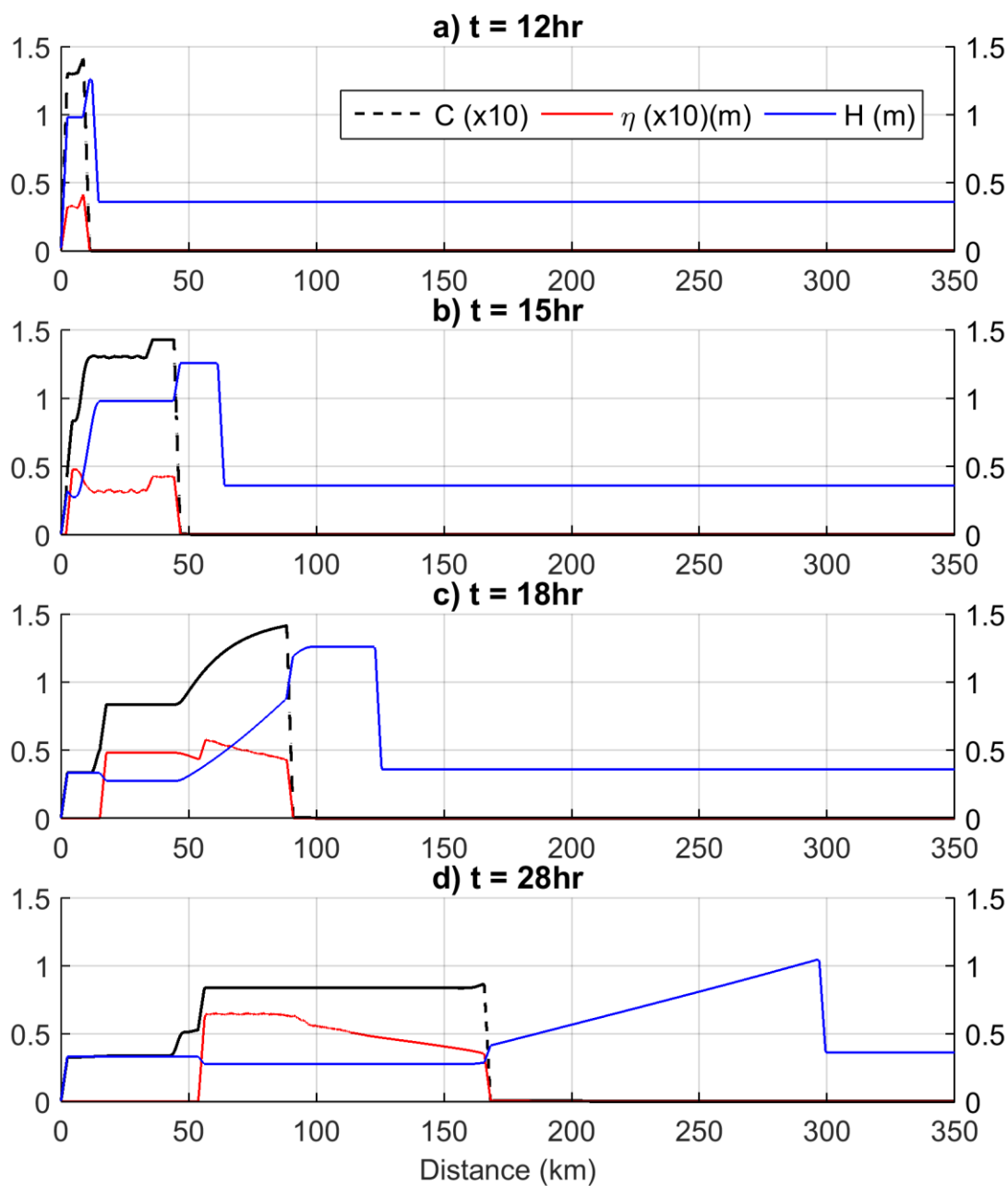
Figure 6-8. The various phases of the spatial wave dynamics: depth (H) (blue line), concentration (C) (dark broken line) and deposition thickness (η) (red line) at selected time steps
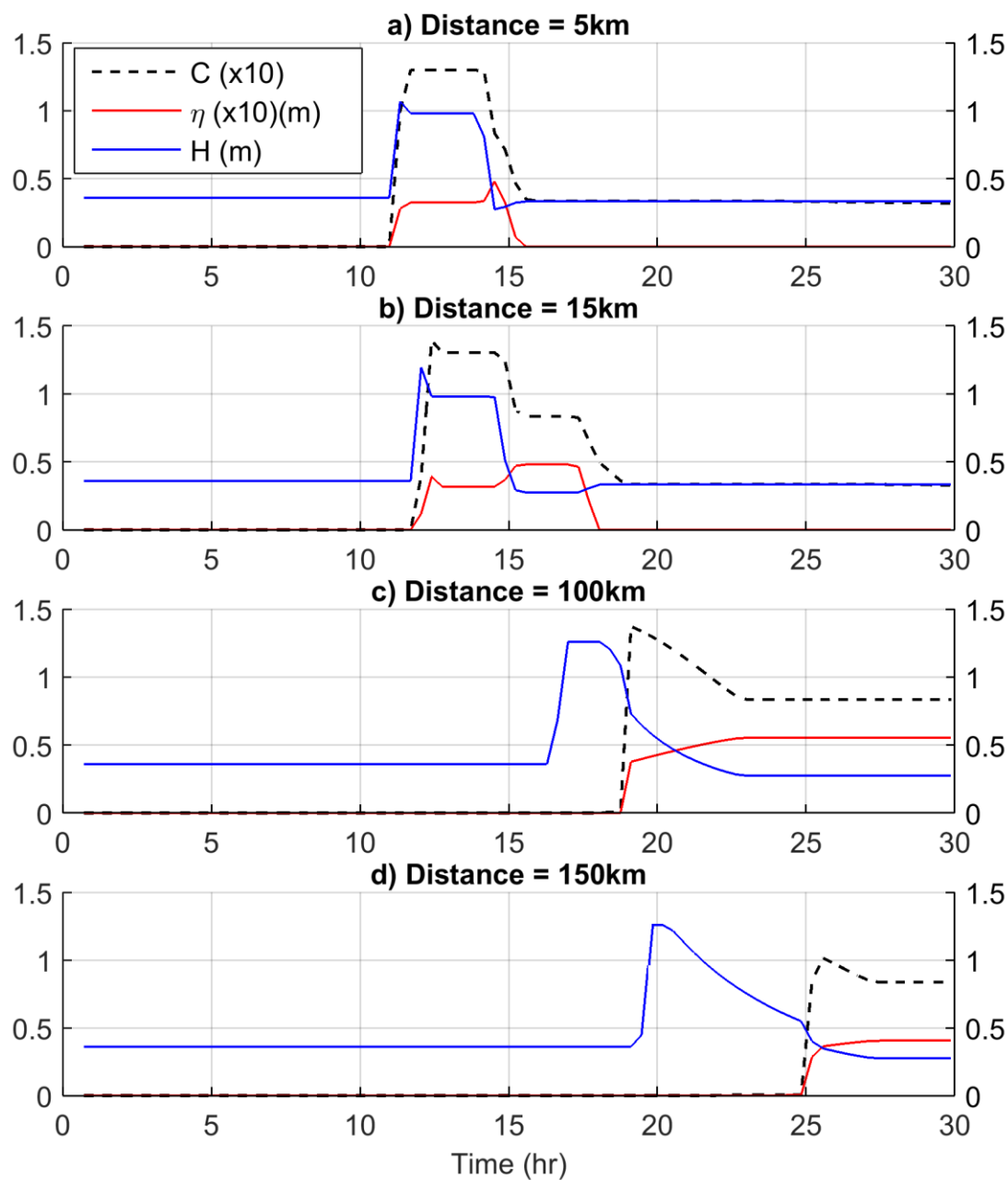
Figure 6-9. The various phases of the temporal wave dynamics: depth (H) (blue line), concentration (C) (dark broken line) and deposition thickness (η) (red line) at selected downstream stations

6.3.3.2. Effect of sediment wave celerity

6.3.3.2.1. Wave celerity factor: Characteristics

The relationship between the celerity factor and selected hydraulic variables (discharge, depth, Rouse number, and relative roughness) are analysed for five different grain sizes. Figure 6-10 shows the plots of the relationships of depth, discharge, Rouse number, and relative roughness with α. The calculated range of variation of α applied in the model is between 0.93 and 0.97 (shown in Figure 6-10 for $d_{50} = 230\mu m$). There is high dependence of α on flow depth and discharge for a given sediment grain size (Figure 6-10a and b). As the flow depth or discharge increases the celerity factor generally increases regardless of the grain size. The celerity factor for fine sediment particles is higher since the Rouse number is relatively small as a result giving a more uniform concentration profile. For increasing Rouse numbers the celerity factor decreases regardless the sediment grain size (Figure 6-10c). The relationship between relative bed roughness and the celerity factor (Figure 6-10d) is similar to the case of Rouse number such that as the relative bed roughness increases the celerity factor decreases regardless of the grain size. We also investigated the computed celerity factor for two different description of the reference height (z_r). We found that the ranges of variation of the computed celerity factor α with depth and discharge for the different grain sizes remained the same for $z_r = 2d_{50}$ and $z_r = 3d_{90}$. Thus, defining the reference height (z_r) as $2d_{50}$ (Zyserman and Fredsoe, 1994) or as $3d_{90}$ (e.g. van Rijn, 1984a) does not affect the estimated value of α.

6.3.3.2.2. Wave celerity factor: Effects on sediment and hydrodynamic waves

The effect of wave celerity on sediment and hydrodynamic wave interactions and sediment deposition are evaluated based on a correction on the advection velocity of sediment by taking into account the vertical profile of concentrations and flow velocities. Figure 6-11 shows the simulated longitudinal profiles of suspended sediment and the hydrodynamic waves at different time steps for two cases: when the sediment wave celerity is corrected (α < 1) and when the regular assumption that the sediment wave travels with average flow velocity (α = 1). In the latter case (shown in Figure 6-11 in broken lines) less deposition thickness is observed comparatively since the wave separation is less enhanced. This subsequently resulted in an increase in the local sediment concentration as noticed in Figure 6-11. This agrees well with two-dimensional (2-D) model simulation results reported by Huybrechts et al. (2010). The total volume of simulated sediment deposit per unit width (V_s), in the simulation domain, is computed by integrating the depth over the length of simulation domain ($V_s = \int_0^{L_d} \eta dx$) for the two cases: with (α < 1) and without (α = 1) the celerity factor.
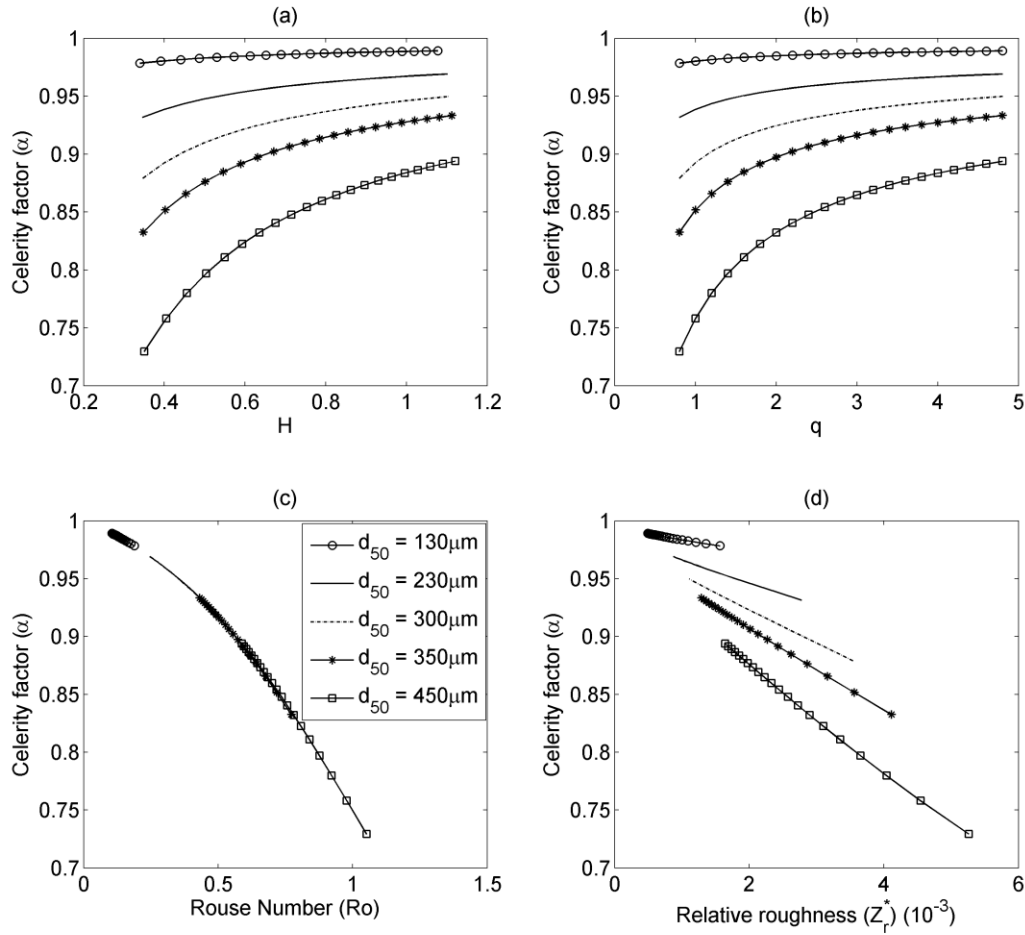
Figure 6-10. The relationship of celerity factor with flow depth (H), discharge (q), Rouse number (R_0), and relative roughness (z^*_r)

Figure 6-12 (top) shows the difference between the estimates for $\alpha < 1$ and $\alpha = 1$. It shows that the volume of sediment deposit is higher when $\alpha < 1$. The length of sediment deposit is also computed, for sediment thickness larger than 1.0 mm, for the two cases. Figure 6-12 (bottom) shows that the length of sediment deposit is higher (up to 6 - 8 km) when $\alpha = 1$ and the hydrodynamic wave tends to spread the sediment over a larger area since the wave separation is less. Generally, it can be argued that the regions of sediment deposition are relatively different. It is also observed (Figure 6-11 c, d) that without celerity factor the suspended load is over-predicted compared to the case with $\alpha < 1$. Huybrechts et al. (2010) reported a good agreement between 2-D model simulations of suspended load with three-dimensional (3-D) model results when celerity factor was taken into account in 2-D model. The effect of the celerity factor is also more evident and higher on the suspended load than on the concentration since the

estimation of the suspended sediment load is directly related to the correction factor. Particularly, the wave front of the suspended load is larger when α = 1 since the peak of the concentration and the flow depth at the tail of hydrodynamic wave, which are lower in the case of α < 1, are higher. The temporal wave dynamics are presented in Figure D-12 (Appendix D).
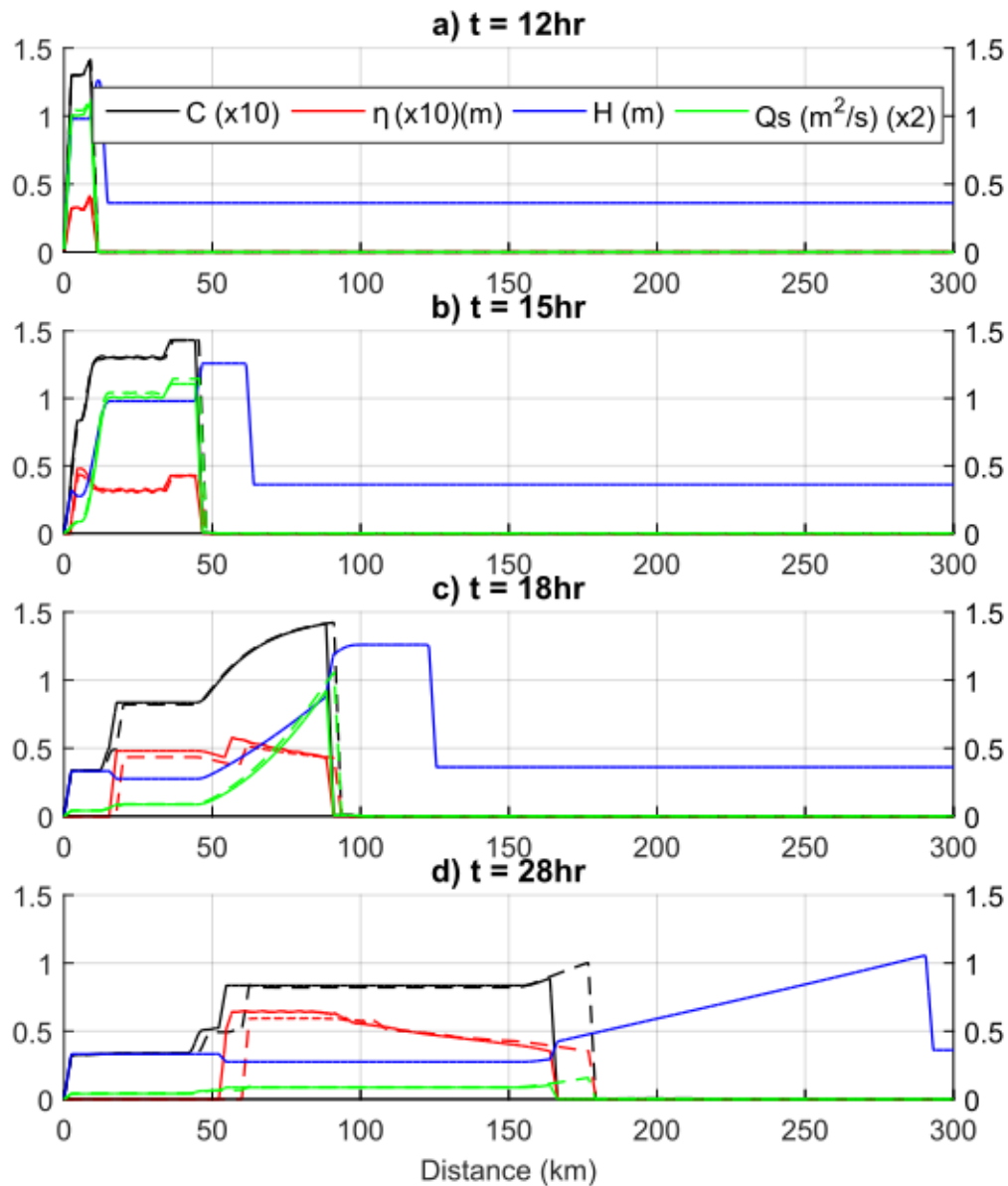
Figure 6-11. The various phases of the spatial wave dynamics with celerity correction α < 1 (solid lines) and without (α= 1, broken lines): flow depth (h) (blue line), concentration (C) (dark line), and suspended load (q_s) (green line) and deposition thickness (η) (red line)

The effect of wave celerity factor when channel bed is dominated by sand (fine sediment) materials is also evaluated. This enables to evaluate its effect on the wave dynamics and deposition when the channel bed is smooth. Figure 6-13 shows the simulated longitudinal profile of suspended sediment and the hydrodynamic waves at different time steps for two cases when the released sediments are transported in sand bed condition. The sediment and hydrodynamic waves are similar to the characteristics observed in the immobile bed condition. Nevertheless, the time and distance at which sediment and hydrodynamic waves completely separate are quite different. At time step t = 28 hr the waves become more or less completely separated in immobile bed conditions nevertheless in the latter case this occurs at later time steps (see Figure 6-13). Thus, it could be argued that in channel composed of smooth bed sediments will be deposited further downstream. The effect of wave celerity on the volume of sediment deposits showed also similar to the case noted in immobile bed condition (Figure 6-14, top). However, the effect on length of sediment deposit was rather opposite where a larger length of sediment deposit was noticed when $\alpha < 1$ (Figure 6-14, bottom). Overall, the sediment wave celerity affects the spatial pattern of sediment deposition of released fine sediments and its proper implementation in numerical model is expected to improve the modelling of suspended sediment deposition and transport.
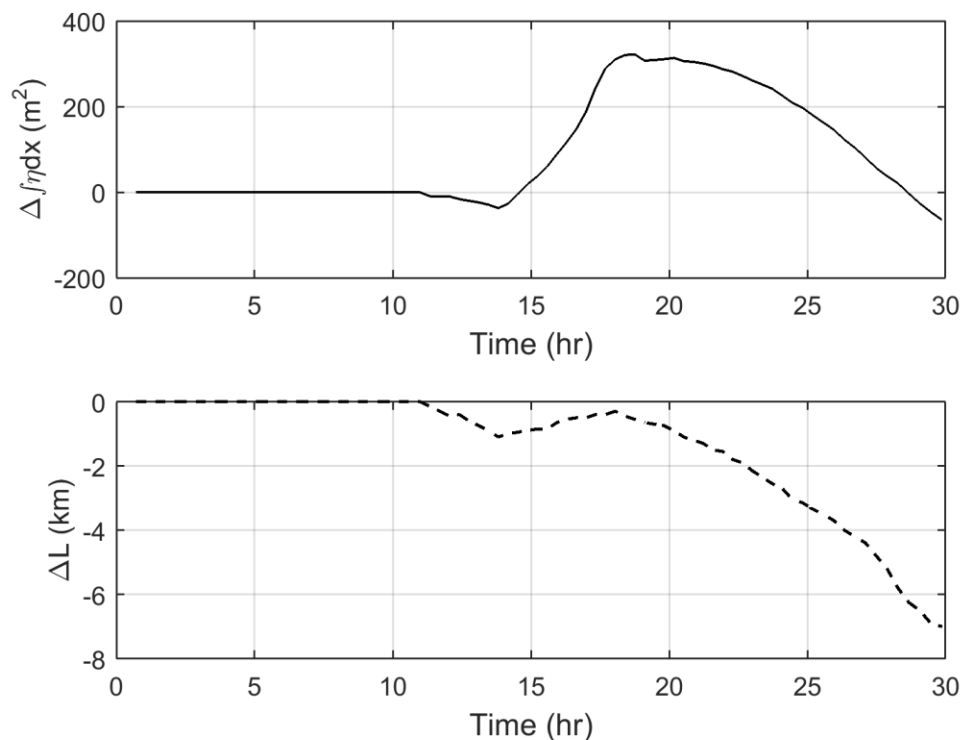
Figure 6-12. The difference between volume of simulated sediment deposit per unit width and length for $\alpha < 1$ and $\alpha = 1$

The characteristics of sediment wave for no bed exchange (E - D = 0) is analysed to highlight the effect of additional terms in sediment continuity equation when α is taken in to account (refer Equation (6-15)). Figure 6-15 shows the simulated longitudinal sediment concentration and loads at time step t = 20 hr for α < 1 and α = 1 respectively when there is no bed exchange. When the celerity factor is applied there is increment of sediment concentration (C_p = 370.00 g/l), larger than concentration applied at the boundary (C_p = 344.50 g/l), at the tail of concentration wave and at the tail of the hydrodynamic wave. When the celerity factor is not applied (α = 1) such local increase in concentration is not evident at all. . As shown in Equation (6-15), the last term of the equation contributes to this behaviour in concentration where there is a gradient of flow depth in time. On the other hand, as shown in Figure 6-15 (in green) the sediment load shows a little decrease at its front with its peak lower than the case of α = 1. Figure 6-16 shows the time evolution of sediment load and concentration at selected downstream station (x = 15 km and 80 km from release point) where sediment and hydrodynamic waves are together and on verge of separation in time respectively. The elevated concentration for α < 1 exists at each station but with higher increase when the recession limb of depth gradient is higher and decreases when the hydrodynamic wave flattens. With the celerity factor sediment load wave shows some decrease at its front at the front of the hydrodynamic wave (see Figure 6-16 a & b) though it is too little. The effect of the celerity factor on the local increment of sediment concentration is evident only on the tail of the spatial hydrodynamic wave and recession limb of rising limb temporal dynamics of hydrodynamic wave (region between the vertical dark lines). When the two waves are fully separated (Figure 6-16b) the local increment gradually decreases since the gradient of the hydrodynamic wave is separated from the sediment wave. Overall, the local increase in sediment concentration, due to the celerity factor, does not increase the sediment load. Finally, the last term in Equation (6-15) as well as the celerity factor can be relevant in modelling suspended sediment transport.
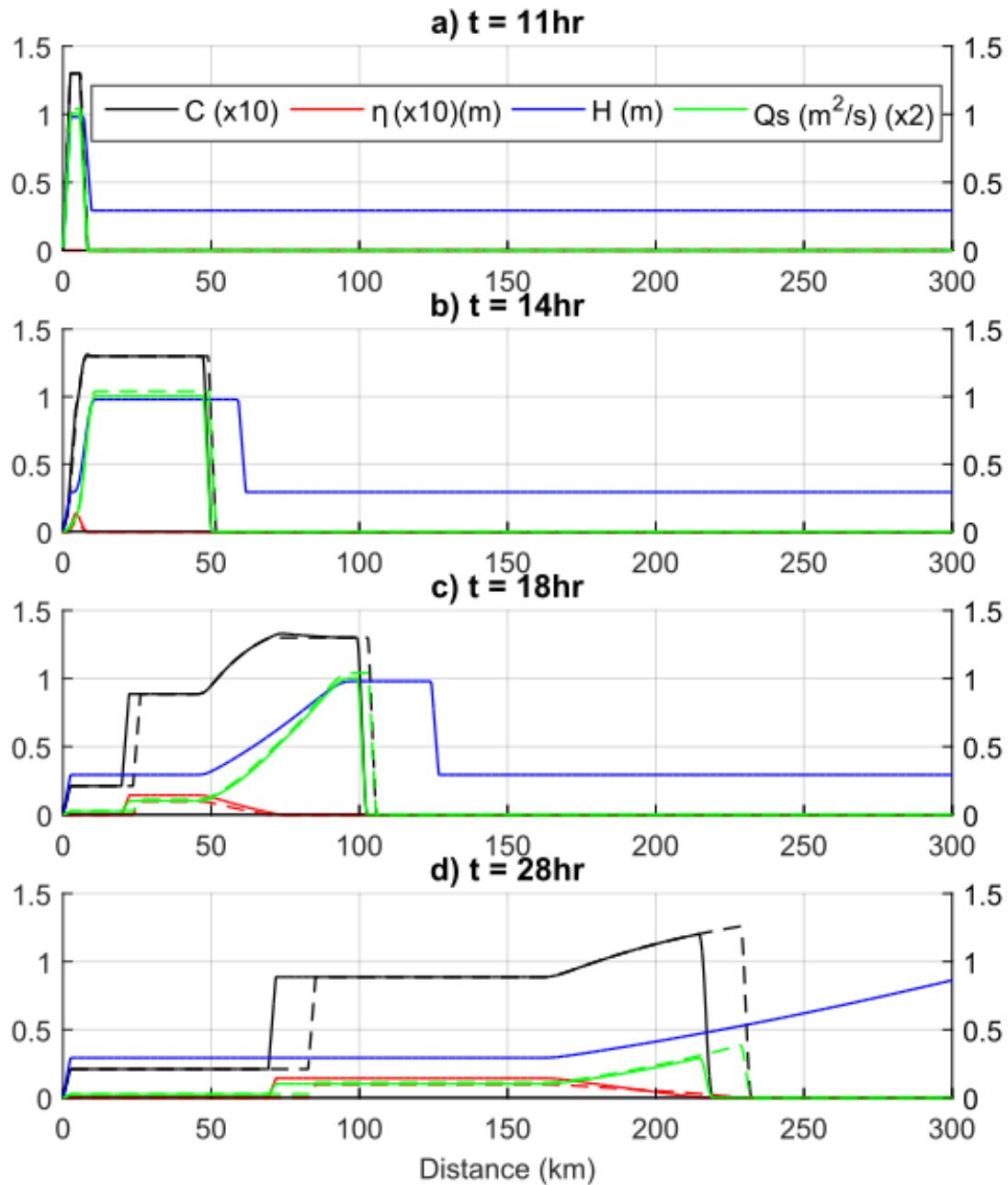
Figure 6-13. The various phases of the spatial wave dynamics with celerity correction α< 1 (solid lines) and without (α = 1, broken lines) in sand bed condition: flow depth (h) (blue line), concentration (C) (dark line), suspended load (qs) (green line) and deposition thickness (η) (red line)
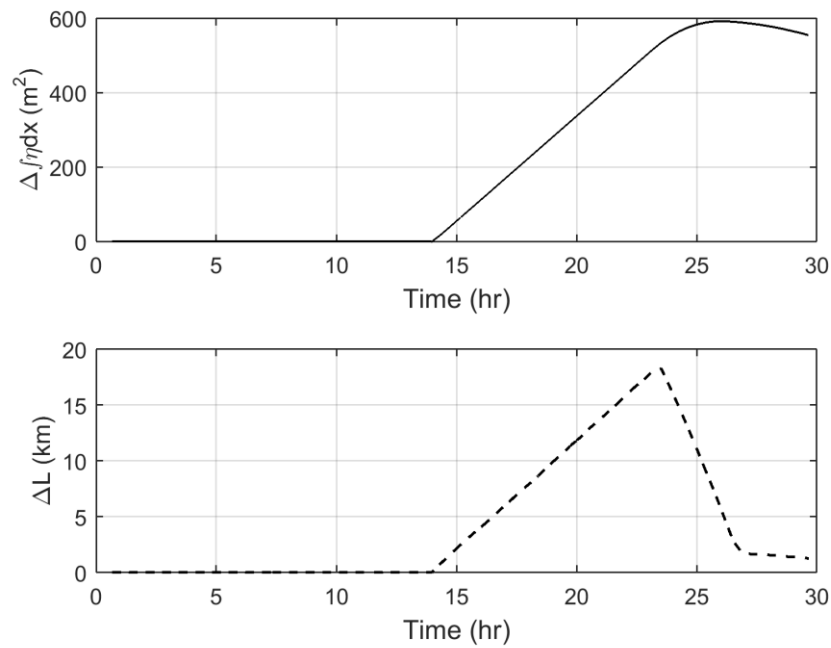
Figure 6-14. The difference between volume of simulated sediment deposit per unit width and length for α < 1 and α = 1 in sand bed condition
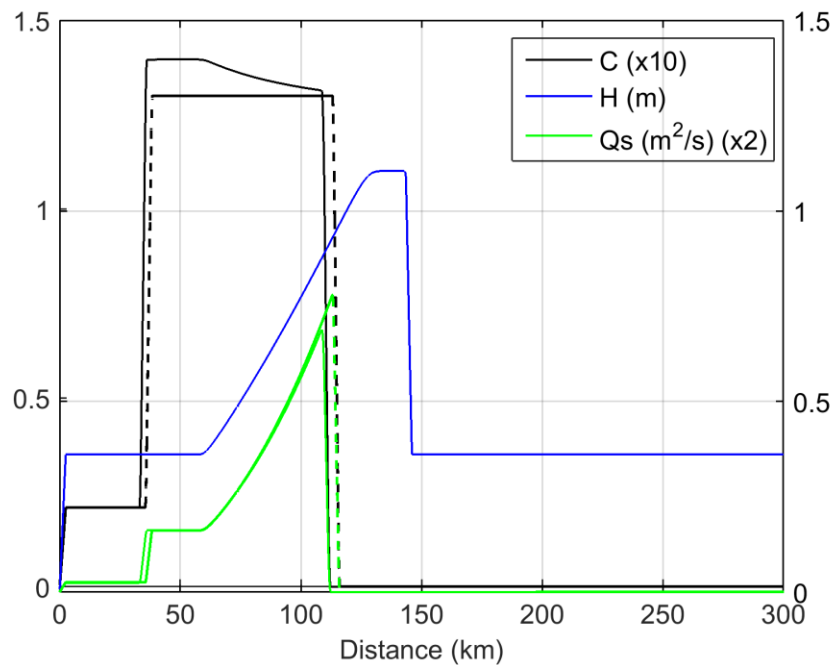
Figure 6-15. Sediment concentration C and sediment load q_s at t = 20 hr for α < 1 (solid lines) and α = 1 (broken lines) when E - D = 0
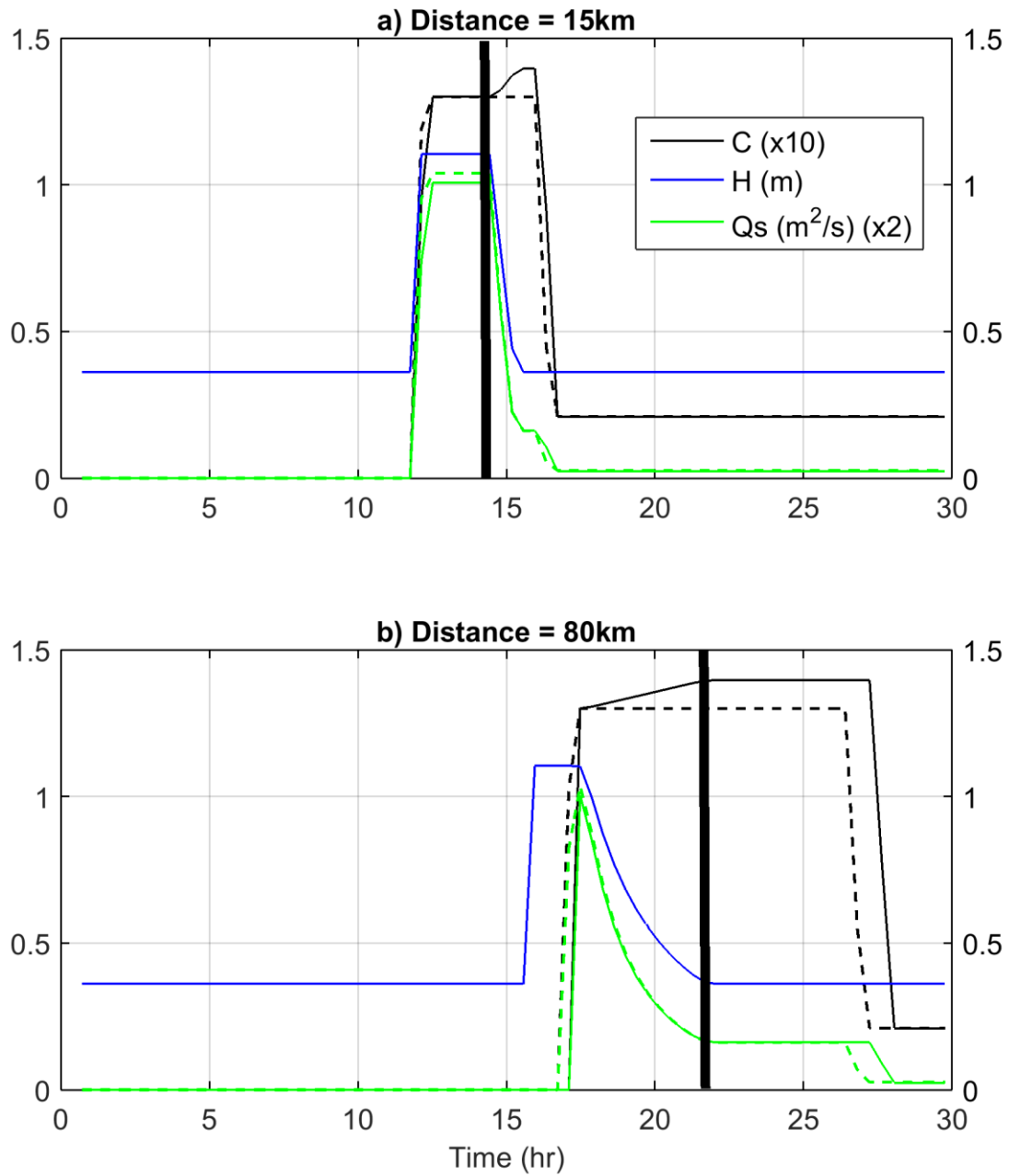
Figure 6-16. Sediment concentration C and sediment load q_s at distance = 15 km (a) and 80 km (b) for α < 1 (solid lines) and α = 1 (broken lines) when E - D = 0

6.3.3.3. Effect of variable bed roughness

The effect of bed roughness description, applied for computation of the flow hydrodynamics, on simulated sediment deposition and flow depth is analysed. Figure 6-17 shows simulated longitudinal profiles of sediment deposition thickness, flow depth and concentration for variable and constant bed roughness descriptions. When the bed roughness is variable (described as a function of sand level in the roughness elements) the flow depth (blue solid line in Figure 6-17) decreases in region of sediment deposition and increases when there is no deposit. This is driven by the changes in bed roughness since the bed gets smoother as the sand level increases in the interfacial sublayer of gravel roughness elements thus reducing the bed roughness. On the other hand when the bed roughness is constant there is no change in the flow depth (Figure 6-17, blue broken line) in regions of sediment deposition. The flow depth is shallower compared to variable roughness case and the peak of the hydrodynamic wave is even much lower. The hydrodynamic wave also travels faster in the case of constant roughness description which could affect the location of sediment deposition in the simulation domain. Nevertheless, rather similar thickness of sediment deposit per unit length is observed in the two cases although the variable bed roughness case showed a bit higher.
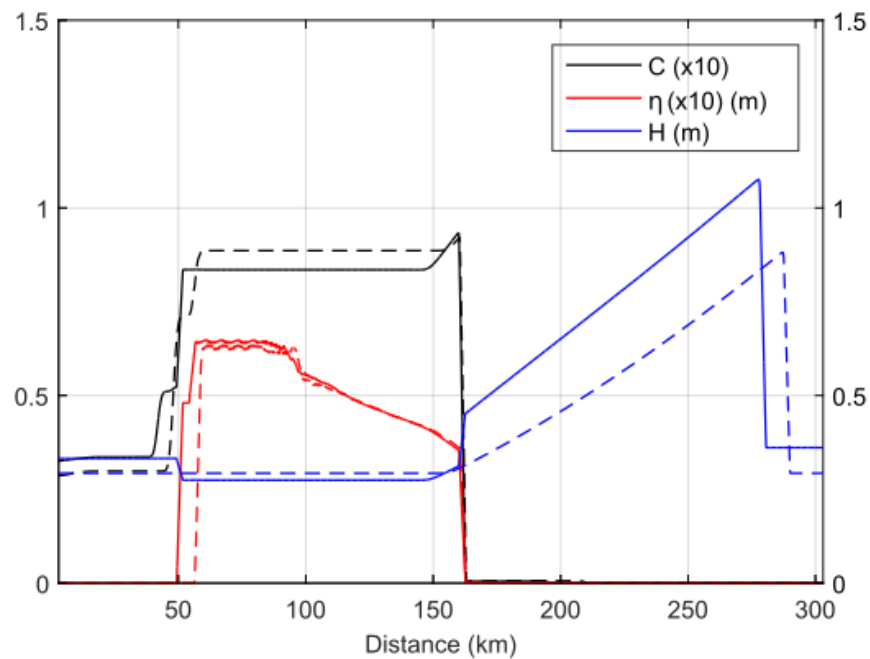
Figure 6-17. Simulated flow depth, sediment concentration and deposition thickness for variable (solid lines) and constant (broken) bed roughness at time step t = 27 hr

This can be noticed from estimates of the difference in the simulated thickness of sediment deposit per unit length (the measure of sediment thickness) of the two cases which is very small, a difference not larger than 1.5 mm (Figure 6-18, top). The length of deposition (indicator of the area covered by sediment deposition), on the other hand, is found to be larger for rough bed as shown in Figure 6-18 (bottom).
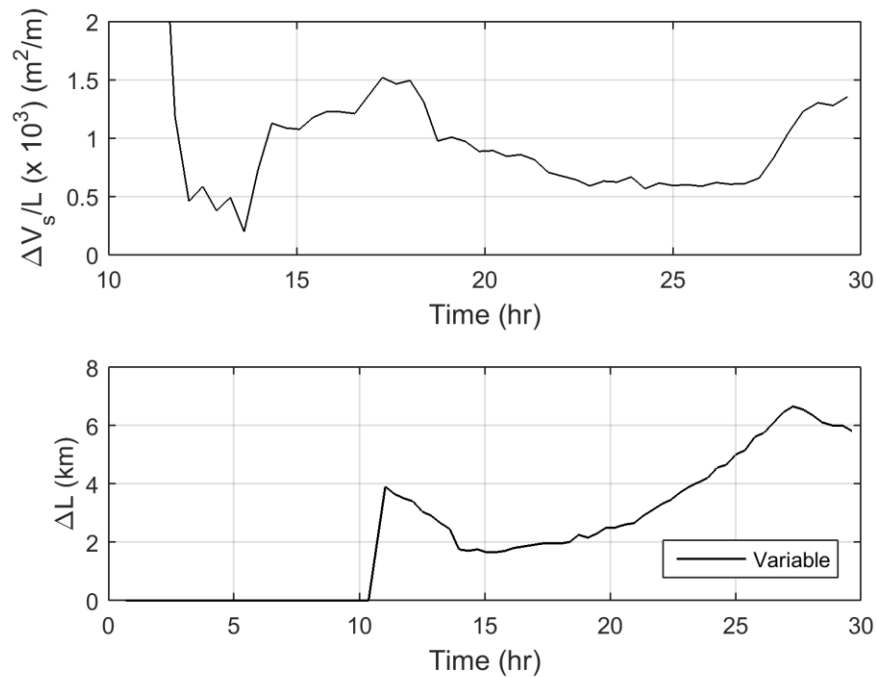
Figure 6-18. The difference between sediment deposit per unit length for variable (solid lines) and constant (broken) bed roughness

6.3.3.4. Evaluation of entrainment relations

The reliable estimation of the bottom sediment flux is the most important and challenging component in suspended sediment transport modelling, especially due to the empiricism of many of existing relationships. In many occasions the rate of entrainment are expressed as near bed equilibrium concentration and four different relations (VR, SM, GP and ZF) are tested considering sand bed condition. Estimates of entrainment rate (C_E, equilibrium near bed concentration) by ZF and GP relations are larger than those of VR and MS (Figure 6-19, top). Such differences can be attributed to the difference in reference level above the bed where the near bed equilibrium sediment concentration is estimated, some very close to the bed, as a large as bed grain size (e.g. ZF), others further above the bed, a fraction of the flow depth (e.g. GP). The reference level is important since the prediction of erosion rate depends

on the estimated sediment concentration at the reference level, in addition to the grain size and shear stress.
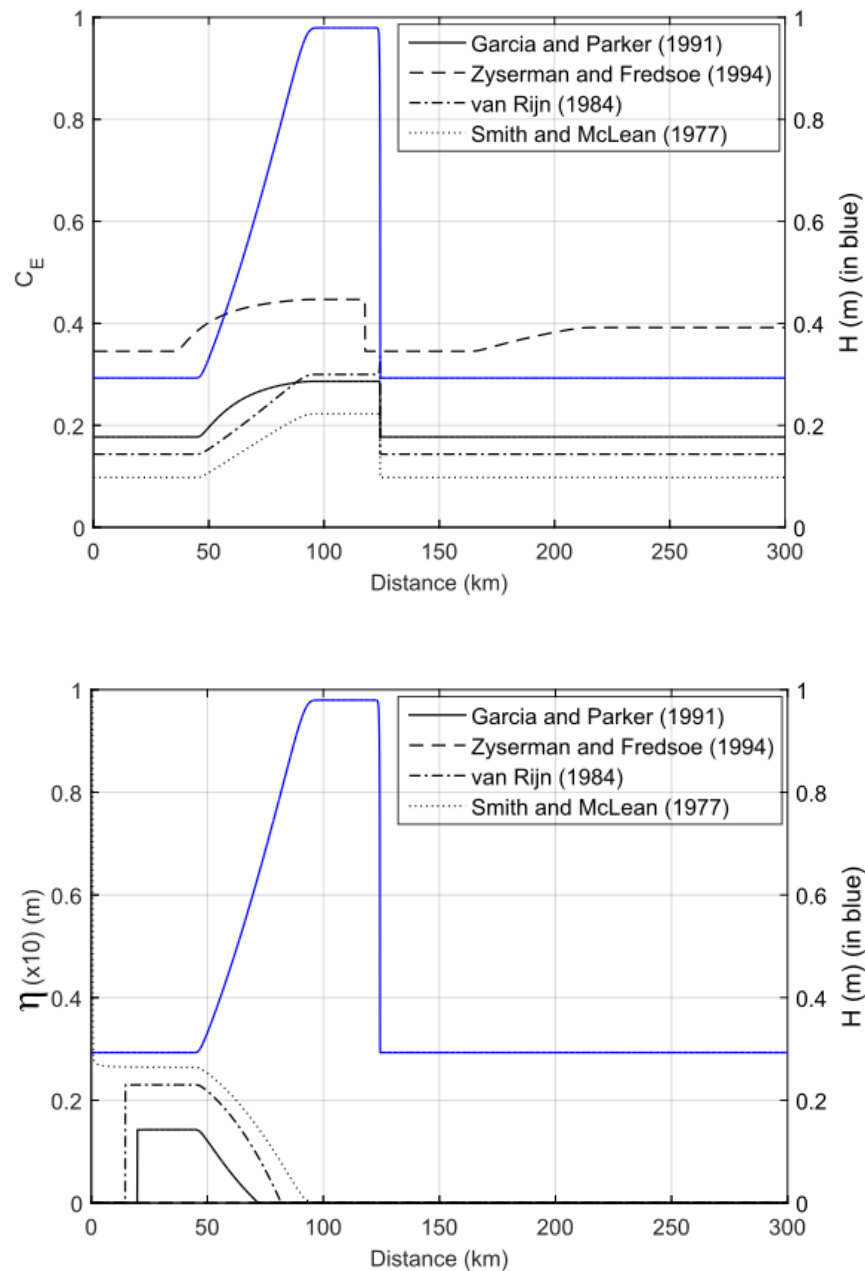
Figure 6-19. Comparison between different entrainment relation formulas (a) and deposition profiles for SM and VR formulations (b) at t = 18 hr

The higher estimate of entrainment rate by GP can be related to higher exponent of the shear stress (i.e. shear velocity) in the empirical equation which could lead to higher erosion rate when the flow velocity is larger (Garcia, personal communication) such as in the case of flushing flows (where in this case $\theta =$ 5.5

to 18). The estimate by ZF is the largest among all and such over-estimation is more likely related to the definition of reference level ($= 2d_{50}$), which is very close to the bed given the bed sediments are very fine ($d_{50} = 230\mu m$) and also high bed shear stress. The high entrainment rate by ZF is also highlighted by Cao (1999). SM and VR estimates of erosion rate are relatively in close agreement with GP although this agreement is not reflected in simulated depth of deposition (Figure 6-19, bottom).
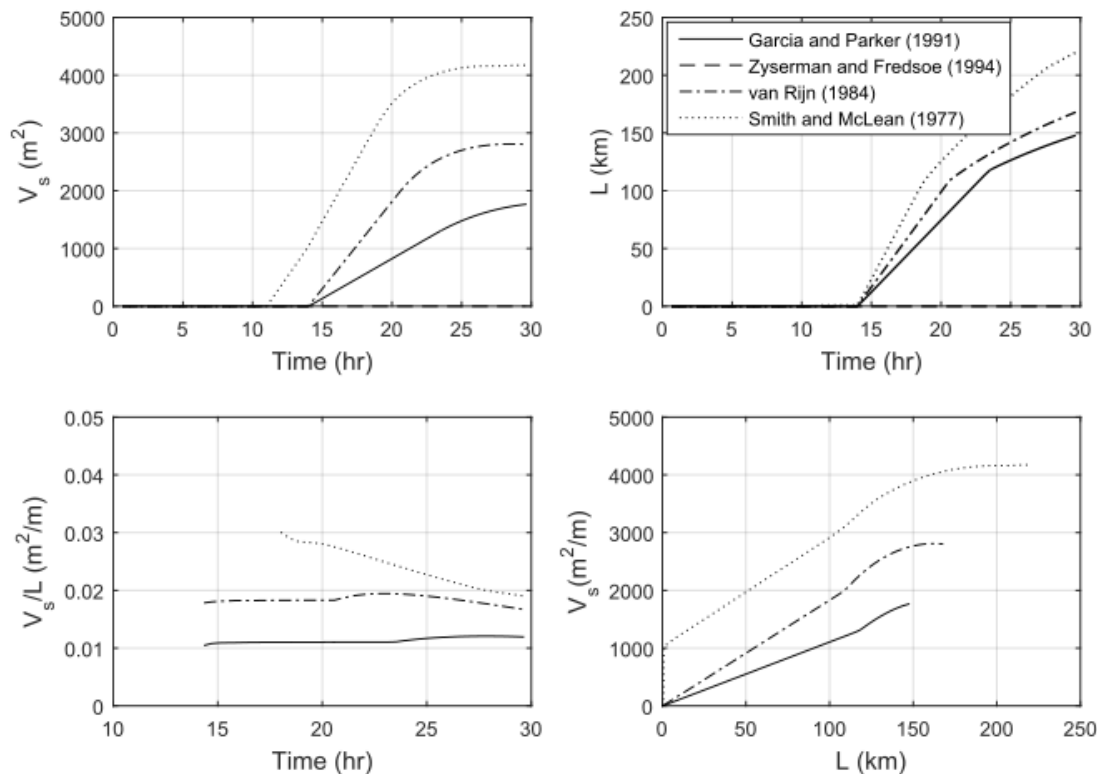
Figure 6-20. Comparison of simulated sediment deposition volume, length and thickness for different entrainment relations

The overall observation entails that the thickness of the simulated sediment deposits are directly related to the estimates of the entrainment rates since deposition rate was estimated with the same relation in all cases. The effect on simulated sediment deposition thickness can be noticed from Figure 6-19 (bottom) and Figure 6-20. Larger volumes of sediment deposition are observed in the case of VR and SM (Figure 6-20). Thus, selection of entrainment relations to study events such as flushing waves at large spatial scales need to take into account such effects. There are some studies that indicate VR is well suited in large scale applications (e.g. Duan and Nanda, 2006; Harris and Wiberg, 2001; Duan and Julien, 2010) and in high velocity flow and transport conditions (Voogt et al., 1991) and using this relation can be useful.

6.3.4. Analysis of release scenarios of sediment flushing

In this section the spatial patterns of sediment deposition for selected flushing releases are investigated. The input parameters indicated in Table 6-2 were used except those related to flow and sediment boundary conditions. The flushing release scenarios are designed based on different peak to base flows as shown in Figure 6-21 (in broken lines is discharge). For all selected release scenarios the total quantity of flushed sediment loads and liquid discharges are equal and the only difference lies on ratio of base to peak flow discharge and temporal pattern of the concentration. The base flow has limited capacity to carry all the released fine sediments, so more deposition is anticipated for large peak-to-base flow ratios. Figure 6-22 shows the simulated volume, thickness and length of sediment deposition in the simulation domain after the release of sediments for different peak-to-base flow ratios (q_p/q_b = 4.7, 6.25, 7.80 and 13.0). The total volume of sediment deposit (Vs) for releases of small ratios (q_p/q_b = 4.7 and 6.25) are observed to be lower than larger ratios (q_p/q_b = 7.8 and 13) mainly in the falling limb of the releases (Figure 6-22, top). The length of sediment deposition regions shows that it was larger for lower ratios (q_p/q_b = 4.7 and 6.25) in the rising limb of the releases and smaller in the falling lime compared to larger ratio releases (q_p/q_b = 7.80 and 13.0) (Figure 6-22, middle).
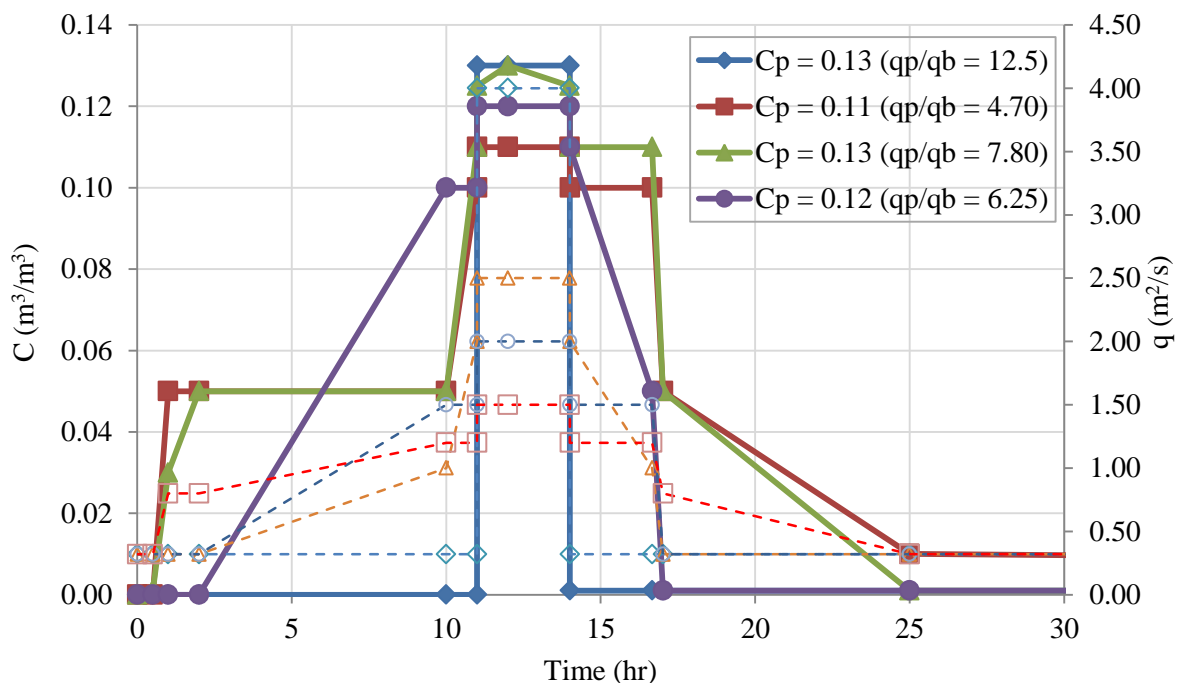
Figure 6-21. The different release scenarios designed based on peak to base release discharges: concentration (C) (solid lines) and discharge per unit width (q) (broken lines)

In Figure 6-22 (bottom) the volume of sediment deposit is plotted against the corresponding length (area coverage). The thickness of sediment deposit (V_s /L) shows a similar pattern to the sediment volume (Figure 6-22, top) where the higher the release ratio the higher is the deposit thickness. The results indicate that the ratio of the peak-to-base flow can significantly control the volume, thickness and area coverage of sediments that deposit during flushing operations. The release with highest ratio produced the longest and thickest region of deposition, while the one with the lowest ratio produced the shortest and thinnest. Thus, a proper selection of this ratio might help to plan a flushing operation with minimal deposition and reduce the downstream environmental impacts.
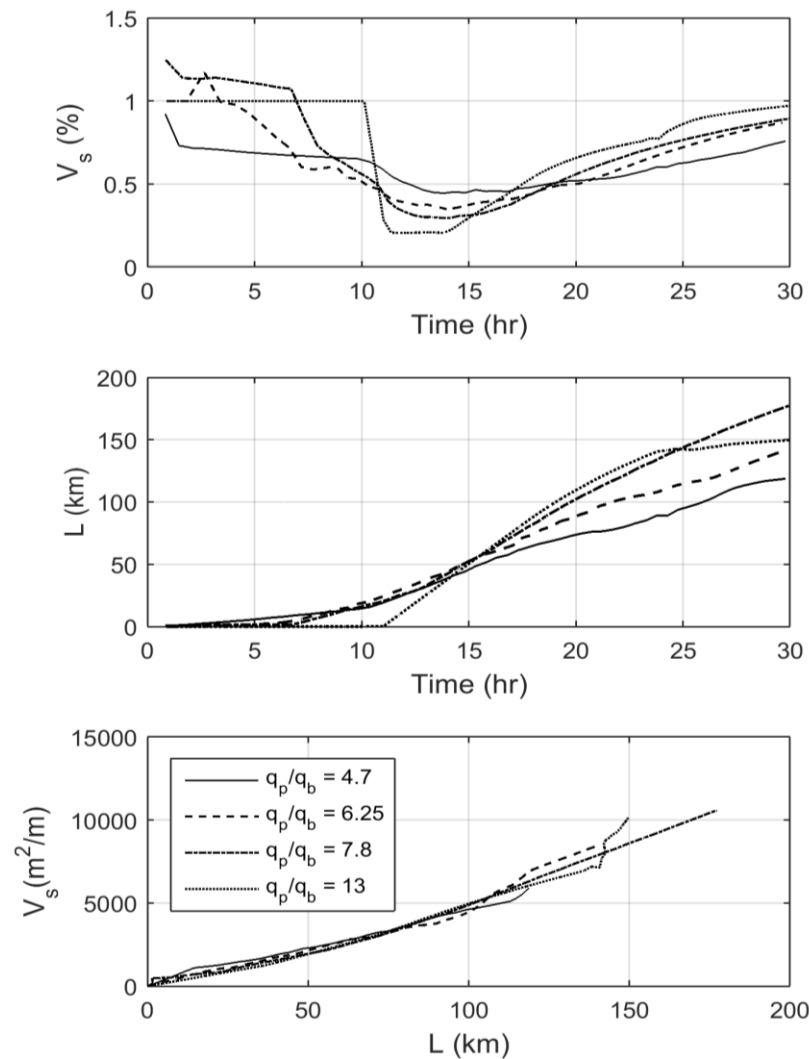
Figure 6-22. Comparison of volume of sediment deposit (top), length of sediment deposition (middle) and volume of sediment deposit per unit length (bottom) for selected peak-to-base flow releases
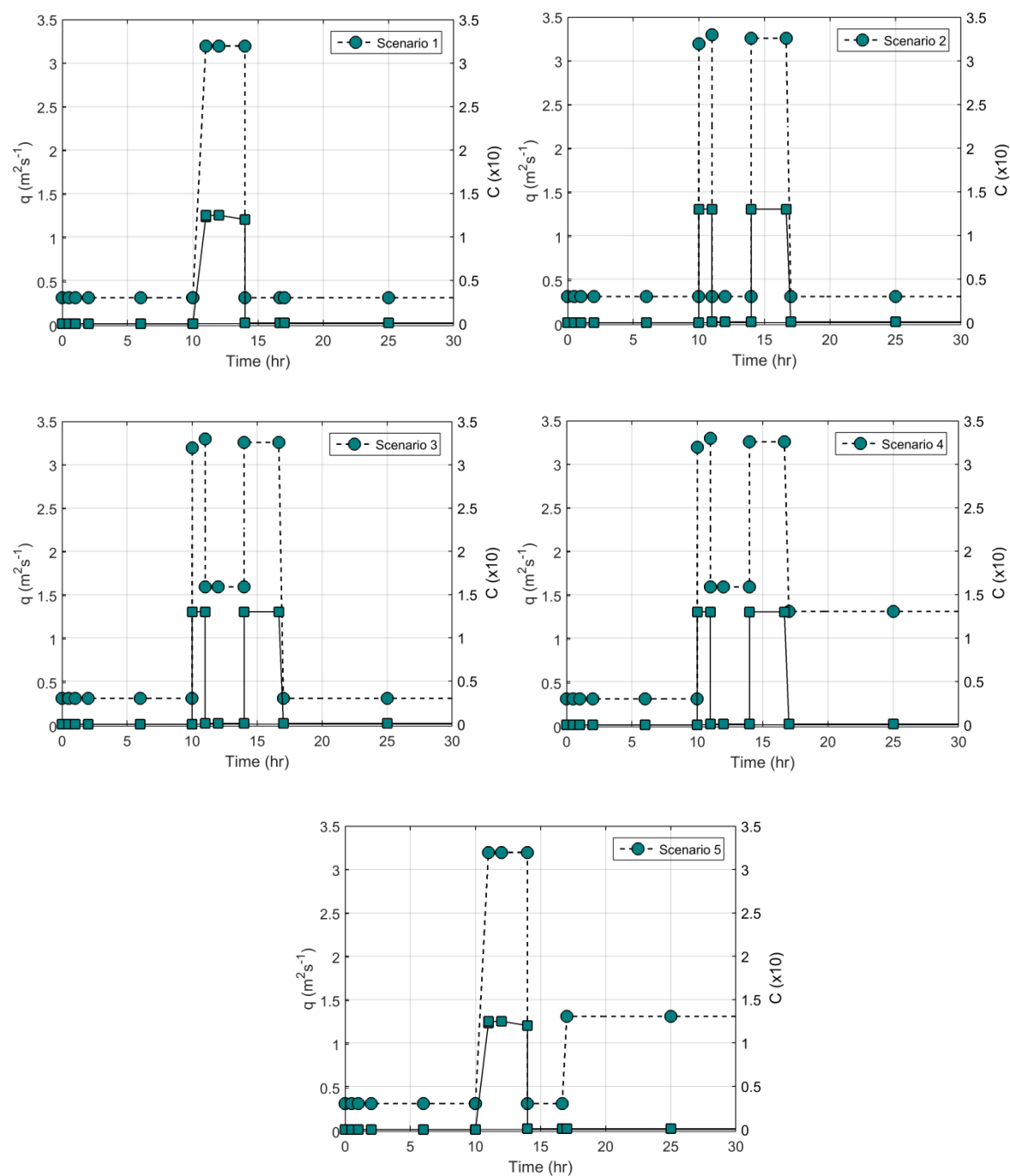
Figure 6-23. The different release scenarios (intermittent) followed by clear water releases: broken lines (q) and solid lines (C)

Five scenarios which consider sediment flushing followed by clear water releases for two conditions: single flushing and intermittent (two peak releases separated by no flushing period) flushing (refer Figure

6-23) are evaluated for sediment deposition with a base release, $q_b = 0.32$ m²/s and peak release of duration 4hrs, $q_p = 3.20$ m²/s. The duration of clear water releases in all scenarios are also the same.
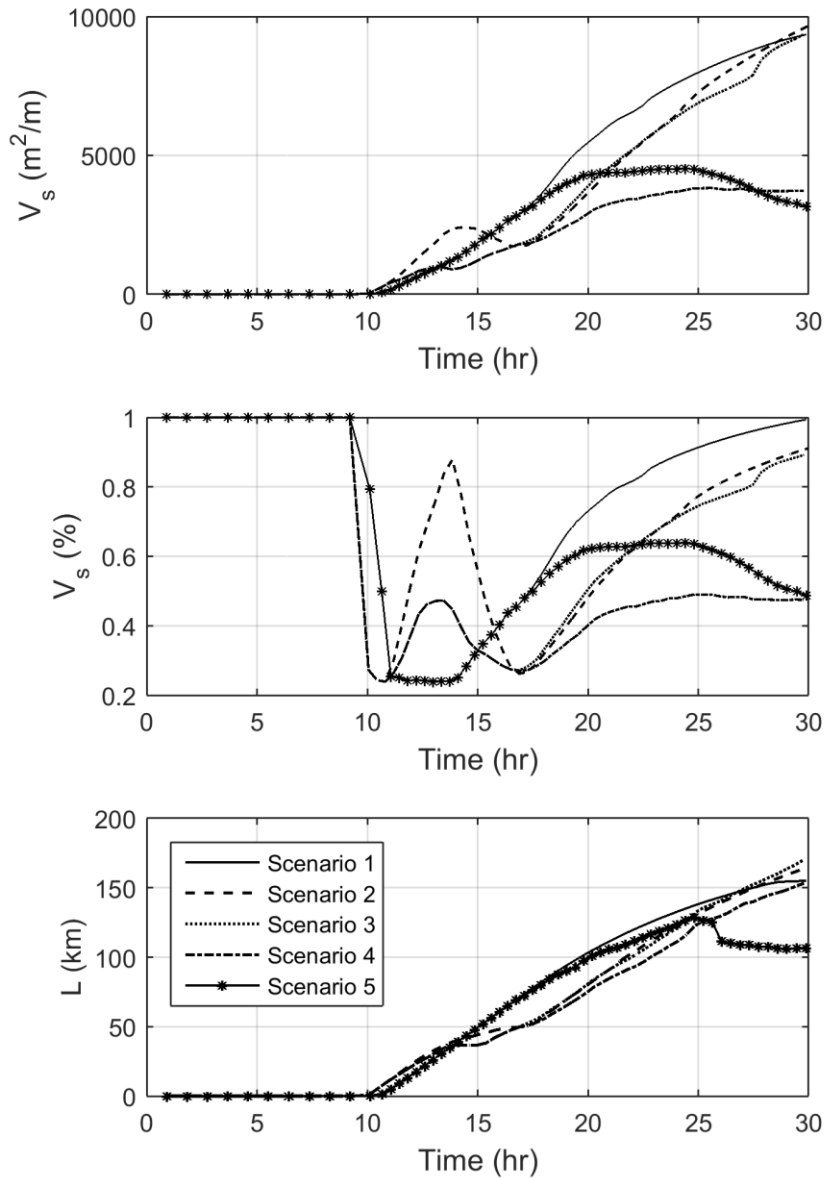
Figure 6-24. Comparison of volume of sediment deposit (top), length of sediment deposition (middle) and volume of sediment deposit per unit length (bottom) for selected flushing followed by clear water releases

In all scenarios the amount and temporal pattern of concentration and the total duration of peak releases are the same. The scenarios are designed by selectively changing the released quantity of liquid discharges. The total quantity of liquid and solid discharges in scenario 1, 2 and 3 are the same except scenario 4 and 5 where additional clear water releases are introduced. In scenario 1 and 2 the peak to base

flow is 10 but released in single and intermittent patterns respectively. In scenario 3 inter-flushing clear water release are assumed. In scenario 4 and 5 inter-flushing clear water releases and post-flushing clear water releases are assumed. Figure 6-24 shows the simulated sediment deposition volume, proportion and length computed over the entire length of the simulation domain. The proportion of volume of sediment deposition for scenario 1 is larger than that of scenario 2 despite the same quantity of liquid and solid discharge are released. The intermittent release (scenario 2) shows relatively lower proportion of sediment deposition at the end of simulation but large sediment deposition can be noticed during the inter-flushing period (11-15 hrs). When the inter-flushing clear water release was increased from q_b to $0.5q_p$ (1.6 m^2/s) (scenario 3) no significant difference in the proportion of volume sediment deposit was noticed at the end of simulation when compared to scenario 2 except during the inter-flushing release period where the deposition noticed was less (Figure 6-24, middle). Scenario 4 and 5 show the deposition patterns when post-flushing clear water releases are considered. It can be noticed that the proportion of sediment deposit in scenario 4 is much lower than scenario 1 at the end of simulation and this shows that post flushing clear water release reduced the deposition significantly (Figure 6-24, middle). In scenario 5 the proportion is even much lower since clear water releases were applied during the inter-flushing period and post-flushing (Figure 6-24, middle). When scenario 4 and 5 are compared a single flushing with sufficient clear water release showed similar proportion of deposition as scenario 5 at the end of simulation (Figure 6-24, middle). The total length of sediment deposit at the end of simulation was the lowest for scenario 5 but for all intermittent releases the length remained nearly the same and higher than scenario 4 (Figure 6-24, bottom). On one hand, this shows that a single flushing release followed by clear water release could reduce area or length of sediment deposition. On the other hand, intermittent flushing releases followed by inter-flushing and post-flushing clear water releases does not necessarily decrease the volume and length of sediment deposition. Single flushing releases of large peaks are more likely to reduce length and depth or volume of deposition. This agrees with argument that rapid release of the fine sediments is less likely to increase sediment infiltration (or deposition) (Wooster et al., 2008). It was also indicated that high rate of releases of short duration have minimal ecological impacts (Major et al., 2008; Downs et al., 2009). Figure D-13 (Appendix D) shows the simulated volume of suspension (as percentage of total sediment volume) and peak concentration (as proportion of input peak) in simulation domain for simulation period. The volume of suspended sediment at the end of simulation was smaller in single release scenario followed by scenario 3 and 4. The peak of sediment concentration is higher (could go even larger than the concentration of input) for single releases but lasted shorter than intermittent releases (e.g. scenario 3 and 4). The intermittent release reduced sediment peak for the duration of clear water releases but high suspended concentration was sustained for longer period than the single release. This result may contradict with management strategy proposed by Crosa et al. (2010) and Espa et al. (2013).

However, to keep sediment concentration lower large inter-flushing clear water must be available which would be practically constrained from water conservation point of view.

6.4. CONCLUSIONS

The model developed in this study is aimed to study the downstream transport dynamics of suspended sediments released during sediment flushing operations. The model is simplified to observe large-scale sediment and hydrodynamic waves. The model is first tested with laboratory data of fine sediment transport in immobile coarse bed for three entrainment relations developed for immobile coarse bed conditions and satisfactory agreement was observed at least qualitatively. The erosion rate relation developed in this study (Chapter 5) is also tested in the model and showed encouraging results. The consideration of variable bed porosity in immobile bed transport condition enabled to quantify the deposition thickness (clogged depth) in the immobile bed roughness elements and its effect on sediment concentration. It is observed that sediment peak concentration was attenuated and lagged when bed porosity is considered due to sediment storage in the immobile bed. We studied how the interaction between the waves of suspended sediments and liquid discharge controls the sediment deposition process during flushing operations. The effect of the sediment wave celerity on the wave interaction and deposition processes has been investigated. It is observed that the wave celerity controls the wave interaction to some extent especially when the channel bed materials are fine sediments and thus the traditional assumption of representing wave celerity as equal to the average flow velocity may lead to under-prediction of sediment deposition. When the channel bed was covered by immobile gravel materials, the effect of the celerity factor on sediment deposition was rather less. The study also investigated the dependence of the celerity factor on flow depth, discharge, Rouse number and relative roughness. There is generally an increasing trend in celerity factor with depth and discharge, while a decreasing trend is observed with Rouse number and relative roughness.

The description of variable bed roughness used in the hydrodynamic computation affected the depth and speed of the hydrodynamic wave and the location of its front. As a result larger length of sediment deposit was noted even though the thickness was not different from constant bed roughness. It could be also highlighted that some feedbacks can occur between the propagation of the flood wave and the transport and deposition of fine sediments. The most important effect is the reduction of the bed roughness in the regions of deposition. Since the deposition typically occurs at the tail of the hydrodynamic wave, the flow in this region tends to accelerate. It showed that description of changes in bed roughness as a function of deposition thickness in the rough immobile bed has implication both on the flow field (hydrodynamic

computation) and sediment deposition and must be taken into account in modelling exercise. The other important observation of the study is that there is high dependence of deposition on the ratio of peak-to-base flow during sediment flushing releases where highest ratios produced the longest and thickest region of deposition, while the one with the lowest ratio produced the shortest and thinnest. Thus, a proper selection of this ratio might help to plan a flushing operation with minimal deposition and reduce the downstream environmental impacts. The evaluation of single and intermittent flushing operations followed by inter- and post- flushing clear water releases indicated that a single flushing release followed by clear water release could reduce area or length of sediment deposition. The other important observation is that an intermittent flushing release followed by inter-flushing and post-flushing clear water releases does not necessarily decrease the volume and length of sediment deposition. Single flushing releases of large peaks are more likely to reduce length and depth or volume of deposition. The intermittent release reduced sediment peak for the duration of clear water releases but high suspended concentration was sustained for longer period than the single release. However, to keep sediment concentration lower, large inter-flushing clear water must be available which would be practically constrained from water conservation point of view.

Finally, the evaluation of various entrainment relations of sand bed condition implemented in the model showed very distinct entrainment rates and hence different amounts of deposition. This suggests that the entrainment relations require careful evaluation for their applicability for large scale and high velocity transport conditions such as flushing waves, which are observed at large spatial scales and are characterized by relatively high velocities. In conclusion, the results presented in this study are based on several assumptions. The assumption most important is that there is no sediment supply from the bed (fine sediment bed level in immobile coarse bed is negligible in the initial state) and only the sediments supplied from the upstream are entrained and transported. The effect of changes of bed slope and channel geometry and dimensions (e.g., width) was not taken in to account in this first analysis, although they are undoubtedly important and can be among the main drivers of the deposition patterns over large scales. Finally, it is important to note that this one-dimensional study did not consider the differential deposition that typically occurs on the regions of the cross-section with higher elevation during the falling phase of the hydrodynamic wave. The model also assumed the suspended sediments are uniform in grain size. All these factors could be introduced in a relatively easy way in the model, but the analysis of the individual factors would become quite complex, thus jeopardizing the kind of sensitivity analysis that this study has proposed in this work.

7. SUMMARY

The growing demand for energy and water resources has increased the global boom of dam developments in many of ecologically important rivers across the globe. The sedimentation problems associated with dams have become one of the challenges for policy makers and scientific community and needs urgent and sustainable solutions for next generation of dam users. In this regards, sediment flushing has become a widely used strategy to overcome sedimentation problems in many reservoirs. On the one hand, the downstream environmental impacts associated with flushing releases have become major concern and there is insufficient knowledge to predict the impacts. On the other hand, there is a lack of detailed and comprehensive studies to understand the mechanism of transport and deposition of the released fine sediments in rarely transported coarse channel beds downstream of these dams. Thus, there are necessities for scientific studies that address the gaps in knowledge and propose better management strategy. This study is one of such attempts which focused on describing downstream impacts of sediment flushing and explore processes and dynamics of fine sediment transport in immobile coarse bed such as gravels.

Fine sediment release by flushing operations triggers a cascade of processes that cause complex responses with numerous downstream impacts. This study reports important negative implications of the practice and proposes management strategies. First, based on previously published research, a conceptual framework (Figure 2-2) of the first order, second order and third order impacts of fine sediment releases is developed. The most important first order impacts are extremely high sediment concentration and load, high level of sediment bound contaminants and downstream flooding. The high sediment concentration and load causes aggradation in channel and banks of downstream river although channel degradation could occur during initial stage of the release. The negative biological impacts of sediment releases are mainly due to the direct effects of increased flow and suspended sediments, nutrients and contaminants during flushing and downstream morphological alterations of river habitats following sedimentation of the released sediments. Of all impacts, biological impacts are the most studied impacts with most emphasis on fish and macro-invertebrates. The impacts on vegetation dynamics is less documented although it is reported that vegetation growth is initiated by nutrient rich fine sediment releases that eventually alter downstream channel morphology and flooding pattern. The impacts of contaminants released during sediment flushing are not documented in most of the case studies which highlights particular attention. The spatial and temporal scales of adverse downstream impacts varied from case to case. Generally it is found out that the downstream impacts of sediment flushing were proportional to the distance from the dam. The sediment concentration, grain size distribution of deposits, channel and bank aggradation, effects on fish and macro-invertebrates, effect on dissolved oxygen concentration decreases

with distance away from the dam. The grain size of the released sediments and the timing of subsequent flooding control the temporal scale and long-term morphologic impacts of sediment flushing. The temporal scale of impacts on macro-invertebrates could span from few weeks or a month to several months while the effect on fish could last for a number of years. The impacts on channel vegetation are reported as driven by many years of flushing activities. Although the magnitude of adverse impacts of sediment flushing and the time required for recovery are generally site specific this study proposed general recommendations for best management practices (Section 2.4).
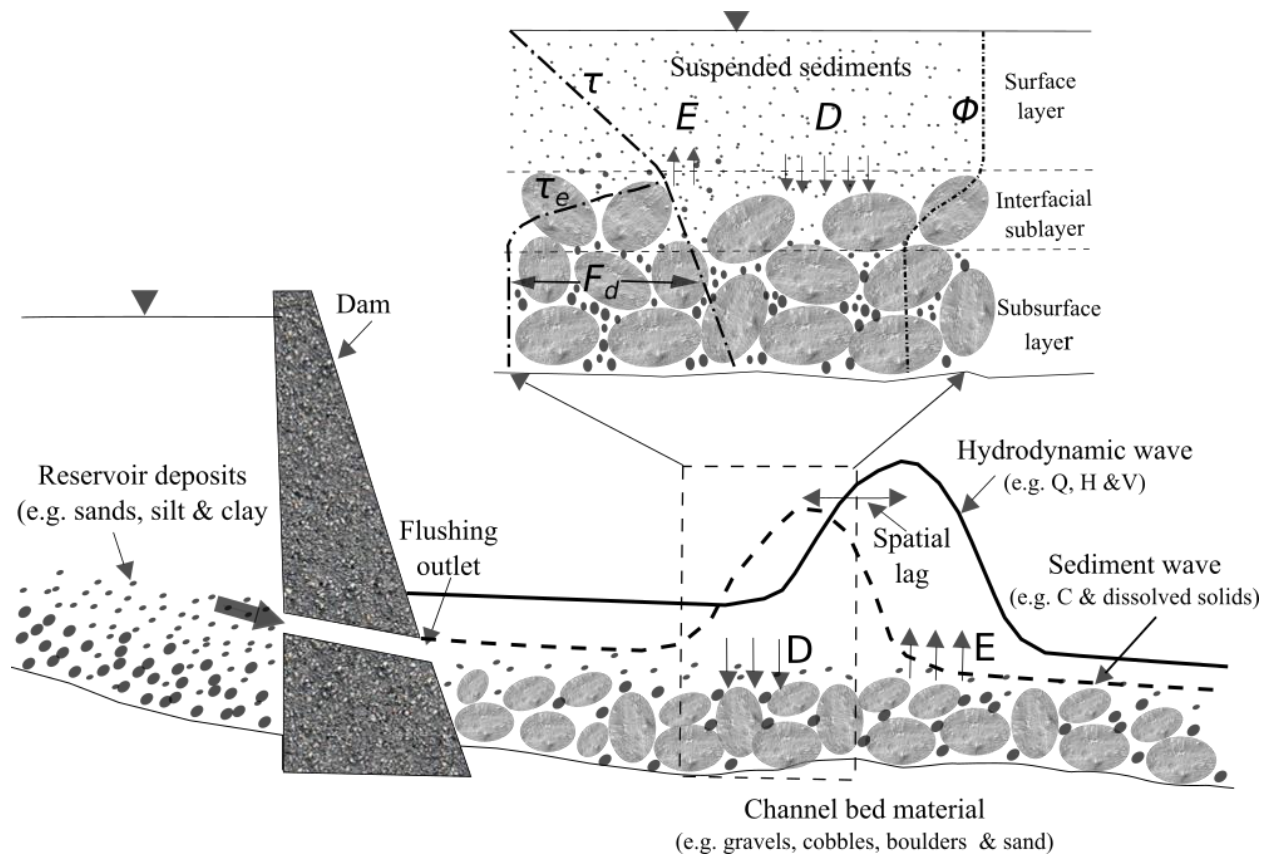
Figure 7-1. The conceptual framework of important processes of flushing releases that were the focus of this study where D = deposition; E = erosion; F_d = drag force; τ = total shear stress; τ_e = effective shear stress in interfacial sublayer; Φ = gravel porosity profile.

As aforementioned, the downstream biological impacts of flushing are mainly related to sediment depositions, during and following the release, in channel habitats that comprise gravels and cobbles. Thus, this study focused on understanding the overall downstream flow and transport dynamics associated with sediment flushing. A general framework that spans from the release point of fine sediments to their

downstream propagation and the interactions with river channel bed composed of coarse immobile gravel bed is developed. Figure 7-1 shows the general conceptual framework of the study.

Better management of sediment flushing activities is aided by best understanding of the underlying downstream processes of fine sediment transport. Thus, investigating the mechanism of fine sediment deposition, erosion and transport in coarse immobile gravel bed is a step forward. A laboratory experiment of fine sediment transport in immobile gravel bed is conducted. First, gravel bed roughness characteristics, porosity and roughness density were derived from gravel surface elevation data. These variables are essential components that govern the flow hydrodynamics of gravel bed. The elevation errors noticed in gravel surface elevation data were characterized and successfully removed by developing a spatial filter (nAMDF) which could be used for any other elevation data with similar errors such as Terrestrial Laser Scanner (TLS). A theoretical relation of roughness density for coarse gravel bed is proposed and its relevance for estimating drag force (F_d) and drag coefficient in rough bed is presented. The analysis also identified interfacial sublayer, an interface in between surface and subsurface flow, that governs flow structure and bed exchange (erosion and deposition) (Figure 7-1, top).

This study presents a new technique that enables direct measurement of fine sediment erosion in immobile gravel bed in running water. The technique can be very useful to monitor rapid bed evolutions such as in dam-break transport at laboratory scale. In connection to this, ten different experiments were conducted to characterize fine sediment erosion in gravel bed ($d_{50} = 24.89$ mm) and develop a relation to predict it. The most important observation from the experiments was the spatial heterogeneity of erosion rate where higher erosion rate was observed in stoss side of gravel particles than the lee side. This agreed with sweep and ejection patterns in turbulent flow structure of rough bed flow and entrainment rate measurements in ripple beds from previous research. Even though turbulent flow structures were not measured in this study it was possible to relate the results with measurements conducted in similar bed configurations. This is a first work of direct measurement of erosion rate and characterizing its spatial heterogeneity in gravel bed that are driven by complex orientation of the roughness elements and turbulent flow structures. It is also found out that increase in gravel roughness had led to increased erosion rate but no significant change in stream-wise velocity. The vertical profile of erosion rate in the roughness elements of gravel showed a linear decrease but the temporal evolution of fine sediment bed level in the roughness elements was found to decay exponentially. Moreover, the temporal pattern of the total depth of erosion in the roughness elements is predictable with an exponential relation.

This study investigated drag force (F_d) profile in the interfacial sublayer of clean gravel bed and found out that it is scaled well with roughness density for all experimental data under consideration. This allowed

describing the effective shear stress distribution (τ_e) available for fine sediment entrainment with an empirical equation. Figure 7-1 (top) shows the conceptual distribution of both effective shear stress and drag force within gravel matrix. With this physical background a new relation of non-equilibrium fine sediment erosion rate in immobile gravel bed is proposed. The new relation is the non-equilibrium pick-up rate function of van Rijn (1984b) in which the empirically predicted shear stress in the roughness layer is implemented. The most important finding of this study is that if the shear stress distribution in the interfacial sublayer is predicted, a relation for sand bed condition can be applied to predict fine sediment erosion rate in immobile gravel bed. This approach is conceptually superior to previous approaches where erosion rate in sand bed condition is scaled empirically for various fine sediment bed level within the interfacial sublayer.

The interaction between hydrodynamic and sediment wave dynamics generated during flushing operations is an important process that control the deposition of fine sediments. In Figure 7-1 the spatial lag between hydrodynamic (solid line) and sediment (broken line) wave and potential zone (in box) of deposition as the waves tend to separate is depicted in a conceptual model. In previous research a glimpse of the role of time lag between liquid and solid discharge on sediment deposition was highlighted. This study focused on the effect of the interactions on spatial pattern of sediment deposition which would be of practical use. A 1-D model of suspended sediment transport was developed comprising major processes that include sediment wave celerity correction, variable bed roughness, bed exchange in immobile bed, hindered settling velocity and rough bed porosity. The model performance was found to be satisfactory to predict fine sediment transport in mobile bed qualitatively. The proposed erosion rate relation showed encouraging results when implemented in the 1-D model. The immobile bed porosity allowed to model clogged depth of fine sediments and found to affect concentration wave by attenuating its peak and enhancing the time lag due to increased sediment storage. The effect of the celerity factor on sediment deposition was rather less in immobile coarse bed but its effect could be significant for sand bed conditions as reported in Tarekegn et al. (2014). Theoretical investigation of the behaviour of celerity factor showed that an increasing trend in celerity factor with depth and discharge, while a decreasing trend was observed with Rouse number and relative roughness. The study also showed that changes in bed roughness by fine sediment deposition in the rough immobile bed modified both the flow field and sediment deposition. This was verified by larger length of sediment deposit noted when variable roughness was considered. Model investigations of fine sediment release scenarios showed high dependence of deposition on the ratio of peak-to-base flow where highest ratios produced the longest and thickest region of deposition while those with the lowest ratio produced the shortest and thinnest. The evaluation of single and intermittent flushing operations followed by inter- and post-flushing clear water

releases indicated that a single flushing release followed by clear water release could reduce area or length of sediment deposition. The other important observation is that intermittent flushing releases followed by inter-flushing and post-flushing clear water releases do not necessarily decrease the volume and length of sediment deposition. Single flushing releases of large peaks are more likely to reduce length and depth or volume of deposition which conform to management strategies proposed in Chapter 2 (e.g. Major et al., 2008; Downs et al., 2009; Wooster et al., 2008). The duration of high concentration for intermittent releases might be higher unless large quantity of inter-flushing clear water releases is made available and this could limit the use of management strategy proposed in Chapter 2 (e.g. Espa et al., 2013; Crosa et al., 2010).

Finally, sediment flushing activities seem to be a viable technique for managing sedimentation as far as dam developments grow at current pace. The impacts will remain challenging and recommending management strategies and alternatives for managers and policy makers remains in the hands of scientists.

BIBLIOGRAPHY

Abad, J.D. and Garcia, M.H., 2009. Experiments in a high-amplitude Kinoshita meandering channel. 2. Implications of bend orientation on bed morphdynamics. *Water Resources Research* 45, W02402.

Aberle, J., 2007. Measurements of armour layer roughness geometry function and porosity. *Acta Geophysica* 55 (1), 23.

Aberle,J., Koll,K., Dittrich, A.,2008. Form induced stresses over rough gravel-beds. *Acta Geophysica* 56 (3), 584-600.

Aberle, J. and Nikora, V., 2006. Statistical properties of armored gravel bed surfaces. *Water Resources Research* 42(11).

Arnon S., Marx L.P., Searcy K.E., Packman A.I., 2010. Effects of overlying velocity, particle size, and biofilm growth on stream-subsurface exchange of particles. *Hydrological Processes* 24(1), 108-114.

Asaeda, T. and Rashid, M.H., 2012. The impacts of sediment released from dams on downstream sediment bar vegetation. *Journal of Hydrology* 430 (431), 25–38.

Asaeda, T., Rashid, M. H., Sanjaya, H. L. K., 2014. Flushing sediment from reservoirs triggers forestation in the downstream reaches. *Ecohydrology*. DOI: 10.1002/eco.1513.

Asselman, N. E. M., Middelkoop, H., van Dijk, P. M., 2003. The impact of changes in climate and land use on soil erosion, transport and deposition of suspended sediment in the River Rhine. *Hydrological Processess* 17, 3225–3244.

Bagnold, R. A., 1966. An approach to the sediment transport problem from general physics. *Geological Survey Proffessional Paper* 442-I.

Basson, G., 2010. *Sedimentation and Sustainable use of reservoirs and river systems*. International Commission on Large Dams (ICOLD) Bulletin.

Bechteler, W., 2006. *Sediment sources and transport processes- Sustainable sediment management of alpine reservoirs considering ecological and economical aspects-Volume 2*. www.alpresrev.eu (Accessed 12.12.2012).

Bednarek, A., 2001. Undamming rivers: a review of the ecological impacts of dam removal. *Environmental Management* 27 (6), 803–814.

Bergstedt, L. C., and Bergersen, E. P., 1997. Health and movements of fish in response to sediment sluicing in the Wind River, Wyoming. *Canadian Journal of Fisheries and Aquatic Sciences* 54(2), 312-319.

Bertoldi, W., and Tubino, M., 2005. Bed and bank evolution of bifurcating channels. *Water Resources Research* 41, W07001.

Bathurst, J.C., 1985. Flow resistance estimation in Mountain Rivers. *Journal of Hydraulic Engineering* 111(4), 625-643.

Bertin, S. and Friedrich, H., 2013. Measurement of gravel-bed topography: evaluation study applying statistical roughness analysis. *Journal of Hydraulic Engineering* 140 (3), 269-279.

Bertin, S., Friedrich, H., Delmas, P., Chan, E., Gimel'farb, G., 2014. Dem quality assessment with a 3d printed gravel bed applied to stereo photogrammetry. *The Photogrammetric Record* 29(146), 241-264.

Bilotta, G. S., Burnside, N. G., Cheek, L., Dunbar, M. J., Grove, M. K., Harrison, C., Davy-Bowker, J., 2012. Developing environment-specific water quality guidelines for suspended particulate matter. *Water Research* 46 (7), 2324-2332.

Brandt, S.A., 2000. Classification of geomorphological effects downstream of dams. *Catena* 40(4), 375-401.

Brandt, S.A. , 1999. *Reservoir desiltation by means of hydraulic flushing: sedimentological and geomorphological effects in reservoirs and downstream reaches as illustrated by the Cachi reservoir and the Reventazon River, Costa Rica*. Ph.D. Thesis, Institute of Geography, Faculty of Science, University of Copenhagen, Denmark.

Brandt, A., 2005. Conceptualization of hydraulic and sedimentary processes in downstream reaches during flushing of reservoirs. In *Proceedings of the XXXI IAHR Congress: Water engineering for the future: choices and challenges: COEX Seoul September 11-16, 2005*, pp. 2577-2588

Brandt, S. A. and Swenning, J., 1999. Sedimentological and geomorphological effects of reservoir flushing: the Cachõ Reservoir, Costa Rica, 1996. *Geografska Annaler* 81(3), 391- 407.

Braschi, G. and Gallati, M., 1992. Survey and characteristics of the submersion wave due to the sudden opening of the bottom outlet of Alto Mora dam (Italy). In Saul et al. (eds.), *Floods and Flood Management*, pp. 231-246.

Brasington, J. and Smart, R. M. A., 2003. Close range digital photogrammetric analysis of experimental drainage basin evolution. *Earth Surface Processes Landforms* 28(3), 231–247.

Bresusers, H.N., Klaassen, G.J., Brakel, J, van Roode, F.C., 1982. Environmental impact and control of reservoir sedimentation. In *14th Congress on Large Dams, ICOLD*, Ri de Janeiro, Q54, R23, pp.353-372.

Brownlie, W.R., 1982. *Prediction of Flow Depth and Sediment Discharge in Open Channels*. Report No. KH-R-43A, Keck Laboratory of Hydraulics and Water Resources, California Institute of Technology, Pasadena, California.

Brooker, M. P., 1981. The impact of impoundments on the downstream fisheries and general ecology of rivers. *Advances in Applied Biology* 6, 91-152.

Buermann, Y., Du Preez, H. H., Steyn, G. J., Harmse, J. T., Deacon, A., 1995. Suspended silt concentrations in the lower Olifants River (Mpumalanga) and the impact of silt releases from the Phalaborwa Barrage on water quality and fish survival. *Koedoe* 38(2), 11-34.

Buchholz, R. J. and Knofczynski, M., 1988. Sediment Flushing Experiences at Cherry Creek Dam. In *Hydraulic Engineering*, 1062-1067.

Butler, J. B., Lane, S. N., Chandler, J. H., 2001. Characterization of the structure of river-bed gravels using two-dimensional fractal analysis. *Mathematical Geology* 33(3), 301–330.

Cao, Z., 1999. Equilibrium near-bed concentration of suspended sediment. *Journal of Hydraulic Engineering* 125, 1270-1278.

Cao, Z. and Carling, P., 2002. Mathematical modelling of alluvial rivers:reality and myth. part 1: General review. *Proceedings of the ICE-Water and Maritime Engineering* 154, 207-219.

Cao, Z., Pender, G.,Wallis,S., Carling, P., 2004. Computational dam-break hydraulics over erodible sediment bed. *Journal of Hydraulic Engineering* 130, 689-703.

Cao, Z., Pender, G., Carling, P., 2006. Shallow water hydrodynamic models for hyperconcentrated sediment-laden floods over erodible bed. *Advances in Water Resources* 29, 546-557.

Camenen, B., Jodeau, M., Jaballah, M., 2013. Estimate of net sediment deposit dynamics over a gravel bar using photography analysis. *International Journal of Sediment Research* 28 (2), 220 - 233.

Celik, I. and W. Rodi, 1988.Modeling suspended sediment transport in non-equilibrium situations. *Journal of Hydraulic Engineering* 114, 1157-1191.

Chang, H.H., Harrison, L.L., Lee, W., Tu, S., 1996. Numerical modeling for sediment-pass-through reservoirs. *Journal of Hydraulic Engineering* 122(7), 381-388.

Cheng, N., 1997. Simplified settling velocity formula for sediment particle. *Journal of Hydraulic Engineering* 123, 149-152.

Chien, N., 1985. Changes in river regime after the construction of upstream reservoirs. *Earth Surface Processes and Landforms* 10(2), 143-159.

Chiew, Y. M. and Parker, G., 1994. Incipient motion on non-horizontal slopes. *Journal of Hydraulic Research* 32(5), 649–660.

Collier, K. J., 2002. Effects of flow regulation and sediment flushing on instream habitat and benthic invertebrates in a New Zealand river influenced by a volcanic eruption. *River Research and Applications* 18(3), 213-226.

Colebrook, C. F. and White, C. M., 1937. Experiments with fluid friction in roughened pipes. *Proceedings of the Royal Society of London. Series A, Mathematical and Physical Sciences* 161(904), 367-381.

Cooper, J.R. and Tait, S.J., 2009. Water-worked gravel beds in laboratory flumes - a natural analogue? *Earth Surface Processes and Landforms* 34 (3), 384-397.

Cooper, J. R., Aberle, J., Koll, K., McLelland, S. J., Murphy, B. M., Tait, S. J., Marion, A., 2008. Observation of the near-bed flow field over gravel bed surfaces with different roughness length scales. In *Proc. Int. Conf. on Fluvial Hydraulics River Flow 2008*, Vol. 3, No. 5.

Crank, J., and Nicolson, P., 1947. A practical method for numerical evaluation of solutions of partial differential equations of the heat conduction type. In *Mathematical Proceedings of the Cambridge Philosophical Society* 43, 50-67.

Crosa, G., Castelli, E., Gentili, G., Espa, P., 2010. Effects of suspended sediments from reservoir flushing on fish and macro-invertebrates in an alpine stream. *Aquatic Sciences* 72, 85–95.

Cui,Y.,Wooster, J.,K., Venditti, J.,G., Dusterhoff, S.,R., Dietrich, W.,E., Skla, L.,S., 2008. Simulating Sediment Transport in a Flume with Forced Pool-Riffle Morphology: Examinations of Two One-Dimensional Numerical Model. *Journal of Hydraulic Engineering* 134 (7), 892–904.

Cui, Y., Parker, G., Lisle, T. E., Gott, J., Hansler-Ball, M. E., Pizzuto, J. E., Reed, J. M., 2003. Sediment pulses in mountain rivers: 1. Experiments. *Water Resources Research* 39(9).

Curran, J. C. and Waters, K. A., 2014. The importance of bed sediment sand content for the structure of a static armor layer in a gravel bed river. *Journal of Geophysical Research: Earth Surface* 119 (7), 1484-1497.

Davis, P., and Atkinson, T., 2000. Longitudinal dispersion in natural channels: 3. an aggregated dead zone model applied to the river Severn, UK. *Hydrology Earth System Sciences* 4, 373-381.

de Junet, A., Abril, G., Guérin, F., Billy, I., de Wit, R., 2005. Sources and transfers of particulate organic matter in a tropical reservoir (Petit Saut, French Guiana): a multi-tracers analysis using d13C, C/N ratio and pigments. *Biogeosciences Discussions* 2 (4), 1159–1196.

Dey, S. and Das, R., 2012. Gravel-Bed Hydrodynamics: Double-Averaging Approach. *Journal of Hydraulic Engineering* 138,707-725.

Dietrich, W. E., 1982. Settling velocity of natural particles. *Water Resources Research* 18, 1615-1626.

Di Silvio G., 2004. Modelling long-term reservoir sedimentation for optimal managementstrategies. In *the International Conference for Hydro-Science and Engineering*, Brisbane, Australia.

Duan, J. and Nanda, S., 2006. Two-dimensional depth-averaged model simulation of suspended sediment concentration distribution in a groyne field. *Journal of Hydrology* 327, 426-437.

Duan, J. G. and Julien, P. Y., 2010. Numerical simulation of meandering evolution. *Journal of Hydrology* 391, 34-46.

Downs, P. W., Cui, Y., Wooster, J. K., Dusterhoff, S. R., Booth, D. B., Dietrich, W. E., Sklar, L. S., 2009. Managing reservoir sediment release in dam removal projects: an approach informed by physical

and numerical modelling of non-cohesive sediment. *International Journal of River Basin Management* 7(4), 433-452.

Einstein, H.A., 1950. *The bed load function for sediment transport in open channel flow*. United States Department of Agriculture, Technical Bulletin No. 1026. Washington, D.C.

Einstein, H. A. and Chien, N., 1953. Transport of sediment mixtures with large ranges of grain sizes. *MRD Sediment Series* 2,73. Institute of Engineering Research, University of California, Berkeley.

Elder, J., 1959. The dispersion of marked uid in turbulent shear flow. *Journal of Fuid Mechanics* 5, 544-560.

Espa, P., Castelli, E., Crosa, G., Gentili, G., 2013. Environmental effects of storage preservation practices: Controlled flushing of fine sediment from a small hydropower reservoir. *Environmental Management* 52, 261–276.

Espa, P., Crosa, G., Gentili, G., Quadroni, S., Petts, G., 2014. Downstream ecological impacts of controlled sediment flushing in an alpine valley river: a case study. *River Research and Applications*. DOI: 10.1002/rra.

Evans, E., and Wilcox, A. C., 2014. Fine sediment infiltration dynamics in a gravel-bed river following sediment pulse. *River Research and Applications* 30(3), 372-384.

Fischer, H., List, E., Koh, R., Imberger, J., Brooks, N., 1979. *Mixing in Inland and Coastal Waters*. Academic Press, NewYork.

Foster, I. D. L. and Charlesworth, S. M., 1996. Heavy metals in the hydrological cycle: trends and explanation. *Hydrological processes* 10(2), 227-261.

Francalanci, S., Solari, L., Toffolon, M., Parker, G., 2012. Do alternate bars affect sediment transport and ow resistance in gravel-bed rivers? *Earth Surface Process Landforms* 37,866-875.

Frings, R. M., Kleinhans, M. G., and Vollmer, S. , 2008. Discriminating between pore-filling load and bed-structure load: a new porosity-based method, exemplified for the river rhine. *Sedimentology* 55, 1571-1593.

Fruchard, F., and Camenen, B., 2012. Reservoir sedimentation: different type of flushing - friendly flushing example of Genissiat dam flushing. In *ICOLD International Symposium on Dams for a changing world,* 6-p, Kyoto, Japan.

Gallerano, F. and Cannata, G., 2011.Compatibility of reservoir sediment flushing and river protection. *Journal of Hydraulic Engineering* 137 (10), 1111–1125.

Garcia, M., and Parker, G., 1991. Entrainment of bed sediment into suspension. *Journal of Hydraulic Engineering* 117(4), 414–435.

Garcia, M., 2008. *Sedimentation engineering: processes, measurements, modeling, and practice*. ASCE Manuals and Reports on Engineering Practice No. 110.

Garric, J., Migeon, B., Vindimian, E., 1990. Lethal effects of draining on brown trout: a predictive model based on field and laboratory studies. *Water Research* 24, 59–65.

Gaudio, R. and Marion, A., 2003. Time evolution of scouring downstream of bed sills. Journal of Hydraulic Research 41(3), 271-284.

Grams, P. E., and Wilcock, P. R., 2007. Equilibrium entrainment of fine sediment over a coarse immobile bed. *Water Resources Research* 43, W10420.

Grams, P. E. and Wilcock, P. R. , 2014. Transport of fine sediment over a coarse, immobile riverbed. *Journal of Geophysical Research: Earth Surface* 119, 188-211.

Gerster S. and P. Rey, 1994. *Consequences ecologiques des curages des bassin de retenue*. Office federal de l'environment, des forets et du paysage (OFEFP), Berne, Suisse.

Gonzalez, R.C., Woods, R.E., Eddins, S. L., 2004. *Digital image processing using MATLAB*. Upper Saddle River, N. J: Pearson Prentice Hall.

Goring, D. G., Nikora, V. I., McEwan, I. K., 1999. Analysis of the texture of gravel-beds using 2-D structure functions. *Proc., I.A.H.R.Symp. on River, Coastal and Esturine Morphodynamics*, Springer,Germany, 111–120.

Graf, W. L., 1990. Fluvial dynamics of Thorium-230 in the Church Rock Event, Puerco River, New Mexico. *Annals Association of American Geographers* 80, 327-342.

Graf, W. L., Clark, S. L., Kammerer, M. T., Lehman, T., Randall, K., Schroeder, R., 1991, Geomorphology of heavy metals in the sediments of Queen Creek, Arizona, USA. *Catena*18, 567-582.

Grant, G.E. and Lewis, S.L., 2015. The Remains of the Dam: What have we learned from 15 years of US dam removals. In, *G. Lollino et al. (eds.), Engineering Geology for Society and Territory -* Volume 3, DOI: 10.1007/978-3-319-09054-2_7.

Gray, L. J. and Ward, J. V., 1982. Effects of sediment releases from a reservoir on stream macroinvertebrates. *Hydrobiologia* 96(2), 177-184.

Gray, L. J. and Ward, J. V., 1982b. Effects of releases of sediment from reservoirs on stream biota. *Technical Completion Report* No.116. Colorado Water   Resources Research Institute.

Griffiths, G.A., 1989. Form resistance in gravel channels with mobile beds. *Journal of Hydraulic Engineering* 115(3) 340-355.

Gutzmer, M. P., King, J. W., Overhue, D. P., 1996. Environmental impacts in the vicinity of Spencer Hydropower Dam during sluicing activities in the Niobrara River, Nebraska. *Transactions of the Nebraska Academy of Sciences* 23, 1-8.

Harris, C. and P. Wiberg, 2001. A two-dimensional, time-dependent model of suspended sediment transport and bed reworking for continental shelves. *Computers and Geosciences* 27, 675-690.

Huybrechts, N., Hervouet, C. ,Villaret, J., 2010. Comparison between 2d and 3d modelling of sediment transport: application to the dune evolution. In *Proceedings of the 5th IAHR International Conference on Fluvial Hydraulics(River Flow 2010)*, Braunschweig,Germany,8-10 September 2010.

Hannan, H.H., 1979. Chemical modifications in reservoir-regulated streams. In *Ward, J.V. and Stanford, J.A. (eds.), The Ecology of regulated streams,*75-94. New York: Plenum Press.

Heppell, C. M., Wharton, G., Cotton, J. A. C., Bass, J. A. B., Roberts, S. E., 2009. Sediment storage in the shallow hyporheic of lowland vegetated river reaches. *Hydrological Processes* 23(15), 2239-2251.

Haun, S. and Lizano, L., 2014. Measurements of spatial distribution of suspended sediment concentrations in a hydropower reservoir. In *Schleiss et al. (eds.), Reservoir Sedimentation: International Conference on Fluvial Hydraulics*, 63-70. Lausanne, Switzerland.

Halg R. 1996. *Spulung des Stausees Ova Spin (Flushing of the Ova Spin Reservoir). Internationales Symposium Verlandung von Stauseen und Stauhaltungen, Sedimentprobleme in Leitungen und Kanalen, l. Teil, 28./29*. Marz 1996 an der ETH Zurich. Mitteilungen 142, Versuchanstalt fur Wasserbau, Hydrologies und Glaziologie der Eidgenossischen Technischen Hochschule Zurich, D. Vischer, ed., 171- 187. (in German).

Hodge, R., Brasington, J., Richards, K., 2009. In situ characterization of grain-scale fluvial morphology using Terrestrial Laser Scanning. *Earth Surface Process Landforms* 34, 954–968.

Hori, M., Tanonaka, A., Wakabayashi, H., Kojima, T., 2006. Influence of sediment flushing from dam on growth of rice. *Transactions of Japanese Society of Irrigation, Drainage and Reclamation Engineering* 245, 683-689 (in Japanese).

Hesse, L. W. and Newcomb, B. A., 1982. Effects of flushing Spencer Hydro on water quality, fish, and insect fauna in the Niobrara River, Nebraska. *North American Journal of Fisheries Management* 2(1), 45-52.

Huang, M., Huang, A., and Capart, H., 2010. Joint mapping of bed elevation and flow depth in micro-scale morphdynamics experiments. *Experiments in Fluids* 49, 1121–1134.

International Energy Agency (IEA), 2006. *Annex VIII - Hydropower Good Practices - Environmental Mitigation and Benefits-Case study 04-01: Reservoir Sedimentation - Dashidaira Dam, Japan*. Report on IEA Hydropower Implementing Agreement.

International Commission on Large Dams (ICOLD), 2103. *Register of Dams - General Synthesis*. (Accessed September 2015 at www.icold-cigb.org/).

Iervolino, M., Pontillo, M., Di Cristo, C., 2010. Comparison among different entrainment/deposition functions in the simulation of a 1D dam-break. In *Proceedings of River Flow, Dittrich A, Koll K, Aberle J, Geisenhainer P (eds). Bundesanstalt für Wasserbau: Braunschweig*, 585-590.

Jackson, R.G., 1976. Sedimentological and fluid-dynamic implications of the turbulent bursting phenomenon in geophysical flows. *Journal of Fluid Mechanics* 77 (3), 531-560.

Jansson, M.B., Erlingsson, U., 2000. Measurement and quantification of a sedimentation budget for a reservoir with regular flushing. *Regulated Rivers: Research and Management* 16, 279-306.

Kanthack, F.E., 1924. *The principles of Irrigation Engineering-with special Reference to South Africa*. London, 299.

Kantoush S.A., Sumi, T., Takemon, Y., 2011. *Lighten the load. International Water Power and Dam Construction, 38-45*. http://www.waterpowermagazine.com/features/featurelighten-the-load (Accessed 15th March 2015).

Keshavarzi, A., Ball, J., Nabavi, H., 2012. Frequency pattern of turbulent flow and sediment entrainment over ripples using image processing. *Hydrology and Earth System Sciences* 16(1), 147-156.

Keulegan, G.H., 1938. Laws of turbulent flow in open channels. *Journal of Research of the National Bureau of Standards* 21, 707-741.

Khullar, N.K., Kothyari, U.C., Raju, K.G.R., 2013. Study of deposition of fine sediment within the pores of a coarse sediment bed stream. *International Journal of Sediment Research* 28 (2), 210-219.

Kinoshita, J., Takahisa, A., Mizuyama, M. F., Sawada, T., 2002. The impact on fish of sediment flushing from a sabo dam. In *International Congress INTERPRAEVENT 2002 in the Pacific Rim: Congress publication* 2, 927-934. Matumoto, Japan.

Kirkgoz, M. S., and Ardichoglu, M., 1997. Velocity profiles of developing and developed open channel flow. *Journal of Hydraulic Engineering* 123(12), 1099-1105.

Kleinhans, M. G., Wilbers, A. W. E., De Swaaf, A., Van Den Berg, J. H., 2002. Sediment supply-limited bedforms in sand-gravel bed rivers. *Journal of Sedimentary Research* 72 (5), 629-640.

Kurobe River Office, 2008. Ministry of Land, Infrastructure, Transport and Tourism, Japan. http://www.japanriver.or.jp/EnglishDocument/DB/file/005%20Hokuriku%2013(Accessed 17.03.15).

Kereselidze N.B., Kutavaya V.I., Tsagareli Y.A., 1986. Silting and flushing mountain reservoirs, exemplified by the Rioni series of hydroelectric stations. *Hydrotechnical Construction* 19 (9), 514-520.

Kemenes, A., Forsberg, B. R., Melack, J. M., 2007. Methane release below a tropical hydroelectric dam. *Geophysical Research Letters* 34, L12809, doi: 10.1029/2007GL029479.

Kondolf, G.M., 1997. Hungry water: effects of dams and gravel mining on river channels. *Environmental Management* 21 (4), 533–551

Kuhnle, R. A., Wren, D. G., Langendoen, E. J., Rigby, J. R., 2013. Sand transport over an immobile gravel substrate. *Journal of Hydraulic Engineering* 139 (2), 167–176.

Lai, J.S. and Shen, H.W., 1996. Flushing sediment through reservoirs. *Journal of Hydraulic Research* 34(2), 237-255.

Lajeunesse, E., Malverti, L., Charru, F., 2010. Bed load transport in turbulent flow at the grain scale: Experiments and modeling. *Journal of Geophysical Research* 115, F04001.

Lanzoni, S., 2000. Experimental on bar formation in a straight flume. 1. Uniform sediment. *Water Resources Research* 36, 3337 – 3349.

Lane, S. N., Reid, S. C., Westaway, R. M., Hicks, D. M., 2005. Remotely sensed topographic data for river channel research: the identification, explanation and management of error. Chapter 6 *in Spatial Modelling of the Terrestrial Environment (Eds. R. E. J. Kelly, N. A. Drake & S. L. Barr)*,113-136. Wiley, Hoboken, New Jersey, USA.

Leeder, M. R., Gray, T. E., Alexander, J. A. N., 2005. Sediment suspension dynamics and a new criterion for the maintenance of turbulent suspensions. *Sedimentology* 52, 683-691.

Limare, A., Tal, M., Reitz, M. D., Lajeunesse, E., Métivier, F., 2011. Optical method for measuring bed topography and flow depth in an experimental flume. *Solid Earth* 2 (2), 143-154.

Lisle, T. E. and Lewis, J., 1992. Effects of sediment transport on survival of salmonid embryos in a natural stream: A simulation approach. *Canadian Journal of Fisheries and Aquatic Sciences* 49, 2337-2344.

Li, Z. and Davies, A., 2001. Turbulence closure modelling of sediment transport beneath large waves. *Continental Shelf Research* 21, 243-262.

Liu, J., S. Minami, Otsuki, H. , Liu, B. , and Ashida, K., 2004a. Environmental impacts of coordinated sediment flushing. *Journal of Hydraulic Research* 42, 461-472.

Liu, J., S. Minami, H. Otsuki, B. Liu, and K. Ashida, K., 2004b. Prediction of concerted sediment flushing. *Journal of Hydraulic Engineering* 130, 1089-1096.

Ma, Y., Huang, H., Nanson, G. C., Li, Y., Yao, W., 2012. Channel adjustments in response to the operation of large dams: the upper reach of the lower Yellow River. *Geomorphology*147, 35-48.

Meade, R. H., Yuzyk, T. R., Day, T. J., 1990. Movement and storage of sediment in rivers of the United States and Canada. In *Wolman, M. G., and Riggs, H. C., eds., Surface Water Hydrology: The Geology of North America: Boulder, CO, Geological Society of America*, 255-280.

Madej, M. A. and Ozaki, V., 1996. Channel response to sediment wave propagation and movement, Redwood Creek, California, USA. *Earth Surface Processes and Landforms* 21, 911-927.

Major, J. J., Spicer, K. R., Rhode, A., O'Connor, J. E., Bragg, H. M., Tanner, D. Q., and Grant, G. E., 2008. Initial fluvial response to the removal of Oregon's Marmot Dam. *Eos, Transactions American Geophysical Union* 89(27), 241-242.

Marion, A., Tait, S.J., McEwan, I.K., 2003. Analysis of small-scale gravel bed topography during armoring. *Water Resources Research* 39, 12. doi: 10.1029/2003WR002367.

McLean, S. R. and Nikora, V. I., 2006. Characteristics of turbulent unidirectional flow over rough beds: Double-averaging perspective with particular focus on sand dunes and gravel beds. *Water Resources Research* 42(10).

MEL Mikroelektronik GmbH, 2002. *Measuring Systems M5, manual*. Laser Sensor: M5L/4.

Metflow, 2000. *UVP Monitor - Model UVP-XW: Users guide*. Metflow SA, Lausanne, Switzerland.

Meyer-Peter, E. and Müller, R., 1948. *Formulas for bed-load transport*. IAHR, 1948.

Meyer, F., 1979. Iterative image transformations for an automatic screening of cervical smears. *Journal of Histochemistry and Cytochemistry* 27(1), 128-135.

Mignot, E., Barthelemy, E., Hurther, D., 2009. Double-averaging analysis and local flow characterization of near-bed turbulence in gravel-bed channel flows. *Journal of Fluid Mechanics* 618, 279-303.

Mohajeri, S. H. 2014. *Hydrodynamics of Gravel Bed Flows (Implication on Colmation)*. PhD thesis, University of Trento, Italy.

Moore, C.A., Van Veelen, M., Ashton, P.J., Walmsley, R.D., 1991. Preliminary water quality guidelines for the Kruger National Park Rivers. *KNP Rivers Research Program Report No* 1(xi), 1-91.

Morris, G. L. and Fan, J., 2010. *Reservoir sedimentation handbook: design and management of dams, reservoirs, and watersheds for sustainable use, Voulme 9*. McGraw-Hill New York.

Miller, J., Barr, R., Grow, D., Lechler, P., Richardson, D., Waltman, K., and Warwick, J., 1999. Effects of the 1997 flood on the transport and storage of sediment and mercury within the Carson River Valley, west-central Nevada. *Journal of Geology* 107, 313-327.

Mastrorillo, S. and Dauba, F., 1999. Short-term impact of reservoir cleaning on the microhabitat use of three non-salmonid fishes in a piedmont river in south west France. *Aquatic sciences* 61(4), 323-336.

Nelson, R. W., Dwyer, J. R., Greenberg, W. E., 1987. Regulated flushing in a gravel-bed river for channel habitat maintenance: A Trinity River fisheries case study. *Environmental Management* 11(4), 479–493.

Nielsen, P., 1992. *Coastal bottom boundary layers and sediment transport*. World Scientific Publishing Co. Pte. Ltd.

Nezu, I. and Nakagawa, H., 1993. *Turbulence in Open-Channel Flows*. A.A. Balkema.

Nickling, W. G. and McKenna Neuman, C., 1995. Developments of deflation lag surfaces: *Sedimentology* 42, 403-414.

Nikora, V. I., Goring, D. G., Biggs, B. J. F., 1998. On gravel-bed roughness characterisation. *Water Resources Research* 34(3), 517–527.

Nikora, V., Goring, D., McEwan, I., and Griffiths, G., 2001. Spatially averaged open-channel flow over rough bed. *Journal of Hydraulic Engineering* 127, 123-133.

Nikora, V., Koll, K., McEwan, I., McLean, S., Dittrich, A., 2004. Velocity distribution in the roughness layer of rough-bed flows. *Journal of Hydraulic Engineering* 130(10), 1036-1042.

Nikuradse J., 1933. *Strömungsgesetze in rauhen Rohren*. Forschungs-Arbeit des IngenieurWesens, No.361 (in German).

Nnadi, F. and Wilson, K., 1995. Bed-Load Motion at High Shear Stress: Dune Washout and Plane-Bed Flow. *Journal of Hydraulic Engineering* 121(3), 267–273.

Nnadi, F. and Wilson, K., 1992. Motion of Contact Load Particles at High Shear Stress. *Journal of Hydraulic Engineering* 118(12), 1670–1684.

Okayasu, A., Fujii, K., Isobe, M., 2011. Effect of external turbulence on sediment pickup rate. *Coastal Engineering Proceeding* 1(32), 14.

Olsen, N.R.B., 1999. Two-dimensional numerical modeling of flushing process in water reservoirs. *Journal of Hydraulics Research* 37(1), 3-16.

Packman A.I. and MacKay J.S., 2003. Interplay of stream-subsurface exchange, clay particle deposition, and streambed evolution. Water Resources Research 39 (4).

Pellachini, C., 2011. *Modelling fine sediment transport over an immobile gravel bed*. Ph.D. thesis, University of Trento, 2011.

Papanicolaou, A. N., Diplas, P., Dancey, C. L., Balakrishnan, M., 2001. Surface roughness effects in near-bed turbulence: Implications to sediment entrainment. *Journal of Engineering Mechanics* 127 (3), 211-218.

Papanicolaou, A.N., Dermisis, D.C., Elhakeem, M., 2011. Investigating the role of clasts on the movement of sand in gravel bed rivers. *Journal of Hydraulic Engineering* 137(9),871-883.

Papanicolaou, A.N., Bdour, A., Wicklein, E. 2004. One-dimensional hydrodynamic/sediment transport model applicable to steep mountain streams. *Journal of Hydraulic Research* 42 (4), 357–375.

Petts, G. E., 1984. *Impounded Rivers: Perspectives for Ecological Management*. Wiley and Sons.

Petts, G.E., Gurnell, A.M. 2005. Dams and geomorphology: research progress and new directions. *Geomorphology* 71, 27-47.

Poggi, D., Porporato, A., Ridolfi, L., Albertson, J. D., Katul, G. G., 2004. The effect of vegetation density on canopy sub-layer turbulence. *Boundary-Layer Meteorology* 111, 565–587.

Pokrajac, D. and Manes, C., 2009. Velocity measurements of a freesurface turbulent ow penetrating a porous medium composed of uniform-size spheres. *Transport in Porous Media* 78, 367-383.

Pokrajac, D. and Manes ,C., 2008. Interface between turbulent flows above and within rough porous walls. *Acta Geophysica* 56(3), 824-844.

Richardson, J. and Zaki, W., 1954. The sedimentation of a suspension of uniform spheres under conditions of viscous flow. Chemical Engineering Science 3, 65-73.

Rutherford, J., 1994. *River mixing*. John Wiley & Son Ltd.

Rathburn, S. and Wohl, E., 2003. Predicting fine sediment dynamics along a pool-riffle mountain channel. *Geomorphology* 55(1), 111-124.

Rathburn. S. and Wohl, E., 2001. One-dimensional sediment transport modeling of pool recovery along a mountain channel after a reservoir sediment release. *Regulated Rivers: Research and Applications* 7 (3), 251–273.

Roux, A. L. 1984. The impact of emptying and cleaning reservoirs on the physico-chemical and biological water quality of the Rhône downstream of the dams. *Regulated Rivers*, 61-70.

Sambrook Smith, G. H. and Nicholas, A. P., 2005. Effect on flow structure of sand deposition on a gravel bed: Results from a two-dimensional flume experiment. *Water Resources Research* 41, W10405.

Sarkar, S. and Dey, S., 2010. Double-averaging turbulence characteristics in flows over a gravel bed. *Journal of Hydraulic Research* 48, 801-809.

Scheuerlein, H., 1991. Sediment sluicing in mountain reservoirs. In *Armanini, A. and Di Silvio, G. (eds.), Fluvial Hydraulics of Mountain Regions: Lecture Notes in Earth Sciences* 37, 223-234.

Scheuerlein, H., 1995. Downstream effects of dam construction and reservoir operation. In *Sixth International Symposium on River Sedimentation, Management of Sediment: Philosophy, Aims, and Techniques, New Delhi, 7-11 November, 1995, pp.1101-1108*. Balkema, Rotterdam.

Schmeeckle, M. W., Nelson, J. M., Shreve, R. L. , 2007. Forces on stationary particles in near-bed turbulent flows. *Journal of Geophysical Research: Earth Surface* 112(F2).

Seddighiy,M., He, S., Pokrajac, D., O'Donoghue, T., Vardy, A. E., 2015.Turbulence in a transient channel flow with a wall of pyramids roughness. *Journal of Fluid Mechanics*781, 226–260.

Soares-Frazão, S., Le Grelle, N., Spinewine, B., Zech, Y., 2007. Dam-break induced morphological changes in a channel with uniform sediments: measurements by a laser-sheet imaging technique. *Journal of Hydraulic Research* 45, 87–95.

Spinewine, B., Capart, H., Larcher, M., Zech, Y., 2003. Three-Dimensional Voronoï Imaging Methods for the Measurement of Near-Wall Particulate Flows. *Experiments in Fluids* 34, 227–241.

Spork, V., Ruland, P., Kongeter, J., 1995. Polluted sediments in small reservoirs. In *Gardiner, J. (ed.), Proceedings of the XXVIth Congress of the IAHR: The Hydraulics of Water Resources and their Development* 4, 248-253. London, 11-15 September 1995.

Stillwater Sciences, 2002. *Sediment transport modeling following the removal of Marmot Dam*. Technical Report to Portland General Electric Company, Stillwater Science, Portland, Oregon.

Sumi, T., and Kantoush, S. A., 2010. Integrated management of reservoir sediment routing by flushing, replenishing, and bypassing sediments in Japanese river basins. In *International Symposium on Ecohydrology, 831-838*. Kyoto.

Sakamoto, K., Sekine, H., Kawashima, T., 2010. Accumulation of allochthonous sediment and litter on a sediment bar subject to sand release from an upstream dam. *Landscape and Ecological Engineering* 6(2), 317-323.

Siviglia, A. and Toro, E. F., 2009. WAF method and splitting procedure for simulating hydro-and thermal-peaking waves in openchannel flows. *Journal of Hydraulic Engineering* 135, 651-662.

Smith, J. D. and McLean, S., 1977. Spatially averaged ow over a wavy surface. *Journal of Geophysical Research* 82, 1735-1746.

Sloff, C. J., 1991. *Reservoir sedimentation; a literature survey*. TU Delft.

Schälchli, U., 1995. Basic equations for siltation of riverbeds. *Journal of Hydraulic Engineering* 121(3), 274-287.

Schälchli, U., 1992. The clogging of coarse gravel river beds by fine sediment. *Hydrobiologia* 235-236 (1), 189-197.

Stanley, E. H. and Doyle, M. W., 2003. Trading off: the ecological effects of dam removal. *Frontiers in Ecology and the Environment* 1(1), 15-22.

Sundborg, A. and Jansson, M. B., 1992. Present and future conditions of reservoir sedimentation. *UNGI Rapport* 81, 157-164.

Sung, K., Lee, H., Choi, Y. S., 2009. Development of a multiline laser vision sensor for joint tracking in welding. *Welding Journal* 88(4),79-85.

Sutherland, A. J., 1967. Proposed mechanism for sediment entrainment by turbulent flows. *Journal of Geophysical Research* 72, 6183–6194.

Takazi, K., Nawatani, N., Kunimine, Y., Morikawa, T., Nagura,T., Wakimoto, R., Asada, R., Watanabe,H., Nagai, K., Ikeda, Y., Sato,K, Segawa, H., Miyata, K., 2002. Sediment characteristics of Dashidaira dam reservoir at Kurobe River and Toyama Bay, and flushed suspension impacts on fishes. *Journal of Geological Society of Japan* 108(7), 435-452 (in Japanese).

Takazi, K., Shraki, K., Imanishi, H., Asada, R., Wakimot, R., Sato, K., 2007. Characteristics of Flushing Dam Sediments From Dashidaira Dam at Kurobe River, Toyama, Japan, After One Year. *Journal of the Clay Science Society of Japan* 46(1), 46-60 (in Japanese).

Tarekegn, T.H., Toffolon, M., Righetti, M., Siviglia, A., 2014. Modelling suspended sediment wave dynamics of reservoir flushing. In *Schleiss et al. (eds.), Reservoir Sedimentation, International Conference on Fluvial Hydraulics, River Flow 2014*,163-173.

Teodoru, C. and Wehrli, B., 2005. Retention of sediments and nutrients in the Iron Gate I Reservoir on the Danube River. *Biogeochemistry* 76, 539–565.

Thorne, P. and Hanes, D., 2002. A review of acoustic measurement of small-scale sediment processes. *Continental Shelf Research* 22, 603 – 632.

Tigrek, S., and Aras, T., 2011. *Reservoir Sediment Management*. Taylor and Francis.

Toffolon, M., Siviglia, A., Zolezzi,G., 2010. Thermal wave dynamics in rivers affected by hydropeaking. *Water Resources Research* 46.

Toro, E.,2001. *Shock-capturing methods for free-surface shallow flows*. Chichester, etc.: Wiley.

van Maren, D. S., Winterwerp, J. C., Wu, B. S., Zhou, J. J., 2009. Modeling hyper-concentrated flow in the Yellow River. *Earth Surface Processes and Landforms* 34(4), 596-612.

Vanoni, V.A. and Brooks, N.H., 1957. Laboratory studies of the roughness and suspended load of alluvial streams. California Inst. of Technology Sedimentation Laboratory, U.S. Army Engineer Division. *M.R.D. Sediment Series* 11, 121.

van Rijn, L. C., 2007. Unified view of sediment transport by currents and waves III: Graded beds. *Journal of Hydraulic Engineering* 133, 761-775.

van Rijn, ,L.C., 1981. *Computation of bed-load concentration and bed laod transport*. Delft Hydraulics Laboratory, Research Report S487-I, Delft, The Netherlands.

van Rijn, ,L.C., 1982. *Computation of bed-load concentration and bed laod transport*. Delft Hydraulics Laboratory, Research Report S487-II, Delft, The Netherlands.

van Rijn, L., 1984a. Sediment transport, Part II: Suspended load transport. *Journal of Hydraulic Engineering* 110, 1613-1641.

van Rijn, L. C., 1984b. Sediment pick-up functions. *Journal of Hydraulic Engineering*110 (10), 1494-1502.

van Rijn, L., 2007. Unified view of sediment transport by currents and waves. I: Initiation of motion, bed roughness, and bed-load transport. *Journal of Hydraulic Engineering* 133 (6), 649-667.

Vericat, D., and Batalla, R. J., 2005. Sediment transport in a highly regulated fluvial system during two consecutive floods (lower Ebro River, NE Iberian Peninsula). Earth Surface Processes and Landforms 30(4), 385-402.

Visconti, F., Camporeale, C., Ridolfi, L., 2010. Role of discharge variability on pseudo-meandering channel morphdynamics: results from laboratory experiments. *Journal of Geophysical Research - Earth Surface* 115, F04042.

Vitali R., Bartolettim G., Ioannilli, E., 1995. Enel experience in the environmental management of maintenance of hydroelectric reservoirs. *Hydroécologie Appliqué* 7, 51-74.

Villaret, C., Hervouet, J-F., Kopmann, R., Merkel, U., Davies, A.G., 2013. Morphodynamic modeling using the Telemac finite-element system. *Computers and Geosciences* 53, 105–113.

Voogt, L., van Rijn, L. C., v.d. Berg, J. H., 1991. Sediment transport of fine sands at high velocities. *Journal of Hydraulic Engineering* 117, 869-890.

Westerweel, J. and Scarano, F., 2005. Universal outlier detection for PIV data. *Experiments in Fluids* 39, 1096-1100.

White R., 2001. *Evacuation of sediments from reservoirs*. Thomas Telford, London, 17–36.

Wilcock, P. R. and Kenworthy, S. T., 2002. A two-fraction model for the transport of sand/gravel mixtures. *Water Resources Research* 38, 10. doi:10.1029/2001WR000684.

Wren, D. G., Langendoen, E. J., Kuhnle, R.A., 2011. Effects of sand addition on turbulent flow over an immobile gravel bed. *Journal of Geophysical Research* 116, F01018.

Wren, D. G., Kuhnle, R. A., Langendoen, E. J., Rigby, J. R., 2014. Turbulent Flow and Sand Transport over a Cobble Bed in a Laboratory Flume. *Journal of Hydraulic Engineering* 140 (4), 04014001.

Wright, S. and Parker, G., 2004. Flow resistance and suspended load in sand-bed rivers: Simplified stratification model. *Journal of Hydraulic Engineering* 130, 796-805.

Wu, W. and Wang, S.S., 2007. One-dimensional modeling of dambreak ow over movable beds. *Journal of Hydraulic Engineering* 133, 48-58.

Wu, W., Wang, S. S., Jia, Y., 2000. Nonuniform sediment transport in alluvial rivers. *Journal of Hydraulic Research* 38, 427-434,.

Wohl, E., McConnell, R., Skinner,J., Stenzel, R., 1998. *Inheriting our past: river sediment sources and sediment hazards in Colorado*. Colorado Water Resources Research Institute.

Wohl, E. E., 2000. *Mountain rivers*. Water Resources, Monograph 14. American Geophysical Union, Washington, DC.

Wooster, J. K., Dusterhoff, S. R., Cui, Y., Sklar, L. S., Dietrich, W. E., Malko, M., 2008. Sediment supply and relative size distribution effects on fine sediment infiltration into immobile gravels. *Water Resources Research* 44, W03424, doi: 10.1029/2006WR005815.

Wohl, E. and Cenderelli, D. A., 2000. Sediment deposition and transport patterns following reservoir sediment release. *Water Resources Research* 36(1), 319-333.

Wohl,E. and Rathburn, S., 2003. Mitigation of sedimentation hazards downstream from reservoirs. *International Journal of Sediment Research*18, 97-106.

Wu, J and Hong, Y., 1989. Impact of impoundment and sediment flushing of Gezhouba Reservoir on water quality. In *Fourth International Symposium on River Sedimentation,* 1276-1283, June 5-9, Benjing, China.

Wildi, W., Dominik, J., Loizeau, J. L., Thomas, R. L., Favarger, P. Y., Haller, L., Peytremann, C., 2004. River, reservoir and lake sediment contamination by heavy metals downstream from urban areas of Switzerland. *Lakes & Reservoirs: Research & Management* 9(1), 75-87.

Yang, C.T. and Simões, F.J., 1998. Simulation and prediction of river morphologic changes using GST ARS 2.0. In *Proceedings of Third International Conference on Hydro-Science and Engineering*, Cottbus Berlin, Germany, Aug. 31-Sept. 3.

Zuellig, R. E., Kondratieff, B. C., Rhodes, H. A., 2002. Benthos recovery after an episodic sediment release into a Colorado Rocky Mountain River. *Western North American Naturalist* 62(1), 59-72.

Zarfl, C., Lumsdon, A. E., Berlekamp, J., Tydecks, L., Tockner, K., 2015. A global boom in hydropower dam construction. *Aquatic Sciences* 77(1), 161-170.

Zolezzi, G., Siviglia, A., Toffolon, M., Maiolini, B. , 2011. Thermopeaking in alpine streams: event characterization and time scales. *Ecohydrology* 4, 564-576.

Zyserman, J. and Fredsoe, J., 1994. Data analysis of bed concentration of suspended sediment. *Journal of Hydraulic Engineering* 120, 1021-1042.

APPENDICES

Appendix A   Figures related to the outputs of gravel surface data analysis
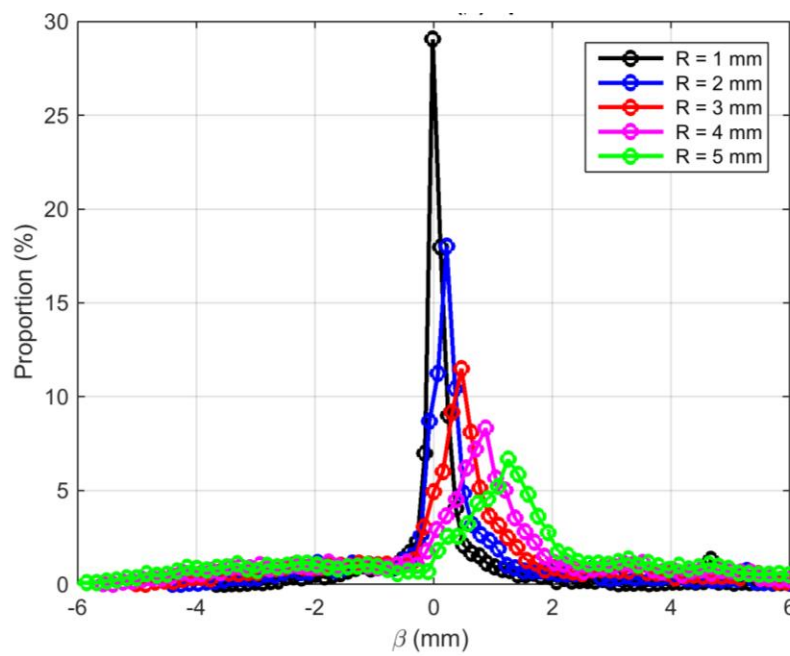
Figure A-1. The distribution of β of surface elevation of sphere bed for AMNF (R = 1.0 -5.0 mm)
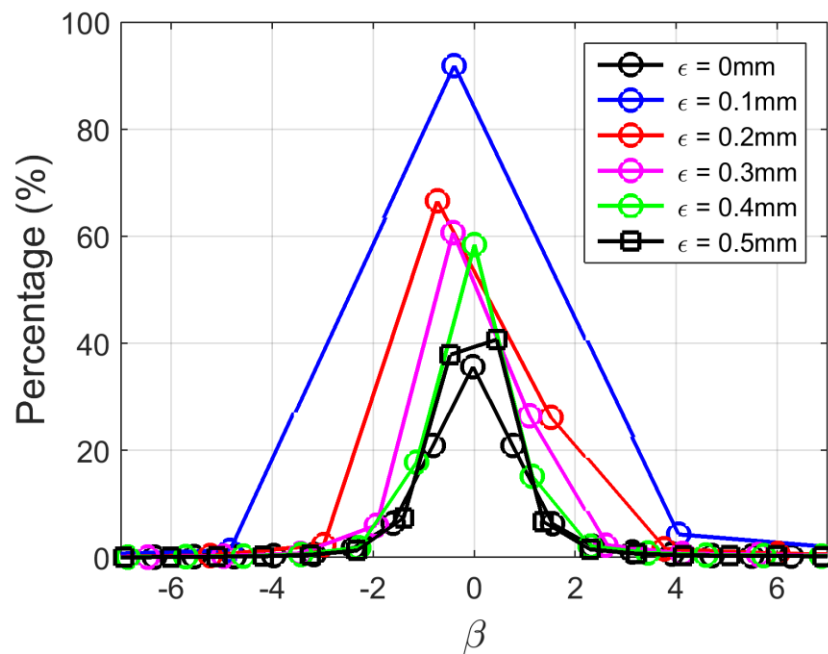
Figure A-2. The distribution of β of surface elevation of gravel for nAMDF (R =4mm and ε = 0 - 0.5mm)

Appendix B   Figures related to the outputs of image analysis
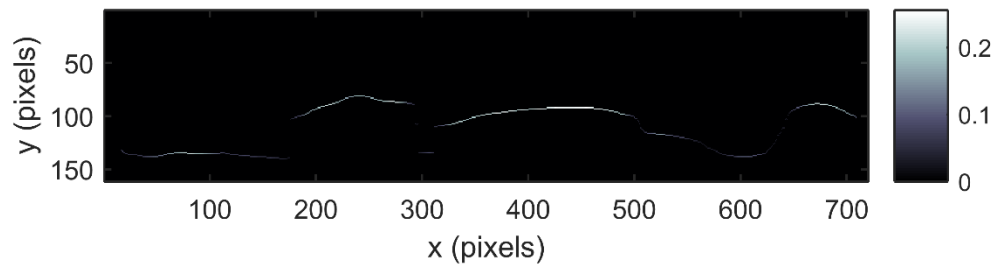

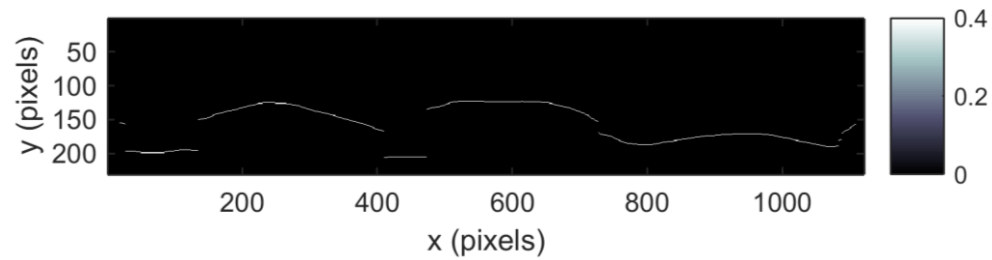Figure B-3. Reference image to identify regions of sand and gravel along the laser line (Plane 1)

Figure B-4. Reference image to identify regions of sand and gravel along the laser line (Plane 2)
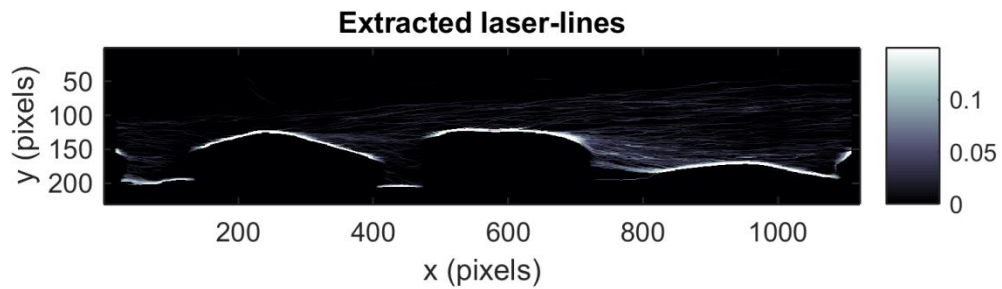
Figure B-5. Image positions of all laser lines that are used to estimate erosion rate (Plane 2, full sand cover)
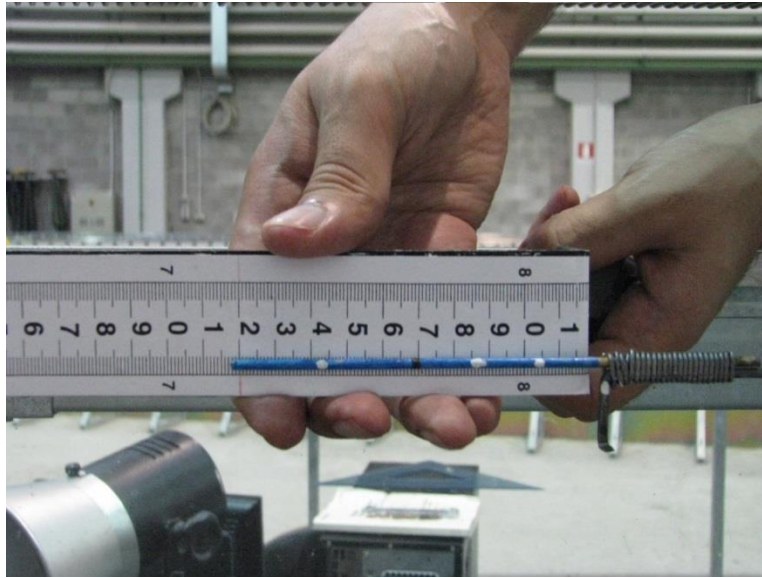
Figure B-6. Estimation of calibration rode length used to estimate horizontal scale of images
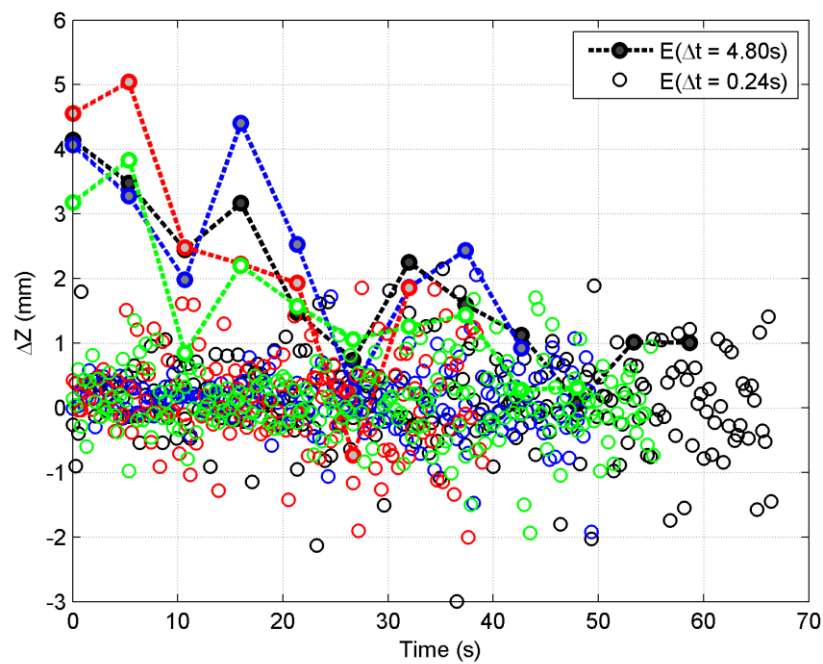
Figure B-7. Depth of erosion estimates for partial sand cover condition based on fine sediment bed level $\Delta t = 0.24s$ and $\Delta t = 4.8s$ (Plane 1)

Appendix C   Figures related to analysis of shear stress distribution in gravels bed flow from experiments reported in literatures
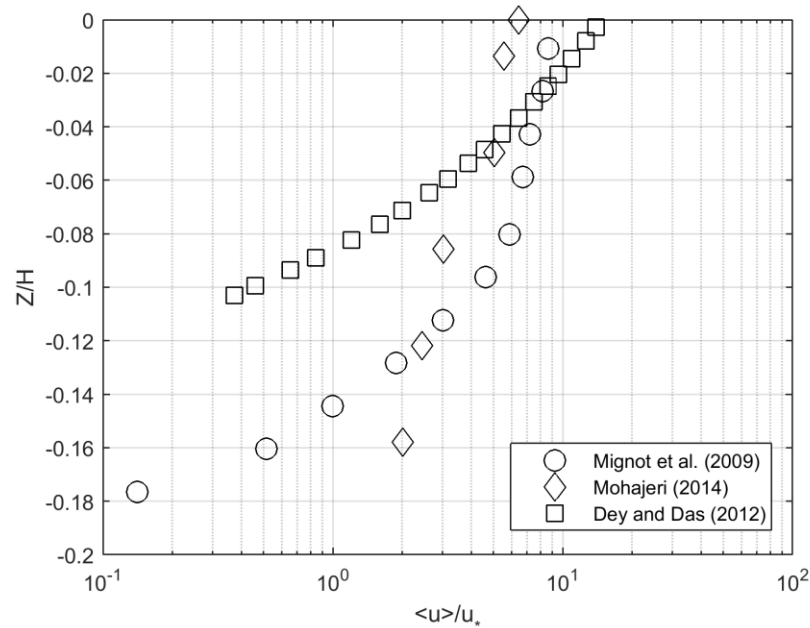

Figure C-8. Velocity profile in the interfacial sublayer of gravel bed estimated from experiments of published research
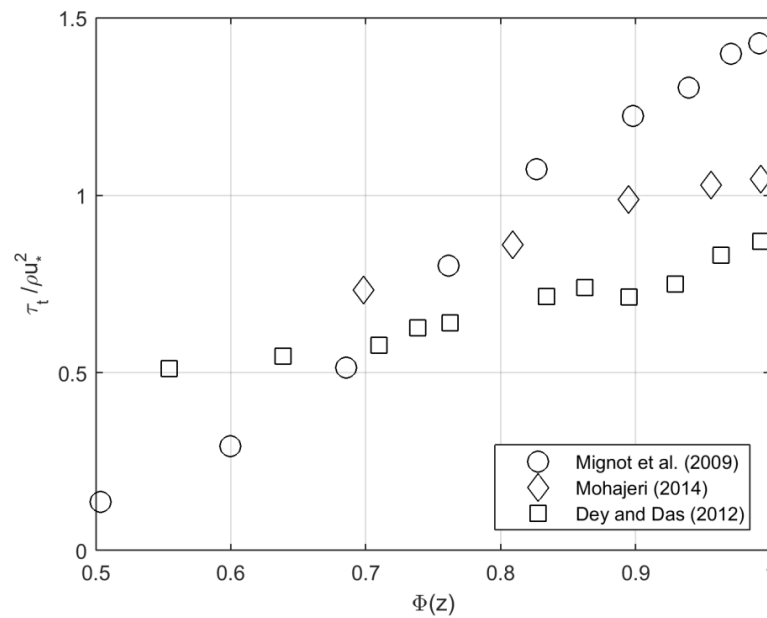
Figure C-9. The relationship between porosity and shear stress in interfacial sublayer estimated from experiments of published research
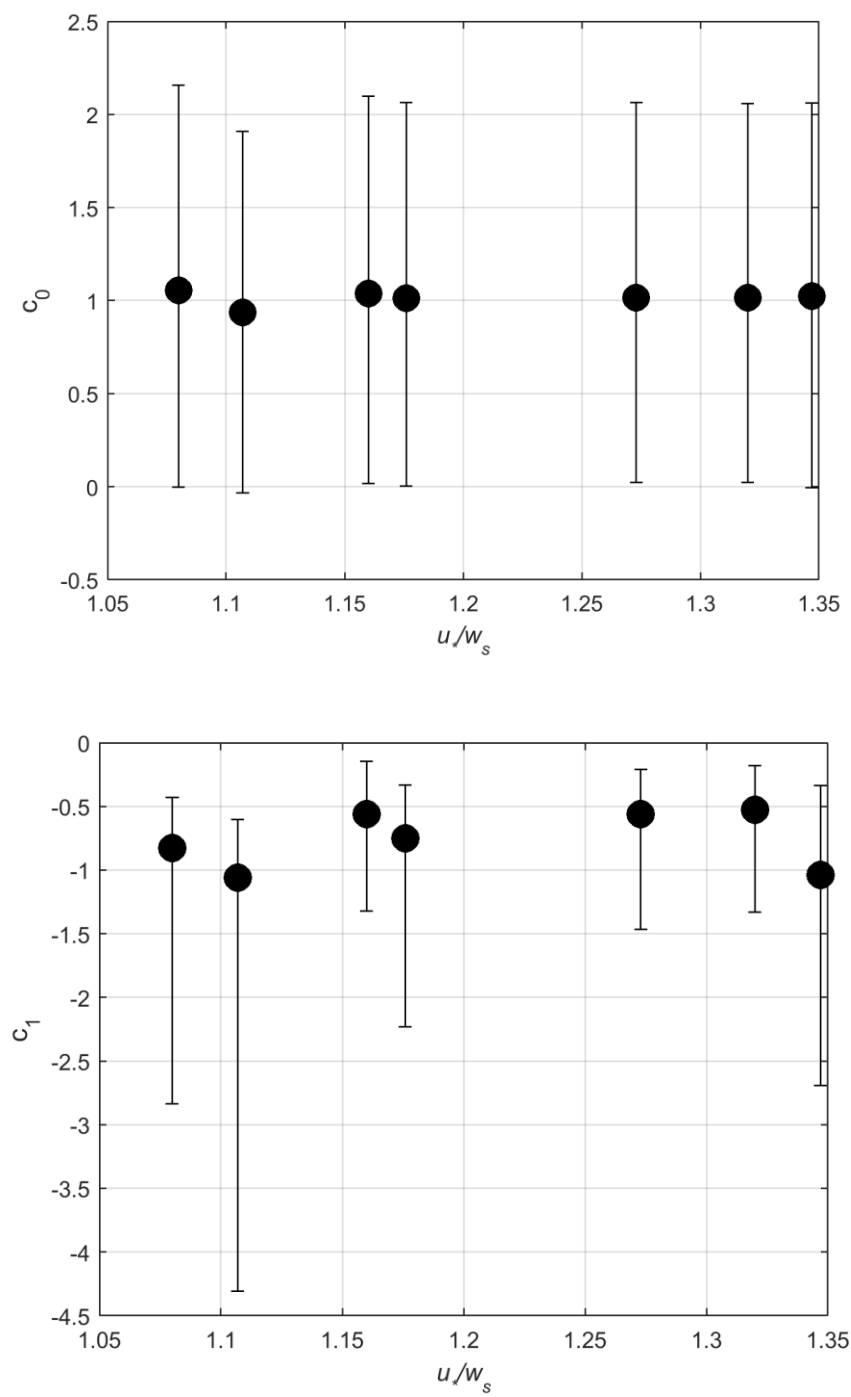
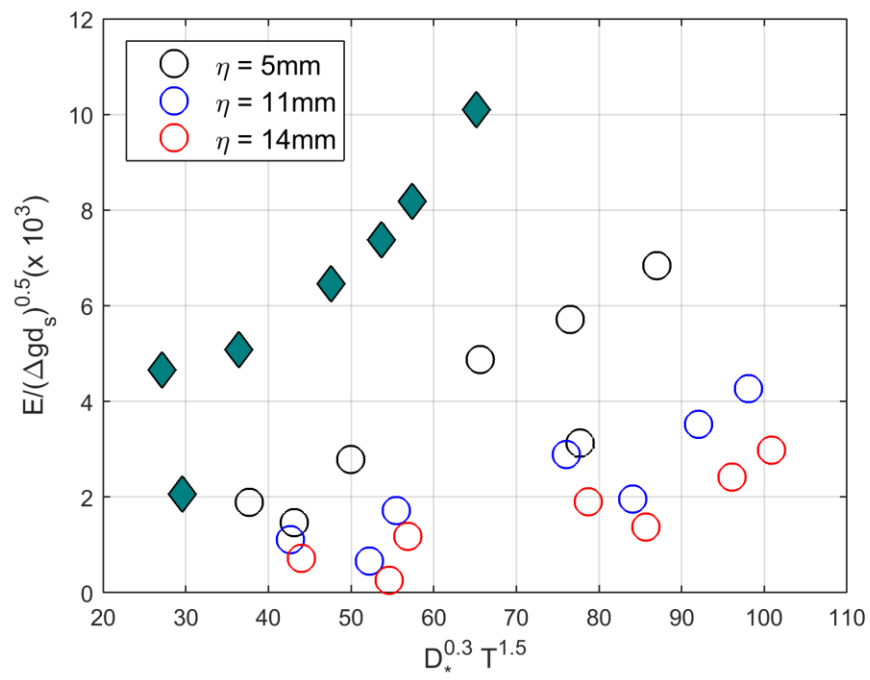Figure C-10. Empirical coefficients (C_0 and C_1) of erosion rate prediction

Figure C-11. Observed dimensionless erosion rates plotted against T estimate from momentum supply

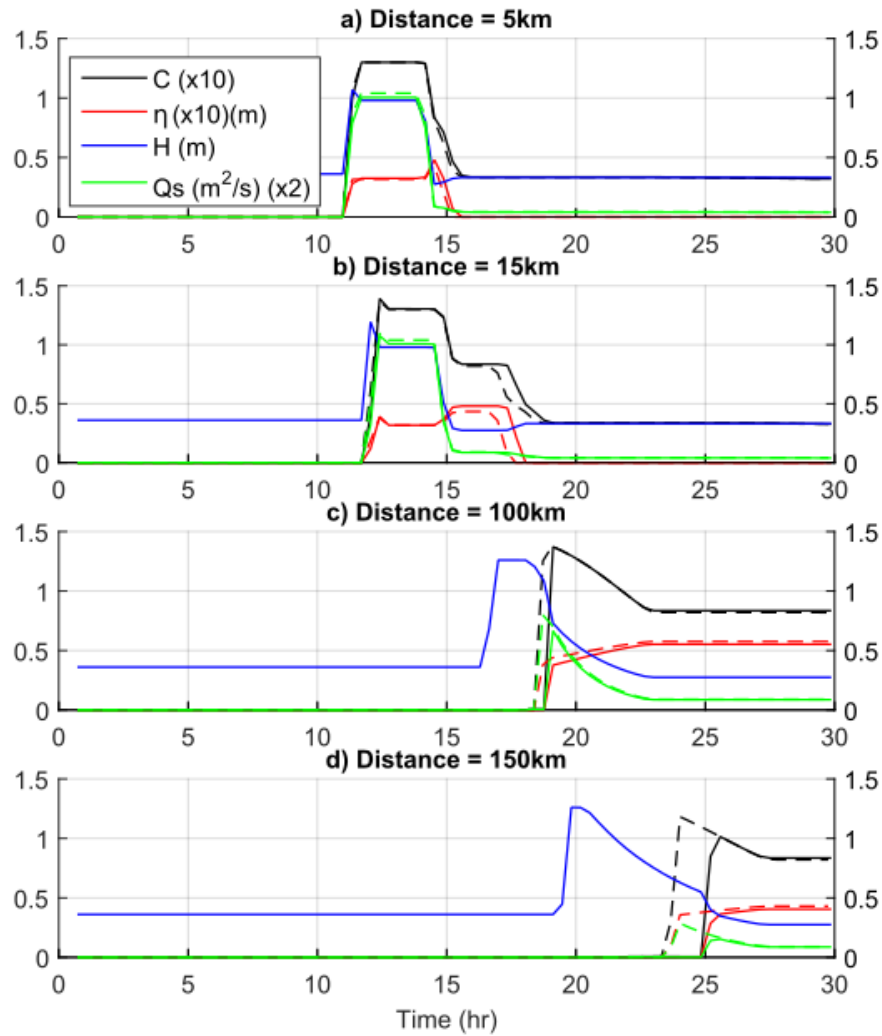**Appendix D**   Figures related to temporal dynamics of sediment flushing

Figure D-12. The various phases of the temporal wave dynamics with celerity correction α < 1 (solid lines) and without (α = 1, broken lines): flow depth (h) (blue line), concentration (C) (dark line), and suspended load (qₛ) (green line) and deposition thickness (η) (red line)
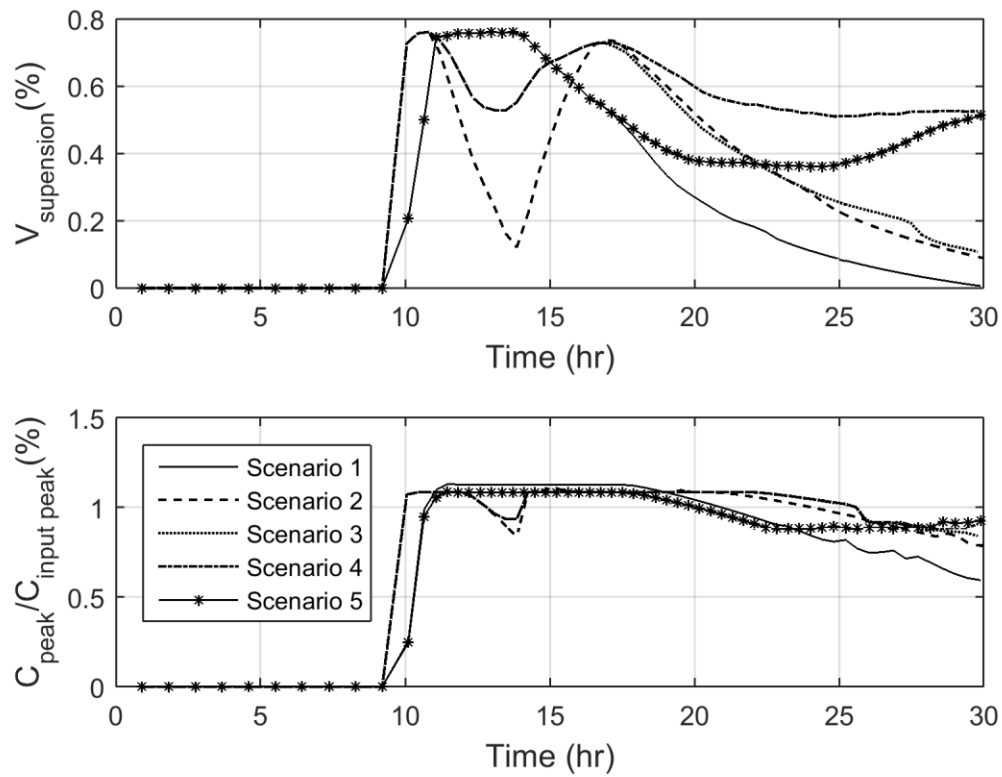
Figure D-13. Comparison of volume of sediment in suspension (top) and the proportion of peak of concentration in the simulation domain (bottom) for selected flushing followed by clear water releases ($C_{input\ peak}$ = peak of upstream boundary condition and C_{peak} = peak of concentration in simulation domain at a given time step)